

**Experimental and Computational Insight into Human Mesenchymal Stem Cell Effects on  
Cardiac Contractility and Arrhythmogenicity**

By

Joshua Mayourian

A dissertation submitted to the Graduate Faculty of the Graduate School of Biomedical Sciences Doctoral Program, in partial fulfillment of the requirements for the degree of Doctor of Philosophy, Icahn School of Medicine at Mount Sinai

2018

---

2018

Joshua Mayourian

All Rights Reserved

---

This manuscript has been read and accepted by the Graduate Faculty of the Graduate School of Biomedical Sciences, in satisfaction of the dissertation requirement for the degree of Doctor of Philosophy.

---

Dissertation Advisor: Kevin D. Costa, PhD

Date

---

Dean: Marta Filizola, PhD

Date

James Iatridis, PhD (chair)

Nicole Dubois, PhD

Jason Kovacic, MD, PhD

Fadi Akar, PhD

J. Jeremy Rice, PhD

Icahn School of Medicine at Mount Sinai

## **Abstract**

### **Experimental and Computational Insight into Human Mesenchymal Stem Cell Effects on Cardiac Contractility and Arrhythmogenicity**

By

Joshua Mayourian

Advisor: Kevin D. Costa, PhD

The statistically significant, but modest and transient, clinical benefits of delivering human mesenchymal stem cells (hMSCs) for treating heart disease warrant a better understanding of the underlying mechanisms of action to ultimately enhance and prolong treatment efficacy. Independent of well-established pro-angiogenic and anti-fibrotic mechanisms, hMSCs can modulate cardiac contractility and arrhythmogenicity via a number of partially understood mechanisms. In my thesis, I aim to better understand these mechanisms by addressing three interrelated questions: 1) What are the relative contributions of the two predominant components of the hMSC-cardiomyocyte interactome—namely paracrine signaling (PS) and heterocellular coupling (HC)—in modulating cardiac contractility and arrhythmogenicity? 2) Is the soluble or insoluble exosomal fraction of the hMSC paracrine secretome primarily responsible for these dominant paracrine-mediated effects on contractility? and 3) Which microRNA cargo are responsible for the hMSC exosome-enriched fraction largely modulating contractility, and through what mechanism? Throughout my thesis, I address these questions by integrating tissue engineering and computational approaches.

To address question 1, I first developed novel models of hMSC PS and HC effects on cardiomyocytes; excitation-contraction simulations of hMSC PS-only and combined HC+PS effects on human cardiomyocytes were representative of human engineered cardiac tissue

(hECT) contractile function measurements under matched experimental treatments. Model simulations and hECTs demonstrated hMSC-mediated effects were most pronounced under PS-only conditions, where developed force increased approximately 4-fold compared to non-hMSC-supplemented controls during 1-Hz pacing. Dominance of hMSC PS was also revealed in simulations of fibrotic cardiac tissue, where hMSC PS protected from potential pro-arrhythmic effects of HC at various levels of engraftment, consistent with reported clinical observations.

To address question 2, proteomic analysis of media conditioned by hMSC-supplemented hECTs predicted activation of PI3K/Akt signaling, a recognized target of both soluble and exosomal fractions of the hMSC secretome. Treating hECTs with exosome-enriched, but not exosome-depleted, fractions of the hMSC secretome recapitulated the effects observed with hMSC conditioned media on hECT developed force and expression of calcium handling genes (e.g., SERCA2a, L-type calcium channel), demonstrating the predominant role of exosomes in hMSC-mediated enhancement of cardiac contractility.

Finally, to answer question 3, I integrated systems biology and hECT technologies to identify microRNA-21-5p (miR-21-5p) as a lead hMSC cardioactive exosomal miR. Delivery of miR-21-5p recapitulates effects of hMSC exosome treatment on hECT contractile function, while knocking down miR-21-5p in hMSCs diminishes exosomal enhancement of contractility. Mechanistically, miR-21-5p increases calcium handling and thereby contractility likely via the PI3K signaling cascade.

Altogether, this dissertation provides novel experimental and computational insight into hMSC effects on human cardiac tissue contractility and arrhythmogenicity. These findings support the safety of hMSC-based therapies in models of diseased myocardium, and provide a mechanistic foundation that may open up new avenues of research to harness the role of hMSC exosomes and their cargo (e.g., miR-21-5p) for optimizing future stem cell-based cardiotherapies, as well as human pluripotent stem cell-derived cardiomyocyte maturation techniques.

## **Acknowledgments**

This thesis would not have been possible without the help and support of those around me—both personal and professional. First, I would like to thank my academic and life mentor, Dr. Kevin Costa. Thank you for giving me an opportunity as a summer undergraduate student, helping me find my passion, providing advice 24/7, putting up with me knocking on your door constantly, interrupting your lunch, and allowing me to pursue my own custom track. I couldn't ask for a better role model, mentor, and friend. I would also like to thank my internal thesis committee members—Drs. Akar, Dubois, Iatridis, and Kovacic—for their guidance throughout the project and for supporting me and my timeline. I'd also like to thank my external thesis committee member, Dr. Jeremy Rice, for kindly giving me the unique opportunity to be an IBM Thomas J. Watson Intern.

Next, I'd like to thank my colleagues and friends in the Costa Lab and the Cardiovascular Research Center. Dr. Irene Turnbull—I couldn't ask for a more kind, selfless, patient, and understanding colleague and friend. Thank you for always being there for me, patiently teaching me techniques, and allowing me to bounce ideas off of you. Dr. Delaine Ceholski—it has been a pleasure collaborating with you on nearly all my projects. I'm lucky to have you as a collaborator and friend; I look forward to working together again in the future. I'd also like to thank Dr. Susmita Sahoo and her lab for all the wonderful collaborations. Finally, Dr. Roger Hajjar—thank you for all your mentorship, support, advice, and feedback.

I'd also like to thank several experts in the computational cardiology field—Drs. Sobie, Rice, and Gurev—for all their wisdom, advice, and feedback in all relevant *in silico* projects. It has been a pleasure learning from you.

Finally, I'd like to thank my family for their unconditional love and support throughout this adventure. None of this would have been possible without you. I love you all and could not be more thankful for having every one of you in my life.

## **Dedication**

To my fiancée and best friend, Danielle Weiss. I love you.

<b>Table of Contents</b>	<b>Page</b>
Title	i
Copyright	ii
Approval	iii
Abstract	iv
Acknowledgments	vi
Dedication	viii
Table of Contents	ix
List of Main Figures	xviii
List of Main Tables	xxi
Chapter I: Introduction	1
1.1 Ischemic and Non-Ischemic Cardiomyopathy Progression to Heart Failure	1
1.2 Overview of Cell Therapies for Ischemic and Non-Ischemic Cardiomyopathy	3
1.3 Human Mesenchymal Stem Cell Therapy for Heart Disease	4
1.4 Human Mesenchymal Stem Cell Mechanisms of Action	4
1.5 Summary and Conclusions	6
1.6 Project Introduction and Summary	6
1.6.1 Project I: Physiologic, Pathologic, and Therapeutic Paracrine Modulation of Cardiac Excitation-Contraction Coupling	9
1.6.2 Project II: An Introduction to Tissue Engineering and Computational Approaches to Investigate Modulation of Cardiac Electrophysiology and Contractility	10
1.6.3 Project III: Modeling Electrophysiological Coupling and Fusion Between Human Mesenchymal Stem Cells and Cardiomyocytes	11
1.6.4 Project IV: Experimental and Computational Insight into Human Mesenchymal Stem Cell Paracrine Signaling and Heterocellular	12

Coupling Effects on Cardiac Contractility and Arrhythmogenicity	
1.6.5 Project V: microRNA-21-5p as an Exosomal Mediator of Mesenchymal Stem Cell Paracrine Effects on Human Cardiac Tissue Contractility	14
1.6.6 Project VI: Improved Prediction of Drug Torsadogenicity by Machine Learning with Tissue-level Electrophysiology Simulations	14
1.7 References	16
 Chapter 2: Physiologic, Pathologic, and Therapeutic Paracrine Modulation of Cardiac Excitation-Contraction Coupling	30
2.1 Abstract	31
2.2 Introduction	32
2.3 Paracrine Effects of Cardiac Endothelial Cells on Cardiomyocyte ECC	36
2.3.1 Endothelial Nitric Oxide	38
2.3.2 Endothelial Endothelin-1	39
2.4 Paracrine Effects of Cardiac Fibroblasts on Myocyte ECC	40
2.4.1 Fibroblast-Derived Soluble Factors Can Mediate Cardiomyocyte Hypertrophy	41
2.4.2 Fibroblast-Derived Insoluble Extracellular Vesicles Mediate Cardiomyocyte Hypertrophy	42
2.4.3 Fibroblast Paracrine Factor Effects on Electrophysiology	42
2.4.4 Fibroblast-Derived Paracrine Mediators of ECC and Contractility	44
2.5 Stem Cell Secretomes Can Impact Cardiomyocyte ECC	45
2.5.1 Kinetics of Stem Cell Paracrine Effects on ECC	46
2.5.2 CPC Paracrine Effects on Cardiomyocyte ECC	46
2.5.3 MSC Paracrine Effects on Electrophysiology	47
2.5.4 MSC Paracrine Effects on Calcium Handling	49

2.5.5 MSC Paracrine-Mediated Effects of Cardiac Contractile Function	49
2.5.6 Underlying Mechanisms of MSC Paracrine Effects on ECC	50
2.5.7 Proposed MSC Factors Responsible for Enhancing ECC	51
2.6 Tissue Engineering Approaches to Study Non-Cardiomyocyte Paracrine Effects on Cardiac Contraction	53
2.6.1 Human Engineered Cardiac Tissues as an in vitro Contractility Assay	53
2.6.2 Limitations of Human Engineered Cardiac Tissues	60
2.7 Systems Biology Approaches to Study Stem Cell Paracrine Effects on ECC	60
2.8 Integrating Tissue Engineering and Systems Biology Approaches to Identify Novel Cardioactive Factors	62
2.9 Conclusions	63
2.10 References	64
Chapter 2 Supplementary Material	86
 Chapter 3: An Introduction to Functional Testing of Healthy and Injured Human Engineered Cardiac Tissues	92
3.1 Abstract	93
3.2 Introduction	94
3.3 Materials	95
3.3.1 Cell Collection	95
3.3.2 Tissue Formation	95
3.3.3 Bioreactor Construction	96
3.3.4. Data Acquisition	96
3.4 Methods	97
3.4.1 Cardiomyocyte differentiation of hiPSCs	97
3.4.2. Preparing the Single-Tissue Bioreactor	98

3.4.3. Preparing the Multi-Tissue Bioreactor	99
3.4.4 Collecting hiPSC-CMs from the Monolayer	99
3.4.5. Preparing the Collagen/Matrigel Mix	100
3.4.6. Forming hECTs on the Single-Tissue Bioreactor	101
3.4.7 Forming hECTs Using the Multi-Tissue Bioreactor	101
3.4.8 Data Acquisition for Single-hECT and Multi-hECT Bioreactors	102
3.4.9 Cryo-injury hECT cardiomyopathy model	104
3.4.10. Doxorubicin-induced hECT cardiomyopathy model	106
3.5 Notes	108
3.6 References	111
Chapter 4: An Introduction to Computational Modeling of Cardiac	113
Electrophysiology and Arrhythmogenicity	
4.1 Abstract	114
4.2 Introduction	115
4.2.1 Why Do We Need Mathematical Models in Basic and Translational Research?	115
4.2.2 Multi-Scale Characteristics of Cardiac Electrophysiology	116
Models and Their Applications	
4.2.3 Chapter Overview	118
4.3 Brief Overview of Adult Human Cardiomyocyte Electrophysiological	119
Properties	
4.4 Methods	121
4.4.1 How to Model Ion Channel Activity	121
4.4.2 How to Model Whole-Cardiomyocyte Electrophysiology	126
4.4.3 How to Model Cardiac Tissue Strands	129
4.5 Applications of Cardiac Electrophysiology Models	132

4.5.1 Applications of Single-Cell Models: Predicting Torsadogenic Drugs	132
4.5.2 Applications of Tissue-Level Models: Predicting Stem Cell Effects on Electrical Properties of Fibrotic Heart Tissue	135
4.6 References	138
Chapter 5: Modeling Electrophysiological Coupling and Fusion between Human Mesenchymal Stem Cells and Cardiomyocytes	143
5.1 Abstract	145
5.2 Author Summary	146
5.3 Introduction	147
5.4 Methods	149
5.4.1 hMSC Model Development	149
5.4.2 Modeling hMSC Ionic Currents	149
5.4.3 Calcium activated potassium channel current.	150
5.4.4 Delayed rectifier potassium channel current	152
5.4.5 L-type calcium current	154
5.4.6 Transient outward potassium channel current	155
5.4.7 TTX-sensitive sodium channel current	155
5.4.8 Leakage channel current	156
5.4.9 Ion channel assumptions	156
5.4.10 hMSC-hCM Single-Cell Interactions	157
5.4.11 Modeling passive hMSC-hCM coupling	158
5.4.12 Modeling hMSC-hCM fusion	158
5.4.13 Modeling hMSC-hCM Coupling at the Tissue Level	158
5.4.14 Sensitivity Analysis	160
5.5 Results	161

5.5.1 hMSC Electrophysiology Model	161
5.5.2 Simulations of hCM-hMSC Coupling and Fusion	162
5.5.3 Cell coupling and fusion effects on action potential waveform.	162
5.5.4 Sensitivity analysis	169
5.5.5 Vulnerable Window Analysis	171
5.6 Discussion	174
5.6.1 Comparison of Model Results to Empirical Findings	175
5.6.2 Mechanistic Insights into hMSC-hCM Coupling	176
5.6.3 Potential Pathophysiological Consequences of hMSC-hCM Coupling	177
5.6.4 Implications of Findings for Future Cardiotherapies	179
5.6.5 Limitations and Future Work	180
5.7 References	183
Chapter 5 Supplementary Material	194
 Chapter 6: Experimental and Computational Insight into Human Mesenchymal Stem Cell Paracrine Signaling and Heterocellular Coupling Effects on Cardiac Contractility and Arrhythmogenicity	220
6.1 Abstract	221
6.2 Novelty and Significance	223
6.3 Introduction	225
6.4 Methods	226
6.5 Results	226
6.5.1 Multi-Species Parameter Sensitivity Analysis Reveals Key hMSC PS-Modulators of Cardiomyocyte Action Potential and Calcium Handling Metrics	226
6.5.2 Experimental Calibration of the hMSC PS Model	227

6.5.3 hMSC PS and HC Effects on Action Potential and Calcium Handling Behavior	230
6.5.4 Counteracting Effects of hMSC PS and HC on hECT Contractility	232
6.5.5 hMSC PS Protects from HC Effects on Arrhythmogenicity	238
6.5.6 Proteomic Analysis of Experimental Culture Media	240
6.5.7 Exosomes Play a Key Role in Mesenchymal Stem Cell-Mediated Increase of hECT Contractile Function	242
6.6 Discussion	244
6.6.1 Motivation for Model Development	245
6.6.2 Experimental Calibration of the hMSC PS Model	246
6.6.3 Model is Representative of Empirical Data	246
6.6.4 Nature of the hMSC Paracrine-Mediated Increase of hECT Contractility	247
6.6.5 Limitations and Future Work	248
6.7 Conclusions	249
6.8 References	251
Chapter 6 Supplementary Material	258
Chapter 7: Exosomal microRNA-21-5p Mediates Mesenchymal Stem Cell Paracrine Effects on Human Cardiac Tissue Contractility	294
7.1 Abstract	295
7.2 Novelty and Significance	297
7.3 Introduction	299
7.4 Methods	300
7.4.1 Partial Least Squares Regression	300
7.4.2 hECT Contractility Assay	300
7.4.3 Western Blots of Lysate from hPSC-CM Monolayers	301
7.4.4 Calcium Transient Measurements	301

7.4.5 Single-Cell Cardiomyocyte Electrophysiology Models	301
7.4.6 Experimental Calibration of miR-21-5p Effects	302
on Single-Cell Cardiomyocyte Electrophysiology	
7.4.7 Statistical Analyses	303
7.5 Results	303
7.5.1 Lead Candidate Cardioactive hMSC Exosomal miRs Predicted via PLSR	303
7.5.2 miR-21-5p Effects on hECT Contractile Function	308
7.5.3 Knockdown of miR-21-5p in hMSC Diminishes Exosomal Effects on	310
hECT Contractile Function	
7.5.4 miR-21-5p Increases Calcium Handling Gene Expression	312
7.5.5 miR-21-5p Increases hPSC-CM Calcium Transients Likely via the PI3K	314
Signaling Cascade	
7.5.6 Predicting the Effects of miR-21-5p in Ischemic Adult Human Cardiomyocytes	316
7.6 Discussion	319
7.6.1 PLSR for Predicting Lead Candidate Cardioactive miRs	320
7.6.2 Role of miR-21-5p in hMSC Exosome-Mediated	321
Increases in Cardiac Contractility	
7.6.3 Robustness of hMSC Exosome and miR-21-5p	321
Effects Across Human Stem Cell Lines	
7.6.4 Kinetics of hMSC-exo and miR-21-5p Effects on hECT Contractility	322
7.6.5 Human-Specific Effects of miR-21-5p on Cardiac Tissue Remodeling	323
7.6.6 Limitations and Future Directions	323
7.7 Conclusions	325
7.8 References	326
Chapter 7 Supplementary Materials	333

Chapter 8: Summary and Future Directions	350
8.1 Project I Future Directions	351
8.2 Project II Future Directions	351
8.3 Project III Future Directions	352
8.4 Project IV Future Directions	352
8.5 Project V Future Directions	353
8.6 References	354
Supplementary Chapter 9: Improved Prediction of Drug Torsadogenicity by Machine Learning with Tissue-level Electrophysiology Simulations	355
Chapter 9 Supplementary Materials	383

<b>List of Main Figures</b>	<b>Page</b>
Figure 1.1: Increased Survival of Ischemic Cardiomyopathy Patients Contributes to the Emerging Heart Failure Epidemic.	2
Figure 1.2: Schematic Illustrating the Relationship Between Each Chapter, Project, and Question in the Dissertation.	7
Figure 2.1: $\beta$ -Adrenergic Signaling and Cardiomyocyte ECC.	32
Figure 2.2: Endothelial-Cardiomyocyte Interplay Through Paracrine Factors.	37
Figure 2.3: Human Engineered Cardiac Tissue Contractility Assay.	54
Figure 2.4: Effects of hACF Conditioned Media on hECT Contractile Function.	56
Figure 2.5: Molecular Characterization of hECTs.	58
Figure 3.1: Overview of hECT Construction.	99
Figure 3.2: Overview of hECT data acquisition.	104
Figure 3.3: hECT Models of Acquired Cardiac Disease.	106
Figure 4.1: Typical flowchart for incorporating mathematical modeling into an experimental study to answer biological questions.	116
Figure 4.2: Multi-scale integration of experimental data into mathematical models to predict healthy and diseased cardiac electrophysiology.	117
Figure 4.3: Overview of cardiomyocyte action potential electrophysiology.	120
Figure 4.4: Modeling the hERG rapid delayed rectifier ion channel.	124
Figure 4.5: Modeling the human adult cardiomyocyte action potential	128
Figure 4.6: Modeling Action Potential Propagation in a 1-Dimensional Tissue Strand.	130
Figure 4.7: Using Single-Cell Models to Predict Drug-Induced Arrhythmias.	134
Figure 4.8: Modeling hMSC electrophysiological effects on 2-D fibrotic cardiac tissue.	136
Figure 5.1: <i>I-V</i> and Voltage Clamp Simulations of hMSC Currents.	151
Figure 5.2: Voltage-Sensor Transition Model for the Delayed Rectifier Current.	153
Figure 5.3: Total Current Simulations of the Triad of hMSC Families.	153

Figure 5.4: Effects of Direct hMSC-hCM Electrophysiological Interactions on hCM Action Potential.	164
Figure 5.5: Quantification of hCM Action Potential Waveform Following Direct hMSC-hCM Electrical Interactions.	165
Figure 5.6: hMSCs Act as Electrical Sources and Sinks in hCM APD Variations.	167
Figure 5.7: Key hMSC Outward Currents Involved in Electrical Sinking.	168
Figure 5.8: hCM APD Sensitivity to hMSC Current Parameters.	170
Figure 5.9: VW Analysis on Cardiac Tissue With Randomly Inserted hMSCs.	172
Figure 5.10: hMSC Effects on Dispersion of Refractoriness and Restitution Curves.	173
Figure 6.1: Experimentally Calibrating hMSC PS Effects.	228
Figure 6.2: hMSC PS and HC Effects on Multi-Species Cardiomyocyte Action Potential and Calcium Transient.	231
Figure 6.3: Schematic and Structure of hECTs in the Bioreactor.	234
Figure 6.4: Model Comparison with hECT Measurements Under hMSC HC and PS Interventions.	235
Figure 6.5: Simulated hMSC HC and PS Effects on Contractile Function of Derived and Adult Human Cardiomyocytes.	237
Figure 6.6: Simulated Vulnerable Window Analysis on hMSC-Supplemented Fibrotic Cardiac Tissue.	239
Figure 6.7: Proteomic Analysis of hECT Conditioned Media.	241
Figure 6.8. Effects of hMSC Exosomes on hECT Function and mRNA Levels.	243
Figure 7.1: Predicting Lead Candidate Cardioactive hMSC Exosomal miRs via PLSR.	305
Figure 7.2: miR-21-5p Effects on hECT Contractility.	309
Figure 7.3: Knockdown of miR-21-5p in hMSCs Diminishes Pro-Contractile Effects of Exosomes on hECT Contractility.	311
Figure 7.4: Molecular Characterization of miR-21-5p Effects	313

on hECTs and hPSC-CM Monolayers.

Figure 7.5: miR-21-5p Increases hPSC-CM Calcium Transients

315

Likely via the PI3K Signaling Cascade.

Figure 7.6: Experimentally Calibrating miR-21-5p Effects on

317

Human Cardiomyocyte Calcium Transients.

Figure 7.7: Working Hypothesis for hMSC Paracrine-Mediated Increases

319

in Cardiac Contractility.

<b>List of Main Tables</b>	<b>Page</b>
Table 2.11. Brief Summary of Non-Cardiomyocyte Paracrine Effects on Cardiomyocyte ECC	34-35

## **Chapter 1: Introduction**

### **1.1. Ischemic and Non-Ischemic Cardiomyopathy Progression to Heart Failure**

Heart failure—a chronic, progressive condition where cardiac muscle cannot pump sufficient blood to meet the body's needs for oxygen and blood<sup>1</sup>—remains a leading cause of morbidity and mortality in Western countries. With a prevalence of approximately 5.4 million in the United States alone,<sup>2</sup> it costs the nation approximately \$32 billion per year.<sup>3</sup> In Europe, it is the cause of approximately 5% of acute hospital admissions.<sup>2</sup> Despite advancements to treat end-stage heart failure (e.g., heart transplantation<sup>4</sup> or left ventricular assist devices<sup>5</sup>), it still has a dismal prognosis, where nearly 50% of patients die within 5 years of diagnosis.<sup>2</sup> Importantly, given the aging population and longer-term survival of patients with ischemic and non-ischemic cardiomyopathies, due to recent advances in revascularization techniques and medical therapy, the number of patients living with heart failure is increasing (Figure 1).<sup>1</sup>

Ischemic cardiomyopathy—defined as impaired left ventricular function (i.e., left ventricular ejection fraction  $\leq$  35-40%) resulting from coronary artery disease or myocardial infarction—is the cause of greater than 60% of systolic congestive heart failure.<sup>6,7</sup> While nearly 90% of patients with occluded coronary arteries achieve patency post-revascularization, ischemic cardiomyopathy can still progress to heart failure as: 1) approximately 25-30% of myocardial reperfusion fails;<sup>8</sup> and 2) ischemic symptoms via restenosis can reoccur after several years.<sup>1</sup> Figure 1 summarizes how longer-term survival of ischemic cardiomyopathy patients contributes to the emerging heart failure epidemic.

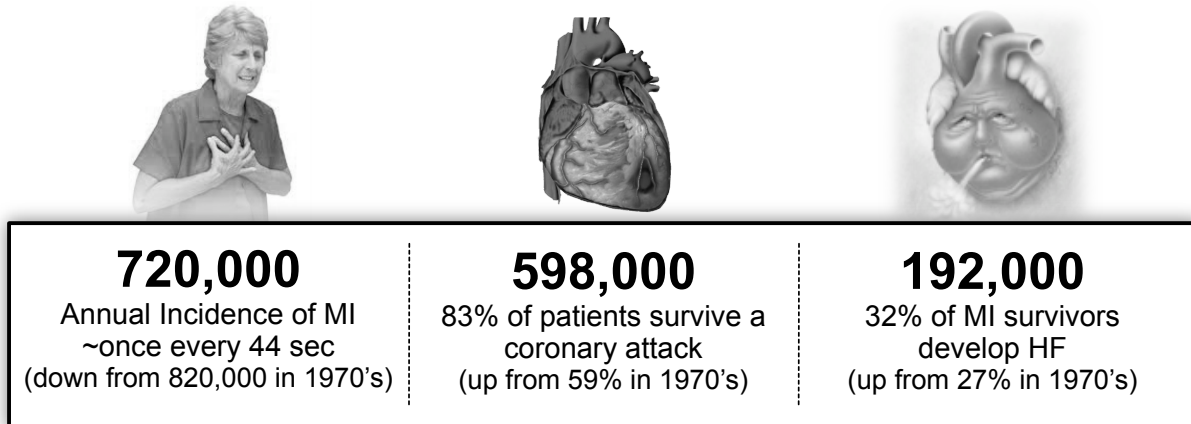


**Figure 1: Increased Survival of Ischemic Cardiomyopathy Patients Contributes to the Emerging Heart Failure Epidemic.** While the incidence of myocardial infarction (MI)—which may trigger ischemic cardiomyopathy—has decreased since the 1970's (left), more patients survive a coronary attack (middle), contributing to the stable incidence of heart failure progression (right). Adapted from Dr. Kevin Costa, PhD. Statistics within each panel originate from elsewhere.<sup>9,10</sup>

Similarly, non-ischemic dilated cardiomyopathy—defined as ventricular dilation and systolic dysfunction in the absence of coronary artery disease—can also progress to heart failure. Impacting 1 in 20,000 individuals per year,<sup>2</sup> it is the most common form of pediatric cardiomyopathy,<sup>11</sup> and is the leading diagnosis (54%) among heart transplant recipients.<sup>4</sup>

For the translational focus of my thesis, systolic heart failure, neurohormonal antagonists are typically used to manage impaired ventricular systolic function and heart failure symptoms.<sup>12</sup> While neurohormonal antagonists—including agents that block the renin-angiotensin-aldosterone system and the sympathetic nervous system<sup>12</sup>—improve morbidity and mortality,<sup>13,14</sup> rates of morbidity and mortality still remain high as these pharmacological interventions do not fully address the underlying pathophysiology.

Altogether, these sobering statistics and lack of effective treatments motivate the development of novel treatments for cardiac restoration of lost contractile function following ischemic or non-ischemic cardiomyopathies to halt or reverse the progression of systolic heart failure.

## **1.2 Overview of Cell Therapies for Ischemic and Non-Ischemic Cardiomyopathy**

While current heart failure therapies improve symptoms and prolong life, they unfortunately do not address the underlying pathophysiological consequences previously described. The theorized curative potential of cell-based therapy using a variety of cell types has led to rapid, and in some cases premature, advancement toward clinical translation.<sup>15</sup>

For example, within only one year of preclinical testing of bone marrow cells for myocardial infarction,<sup>16</sup> they were applied in patients.<sup>17</sup> Similarly, within three years of preclinical testing of stem cells (skeletal myoblasts) for heart failure,<sup>18</sup> they were used in humans with limited success.<sup>19</sup> Since then, numerous preclinical<sup>20-41</sup> and clinical trials<sup>42-76</sup> have been performed for skeletal myoblast, bone marrow mononuclear cell, bone marrow progenitor cell, cardiac stem cell, and mesenchymal stem cell therapy for heart disease. A comprehensive review of these preclinical and clinical studies can be found elsewhere.<sup>15</sup>

At first, a majority of the cell-based clinical trials for patients with heart disease were conducted with autologous bone marrow mononuclear cells, primarily due to their immediate cell availability from the recipient patient.<sup>77</sup> However, the clinical outcomes tended to be negative,<sup>78</sup> which investigators attributed to the broad diversity of the bone marrow mononuclear cell population. Therefore, researchers searched for a specific stem cell subpopulation that is easy to isolate, culture, and manipulate ex vivo—a leading candidate was the human mesenchymal stem cell (hMSC).

### **1.3 Human Mesenchymal Stem Cell Therapy for Heart Disease**

Bone marrow-derived hMSCs—defined by their: 1) adherence to plastic in standard culture conditions; 2) expression of CD73, CD90, and CD105 in the absence of CD34, CD45, HLA-DR, CD14 or CD11b, CD79a, or CD19 hematopoietic surface molecules; and 3) capacity for differentiation into osteoblasts, adipocytes, and chondroblasts *in vitro*<sup>79</sup>—are being used at an exponentially growing rate for a wide range of therapeutic purposes in clinical trials.<sup>80</sup>

hMSC delivery is an emerging approach to treat both ischemic and non-ischemic cardiomyopathies. For patients with ischemic cardiomyopathy, hMSC treatment reliably induces neoangiogenesis and decreases myocardial infarction scar size by 30-50%,<sup>68,81,82</sup> thus beneficially attenuating some of the underlying pathophysiology. Such findings motivated the use of hMSCs for treating non-ischemic cardiomyopathies as well. In a recent clinical trial, Hare et al. demonstrated allogeneic hMSCs were more effective than autologous hMSCs for increasing ejection fraction and improving safety and efficacy endpoints in patients with non-ischemic dilated cardiomyopathy.<sup>83</sup> Furthermore, in a case study, intracoronary administration of autologous hMSCs to an 11-year-old boy with non-ischemic dilated cardiomyopathy and class IV heart failure led to an increase of left ventricular ejection fraction from 20% to 42%.<sup>84</sup>

Despite statistically significant benefits in the short term, the overall consensus on hMSC therapy for heart disease is that the effects on ejection fraction and safety and efficacy endpoints in clinical trials remain of modest magnitude and of limited long-term benefit,<sup>82,85</sup> thus representing an opportunity to improve the therapeutic design strategy. A rational approach to optimize hMSC therapy requires improved understanding of the underlying mechanisms of action.

### **1.4 Human Mesenchymal Stem Cell Mechanisms of Action**

Initially, hMSC transdifferentiation to cardiomyocytes and/or reprogramming of resident cardiomyocytes were hypothesized as key mechanisms of action;<sup>86</sup> however, these

mechanisms have since been largely debunked.<sup>87,88</sup> Since then, hMSCs have been theorized to be immunomodulatory,<sup>79,89</sup> to enhance angiogenesis,<sup>33,90,91</sup> and to decrease fibrosis<sup>33,88</sup> predominately through paracrine signaling mechanisms via soluble factors and exosomes.<sup>86,88,92</sup> These effects are clearly relevant to the underlying pathophysiology of ischemic and non-ischemic cardiomyopathies previously described.

Moreover, recent work has shown that hMSC paracrine factors can also affect cardiomyocyte electrophysiology and calcium handling, as well as modulate excitation-contraction coupling.<sup>93-95</sup> As will be discussed in Chapter 2, several unanswered questions remain in this field, which have become focal points of this dissertation. Specifically, the hMSC paracrine mediators of cardiomyocyte excitation-contraction coupling are unresolved. These effects are largely relevant to both ischemic and non-ischemic cardiomyopathies, where it is well-known that the underlying pathophysiology includes altered excitation-contraction coupling and diminished contractile function.<sup>96</sup>

In addition to paracrine signaling mechanisms, hMSCs have been shown to form gap junctions with cardiomyocytes,<sup>97</sup> leading to direct heterocellular coupling and spontaneous fusion<sup>98</sup> that can also influence cardiomyocyte electrophysiology and calcium handling. As discussed in Chapter 6, a key unanswered question—why hMSCs have been found to be pro-arrhythmic in vitro, but not in vivo—remains in this field as well, which has become another focal point of this dissertation.

Taken together, hMSC heterocellular coupling and paracrine signaling mechanisms have the potential to modulate single-cell cardiomyocyte action potential and calcium handling waveforms, as well as tissue-level conduction, constituting well-established determinants of excitation-contraction coupling and arrhythmogenicity in myocardium. In this dissertation, I aim to better understand the role that each of these mechanisms plays in affecting human cardiomyocyte contractility and arrhythmogenicity. In addition, I seek to identify key components of the hMSC secretome responsible for modulating cardiac contractility.

## **1.5. Summary and Conclusions**

hMSC delivery is an emerging approach to treat both ischemic and non-ischemic cardiomyopathies. However, in most clinical trials, hMSC-mediated effects remain modest and transient,<sup>82,85</sup> thus representing an opportunity for improvement. Optimizing hMSC therapy requires improved understanding of underlying mechanisms of action. hMSC heterocellular coupling and paracrine signaling mechanisms each have the potential to modulate contractility and arrhythmogenicity of myocardium. However, the relative contributions of hMSC-mediated heterocellular coupling and paracrine signaling mechanisms on these components of human cardiac function have yet to be established, reflecting challenges with isolating these effects in traditional *in vitro* and *in vivo* experimental preparations. In addition, hMSC paracrine modulators of cardiac excitation and contraction remain largely unresolved. A better understand of the underlying mechanisms and mediators may ultimately maximize the safety and efficacy of hMSC-based cardiac therapies.

## **1.6. Project Introduction and Summary**

For my dissertation, I integrate tissue engineering and computational approaches to develop insight into the following three questions on hMSC effects on cardiac contractility and arrhythmogenicity: 1) what are the relative contributions of the two predominant components of the hMSC-cardiomyocyte interactome—namely paracrine signaling (PS) and heterocellular coupling (HC)—in modulating cardiac contractility and arrhythmogenicity? 2) is the soluble or insoluble exosomal fraction of the hMSC paracrine secretome primarily responsible for these dominant paracrine-mediated effects on contractility? and 3) which microRNA cargo is responsible for the hMSC exosome-enriched fraction largely modulating contractility, and through what mechanism? These questions are addressed within seven chapters comprising five projects (Figure 2). One addition project is provided; it is beyond the scope of this focused

dissertation, and shows that computational approaches not only predict therapeutic interventions (the focus of my dissertation), but also screen for cardiotoxicity.

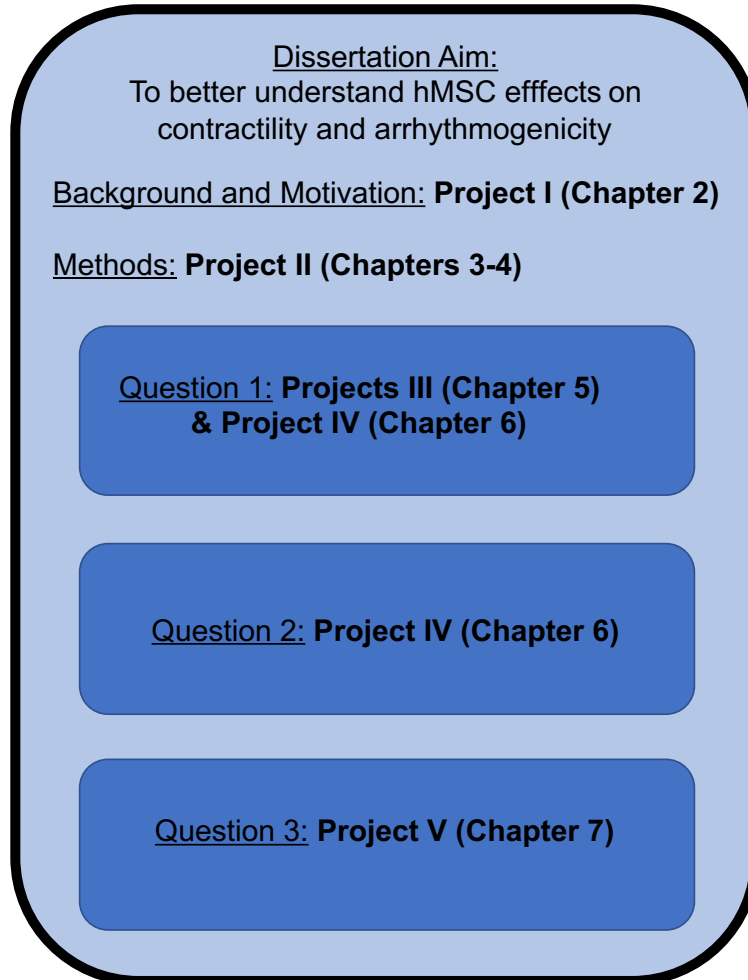


**Figure 2: Schematic Illustrating the Relationship Between Each Chapter, Project, and Question in the Dissertation.** As a whole, my thesis attempts to advance the field of hMSC-based cardiotherapies using an integrating tissue engineering and computational approach in three interrelated questions and five projects, corresponding to six main chapters. Bold chapters correspond to original text published or in press.

To provide background, motivation and methods for all three questions, I first provide background on physiologic, pathologic, and therapeutic paracrine modulation of excitation-

contraction coupling as a comprehensive literature review on the current state of the field (Chapter 2). In addition, I discuss the utility of tissue engineering and computational approaches to study paracrine effects on cardiac excitation-contraction coupling (Chapter 2). Next, I provide an introduction to methods and applications of tissue engineering (Chapter 3) and mathematical modeling (Chapters 4) to study physiological and pathophysiological cardiac electrophysiology and contractility—both focuses of my dissertation.

I subsequently utilize these two approaches to address question 1 and develop novel insight into relative contributions of hMSC heterocellular coupling and paracrine signaling effects on cardiac contractility and arrhythmogenicity (Chapters 5-6).

To address question 2, proteomic analysis of media conditioned by hMSC-supplemented hECTs predicted activation of PI3K/Akt signaling, a recognized target of both soluble and exosomal fractions of the hMSC secretome (Chapter 6). Treating hECTs with exosome-enriched, but not exosome-depleted, fractions of the hMSC secretome recapitulated the effects observed with hMSC conditioned media on hECT developed force and expression of calcium handling genes (e.g., SERCA2a, L-type calcium channel), demonstrating the predominant role of exosomes in hMSC-mediated enhancement of cardiac contractility (Chapter 6).

Finally, to answer question 3, I integrated partial least squares regression systems biology and hECT technologies to identify miR-21-5p as a lead candidate exosomal cargo responsible for hMSC paracrine-mediated increases in hECT contractility through the PI3K/Akt signaling cascade (Chapter 7).

Below, I provide a brief introduction into each project of my thesis; these projects cohesively provide novel experimental and computational insight into hMSC effects on human cardiac tissue contractility and arrhythmogenicity. In addition, Chapter 9 describes a project that extends the primary focus of this dissertation, which demonstrates the utility of computational approaches not only to predict therapeutic interventions (Chapters 5-7), but to also to screen for cardiotoxicity (Chapter 9). Altogether, the findings of my dissertation projects support the safety

of hMSC-based therapies in diseased myocardium *in silico*, and may open up new avenues of research to harness the role of hMSC exosomes and their cargo for optimizing future stem cell-based cardiotherapies.

#### *1.6.1 Project I: Physiologic, Pathologic, and Therapeutic Paracrine Modulation of Cardiac Excitation-Contraction Coupling*

In this combined experimental and literature review project (Chapter 2), I first focus on the paracrine-mediated effects of resident and therapeutic non-cardiomyocytes on cardiomyocyte hypertrophy, electrophysiology, and calcium handling, each of which can modulate cardiomyocyte excitation-contraction coupling (ECC), and then discuss the current knowledge about key paracrine factors and their underlying mechanisms of action. Next, I provide a case example demonstrating the promise of tissue-engineering approaches to study paracrine effects on tissue-level contractility. More specifically, I present new functional and molecular data on the effects of human adult cardiac fibroblast conditioned media on human engineered cardiac tissue (hECT) contractility and ion channel gene expression that generally not only agrees with published murine studies but also suggests intriguing species-specific differences. By contrast, paracrine secretions by human dermal fibroblasts had no discernible effect on hECT contractile function and gene expression, showing that fibroblast phenotype is also important. Finally, I discuss systems biology approaches to help identify key stem cell paracrine mediators of ECC and their associated mechanistic pathways. Such integration of tissue engineering and systems biology methods shows promise to reveal novel insights into paracrine mediators of ECC and their underlying mechanisms of action, ultimately leading to improved cell-based therapies for patients with heart disease.

The literature review and results of Project I were published in *Circulation Research* as a first-author publication:

**Mayourian J**, Ceholski DK, Gonzalez DM, Cashman TJ, Sahoo S, Hajjar RJ, Costa KD. Physiologic, Pathologic, and Therapeutic Paracrine Modulation of Cardiac Excitation-Contraction Coupling. *Circulation Research*. 2017; in press.

#### *1.6.2 Project II: An Introduction to Tissue Engineering and Computational Approaches to Investigate Modulation of Cardiac Electrophysiology and Contractility*

In this project, I provide a pair of methods articles as an introduction to non-biomedical engineers on utilizing tissue engineering and computational approaches (Chapters 3 and 4, respectively) to study cardiac electrophysiology and contractility.

In Chapter 3, I describe the use of human engineered cardiac tissues (hECTs)—autonomous, beating structures that recapitulate key aspects of native cardiac muscle physiology that offer an attractive alternative to traditional in vitro models—to advance our understanding and modeling of cardiac diseases in order to test therapeutic interventions, with a focus on contractile dysfunction in the setting of acquired forms of cardiomyopathies. Three major procedures are discussed in this chapter: 1) preparation of hECTs from human induced pluripotent stem cell-derived cardiomyocytes (hiPSC-CMs) on single- and multi-tissue bioreactors; 2) data acquisition of hECT contractile function on both of these platforms; and 3) cryo-injury and doxorubicin-induced hECT models of acquired cardiomyopathy.

In Chapter 4, I briefly introduce *in silico* methods to describe the dynamics of physiological and pathophysiological single-cell and tissue-level cardiac electrophysiology. Using a “bottom-up” approach, I first describe the basis of ion channel mathematical models. Next, I discuss how the net flux of ions through such channels leads to changes in transmembrane voltage during cardiomyocyte action potentials. By applying these fundamentals, I describe how action potentials propagate in models of cardiac tissue. In addition, I provide case studies simulating single-cell and tissue-level arrhythmogenesis, as well as promising approaches to circumvent or overcome such adverse events. Overall, basic

concepts and tools are discussed in this chapter as an accessible introduction to non-mathematicians to facilitate an understanding of electrophysiological modeling studies and communication with dry lab colleagues and collaborators.

Project II is in press as two publications (one first-author and one second-author):

Turnbull IC, **Mayourian J**, Murphy JF, Stillitano F, Ceholski DK, Costa KD. Cardiac Tissue Models of Inherited and Acquired Cardiomyopathies. *Methods in Molecular Biology* (in press).

**Mayourian J**, Sobie EA, Costa KD. An Introduction to Computational Modeling of Cardiac Electrophysiology and Arrhythmogenicity. *Methods in Molecular Biology* (in press).

#### *1.6.3 Project III: Modeling Electrophysiological Coupling and Fusion Between Human Mesenchymal Stem Cells and Cardiomyocytes*

In this project (Chapter 5), to better understand the electrophysiological consequences of direct heterocellular connections between hMSCs and human cardiomyocytes (hCMs), three original mathematical models were developed, representing an experimentally verified triad of hMSC families with distinct functional ion channel currents. The arrhythmogenic risk of such direct electrical interactions in the setting of healthy adult myocardium was predicted by coupling and fusing these hMSC models to a published human cardiomyocyte model. Substantial variations in action potential waveform—such as decreased action potential duration (APD) and plateau height—were found when hCMs were coupled to the two hMSC models (Types A and B) expressing functional delayed rectifier-like human ether à-go-go K<sup>+</sup> channel 1 (hEAG1); the effects were exacerbated for fused hMSC-hCM hybrid cells. The third family of hMSCs (Type C), absent of hEAG1 activity, led to smaller single-cell action potential alterations during coupling and fusion, translating to longer tissue-level mean action potential wavelength. In a simulated 2-D monolayer of cardiac tissue, re-entry vulnerability with low (5%) hMSC

insertion was approximately eight-fold lower with Type C hMSCs compared to hEAG1-functional hMSCs. A 20% decrease in APD dispersion by Type C hMSCs compared to hEAG1-active hMSCs supports the claim of reduced arrhythmogenic potential of this cell type with low hMSC insertion. However, at moderate (15%) and high (25%) hMSC insertion, the vulnerable window increased independent of hMSC type.

In summary, this project (Chapter 5) provides novel electrophysiological models of hMSCs, predicts possible arrhythmogenic effects of hMSCs when directly coupled to healthy hCMs, and proposes that isolating a subset of hMSCs absent of hEAG1 activity may offer increased safety as a cell delivery cardiotherapy at low levels of hMSC-hCM coupling.

The results of Project III were published in *PLoS Computational Biology* as a first-author publication. This publication was selected as an Editor's pick, and as the cover of the July 2016 issue:

**Mayourian J**, Savizky RM, Sobie EA, Costa KD. Modeling Electrophysiological Coupling and Fusion between Human Mesenchymal Stem Cells and Cardiomyocytes. *PLoS Comput Biol*. 2016;12(7):e1005014. doi:10.1371/journal.pcbi.1005014

#### *1.6.4 Project IV: Experimental and Computational Insight into Human Mesenchymal Stem Cell Paracrine Signaling and Heterocellular Coupling Effects on Cardiac Contractility and Arrhythmogenicity*

In this project (Chapter 6), I integrate experimental and computational approaches to better understand hMSC paracrine signaling (PS) and heterocellular coupling (HC) effects on human cardiac contractility and arrhythmogenicity. Extending my previous hMSC-cardiomyocyte HC computational model (Chapter 5), I incorporated experimentally calibrated hMSC PS effects on cardiomyocyte L-type calcium channel/SERCA activity and cardiac tissue fibrosis. Excitation-contraction simulations of hMSC PS-only and combined HC+PS effects on human

cardiomyocytes were representative of human engineered cardiac tissue (hECT) contractile function measurements under matched experimental treatments. Model simulations and hECTs both demonstrated hMSC-mediated effects were most pronounced under PS-only conditions, where developed force increased approximately 4-fold compared to non-hMSC-supplemented controls during physiologic 1-Hz pacing. Simulations predicted contractility of isolated healthy and ischemic adult human cardiomyocytes would be minimally sensitive to hMSC HC, driven primarily by PS. Dominance of hMSC PS was also revealed in simulations of fibrotic cardiac tissue, where hMSC PS protected from potential pro-arrhythmic effects of HC at various levels of engraftment. Finally, to study the nature of the hMSC paracrine effects on contractility, proteomic analysis of hECT/hMSC conditioned media predicted activation of PI3K/Akt signaling, a recognized target of both soluble and exosomal fractions of the hMSC secretome. Treating hECTs with exosomes-enriched, but not exosomes-depleted, fractions of the hMSC secretome recapitulated the effects observed with hMSC conditioned media on hECT developed force and expression of calcium handling genes (e.g., SERCA2a, L-type calcium channel). Collectively, this integrated experimental and computational project helps unravel the relative contributions of hMSC PS and HC effects on human cardiac contractility and arrhythmogenicity, and provides original insight into the role of exosomes in hMSC paracrine-mediated effects on contractility.

Project IV was published in *Circulation Research* as a first-author publication, and was selected as an Editor's pick:

**Mayourian J, Cashman TJ, Ceholski DK, Johnson BV, Sachs D, Kaji DA, Sahoo S, Hare JM, Hajjar RJ, Sobie EA, Costa KD.** Experimental and Computational Insight into Human Mesenchymal Stem Cell Paracrine Signaling and Heterocellular Coupling Effects on Cardiac Contractility and Arrhythmogenicity. *Circulation Research*. 2017;121(4),411-423.

### *1.6.5 Project V: microRNA-21-5p as an Exosomal Mediator of Mesenchymal Stem Cell Paracrine Effects on Human Cardiac Tissue Contractility*

In this project (Chapter 7), I utilized an integrated systems biology and tissue engineering approach to identify key cardioactive hMSC exosomal miRs. First, I provide bioinformatic and experimental data supporting miR-21-5p as a lead candidate exosomal miR in therapeutic hMSC-based paracrine signaling. Next, using our hECT system, I provide the first (to our knowledge) human-specific experimental data revealing: 1) treating hECTs with miR-21-5p alone was sufficient to recapitulate effects observed with hMSC-exo on hECT developed force and associated calcium handling genes; and 2) knocking down miR-21-5p in hMSC-exo significantly diminished pro-contractile and associated calcium handling gene expression (e.g., SERCA2a and L-type calcium channel) effects on hECTs. Finally, I provide a mechanistic basis as to how miR-21-5p may increase cardiac contractility via the PI3K signaling cascade.

In summary, I identified miR-21-5p as a contributory exosomal microRNA responsible for the paracrine mediated effects of hMSCs on contractility and calcium handling via the PI3K signaling cascade. These findings may open up new avenues of research to harness the role of miR-21-5p in optimizing future stem cell- and synthetic miR-based cardiotherapies, as well as human pluripotent stem cell-derived cardiomyocyte maturation techniques.

Project V was published in *Circulation Research* as a first-author publication:

**Mayourian J**, Ceholski DK, Gorski PA, Mathiyalagan P, Murphy JF, Salazar SI, Stillitano F, Hare JM, Sahoo S, Hajjar RJ, Costa KD. Exosomal microRNA-21-5p Mediates Mesenchymal Stem Cell Paracrine Effects on Human Cardiac Tissue Contractility. *Circulation Research*. 2018; in press.

### *1.6.6 Project VI: Improved Prediction of Drug Torsadogenicity by Machine Learning with Tissue-level Electrophysiology Simulations*

Project VI extends beyond the primary focus of this dissertation; it is therefore provided as a Supplementary Chapter. In the final project, I demonstrate the utility of computational approaches not only to predict therapeutic interventions (Chapters 5-7), but also to screen for cardiotoxicity.

In this Supplementary Project (Chapter 9), I investigate the predictive value of a machine-learning framework that incorporates in silico simulations of clinically relevant cardiac tissue-level electrophysiology for automated discrimination of TdP from non-TdP drugs. Four simulation-based classifiers (normokalemic single-cell, hypokalemic single-cell, normokalemic tissue-level, and hypokalemic tissue-level) individually outperformed conventional hERG inhibition-based assay classification that had a 38.8% misclassification rate. Interestingly, the normokalemic tissue-level classifier led to the lowest misclassification rate of 13.8%, with feature selection analysis implicating action potential duration heterogeneity as a key metric accessible in tissue-level, but not single-cell, simulations. However, under hypokalemia, tissue-level mean action potential duration and upstroke velocity superseded action potential duration heterogeneity as top predictive features, thus providing no added benefit in drug classification versus normokalemia. Finally, simulations using 100 hypothetical drugs identified the inward rectifier and slow delayed rectifier K<sup>+</sup> channels as unconventional modulators of TdP risk. These findings underscore the value of tissue-level assays for TdP risk, and present novel in silico approaches to enhance next-generation regulatory standards for drug cardiotoxicity screening.

Project VI is in preparation as a first-author publication.

## 1.7 References

1. Fisher SA, Doree C, Mathur A, Martin-Rendon E. Meta-analysis of cell therapy trials for patients with heart failure. *Circ Res.* 2015;116:1361-1377
2. Writing Group M, Mozaffarian D, Benjamin EJ, et al. Heart disease and stroke statistics--2016 update: A report from the american heart association. *Circulation.* 2016;133:e38-360
3. Heidenreich PA, Trogdon JG, Khavjou OA, et al. Forecasting the future of cardiovascular disease in the united states: A policy statement from the american heart association. *Circulation.* 2011;123:933-944
4. Stehlík J, Edwards LB, Kucheryavaya AY, Benden C, Christie JD, Dipchand AI, Dobbels F, Kirk R, Rahmel AO, Hertz MI, International Society of H, Lung T. The registry of the international society for heart and lung transplantation: 29th official adult heart transplant report--2012. *J Heart Lung Transplant.* 2012;31:1052-1064
5. Kirklin JK, Naftel DC, Kormos RL, Pagani FD, Myers SL, Stevenson LW, Givertz MM, Young JB. Quantifying the effect of cardiorenal syndrome on mortality after left ventricular assist device implant. *J Heart Lung Transplant.* 2013;32:1205-1213
6. Delgado R. *Interventional treatment of advanced ischemic heart disease.* London: Springer; 2009.
7. Griffin BP, Callahan TDIV, Menon V, Wu WM, Cauthen CA, Dunn JM. *Manual of cardiovascular medicine.*
8. Taggart DP. Incomplete revascularization: Appropriate and inappropriate. *Eur J Cardiothorac Surg.* 2012;41:542-543
9. Go AS, Mozaffarian D, Roger VL, et al. Heart disease and stroke statistics--2014 update: A report from the american heart association. *Circulation.* 2014;129:e28-e292

10. Velagaleti RS, Pencina MJ, Murabito JM, Wang TJ, Parikh NI, D'Agostino RB, Levy D, Kannel WB, Vasan RS. Long-term trends in the incidence of heart failure after myocardial infarction. *Circulation*. 2008;118:2057-2062
11. Towbin JA, Lowe AM, Colan SD, Sleeper LA, Orav EJ, Clunie S, Messere J, Cox GF, Lurie PR, Hsu D, Canter C, Wilkinson JD, Lipshultz SE. Incidence, causes, and outcomes of dilated cardiomyopathy in children. *JAMA*. 2006;296:1867-1876
12. Krum H, Teerlink JR. Medical therapy for chronic heart failure. *Lancet*. 2011;378:713-721
13. Ma TK, Kam KK, Yan BP, Lam YY. Renin-angiotensin-aldosterone system blockade for cardiovascular diseases: Current status. *Br J Pharmacol*. 2010;160:1273-1292
14. Krum H, Abraham WT. Heart failure. *Lancet*. 2009;373:941-955
15. Sanganalmath SK, Bolli R. Cell therapy for heart failure: A comprehensive overview of experimental and clinical studies, current challenges, and future directions. *Circ Res*. 2013;113:810-834
16. Orlic D, Kajstura J, Chimenti S, Jakoniuk I, Anderson SM, Li B, Pickel J, McKay R, Nadal-Ginard B, Bodine DM, Leri A, Anversa P. Bone marrow cells regenerate infarcted myocardium. *Nature*. 2001;410:701-705
17. Strauer BE, Brehm M, Zeus T, Kostering M, Hernandez A, Sorg RV, Kogler G, Wernet P. Repair of infarcted myocardium by autologous intracoronary mononuclear bone marrow cell transplantation in humans. *Circulation*. 2002;106:1913-1918
18. Taylor DA, Atkins BZ, Hungspreugs P, Jones TR, Reedy MC, Hutcheson KA, Glower DD, Kraus WE. Regenerating functional myocardium: Improved performance after skeletal myoblast transplantation. *Nat Med*. 1998;4:929-933
19. Menasche P, Hagege AA, Scorsin M, Pouzet B, Desnos M, Duboc D, Schwartz K, Vilquin JT, Marolleau JP. Myoblast transplantation for heart failure. *Lancet*. 2001;357:279-280

20. Suzuki K, Murtuza B, Suzuki N, Smolenski RT, Yacoub MH. Intracoronary infusion of skeletal myoblasts improves cardiac function in doxorubicin-induced heart failure. *Circulation*. 2001;104:I213-217
21. Ghostine S, Carrion C, Souza LC, Richard P, Bruneval P, Vilquin JT, Pouzet B, Schwartz K, Menasche P, Hagege AA. Long-term efficacy of myoblast transplantation on regional structure and function after myocardial infarction. *Circulation*. 2002;106:I131-136
22. Pouly J, Hagege AA, Vilquin JT, Bissery A, Rouche A, Bruneval P, Duboc D, Desnos M, Fiszman M, Fromes Y, Menasche P. Does the functional efficacy of skeletal myoblast transplantation extend to nonischemic cardiomyopathy? *Circulation*. 2004;110:1626-1631
23. Chachques JC, Duarte F, Cattadori B, Shafy A, Lila N, Chatellier G, Fabiani JN, Carpentier AF. Angiogenic growth factors and/or cellular therapy for myocardial regeneration: A comparative study. *J Thorac Cardiovasc Surg*. 2004;128:245-253
24. He KL, Yi GH, Sherman W, Zhou H, Zhang GP, Gu A, Kao R, Haimes HB, Harvey J, Roos E, White D, Taylor DA, Wang J, Burkhoff D. Autologous skeletal myoblast transplantation improved hemodynamics and left ventricular function in chronic heart failure dogs. *J Heart Lung Transplant*. 2005;24:1940-1949
25. Gavira JJ, Perez-Ilzarbe M, Abizanda G, Garcia-Rodriguez A, Orbe J, Paramo JA, Belzunce M, Rabago G, Barba J, Herreros J, Panizo A, de Jalon JA, Martinez-Caro D, Prosper F. A comparison between percutaneous and surgical transplantation of autologous skeletal myoblasts in a swine model of chronic myocardial infarction. *Cardiovasc Res*. 2006;71:744-753
26. Farahmand P, Lai TY, Weisel RD, Fazel S, Yau T, Menasche P, Li RK. Skeletal myoblasts preserve remote matrix architecture and global function when implanted early

or late after coronary ligation into infarcted or remote myocardium. *Circulation*. 2008;118:S130-137

27. Fukushima S, Coppen SR, Lee J, Yamahara K, Felkin LE, Terracciano CM, Barton PJ, Yacoub MH, Suzuki K. Choice of cell-delivery route for skeletal myoblast transplantation for treating post-infarction chronic heart failure in rat. *PLoS One*. 2008;3:e3071
28. Tomita S, Li RK, Weisel RD, Mickle DA, Kim EJ, Sakai T, Jia ZQ. Autologous transplantation of bone marrow cells improves damaged heart function. *Circulation*. 1999;100:II247-256
29. Waksman R, Fournadjiev J, Baffour R, Pakala R, Hellinga D, Leborgne L, Yazdi H, Cheneau E, Wolfram R, Seabron R, Horton K, Kolodgie F, Virmani R, Rivera E. Transepicardial autologous bone marrow-derived mononuclear cell therapy in a porcine model of chronically infarcted myocardium. *Cardiovasc Radiat Med*. 2004;5:125-131
30. Nagaya N, Kangawa K, Itoh T, Iwase T, Murakami S, Miyahara Y, Fujii T, Uematsu M, Ohgushi H, Yamagishi M, Tokudome T, Mori H, Miyatake K, Kitamura S. Transplantation of mesenchymal stem cells improves cardiac function in a rat model of dilated cardiomyopathy. *Circulation*. 2005;112:1128-1135
31. Silva GV, Litovsky S, Assad JA, et al. Mesenchymal stem cells differentiate into an endothelial phenotype, enhance vascular density, and improve heart function in a canine chronic ischemia model. *Circulation*. 2005;111:150-156
32. Miyahara Y, Nagaya N, Kataoka M, Yanagawa B, Tanaka K, Hao H, Ishino K, Ishida H, Shimizu T, Kangawa K, Sano S, Okano T, Kitamura S, Mori H. Monolayered mesenchymal stem cells repair scarred myocardium after myocardial infarction. *Nat Med*. 2006;12:459-465
33. Liu JF, Wang BW, Hung HF, Chang H, Shyu KG. Human mesenchymal stem cells improve myocardial performance in a splenectomized rat model of chronic myocardial infarction. *J Formos Med Assoc*. 2008;107:165-174

34. Li L, Zhang S, Zhang Y, Yu B, Xu Y, Guan Z. Paracrine action mediate the antifibrotic effect of transplanted mesenchymal stem cells in a rat model of global heart failure. *Mol Biol Rep.* 2009;36:725-731
35. Schuleri KH, Feigenbaum GS, Centola M, et al. Autologous mesenchymal stem cells produce reverse remodelling in chronic ischaemic cardiomyopathy. *Eur Heart J.* 2009;30:2722-2732
36. Mazo M, Gavira JJ, Abizanda G, Moreno C, Ecay M, Soriano M, Aranda P, Collantes M, Alegria E, Merino J, Penuelas I, Garcia Verdugo JM, Pelacho B, Prosper F. Transplantation of mesenchymal stem cells exerts a greater long-term effect than bone marrow mononuclear cells in a chronic myocardial infarction model in rat. *Cell Transplant.* 2010;19:313-328
37. Rota M, Padin-Iruegas ME, Misao Y, et al. Local activation or implantation of cardiac progenitor cells rescues scarred infarcted myocardium improving cardiac function. *Circ Res.* 2008;103:107-116
38. Johnston PV, Sasano T, Mills K, Evers R, Lee ST, Smith RR, Lardo AC, Lai S, Steenbergen C, Gerstenblith G, Lange R, Marban E. Engraftment, differentiation, and functional benefits of autologous cardiosphere-derived cells in porcine ischemic cardiomyopathy. *Circulation.* 2009;120:1075-1083, 1077 p following 1083
39. Tang XL, Rokosh G, Sanganalmath SK, et al. Intracoronary administration of cardiac progenitor cells alleviates left ventricular dysfunction in rats with a 30-day-old infarction. *Circulation.* 2010;121:293-305
40. Lee ST, White AJ, Matsushita S, Malliaras K, Steenbergen C, Zhang Y, Li TS, Terrovitis J, Yee K, Simsir S, Makkar R, Marban E. Intramyocardial injection of autologous cardiospheres or cardiosphere-derived cells preserves function and minimizes adverse ventricular remodeling in pigs with heart failure post-myocardial infarction. *J Am Coll Cardiol.* 2011;57:455-465

41. Bolli R, Tang XL, Sanganalmath SK, Rimoldi O, Mosna F, Abdel-Latif A, Jneid H, Rota M, Leri A, Kajstura J. Intracoronary delivery of autologous cardiac stem cells improves cardiac function in a porcine model of chronic ischemic cardiomyopathy. *Circulation*. 2013;128:122-131
42. Menasche P, Hagege AA, Vilquin JT, Desnos M, Abergel E, Pouzet B, Bel A, Sarateanu S, Scorsin M, Schwartz K, Bruneval P, Benbunan M, Marolleau JP, Duboc D. Autologous skeletal myoblast transplantation for severe postinfarction left ventricular dysfunction. *J Am Coll Cardiol*. 2003;41:1078-1083
43. Smits PC, van Geuns RJ, Poldermans D, Bountioukos M, Onderwater EE, Lee CH, Maat AP, Serruys PW. Catheter-based intramyocardial injection of autologous skeletal myoblasts as a primary treatment of ischemic heart failure: Clinical experience with six-month follow-up. *J Am Coll Cardiol*. 2003;42:2063-2069
44. Herreros J, Prosper F, Perez A, et al. Autologous intramyocardial injection of cultured skeletal muscle-derived stem cells in patients with non-acute myocardial infarction. *Eur Heart J*. 2003;24:2012-2020
45. Siminiak T, Kalawski R, Fiszer D, Jerzykowska O, Rzezniczak J, Rozwadowska N, Kurpisz M. Autologous skeletal myoblast transplantation for the treatment of postinfarction myocardial injury: Phase i clinical study with 12 months of follow-up. *Am Heart J*. 2004;148:531-537
46. Ince H, Petzsch M, Rehders TC, Chatterjee T, Nienaber CA. Transcatheter transplantation of autologous skeletal myoblasts in postinfarction patients with severe left ventricular dysfunction. *J Endovasc Ther*. 2004;11:695-704
47. Siminiak T, Fiszer D, Jerzykowska O, Grygielska B, Rozwadowska N, Kalmucki P, Kurpisz M. Percutaneous trans-coronary-venous transplantation of autologous skeletal myoblasts in the treatment of post-infarction myocardial contractility impairment: The poznan trial. *Eur Heart J*. 2005;26:1188-1195

48. Dib N, Michler RE, Pagani FD, et al. Safety and feasibility of autologous myoblast transplantation in patients with ischemic cardiomyopathy: Four-year follow-up. *Circulation*. 2005;112:1748-1755
49. Biagini E, Valgimigli M, Smits PC, Poldermans D, Schinkel AF, Rizzello V, Onderwater EE, Bountioukos M, Serruys PW. Stress and tissue doppler echocardiographic evidence of effectiveness of myoblast transplantation in patients with ischaemic heart failure. *Eur J Heart Fail*. 2006;8:641-648
50. Hagege AA, Marolleau JP, Vilquin JT, Alheritiere A, Peyrard S, Duboc D, Abergel E, Messas E, Mousseaux E, Schwartz K, Desnos M, Menasche P. Skeletal myoblast transplantation in ischemic heart failure: Long-term follow-up of the first phase i cohort of patients. *Circulation*. 2006;114:I108-113
51. Gavira JJ, Herreros J, Perez A, et al. Autologous skeletal myoblast transplantation in patients with nonacute myocardial infarction: 1-year follow-up. *J Thorac Cardiovasc Surg*. 2006;131:799-804
52. Veltman CE, Soliman OI, Geleijnse ML, Vletter WB, Smits PC, ten Cate FJ, Jordaeans LJ, Balk AH, Serruys PW, Boersma E, van Domburg RT, van der Giessen WJ. Four-year follow-up of treatment with intramyocardial skeletal myoblasts injection in patients with ischaemic cardiomyopathy. *Eur Heart J*. 2008;29:1386-1396
53. Menasche P, Alfieri O, Janssens S, et al. The myoblast autologous grafting in ischemic cardiomyopathy (magic) trial: First randomized placebo-controlled study of myoblast transplantation. *Circulation*. 2008;117:1189-1200
54. Dib N, Dinsmore J, Lababidi Z, White B, Moravec S, Campbell A, Rosenbaum A, Seyedmadani K, Jaber WA, Rizenhour CS, Diethrich E. One-year follow-up of feasibility and safety of the first u.S., randomized, controlled study using 3-dimensional guided catheter-based delivery of autologous skeletal myoblasts for ischemic cardiomyopathy (causmic study). *JACC Cardiovasc Interv*. 2009;2:9-16

55. Duckers HJ, Houtgraaf J, Hehrlein C, et al. Final results of a phase iia, randomised, open-label trial to evaluate the percutaneous intramyocardial transplantation of autologous skeletal myoblasts in congestive heart failure patients: The seismic trial. *EuroIntervention*. 2011;6:805-812
56. Povsic TJ, O'Connor CM, Henry T, et al. A double-blind, randomized, controlled, multicenter study to assess the safety and cardiovascular effects of skeletal myoblast implantation by catheter delivery in patients with chronic heart failure after myocardial infarction. *Am Heart J*. 2011;162:654-662 e651
57. Perin EC, Dohmann HF, Borojevic R, et al. Transendocardial, autologous bone marrow cell transplantation for severe, chronic ischemic heart failure. *Circulation*. 2003;107:2294-2302
58. Perin EC, Dohmann HF, Borojevic R, et al. Improved exercise capacity and ischemia 6 and 12 months after transendocardial injection of autologous bone marrow mononuclear cells for ischemic cardiomyopathy. *Circulation*. 2004;110:II213-218
59. Blatt A, Cotter G, Leitman M, Krakover R, Kaluski E, Milo-Cotter O, Resnick IB, Samuel S, Gozal D, Vered Z, Slavin S, Shapira MY. Intracoronary administration of autologous bone marrow mononuclear cells after induction of short ischemia is safe and may improve hibernation and ischemia in patients with ischemic cardiomyopathy. *Am Heart J*. 2005;150:986
60. Assmus B, Honold J, Schachinger V, Britten MB, Fischer-Rasokat U, Lehmann R, Teupe C, Pistorius K, Martin H, Abolmaali ND, Tonn T, Dimmeler S, Zeiher AM. Transcoronary transplantation of progenitor cells after myocardial infarction. *N Engl J Med*. 2006;355:1222-1232
61. Hendrikx M, Hensen K, Clijsters C, et al. Recovery of regional but not global contractile function by the direct intramyocardial autologous bone marrow transplantation: Results from a randomized controlled clinical trial. *Circulation*. 2006;114:I101-107

62. Seth S, Narang R, Bhargava B, Ray R, Mohanty S, Gulati G, Kumar L, Reddy KS, Venugopal P, Group ACSCS. Percutaneous intracoronary cellular cardiomyoplasty for nonischemic cardiomyopathy: Clinical and histopathological results: The first-in-man abcd (autologous bone marrow cells in dilated cardiomyopathy) trial. *J Am Coll Cardiol.* 2006;48:2350-2351
63. Beeres SL, Bax JJ, Dibbets-Schneider P, Stokkel MP, Fibbe WE, van der Wall EE, Schalij MJ, Atsma DE. Intramyocardial injection of autologous bone marrow mononuclear cells in patients with chronic myocardial infarction and severe left ventricular dysfunction. *Am J Cardiol.* 2007;100:1094-1098
64. Yao K, Huang R, Qian J, Cui J, Ge L, Li Y, Zhang F, Shi H, Huang D, Zhang S, Sun A, Zou Y, Ge J. Administration of intracoronary bone marrow mononuclear cells on chronic myocardial infarction improves diastolic function. *Heart.* 2008;94:1147-1153
65. Ang KL, Chin D, Leyva F, Foley P, Kubal C, Chalil S, Srinivasan L, Bernhardt L, Stevens S, Shenje LT, Galinanes M. Randomized, controlled trial of intramuscular or intracoronary injection of autologous bone marrow cells into scarred myocardium during cabg versus cabg alone. *Nat Clin Pract Cardiovasc Med.* 2008;5:663-670
66. Diederichsen AC, Moller JE, Thayssen P, Videbaek L, Saekmose SG, Barington T, Kassem M. Changes in left ventricular filling patterns after repeated injection of autologous bone marrow cells in heart failure patients. *Scand Cardiovasc J.* 2010;44:139-145
67. Perin EC, Silva GV, Henry TD, et al. A randomized study of transendocardial injection of autologous bone marrow mononuclear cells and cell function analysis in ischemic heart failure (focus-hf). *Am Heart J.* 2011;161:1078-1087 e1073
68. Hare JM, Fishman JE, Gerstenblith G, et al. Comparison of allogeneic vs autologous bone marrow-derived mesenchymal stem cells delivered by transendocardial injection in

- patients with ischemic cardiomyopathy: The poseidon randomized trial. *JAMA*. 2012;308:2369-2379
69. Patel AN, Geffner L, Vina RF, Saslavsky J, Urschel HC, Jr., Kormos R, Benetti F. Surgical treatment for congestive heart failure with autologous adult stem cell transplantation: A prospective randomized study. *J Thorac Cardiovasc Surg*. 2005;130:1631-1638
70. Manginas A, Goussetis E, Koutelou M, Karatasakis G, Peristeri I, Theodorakos A, Leontiadis E, Plessas N, Theodosaki M, Graphakos S, Cokkinos DV. Pilot study to evaluate the safety and feasibility of intracoronary cd133(+) and cd133(-) cd34(+) cell therapy in patients with nonviable anterior myocardial infarction. *Catheter Cardiovasc Interv*. 2007;69:773-781
71. Stamm C, Kleine HD, Choi YH, Dunkelmann S, Lauffs JA, Lorenzen B, David A, Liebold A, Nienaber C, Zurkowski D, Freund M, Steinhoff G. Intramyocardial delivery of cd133+ bone marrow cells and coronary artery bypass grafting for chronic ischemic heart disease: Safety and efficacy studies. *J Thorac Cardiovasc Surg*. 2007;133:717-725
72. Fischer-Rasokat U, Assmus B, Seeger FH, Honold J, Leistner D, Fichtlscherer S, Schachinger V, Tonn T, Martin H, Dimmeler S, Zeiher AM. A pilot trial to assess potential effects of selective intracoronary bone marrow-derived progenitor cell infusion in patients with nonischemic dilated cardiomyopathy: Final 1-year results of the transplantation of progenitor cells and functional regeneration enhancement pilot trial in patients with nonischemic dilated cardiomyopathy. *Circ Heart Fail*. 2009;2:417-423
73. Vrtovec B, Poglajen G, Lezaic L, Sever M, Domanovic D, Cernelc P, Socan A, Schrepfer S, Torre-Amione G, Haddad F, Wu JC. Effects of intracoronary cd34+ stem cell transplantation in nonischemic dilated cardiomyopathy patients: 5-year follow-up. *Circ Res*. 2013;112:165-173

74. Perin EC, Silva GV, Zheng Y, Gahremanpour A, Canales J, Patel D, Fernandes MR, Keller LH, Quan X, Coulter SA, Moore WH, Herlihy JP, Willerson JT. Randomized, double-blind pilot study of transendocardial injection of autologous aldehyde dehydrogenase-bright stem cells in patients with ischemic heart failure. *Am Heart J.* 2012;163:415-421, 421 e411
75. Bolli R, Chugh AR, D'Amario D, et al. Cardiac stem cells in patients with ischaemic cardiomyopathy (scipio): Initial results of a randomised phase 1 trial. *Lancet.* 2011;378:1847-1857
76. Makkar RR, Smith RR, Cheng K, et al. Intracoronary cardiosphere-derived cells for heart regeneration after myocardial infarction (caduceus): A prospective, randomised phase 1 trial. *Lancet.* 2012;379:895-904
77. Sanina C, Hare JM. Mesenchymal stem cells as a biological drug for heart disease: Where are we with cardiac cell-based therapy? *Circ Res.* 2015;117:229-233
78. Hare JM, Sanina C. Bone marrow mononuclear cell therapy and granulocyte colony-stimulating factor for acute myocardial infarction: Is it time to reconsider? *J Am Coll Cardiol.* 2015;65:2383-2387
79. Karantalis V, Hare JM. Use of mesenchymal stem cells for therapy of cardiac disease. *Circ Res.* 2015;116:1413-1430
80. Ankrum JA, Ong JF, Karp JM. Mesenchymal stem cells: Immune evasive, not immune privileged. *Nat Biotechnol.* 2014;32:252-260
81. Karantalis V, DiFede DL, Gerstenblith G, et al. Autologous mesenchymal stem cells produce concordant improvements in regional function, tissue perfusion, and fibrotic burden when administered to patients undergoing coronary artery bypass grafting: The prospective randomized study of mesenchymal stem cell therapy in patients undergoing cardiac surgery (prometheus) trial. *Circ Res.* 2014;114:1302-1310

82. Heldman AW, DiFede DL, Fishman JE, et al. Transendocardial mesenchymal stem cells and mononuclear bone marrow cells for ischemic cardiomyopathy: The tac-hft randomized trial. *JAMA*. 2014;311:62-73
83. Mushtaq M, DiFede DL, Golpanian S, Khan A, Gomes SA, Mendizabal A, Heldman AW, Hare JM. Rationale and design of the percutaneous stem cell injection delivery effects on neomyogenesis in dilated cardiomyopathy (the poseidon-dcm study): A phase i/ii, randomized pilot study of the comparative safety and efficacy of transendocardial injection of autologous mesenchymal stem cell vs. Allogeneic mesenchymal stem cells in patients with non-ischemic dilated cardiomyopathy. *J Cardiovasc Transl Res*. 2014;7:769-780
84. Zeinaloo A, Zanjani KS, Bagheri MM, Mohyeddin-Bonab M, Monajemzadeh M, Arjmandnia MH. Intracoronary administration of autologous mesenchymal stem cells in a critically ill patient with dilated cardiomyopathy. *Pediatr Transplant*. 2011;15:E183-186
85. Meyer GP, Wollert KC, Lotz J, Pirr J, Rager U, Lippolt P, Hahn A, Fichtner S, Schaefer A, Arseniev L, Ganser A, Drexler H. Intracoronary bone marrow cell transfer after myocardial infarction: 5-year follow-up from the randomized-controlled boost trial. *Eur Heart J*. 2009;30:2978-2984
86. Cashman TJ, Gouon-Evans V, Costa KD. Mesenchymal stem cells for cardiac therapy: Practical challenges and potential mechanisms. *Stem Cell Rev*. 2013;9:254-265
87. Leiker M, Suzuki G, Iyer VS, Carty JM, Jr., Lee T. Assessment of a nuclear affinity labeling method for tracking implanted mesenchymal stem cells. *Cell Transplant*. 2008;17:911-922
88. Ranganath SH, Levy O, Inamdar MS, Karp JM. Harnessing the mesenchymal stem cell secretome for the treatment of cardiovascular disease. *Cell Stem Cell*. 2012;10:244-258
89. Ringden O, Uzunel M, Rasmusson I, Remberger M, Sundberg B, Lonnies H, Marschall HU, Dlugosz A, Szakos A, Hassan Z, Omazic B, Aschan J, Barkholt L, Le Blanc K.

- Mesenchymal stem cells for treatment of therapy-resistant graft-versus-host disease. *Transplantation*. 2006;81:1390-1397
90. Liang X, Zhang L, Wang S, Han Q, Zhao RC. Exosomes secreted by mesenchymal stem cells promote endothelial cell angiogenesis by transferring mir-125a. *J Cell Sci*. 2016;129:2182-2189
91. Merino-Gonzalez C, Zuniga FA, Escudero C, Ormazabal V, Reyes C, Nova-Lamperti E, Salomon C, Aguayo C. Mesenchymal stem cell-derived extracellular vesicles promote angiogenesis: Potencial clinical application. *Front Physiol*. 2016;7:24
92. Emanueli C, Shearn AI, Angelini GD, Sahoo S. Exosomes and exosomal mirnas in cardiovascular protection and repair. *Vascul Pharmacol*. 2015;71:24-30
93. Askar SF, Ramkisoensing AA, Atsma DE, Schalij MJ, de Vries AA, Pijnappels DA. Engraftment patterns of human adult mesenchymal stem cells expose electrotonic and paracrine proarrhythmic mechanisms in myocardial cell cultures. *Circ Arrhythm Electrophysiol*. 2013;6:380-391
94. DeSantiago J, Bare DJ, Semenov I, Minshall RD, Geenen DL, Wolska BM, Banach K. Excitation-contraction coupling in ventricular myocytes is enhanced by paracrine signaling from mesenchymal stem cells. *J Mol Cell Cardiol*. 2012;52:1249-1256
95. Hwang HJ, Chang W, Song BW, et al. Antiarrhythmic potential of mesenchymal stem cell is modulated by hypoxic environment. *J Am Coll Cardiol*. 2012;60:1698-1706
96. Hasenfuss G, Mulieri LA, Leavitt BJ, Allen PD, Haeberle JR, Alpert NR. Alteration of contractile function and excitation-contraction coupling in dilated cardiomyopathy. *Circ Res*. 1992;70:1225-1232
97. Valiunas V, Doronin S, Valiuniene L, Potapova I, Zuckerman J, Walcott B, Robinson RB, Rosen MR, Brink PR, Cohen IS. Human mesenchymal stem cells make cardiac connexins and form functional gap junctions. *J Physiol*. 2004;555:617-626

98. Shadrin IY, Yoon W, Li L, Shepherd N, Bursac N. Rapid fusion between mesenchymal stem cells and cardiomyocytes yields electrically active, non-contractile hybrid cells. *Sci Rep.* 2015;5:12043

## **Chapter 2: Physiologic, Pathologic, and Therapeutic Paracrine Modulation of Cardiac Excitation-Contraction Coupling**

*Note: The following chapter is a modified draft of an original first-author research article published in Circulation Research:*

Mayourian J, Ceholski DK, Gonzalez DM, Cashman TJ, Sahoo S, Hajjar RJ, Costa KD. Physiologic, Pathologic, and Therapeutic Paracrine Modulation of Cardiac Excitation-Contraction Coupling. *Circulation Research*. 2018;122(1),167-183.

JM conceived the idea, collected and analyzed the tissue engineering functional data, and wrote the manuscript. The current *Circulation Research* CTA states, "authors may use parts of the work (eg, tables, figures) in subsequent works without requesting permission from the AHA."

## 2.1 Abstract

Cardiac excitation-contraction coupling (ECC) is the orchestrated process of initial myocyte electrical excitation, which leads to calcium entry, intracellular trafficking, and subsequent sarcomere shortening and myofibrillar contraction. Neurohumoral  $\beta$ -adrenergic signaling is a well-established mediator of ECC; other signaling mechanisms, such as paracrine signaling, have also demonstrated significant impact on ECC but are less well understood. For example, resident heart endothelial cells are well-known physiologic paracrine modulators of cardiac myocyte ECC mainly via nitric oxide and endothelin-1. Moreover, recent studies have demonstrated other resident non-cardiomyocyte heart cells (e.g., physiologic fibroblasts and pathologic myofibroblasts), and even experimental cardiotherapeutic cells (e.g., mesenchymal stem cells), are also capable of altering cardiomyocyte ECC through paracrine mechanisms. In this review, we first focus on the paracrine-mediated effects of resident and therapeutic non-cardiomyocytes on cardiomyocyte hypertrophy, electrophysiology, and calcium handling, each of which can modulate ECC, and then discuss the current knowledge about key paracrine factors and their underlying mechanisms of action. Next, we provide a case example demonstrating the promise of tissue engineering approaches to study paracrine effects on tissue-level contractility. More specifically, we present new functional and molecular data on the effects of human adult cardiac fibroblast conditioned media on human engineered cardiac tissue contractility and ion channel gene expression that generally agrees with previous murine studies, but also suggests possible species-specific differences. By contrast, paracrine secretions by human dermal fibroblasts had no discernible effect on human engineered cardiac tissue contractile function and gene expression. Finally, we discuss systems biology approaches to help identify key stem cell paracrine mediators of ECC and their associated mechanistic pathways. Such integration of tissue engineering and systems biology methods shows promise to reveal novel insights into paracrine mediators of ECC and their underlying

mechanisms of action, ultimately leading to improved cell-based therapies for patients with heart disease.

## 2.2 Introduction

Cardiomyocyte excitation-contraction coupling (ECC) is the crucial process that links calcium ( $\text{Ca}^{2+}$ ) trafficking to active force generation and subsequent relaxation of the cardiomyocyte. Following supra-threshold myocyte excitation,  $\text{Ca}^{2+}$  rapidly influxes into the myocyte cytosol through depolarization-activated inward  $\text{Ca}^{2+}$  channels. This  $\text{Ca}^{2+}$  influx induces  $\text{Ca}^{2+}$  release from the sarcoplasmic reticulum; together, these mechanisms raise free cytosolic  $\text{Ca}^{2+}$  concentration, increasing the probability of  $\text{Ca}^{2+}$ -troponin C binding and thus activating the contractile machinery.<sup>1</sup> In normal physiology, a fine-tuned percentage of cytosolic  $\text{Ca}^{2+}$  is then pumped back into the sarcoplasmic reticulum reservoir for future calcium induced calcium release.<sup>1</sup> A simplified overview of this highly orchestrated ECC process is shown in Figure 1.

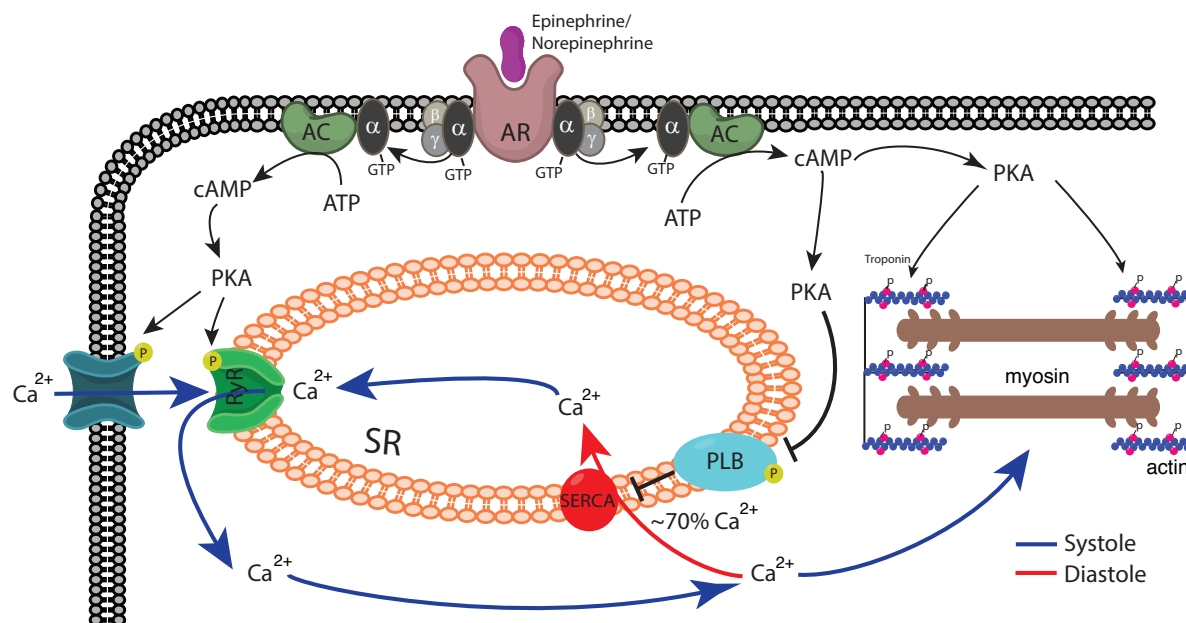


**Figure 1: β-Adrenergic Signaling and Cardiomyocyte ECC.**  $\beta$ -adrenergic receptor ( $\beta$ -AR) activation by binding of epinephrine/norepinephrine leads to the following signaling cascade: 1)

activation of the guanosine triphosphate (GTP)-binding protein  $\alpha$ ; 2) stimulation of adenylyl cyclase (AC); and 3) a rise in cyclic adenosine monophosphate (cAMP). Increase in intracellular cAMP leads to protein kinase A (PKA) activation, which subsequently phosphorylates and thus increases ion flux through the L-type  $\text{Ca}^{2+}$  channel (LTCC) and ryanodine receptor (RyR). Additionally, PKA relieves phospholamban (PLB) inhibition on sarcoendoplasmic reticulum  $\text{Ca}^{2+}$ -ATPase (SERCA), allowing for an increase in  $\text{Ca}^{2+}$  storage within the sarcoplasmic reticulum (SR). In normal physiology, SERCA removes approximately 70% of the activator cytosolic calcium ( $\text{Ca}^{2+}$ ) during diastole (inset). Lastly, PKA phosphorylates troponin I, leading to positive lusitropic effects via myofilament  $\text{Ca}^{2+}$  desensitization. Blue and red arrows denote calcium flow during systole and diastole, respectively.

Sympathetic  $\beta$ -adrenergic signaling is a well-established rapid inotropic<sup>2</sup> and lusitropic<sup>3</sup> modulator of ECC.<sup>1</sup> Briefly,  $\beta$ -adrenergic receptor stimulation of Gs type G-protein coupled receptors activates adenylyl cyclase to form cyclic adenosine monophosphate. Cyclic adenosine monophosphate subsequently activates protein kinases that phosphorylate various proteins essential to electrophysiology, calcium handling, and thus ECC, including the L-type calcium channel,<sup>4,5</sup> phospholamban,<sup>6</sup> ryanodine receptor,<sup>7</sup> troponin I,<sup>8</sup> and myosin binding protein C<sup>9</sup> (Figure 1). A comprehensive review of sympathetic activation effects on ECC is available elsewhere.<sup>1</sup>

Cardiomyocyte ECC and associated  $\beta$ -adrenergic signaling can be further modulated by factors secreted by both distant and nearby cells. For example, chemokine CXCL12, also known as stromal cell-derived factor, can activate its receptor CXCR4 to attenuate  $\beta$ -adrenergic-mediated increases in adult cardiomyocyte calcium handling and fractional shortening.<sup>10</sup> In addition, it is well established that cardiac endothelial cells secrete certain paracrine factors

(e.g., nitric oxide) that can act as physiological signaling mediators of myocyte ECC and compete with  $\beta$ -adrenergic signaling pathways.<sup>11,12</sup>

Recent work has demonstrated that several other neighboring physiological and pathological non-cardiomyocytes in the heart, as well as experimental cardiotherapeutic cells, are capable of modulating cardiomyocyte ECC by paracrine signaling mechanisms. Importantly, these effects are relatively slower than previously described  $\beta$ -adrenergic signaling, likely reflecting underlying cardiomyocyte remodeling. Note that while cardiomyocytes are also known to release cardioactive paracrine factors,<sup>13-15</sup> their mechanisms of action are largely independent of direct ECC-modulation and are thus beyond the scope of this review; for more details, see elsewhere.<sup>16</sup>

In this review, we will first discuss both established and unresolved key ECC-related paracrine factors secreted by endothelial cells, fibroblasts, myofibroblasts, cardiac progenitor cells (CPCs), and mesenchymal stem cells (MSCs), together representing neighboring physiologic, pathologic, and therapeutic paracrine mediators of cardiomyocyte ECC (for a summary of neighboring non-cardiomyocyte paracrine effects on cardiomyocyte ECC, see Table 1). Next, we provide a case example to demonstrate the promise of tissue engineering approaches to study non-cardiomyocyte paracrine effects on contractile function and associated gene expression. Finally, we discuss systems biology approaches to help identify key cardiomyocyte ECC paracrine-mediators of cardiotherapeutic cells, the least studied cell types in this context.

**Table 1. Brief Summary of Non-Cardiomyocyte Paracrine Effects on Cardiomyocyte ECC**

Source	Likely Paracrine Mediator(s)	Paracrine-Mediated Effect on ECC	Potential Mechanisms of Action

Endothelial Cell	Nitric Oxide	↑ basal myocardial contractility	LTCC <sup>17</sup> and RyR2 nitrosylation. <sup>11,18</sup>
		Attenuate β-adrenergic inotropic effects	cGMP-dependent degradation of cAMP via PDEII; <sup>19,20</sup> PKG-mediated decrease of LTCC activity. <sup>19,21</sup>
		Positive lusitropy	cGMP-dependent PKG phosphorylation of troponin I. <sup>22-24</sup>
	Endothelin-1	↑ Ca <sup>2+</sup> entry	PKC-mediated activation of NCX forward/reverse mode; <sup>25-30</sup> PKC-mediated activation of LTCC. <sup>31-35</sup>
		Alter myofilament Ca <sup>2+</sup> sensitivity	PKC/D-dependent phosphorylation of troponin I and myosin-binding protein C. <sup>36-40</sup>
		↑ calcium-induced calcium release	IP <sub>3</sub> -induced calcium release from the SR via IP <sub>3</sub> R, which subsequently sensitizes RyR2. <sup>41-43</sup>
Fibroblast	TGF-β	Hypertrophy; <sup>44,45</sup> ↑ resting membrane potential; <sup>46</sup> ↓ conduction/upstroke velocity; <sup>46</sup> ↑ calcium transient amplitude; <sup>47</sup> ↑ contractility (see Figure 4 and elsewhere <sup>48</sup> )	Non-canonical, non-Smad TGF-β MEK/ERK signaling pathway; <sup>48</sup> Na <sup>+</sup> and K <sup>+</sup> ion channel remodeling (see Figure 5 and elsewhere <sup>46</sup> )
	Exosomal miRNA-21-	Hypertrophy <sup>49</sup>	Targeting the mediators sorbin and SH3 domain-containing protein 2, as

	3p		well as PDZ and LIM domain 5 <sup>49</sup>
Myofibroblast	TGF-β	Hypertrophy; <sup>47</sup> ↓ calcium transient amplitude <sup>47</sup>	TGF-β signaling <sup>47</sup>
CPC	Unresolved	↑ contractility <sup>50</sup>	↑ SERCA/NCX ratio <sup>50</sup>
MSC	Unresolved	↑ action potential duration; <sup>51</sup> ↑ calcium transient amplitude; <sup>52,53</sup> ↑ contractility; <sup>52,54</sup> ↓ calcium transient alternans; <sup>55,56</sup> predominantly anti-arrhythmic effects <sup>53,54,57,58</sup>	PI3K/Akt signaling; <sup>52,54</sup> increase in SERCA and LTCC activity/gene expression <sup>52,54</sup>

Non-standard abbreviations: L-type calcium channel (LTCC); ryanodine receptor (RyR2); cyclic guanosine monophosphate (cGMP); cyclic adenosine monophosphate (cAMP); phosphodiesterase II (PDEII); protein kinase (PK); sodium-calcium exchanger (NCX); inositol trisphosphate ( $IP_3$ ); sarcoplasmic reticulum (SR); inositol trisphosphate receptor ( $IP_3R$ ); transforming growth factor beta (TGF-β); sarco/endoplasmic reticulum  $Ca^{2+}$ -ATPase (SERCA).

### 2.3 Paracrine Effects of Cardiac Endothelial Cells on Cardiomyocyte ECC

Cardiac endothelial cells, including but not limited to endocardial<sup>59</sup> and intramyocardial capillary endothelial cells,<sup>60</sup> regulate cardiac function and are well-established paracrine mediators of myocyte ECC; they release a vast array of cardioactive factors, including nitric oxide, endothelin-1, prostaglandins, natriuretic peptides, angiotensin II, kinins, reactive oxygen species, adenylpurines, neuregulin-1, parathyroid hormone-related peptide, and others.<sup>61-63</sup> Two

major ECC factors, nitric oxide and endothelin-1,<sup>63</sup> are discussed below. A schematic summarizing these mediators and their effects on cardiomyocyte ECC is shown in Figure 2.

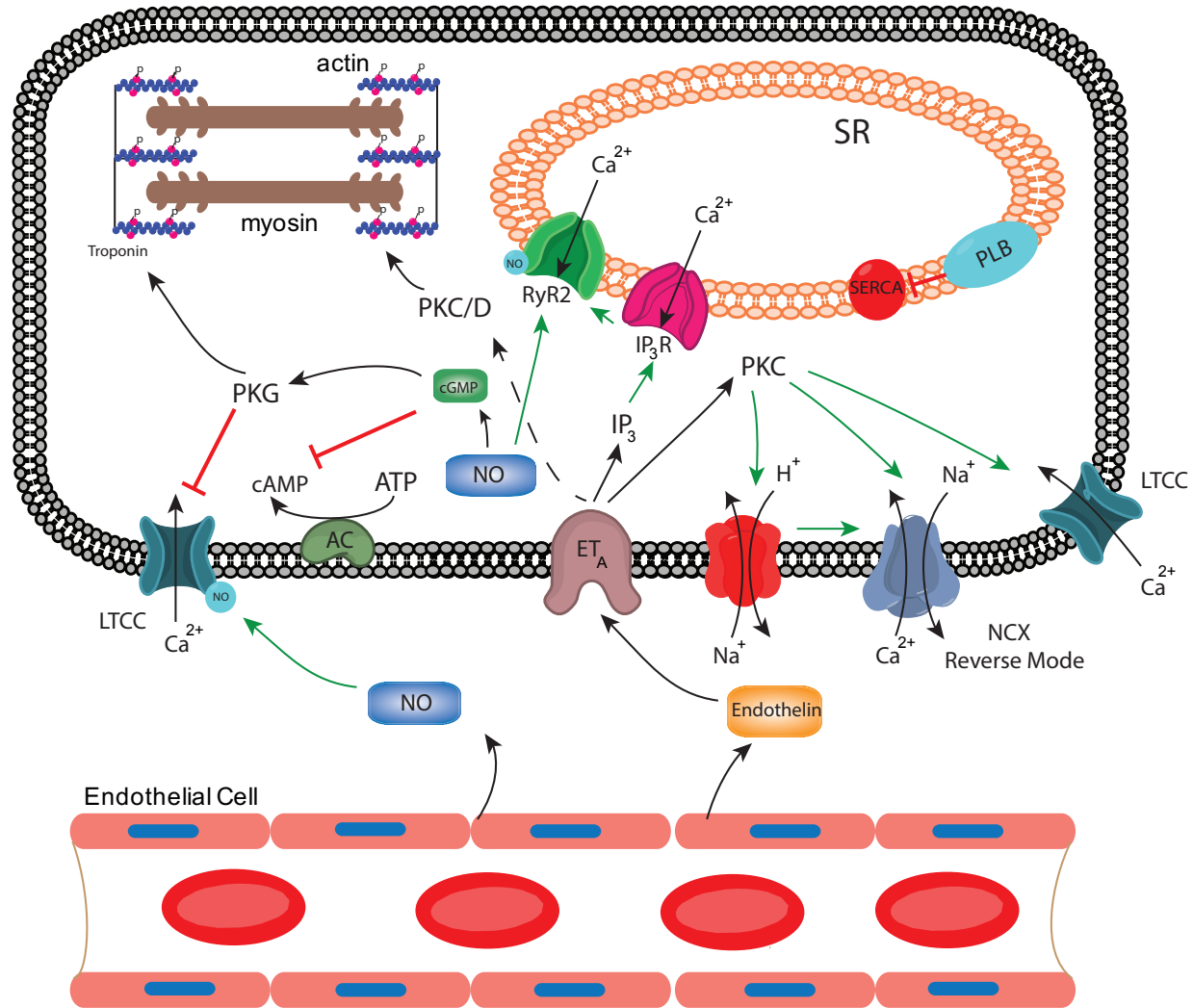


**Figure 2: Endothelial-Cardiomyocyte Interplay Through Paracrine Factors.** Endothelial cell nitric oxide (NO) increases basal contractility via nitrosylation of L-type  $\text{Ca}^{2+}$  channel (LTCC) and ryanodine receptor (RyR2). NO attenuates  $\beta$ -adrenergic effects on cardiomyocyte ECC via cyclic guanosine monophosphate (cGMP)-dependent degradation of cyclic adenosine monophosphate (cAMP) and protein kinase G (PKG)-mediated decrease of LTCC activity. PKG also phosphorylates troponin I, leading to myofilament calcium desensitization and thus

increased lusitropy. Endothelin-1, which mainly acts through the endothelin A ( $ET_A$ ) receptor in ventricular cardiomyocytes, may increase calcium entry via protein kinase C (PKC)-mediated: 1) increase of LTCC activity; 2) indirect activation of sodium-calcium exchanger (NCX) reverse mode by increasing  $Na^+-H^+$  exchanger activity; and 3) direct activation of NCX reverse (shown) and/or forward (not shown) mode. Endothelin-1 alters myofilament  $Ca^{2+}$  sensitivity via protein kinase C/D (PKC/D) phosphorylation of troponin I and myosin-binding protein C. Finally, endothelin-1 may increase calcium-induced calcium release via inositol trisphosphate ( $IP_3$ ) activation of inositol trisphosphate receptor ( $IP_3R$ ), which sensitizes RyR2 on the sarcoplasmic reticulum (SR). Green and red arrows denote activation and inhibition, respectively. Other non-standard abbreviations: phospholamban (PLB); sarcoendoplasmic reticulum  $Ca^{2+}$ -ATPase (SERCA).

### 2.3.1 Endothelial Nitric Oxide

Nitric oxide is reported to have biphasic inotropic effects on basal contractility, where only low doses increase basal contractility.<sup>12,64-68</sup> For example, various *ex vivo* studies on isolated perfused rat hearts<sup>65,69</sup> and cardiac myocytes<sup>70</sup> demonstrated low levels of nitric oxide modestly increase basal myocardial contractility.<sup>11</sup> Mechanistically, these effects are likely cyclic guanosine monophosphate-independent, and instead predominantly via nitrosylation of the voltage-dependent L-type calcium channel<sup>17</sup> and ryanodine receptor 2.<sup>11,18</sup> Activation of these key calcium handling proteins can lead to increased  $Ca^{2+}$  entry and  $Ca^{2+}$ -induced calcium release, respectively.

On the other hand, in the presence of  $\beta$ -adrenergic stimulation, nitric oxide attenuates cardiomyocyte ECC inotropic enhancement by: 1) cyclic guanosine monophosphate-dependent degradation of cyclic adenosine monophosphate via phosphodiesterase II, thus effectively reducing  $Ca^{2+}$  entry through the downstream voltage-dependent L-type calcium channel effector;<sup>19,20</sup> and 2) protein kinase-G-mediated decrease of L-type calcium channel activity.<sup>19,21</sup>

Protein kinase-G has also been shown to phosphorylate troponin I via cyclic guanosine monophosphate-dependent mechanisms;<sup>22-24</sup> this leads to myofilament calcium desensitization, which is associated with positive lusitropic effects.<sup>71</sup>

### 2.3.2 Endothelial Endothelin-1

Endothelin-1 is a peptide that is a potent vasoconstrictor.<sup>72</sup> In addition to its vascular effects, endothelin-1 has demonstrated positive inotropic effects across various species<sup>61,73-75</sup> via activation of endothelin receptors expressed on cardiomyocytes. Studies have shown the positive inotropic effect of endothelin-1 is predominantly attributed to enhanced  $\text{Ca}^{2+}$  entry, increased myofilament sensitivity to cytosolic  $\text{Ca}^{2+}$ , and enhanced calcium-induced calcium release.<sup>76</sup>

Mechanistically, endothelin-1-mediated enhancement of  $\text{Ca}^{2+}$  entry results from: 1) activation of  $\text{Na}^+/\text{Ca}^{2+}$  exchanger forward and/or reverse mode via protein kinase C downstream of the endothelin A receptor;<sup>25-28</sup> and 2) indirect activation of the  $\text{Na}^+/\text{Ca}^{2+}$  exchanger reverse mode by protein kinase C-dependent increase of  $\text{Na}^+-\text{H}^+$  exchanger activity, effectively increasing intracellular  $\text{Na}^+$  and thus driving the  $\text{Na}^+/\text{Ca}^{2+}$  exchanger to increase intracellular calcium.<sup>29,30</sup> Other mechanisms, such as endothelin-1 activation of L-type calcium channel current remain controversial,<sup>31-34</sup> but are also likely mediated via protein kinase C downstream of the endothelin receptor.<sup>35</sup>

The increased extrusion of  $\text{H}^+$  via the  $\text{Na}^+-\text{H}^+$  exchanger was originally hypothesized to affect myofilament calcium sensitivity via cytosolic alkalinazation.<sup>76</sup> However, this was later debunked, as the bicarbonate anion transporter largely compensates for changes in cytosolic  $\text{H}^+$  concentration.<sup>76</sup> Instead, endothelin-1 likely alters myofilament sensitivity by protein kinase C/D-dependent phosphorylation of troponin I and myosin-binding protein C.<sup>36-40</sup>

Finally, endothelin-1 can stimulate inositol trisphosphate-induced calcium release from the sarcoplasmic reticulum of ventricular myocytes via inositol trisphosphate receptors, which

can subsequently sensitize ryanodine receptors.<sup>41-43</sup> However, these mechanisms are not considered large contributors to endothelin-1 inotropic effects on ventricular myocytes, which are known to have low abundance of inositol trisphosphate receptors.<sup>76,77</sup>

## 2.4 Paracrine Effects of Cardiac Fibroblasts on Myocyte ECC

Conventionally, healthy cardiac tissue is believed to have a cellular composition that is up to two-thirds non-myocytes, the majority of which are cardiac fibroblasts.<sup>78-80</sup> Interestingly, Pinto et al. recently demonstrated the number of fibroblasts might not be so high—potentially even less than myocytes—leaving this issue unresolved.<sup>81</sup> Nevertheless, while under normal physiological conditions fibroblasts are key to maintaining homeostasis of myocardial structure and function, they are also activated in pathological wound healing leading to tissue remodeling and fibrosis. The maladaptive remodeling of fibrotic scar formations then forms obstacles at the tissue level that interfere with normal electrical propagation,<sup>82,83</sup> and is considered pro-arrhythmic. Such pathophysiological responses have motivated genetic modification of unexcitable primary human fibroblasts to create engineered cells that can conduct action potentials and rescue conduction slowing in a cell culture model of fibrosis.<sup>84</sup> In general, cardiac fibroblasts are capable of expressing gap junctions and coupling to cardiomyocytes (see elsewhere<sup>85,86</sup> for a comprehensive review), and communicating via paracrine signaling.

As described below, physiologic fibroblasts and pathologic myofibroblasts have been found to alter myocyte size, electrophysiology, and calcium handling, thus influencing ECC at both cellular and tissue levels via paracrine signaling mechanisms.

### 2.4.1 Fibroblast-Derived Soluble Factors Can Mediate Cardiomyocyte Hypertrophy

In addition to their role in fibrosis, cardiac fibroblasts may influence the cardiac hypertrophic response. Indeed, a hypertrophic “nonmyocyte-derived growth factor” released by fibroblasts was hypothesized by Long et al. over 20 years ago.<sup>87</sup> Since then, various soluble

factors—such as angiotensin II, transforming growth factor beta (TGF- $\beta$ ), endothelin-1, insulin-like growth factor 1 (IGF-1), and interleukin 6—have been suggested as fibroblast paracrine mediators of hypertrophy.

Angiotensin II was one of the initial fibroblast paracrine factors hypothesized to induce hypertrophy in myocytes.<sup>88</sup> Later work then demonstrated fibroblasts are required to be present for angiotensin II-dependent hypertrophic effects,<sup>45,89,90</sup> motivating investigators to study downstream paracrine mediators released by angiotensin II stimulated-fibroblasts to induce myocyte hypertrophy.

For example, independent of its pro-fibrotic effects,<sup>91</sup> TGF- $\beta$  has been demonstrated to induce cardiac hypertrophy both in vitro and in vivo. Rosenkranz et al. demonstrated that over-expression of TGF- $\beta$  in transgenic mice led to increased hypertrophy.<sup>92</sup> Importantly, others showed stretched- or angiotensin II stimulated-fibroblast conditioned media neutralized of TGF- $\beta$  circumvents the cultured myocyte hypertrophic responses,<sup>44,45</sup> suggesting TGF- $\beta$  is required for fibroblast paracrine-mediated effects on myocyte hypertrophy. Using a similar approach, fibroblast-released endothelin-1 has also been suggested to induce hypertrophy. Conditioned media from fibroblasts stimulated with cyclic stretching or angiotensin II did not induce hypertrophy in myocytes treated with endothelin receptor antagonists.<sup>44,89,93</sup>

Other paracrine factors have also been suggested to stimulate cardiac myocyte hypertrophy; neutralizing cardiotropin-1—a member of the interleukin 6 family—or IGF-1 also attenuated hypertrophic effects of fibroblast-conditioned media.<sup>93-95</sup> Takeda et al. further demonstrated IGF-1 acts downstream of Küppel-like factor 5 to induce such hypertrophic effects on myocytes.<sup>96</sup> Other fibroblast hypertrophic soluble mediators (e.g., fibroblast growth factor 2<sup>97</sup>) have also been hypothesized, but are less studied. Taken together, the results suggest that beyond their role in fibrosis, cardiac fibroblasts secrete several soluble factors that may impact the hypertrophic response in the heart.

#### *2.4.2 Fibroblast-Derived Insoluble Extracellular Vesicles Mediate Cardiomyocyte Hypertrophy*

Recently, studies have shown that cell-cell communication can also take place via secreted exosomes, which are bilayer membrane-bound nanovesicles packaging cargoes of select lipids, proteins, and RNAs.<sup>98</sup> In the context of cardiovascular disease, various resident heart cells and therapeutic stem cells have been shown to communicate with myocytes and myocardial tissue via exosomes, predominately involved in cardioprotective,<sup>99,100</sup> pro-angiogenic,<sup>101,102</sup> and anti-fibrotic<sup>100,101</sup> effects.<sup>98</sup> However, recently it was shown that exosomes are also potential mediators of hypertrophy. Bang et al. observed that cardiac fibroblasts release exosomal miRNA passenger strand miRNA-21-3p to induce cardiomyocyte hypertrophy in vitro. Mechanistically, they identified sorbin and SH3 domain-containing protein 2, as well as PDZ and LIM domain 5 as the main targets and mediators of miRNA-21-3p induced hypertrophy.<sup>49</sup> Their findings translated in vivo, whereby microinjection of antagomiRNA-21-3p was found to attenuate angiotensin II-induced hypertrophy in mice.<sup>49</sup> Thus, it is possible that beyond secreted proteins, cardiac fibroblast-derived exosomes may also be involved in the cardiac response to stress.

#### *2.4.3 Fibroblast Paracrine Factor Effects on Electrophysiology*

An established electrophysiological phenotype of cardiac hypertrophy is prolonged action potential duration (APD) via reduction of voltage-gated potassium channel currents.<sup>103,104</sup> Thus, it is plausible that hypertrophy-inducing fibroblast conditioned media could also alter myocyte electrophysiology. Indeed, Guo et al. first demonstrated with neonatal rat cardiac myocytes in vitro that 72-hour treatment with fibroblast conditioned media not only induced hypertrophy, but also prolonged APD at 25% repolarization, and decreased transient outward current density.<sup>95</sup> Nearly a decade later, electrophysiological remodeling effects of fibroblast-conditioned media were further elucidated. Pedrotty et al. demonstrated various consistent single-cell and tissue-level pathological, dose-dependent, electrophysiological effects of cardiac

fibroblasts on neonatal rat cardiomyocytes, including: 1) decreased monolayer conduction velocity; 2) prolongation of APD; 3) increased resting membrane potential; and 4) decreased upstroke velocity.<sup>46</sup> These effects were likely caused by ion channel remodeling, as inward rectifying potassium, sodium, and transient outward potassium channel genes were down-regulated while there were no significant changes in fibroblast proliferation, cardiomyocyte apoptosis, or connexin-43 function.<sup>46</sup> Interestingly, these effects were not only dose-dependent but also microenvironment-dependent, as they were not reproduced when the treatment used conditioned media from cardiac myocyte-fibroblast co-cultures.<sup>46</sup>

Such observations of cardiac fibroblast conditioned media on the electrophysiological properties of cardiomyocytes are not limited to neonatal rat cardiac myocytes; indeed, they have been reported consistently across several myocyte sources. With adult rat cardiomyocytes, fibroblast conditioned media was shown to decrease peak transient outward current, lengthen APD, and decrease sodium channel current.<sup>105</sup> Adult mouse cardiac fibroblast conditioned media was found to prolong APD to 50% repolarization, increase peak notch action potential voltage (a possible surrogate of transient outward current activity), and decrease beat rate of mouse embryonic stem cell-derived cardiomyocytes.<sup>106</sup>

The fibroblast-released factors mediating such electrical remodeling remain unresolved. Guo et al. demonstrated fibroblast-released IGF-1 may play a role in hypertrophy, but not ion channel remodeling. They observed that anti-IGF-1 antibody treated fibroblast conditioned media partially inhibited myocyte hypertrophy,<sup>95</sup> while transient outward ion channel activity was unaffected relative to the fibroblast conditioned media group.<sup>95</sup> While TGF- $\beta$  has been shown to induce hypertrophy (as discussed above), it is also a valid candidate as a mediator of the electrophysiological effects of cardiac fibroblast conditioned media, as Kaur et al. showed that TGF- $\beta$  was responsible for ion channel remodeling in adult rat cardiomyocytes.<sup>105</sup> Such effects could potentially contribute to the electrical remodeling that typically accompanies myocardial injury. Additionally, Kaur et al.'s findings were consistent with other studies examining

exogenous TGF- $\beta$ , which has been found to: 1) reduce sodium, inward rectifier potassium, and outward sustained potassium currents in neonatal rat atrial cardiomyocytes;<sup>107</sup> 2) increase and decrease sodium and transient outward potassium currents, respectively, in adult rat cardiomyocytes;<sup>105</sup> and 3) prolong APD in adult rat cardiomyocytes.<sup>105</sup> One important area for future work involves testing the extension of these findings in large animal and human cardiomyocytes, as we begin to investigate below in Figures 3-5.

#### *2.4.4 Fibroblast-Derived Paracrine Mediators of ECC and Contractility*

Recently, fibroblast paracrine factors have also been shown to also alter calcium handling—a direct determinant of ECC—as well as cardiac tissue contractility. Motivated by the hypertrophy and electrophysiology studies described above, Cartledge et al. sought to further elucidate the role of physiological fibroblasts and pathological myofibroblasts on adult rat myocyte viability, size, and calcium transients.<sup>47</sup> Using Transwells® to prevent direct cell-cell contact, they showed that physiological cardiac fibroblasts and pathological cardiac myofibroblasts both secrete paracrine factors that increase myocyte size, accelerate calcium transient decay, and decrease myocyte viability. However, effects on myocyte calcium transients were fibroblast phenotype-dependent: physiological fibroblast paracrine factors increased the myocyte calcium transient amplitude, while pathological myofibroblast paracrine factors decreased the calcium transient amplitude.<sup>47</sup> Interestingly, Cartledge et al. observed TGF- $\beta$  levels increased in Transwells® containing myocytes with either fibroblasts or myofibroblasts relative to myocyte-only cultures.<sup>47</sup>

To test the role of TGF-beta in fibroblast paracrine-mediated effects on myocyte calcium handling, viability, and hypertrophy, they used SB431542 to block TGF- $\beta$  type 1 receptors. Blockage of the TGF- $\beta$  type 1 receptor prevented the previously described effects on cardiomyocyte viability, size, and calcium transient amplitude.<sup>47</sup>

Liau et al. recently extended this work to investigate developmental stage-dependent effects of cardiac fibroblast conditioned media on contraction. Specifically, mouse embryonic stem cell derived-cardiomyocyte miniature tissue “micro-patches” were supplemented with conditioned media from adult or fetal cardiac fibroblasts.<sup>48</sup> Adult cardiac fibroblast conditioned media significantly increased contraction of the mouse micro-patches; these effects were amplified with fetal cardiac fibroblast-conditioned media.<sup>48</sup> Using pathway inhibitor experiments and Western blot analysis, they concluded these effects to be mediated via MEK-ERK signaling,<sup>48</sup> which is a non-Smad pathway in TGF- $\beta$  signaling.<sup>108</sup> Altogether, these findings suggest TGF- $\beta$  is a likely mediator of cardiac fibroblast paracrine-mediated effects on contraction via ion channel remodeling and hypertrophy.

## 2.5 Stem Cell Secretomes Can Impact Cardiomyocyte ECC

Resident adult cardiac stem cells—which include CPCs, endothelial progenitor cells, and MSCs<sup>109</sup>—also have the potential to increase cardiomyocyte ECC through paracrine mechanisms. For example, Tang et al. demonstrated cell-mimicking synthetic microparticles carrying the human cardiac stem cell secretome promoted neonatal rat cardiomyocyte contractility *in vitro*.<sup>110</sup>

Delivery of CPCs<sup>101,111-113</sup> and bone marrow-derived MSCs<sup>58,114-116</sup> are emerging approaches to treat heart disease. Like several other stem cell sources (e.g., embryonic and induced pluripotent stem cells, CD34<sup>+</sup> stem cells, etc.), CPC and MSC paracrine factors have been shown to enhance angiogenesis,<sup>101,112,117-119</sup> decrease fibrosis,<sup>101,112,119,120</sup> and promote other cardiac repair mechanisms (comprehensive reviews on this topic are available elsewhere<sup>121,122</sup>), which can indirectly modulate cardiomyocyte contractility. Moreover, CPC and MSC paracrine factors have each shown the potential to more directly alter myocyte electrophysiology and calcium handling, and thus ECC.

### *2.5.1 Kinetics of Stem Cell Paracrine Effects on ECC*

As depicted in Table 1, CPC and MSC paracrine effects on cardiomyocyte ECC are primarily associated with increasing expression of calcium handling genes. In comparison to nearly instantaneous  $\beta$ -adrenergic signaling mechanisms,<sup>123</sup> paracrine mechanisms are expected to be slower and longer-lasting; indeed, Desantiago et al. demonstrated MSC paracrine effects on ECC take at least 5 minutes in isolated ventricular myocytes,<sup>52</sup> and in our recent work, such in vitro effects of MSCs were evident at least five days post-treatment.<sup>54</sup> Clearly, a better understanding of the kinetics of stem cell paracrine effects is warranted in order to optimize future stem cell cardiotherapies for both ischemic and non-ischemic cardiomyopathies. To do so, further insight is required into CPC and MSC paracrine effects on ECC; current knowledge on each of these respective fields is discussed below.

### *2.5.2 CPC Paracrine Effects on Cardiomyocyte ECC*

Few studies have investigated CPC paracrine effects on cardiomyocyte ECC. Maxeiner et al. observed that human and rat CPC-conditioned media increased fractional shortening in isolated rat adult cardiomyocytes in a concentration-dependent manner relative to pure media control treatment, largely independent of CPC donor age.<sup>50</sup> In addition, conditioned media derived from several human adult and juvenile CPC lines led to an increase in the ratio of sarcoendoplasmic reticulum  $\text{Ca}^{2+}$ -ATPase (SERCA)/sodium-calcium exchanger gene expression.<sup>50</sup> Interestingly, increases in contractile function were most prominent when the conditioned media was highly diluted,<sup>50</sup> with further investigation required to understand these phenomena.

Several preliminary attempts have been made to identify which CPC-secreted factors may impact myocyte ECC. For example, in the same study, Maxeiner et al. performed cytokine arrays on released soluble factors by rat and human CPCs;<sup>50</sup> the interleukin family, vascular endothelial growth factor, and tissue inhibitors of metalloproteinases-1 were consistently up-

regulated in both juvenile and adult rat and human CPCs.<sup>50</sup> Considering other components of the CPC secretome, a series of studies by the Davis group observed that the insoluble exosomal fraction of CPC-conditioned media led to no significant effect on rat ventricular myocyte calcium transient amplitude and sarcomere shortening at 12 hours post-treatment.<sup>101,112</sup> It remains undetermined whether there may be a time- or species-dependence to these observations. Clearly, further investigation is necessary to better understand mechanisms and cargo involved in CPC paracrine-mediated effects on cardiomyocyte ECC. As discussed below, paracrine effects of MSCs on ECC have been more extensively studied.

### *2.5.3 MSC Paracrine Effects on Electrophysiology*

The electrophysiological effects of MSC paracrine factors appear to vary across species and experimental conditions. Mureli et al. first showed mouse MSC conditioned media has a positive dromotropic effect on healthy atrial-like murine HL-1 monolayers by increasing connexin-43 mRNA expression and protein level.<sup>124</sup> Hwang et al. found increased total connexin-43 protein levels significantly increased in hypoxic rat myocytes exposed to hypoxic human MSC (hMSC) conditioned media (exposure to normoxic hMSC conditioned media trended toward increased levels, with no statistical significance).<sup>53</sup> However, these findings were not consistent with healthy ventricular myocytes using hMSC conditioned media,<sup>51</sup> suggesting the effects of hMSC conditioned media may depend on cell phenotype and environment. Askar et al. showed with Transwell® experiments that hMSC conditioned media prolonged healthy neonatal rat cardiomyocyte APD in a dose-dependent manner, but did not affect conduction velocity in myocyte monolayers.<sup>51</sup> Comparable to the 5-10% hMSC supplementation (percent per number of cardiomyocytes and fibroblasts in engineered cardiac tissue) used in our recent experiments,<sup>54</sup> Askar et al. observed that dosages of 7% hMSC conditioned media (percent per number of myocytes in 2-D) led to significant effects on cardiomyocyte electrophysiology.<sup>51</sup> Dose-dependent prolongation of APD led to increased APD dispersion and vulnerability of re-

entry in the setting of healthy neonatal rat cardiomyocyte monolayers.<sup>51</sup> On the other hand, in hydrogen peroxide treated human induced pluripotent stem cell derived-cardiac myocyte monolayers, hMSC conditioned media significantly decreased action potential alternans relative to control.<sup>55</sup>

In a recent study,<sup>54</sup> *in silico* findings from mathematical models provide novel insights that help resolve disparate reports of potential pro-arrhythmic risks of hMSCs *in vitro*<sup>125</sup> that appear contradictory to *in vivo* reports of hMSCs having no effect,<sup>57</sup> or favorable cardioprotective effects,<sup>58</sup> on arrhythmogenesis in pre-clinical animal studies and clinical trials. In simulations representing healthy myocyte monolayers (i.e., similar to experimental conditions from Askar et al.<sup>51</sup>), both hMSC paracrine signaling and heterocellular coupling have the potential to increase arrhythmogenicity (Online Figure IA; see Mayourian et al. for detailed methods<sup>54</sup>). However, in vulnerable window simulations of fibrotic cardiac tissue (i.e., similar to pre-clinical/clinical conditions for hMSC intervention), hMSC paracrine signaling-only conditions were anti-arrhythmic compared to control (Online Figure IB),<sup>54</sup> consistent with a preclinical study in a rat myocardial infarction model, where hMSC paracrine factors were anti-arrhythmic, suppressed fibrosis, and restored conduction.<sup>53</sup> Most importantly, *in silico* vulnerable window analyses predicted that hMSC supplementation (involving both hMSC paracrine signaling and heterocellular coupling mechanisms) did not adversely impact fibrotic cardiac tissue arrhythmogenesis, and may even be anti-arrhythmogenic (Online Figure IB).<sup>54</sup> These simulations may help explain why hMSCs are mainly reported to be safe<sup>57</sup> or even anti-arrhythmic<sup>58</sup> in the clinical trial setting where paracrine effects can be present despite low cell engraftment efficiency.

While our simulations may suggest maximizing hMSC engraftment increases arrhythmogenic risk, it is important to note that several *in vitro* studies demonstrate that hMSCs have the potential to repair conduction block in neonatal rat cardiomyocyte cultures by filling conduction gaps via connexin-mediated heterocellular coupling.<sup>126,127</sup> To our knowledge, this

experimental preparation has yet to be simulated; the potentially important implications in post-myocardial infarction tissue warrant further investigation.

#### *2.5.4 MSC Paracrine Effects on Calcium Handling*

The effects of MSC paracrine factors on calcium handling are observed across several studies that look at healthy and injured myocytes. Desantiago et al. first showed that hMSC conditioned Tyrode-treated healthy mouse cardiomyocytes had increased calcium transient amplitude and accelerated calcium transient decay compared to control.<sup>52</sup> Beneficial effects of hMSC paracrine factors on calcium handling were found in injured myocytes,<sup>53</sup> where both normoxic and hypoxic hMSC conditioned media suppressed effects of hypoxia on neonatal rat ventricular myocyte cytosolic free calcium levels.<sup>53</sup> Sattayaprasert et al. further showed that hMSC conditioned media reduces calcium transient alternans and shortens calcium transient duration in hydrogen peroxide treated human induced pluripotent stem cell derived-cardiac myocyte monolayers.<sup>55</sup> Similarly, mouse MSC conditioned media attenuated the occurrence of arrhythmic calcium transients of ischemia/reperfusion injured isolated ventricular myocytes.<sup>56</sup> Thus, across species, hMSC conditioned media appears to have favorable effects on calcium handling in cultured cardiomyocytes.

#### *2.5.5 MSC Paracrine-Mediated Effects of Cardiac Contractile Function*

In our most recent work, we demonstrated that the effects of hMSC paracrine factors on calcium handling translated to increased contractility in both computer model simulations and our custom human engineered cardiac tissue (hECT) system.<sup>54</sup> We simulated ECC of human induced pluripotent stem cell-derived cardiomyocytes—representative of hECT cellular constituents—subjected to experimentally calibrated hMSC heterocellular coupling<sup>128</sup> and paracrine signaling effects.<sup>54</sup> We then compared the *in silico* results to hECT contractility measurements under matched hMSC treatments. The *in silico* and hECT data together

corroborate the paracrine-mediated effects of hMSCs on cardiomyocyte contractility.<sup>54</sup> Interestingly, when hMSCs were co-cultured within hECTs, the hMSC paracrine-mediated increase on contractility was attenuated;<sup>54</sup> our simulations predicted underlying myocyte-hMSC heterocellular coupling may act as a “sink” and reduce calcium transient amplitude and thus decrease contraction.<sup>54</sup> A similar phenomenon was recently reported by the Parker group, as neonatal cardiomyocytes coupled with stem cell-derived cardiomyocytes led to calcium transients and fractional shortening intermediate between the two cell types.<sup>129</sup> Clearly, further investigation is needed to better understand direct cell-cell contact effects on cardiomyocyte ECC.

The previously described findings of MSC paracrine effects on contractility were consistent with a pair of studies by DeSantiago et al., where MSC conditioned Tyrodes’ solution increased cell shortening in healthy and injured mouse myocytes.<sup>52,56</sup> Furthermore, they complement the findings by Luo et al., where hMSC secreted factors packaged into poly(lactic-co-glycolic acid) microparticles coated with the hMSC membrane promoted neonatal rat cardiomyocyte contraction in vitro.<sup>130</sup> These positive inotropic effects of the hMSC secretome motivate efforts to: 1) investigate the underlying mechanisms; and 2) identify the responsible cardioactive factors.

#### *2.5.6 Underlying Mechanisms of MSC Paracrine Effects on ECC*

Substantial progress has been made toward elucidating the underlying mechanisms responsible for MSC paracrine effects on electrophysiology and calcium handling. Hwang et al. observed that hypoxic rat myocytes treated with normoxic hMSC conditioned media trended towards increased mRNA levels of L-type calcium channel and SERCA2a relative to control, with statistical significance achieved when hMSCs were cultured under hypoxic conditions.<sup>53</sup> We recently demonstrated that treating hECTs with hMSC conditioned media also led to increased mRNA levels of L-type calcium channel and SERCA2a relative to untreated control;<sup>54</sup>

additionally, Desantiago et al. found that the activity of L-type calcium channel and SERCA2a activity increases in healthy mouse myocytes exposed to hMSC paracrine factors relative to control.<sup>52</sup>

Desantiago et al. were one of the first groups to find that the PI3K/Akt signaling pathway was activated in mouse ventricular myocytes by MSC conditioned media.<sup>52</sup> Through proteomic analysis, we also recently also showed that PI3K/Akt signaling is predicted to be activated in hECT/hMSC conditioned media.<sup>54</sup> This signaling pathway was also implicated in MSC paracrine-mediated cardioprotection from ischemia/reperfusion injury in vitro, where hMSC conditioned Tyrode's solution attenuated the hyperpolarization of the mitochondrial membrane potential via PI3K/Akt signaling<sup>56</sup>, prolonging cell survival and reducing arrhythmic early after depolarizations. The role of the PI3K/Akt signaling pathway in hMSC conditioned media-mediated ECC enhancement was further defined in human induced pluripotent stem cell-derived cardiomyocyte calcium handling by Sattayaprasert et al.,<sup>55</sup> where inhibitors of PI3K and endothelial nitric oxide synthase (a downstream mediator of PI3K) attenuated the benefits of hMSC paracrine media on calcium transient alternans and duration, whereas S-nitrosoglutathione, an nitric oxide donor, had opposite effects. Taken together, these findings confirm that the PI3K/AKT pathway is a critical mediator of the effects of hMSC paracrine factors on cardiomyocyte ECC.

### *2.5.7 Proposed MSC Factors Responsible for Enhancing ECC*

Numerous studies have investigated the composition of the hMSC secretome;<sup>120,131-136</sup> however, while many secreted factors have been associated with pro-angiogenic<sup>120,137-139</sup> and anti-fibrotic<sup>120,139-141</sup> effects, little is known regarding the hMSC paracrine factors responsible for the effects on electrophysiology, calcium handling, and contractility described above.

Cardioactive hMSC exosomes have been shown to modulate myocyte PI3K/Akt signaling,<sup>100,142</sup> a crucial pathway involved in hMSC paracrine effects on cardiomyocyte ECC

(Table 1). Indeed, we found that treating hECTs with the exosome-enriched fraction of the hMSC secretome recapitulated the effects observed with complete hMSC conditioned media on hECT contractile force and expression of calcium handling genes (e.g., SERCA2a and L-type calcium channel), whereas treatment with the exosome-depleted fraction was similar to unsupplemented controls.<sup>54</sup> These findings motivate further investigation into the role of hMSC exosomes, their membrane (while certain exosomal membranes appear necessary for pro-angiogenic and anti-fibrotic cardioactivity,<sup>101</sup> in general little is known about their role on cardiomyocyte ECC), and their cargo responsible for increased cardiomyocyte contractility.

hMSC exosomal cargo has been implicated in multiple studies related to cardiac repair,<sup>98,100,143-145</sup> however, little is known about the specific effects of hMSC exosomes and their cargo on contractility. Based on previous literature, exosomal miRNA-21-5p may be one possible candidate responsible for increasing ECC in cardiomyocytes. miRNA-21-5p is the only miRNA consistently in the top 5 most abundantly found in hMSC exosomes across three independent studies.<sup>131,135,146</sup> Interestingly, cardiac progenitor cell exosomal miRNA-21-5p has been shown to prevent cardiomyocyte apoptosis by targeting programmed cell death 4, known to be downstream of the PI3K/Akt signaling pathway.<sup>147</sup> This is consistent with the findings by Wei et al.<sup>148</sup> and Cheng et al.,<sup>149</sup> where miRNA-21-5p also regulated cardiomyocyte apoptosis by targeting programmed cell death 4. miRNA-21-5p has also been shown to bind strongly to phospholamban<sup>150</sup> and to activate endothelial nitric oxide synthase,<sup>151</sup> both of which increase SERCA2a activity.<sup>52,150</sup> Clearly, further work is necessary to elucidate the cardiotropic role of miRNA-21-5p and other key constituents of the hMSC secretome.

A major challenge in identifying key CPC and hMSC paracrine factors is that the composition of their secretomes strongly depends on the microenvironment. For example, the Davis group showed the cardioactivity of CPC exosomes increases under hypoxia.<sup>101,152</sup> Similarly, Hwang et al. showed that hypoxic conditioning of hMSCs leads to more potent paracrine effects on calcium handling enhancement, fibrosis reduction, and cardioprotection.<sup>53</sup>

Kinnaird et al. demonstrated that 72 hours of hypoxic preconditioning of hMSCs led to a significant increase in the secretion of pro-angiogenic factors relative to normoxic control conditions.<sup>153</sup> Furthermore, genetic manipulation of hMSCs<sup>154</sup> or molecular preconditioning of hMSCs<sup>155</sup> can also increase the potency of their paracrine effects. A systematic investigation utilizing a reliable contractility assay is warranted to optimize these environmental variables and to help identify key cardioactive hMSC paracrine factors.

## **2.6 Tissue Engineering Approaches to Study Non-Cardiomyocyte Paracrine Effects on Cardiac Contraction**

### *2.6.1 Human Engineered Cardiac Tissues as an *in vitro* Contractility Assay*

A major advancement in the cardiac research field has been the growing sophistication of in vitro models of functional human myocardium by combining tissue engineering technology with human stem cell biology,<sup>156-158</sup> as recently reviewed.<sup>159-161</sup> In our laboratory, hECTs are created, cultured, and tested using a custom bioreactor<sup>162</sup> with integrated force-sensing end-posts. As the tissue beats (either spontaneously or by electrical pacing), deflections of the end-posts are tracked in real time by high-speed video to non-invasively monitor contractile performance throughout a sequence of twitch cycles (Figure 3A). From the twitch tracings, extracted contractile metrics include, but are not limited to, developed force (DF), maximum rates of contraction and relaxation, and beat rate (Figure 3A, bottom).

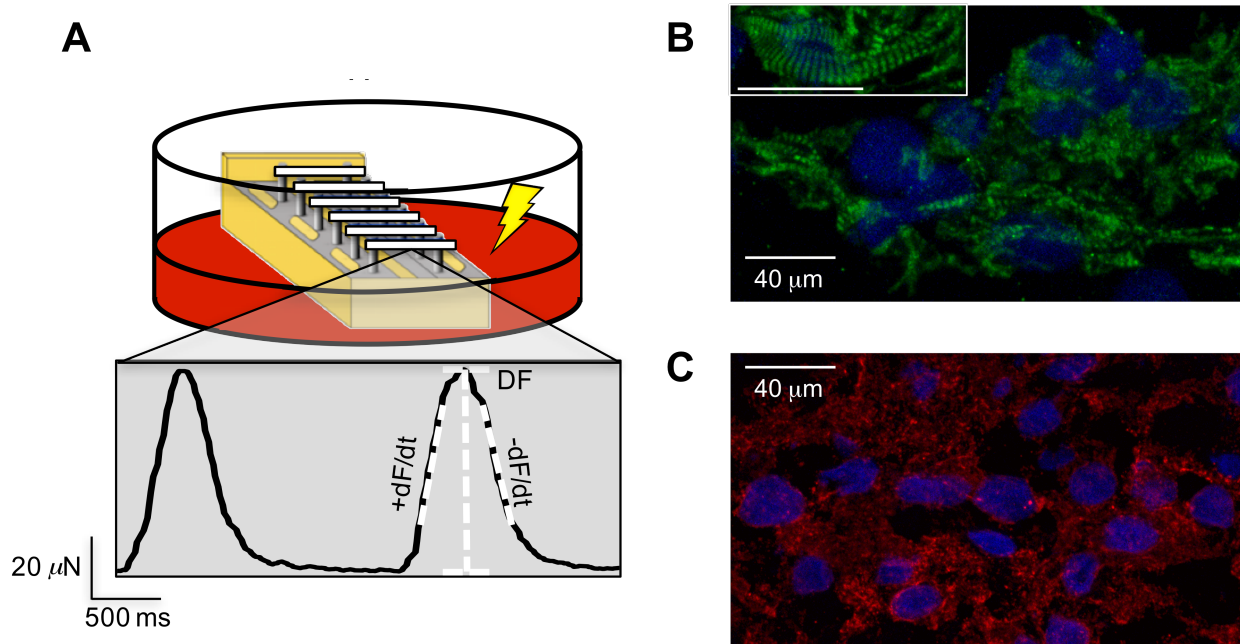


**Figure 3: Human Engineered Cardiac Tissue Contractility Assay.** (A) hECTs are created, cultured, and tested in a custom bioreactor with integrated force-sensing end-posts; as the tissue beats, deflections of the end-posts are tracked. Output contractile metrics include, but are not limited to, developed force (DF), maximum rates of contraction and relaxation (+/- dF/dt, respectively), and beat rate. (B) Confocal microscopy of hECTs labeled with cardiac troponin I (green) and DAPI (blue) displays cardiomyocytes with striated sarcomeres and regions of aligned myofibrils. Inset shows magnified view of registered sarcomeres. (C) hECT labeled with sarcoendoplasmic reticulum Ca<sup>2+</sup>-ATPase 2 (red) and DAPI (blue) shows sarcoplasmic reticulum structures distributed throughout the tissue. Scale bar = 40  $\mu$ m.

These hECTs have been designed to ensure cell viability throughout the full tissue thickness,<sup>163,164</sup> with cardiomyocytes that exhibit regions of aligned myofibrils and registered sarcomeres (Figure 3B). With SERCA2 found throughout the tissue (Figure 3C), hECTs recapitulate key aspects of native cardiac muscle physiology including ECC, the Frank-Starling mechanism, and pharmacologic responses.<sup>163</sup> Such hECTs can be maintained for 4 weeks or

longer, and are particularly suited for longitudinal in vitro investigation of healthy and diseased human cardiac contractile function and effects of therapeutic intervention. To this end, in the cardiac tissue engineering field, we are one of the first groups to model familial dilated cardiomyopathy<sup>165</sup> and to test stem cell therapies.<sup>54,162,164</sup> In the context of this review, our hECT system is advantageous for uniquely providing a configuration of co-cultured tissues in a shared bath in order to investigate paracrine signaling effects on cardiac contractility. Its ability to non-invasively measure contractile function facilitates the collection of multi-day longitudinal data on the effects of paracrine factors on contractile function. Altogether, hECTs offer a system that helps bridge a gap in previous experimental models of the heart, and provides new opportunities for advancing our understanding of stem cell paracrine signaling and exosome biology.

Indeed, our recent work on hMSC paracrine-mediated effects on hECT contractile function and gene expression recapitulated many findings from murine studies using alternative experimental setups,<sup>54</sup> but also reveal some interesting species-specific and/or platform-specific differences. To further demonstrate the use of hECTs for testing paracrine-mediated effects on contractility, we provide new data examining how the effects of the fibroblast secretome on cardiomyocyte contractility and ECC-relevant gene expression translates to human cell sources (for detailed methods, see the Online Supplement). Following baseline contractile function testing on day 5 using our custom 3-D hECT contractility assay system (Figure 3A), we treated hECTs with either: 1) serum-free defined media control; 2) fresh human foreskin fibroblast conditioned media (HFF CdM); or 3) fresh human adult cardiac fibroblast conditioned media (hACF CdM). hECTs were cultured an additional 5 days in their respective treatments, after which contractile function was measured and compared to baseline measurements. Spontaneous beat rate and DF were also measured on a daily basis, providing a simple method of monitoring longitudinal contractile function without having to replace culture media (as is normally done following electrical pacing to eliminate electrolysis byproducts).

As shown in Figure 4A, the hACF CdM treatment led to a statistically significant increase in DF relative to pre-treatment at 0.5 Hz pacing, whereas the HFF CdM and untreated control groups were not significantly different from pre-treatment. Furthermore, hACF CdM led to a statistically significant increase in hECT DF relative to HFF CdM at 0.5 Hz pacing five days post-treatment (Figure 4A).

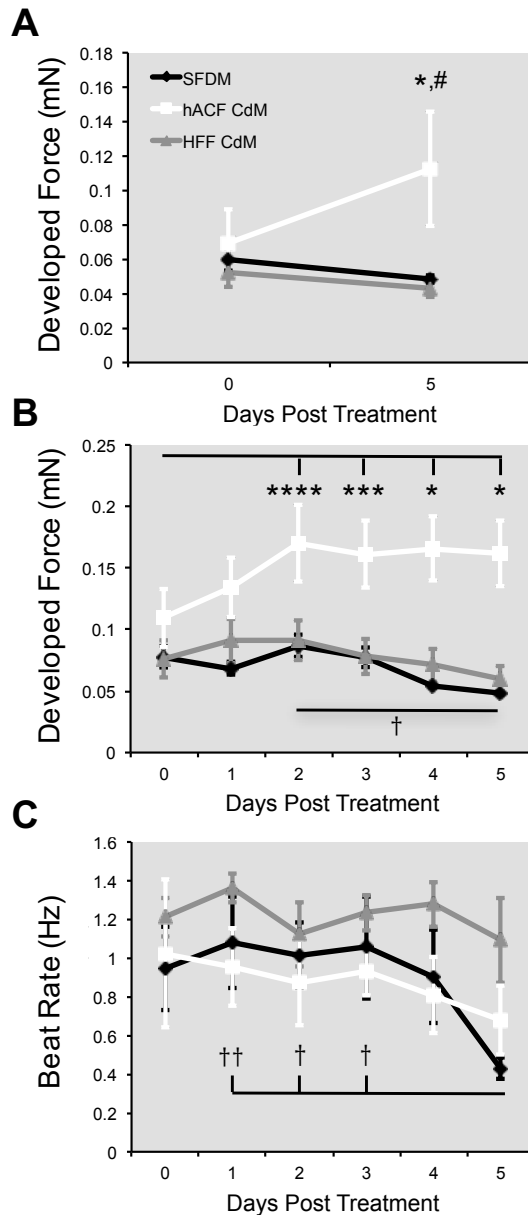


**Figure 4: Effects of hACF Conditioned Media on hECT Contractile Function.** (A) Contractility assay shows hECT developed force during 0.5-Hz pacing (mean $\pm$ SEM, n=4-6) at

pre-treatment (day 5) and 5-days post-treatment with serum-free defined media (SFDM, control), hACF CdM, and HFF CdM. Daily measurements of (**B**) developed force and (**C**) beat rate during spontaneous contractions for each group (mean $\pm$ SEM, n=3-4). \*p<0.05, \*\*p<0.01, \*\*\*p<0.001, \*\*\*\*p<0.0001, comparison of time point relative to pre-treatment in same group;  $^{\#}$ p<0.05, comparison of given group relative to HFF CdM at same time point;  $\dagger$ p<0.05,  $\ddagger$ p<0.01, comparison of same group at two different time points. p-values from repeated measures obtained using ANOVA followed by Bonferroni's multiple comparisons test.

To understand the time-dependence of treatments, we looked at spontaneous beat rate and DF. As shown in Figure 4B, hACF CdM treatment led to statistically significant increases in DF days 2-5 post-treatment relative to day 0 pre-treatment, even though beat rate was not significantly different over time in this group (Figure 4C). In the HFF CdM and control groups, beat rate and DF tended to be relatively stable over time (the control group showed a significant decrease in beat rate on day 5 post-treatment, which coincided with a small but significant decrease in DF at this time point). These results complement murine studies on cardiac fibroblast paracrine-mediated contractility effects, as previously described.<sup>47,48</sup>

These hECT functional measures were corroborated by molecular characterization. Following five days of treatment and testing as above, hECTs from each group were snap-frozen for prospective qRT-PCR of cardiac-specific, calcium handling, apoptosis, and potassium/sodium ion channel (i.e., repolarization/depolarization, respectively) genes. In general, calcium handling and cardiac-specific genes were not significantly different between groups (Figure 5A). Furthermore, apoptosis genes were not significantly different between groups (Figure 5B). Interestingly, this hACF CdM-mediated gene profile is distinctly different from that of hMSC-treated hECTs (noted above and elsewhere<sup>54</sup>) despite similarities in the increase of hECT contractile function by the two cell types. Like others have suggested,<sup>46</sup> this implies the effects of hACF CdM must be mediated through alternative mechanisms.

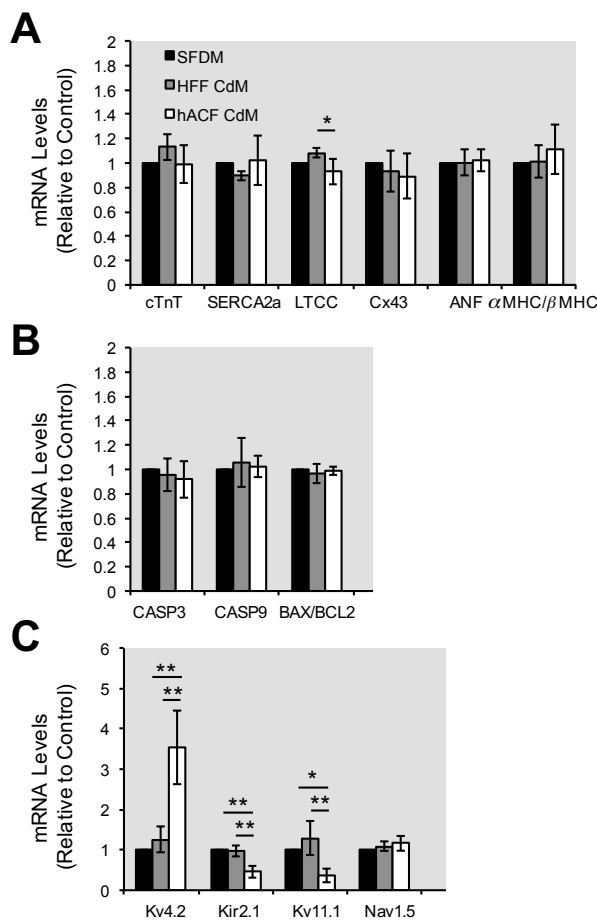


**Figure 5: Molecular Characterization of hECTs.** hECTs from each group (n=3-4, mean $\pm$ SEM)

were snap-frozen for qRT-PCR on day 10, where expression of (A) cardiac-specific/calcium handling, (B) apoptotic, and (C) potassium/sodium channel genes were quantified. \*p<0.05, \*\*p<0.01; p-values from one-way ANOVA with Scheffe's post-hoc test. Non-standard abbreviations: cardiac troponin T (cTnT); L-type calcium channel (LTCC); sarco/endoplasmic reticulum calcium-ATPase (SERCA2a); connexin-43 (Cx43); atrial natriuretic peptide (ANF); myosin heavy chain (MHC); caspase-3 (Casp3); caspase-9 (Casp9); B-cell lymphoma 2 (BCL2); BCL2-associated X protein (BAX); transient outward potassium current (Kv4.2); inward rectifier potassium current (Kir2.1); delayed rectifier potassium current (Kv11.1); sodium current (Nav1.5).

In particular, expression of the Kir2.1 inward rectifier and Kv11.1 delayed rectifier potassium channel genes significantly decrease in the hACF CdM intervention group compared to both HFF CdM and control groups (Figure 5C). These findings are also consistent with others.<sup>46</sup> Surprisingly, there was a statistically significant increase in Kv4.2 transient outward potassium channel gene expression in the hACF CdM intervention group compared to both HFF CdM and control groups (opposite of previous reports in rodent cells<sup>46</sup>), while there is no significant difference in the Nav1.5 sodium channel gene between groups (which was found to decrease in rodent studies<sup>46</sup>). This may partly reflect species-dependent variations in ion channel distributions; for example, Kv4.2 is highly expressed in rat myocytes, but not in human myocytes.<sup>166</sup> Accordingly, out of all genes analyzed, Kv4.2 had the highest threshold cycle (i.e., lowest expression) in control hECTs. Furthermore, transient outward activity plays a much less influential role in the human stem cell-derived myocyte action potential waveform relative to murine action potential (see multi-species sensitivity analysis in our previous work<sup>54</sup> for justification). This suggests the increase in Kv4.2 is likely not physiologically significant, even though it is statistically significant. Altogether, these studies further support the use of hECT functional and molecular characterization for testing non-cardiomyocyte paracrine effects on cardiac ECC.

Based on these findings and the previous studies described, we hypothesize that reduction of outward potassium currents by hACF CdM leads to prolongation of the APD and, therefore, increased calcium handling with a concomitant increase in contractile force. The proposed mechanism is similar to the described inotropic effects of class III antiarrhythmic drugs.<sup>167-169</sup> APD is an established correlate of contractile force;<sup>170-172</sup> therefore, by effectively prolonging the plateau period, calcium availability is increased, augmenting calcium induced calcium release, elevating the calcium transient, and increasing ECC.

## *2.6.2 Limitations of Human Engineered Cardiac Tissues*

Despite the advantages of hECT technology, one recognized limitation is the relatively immature cardiac phenotype that mimics newborn human heart muscle,<sup>163</sup> reflecting an ongoing scientific challenge with cardiomyocytes derived from pluripotent stem cells.<sup>173</sup> While perhaps not ideal for cardiac repair applications,<sup>174</sup> immaturity may be less problematic for in vitro screening of factors that can modulate contraction given that aspects of the fetal gene program are reactivated as a stress-protective mechanism in failing adult myocardium.<sup>175</sup> Also, hMSC therapy has recently been proposed to treat pediatric dilated cardiomyopathy.<sup>176</sup> Thus, immature hECTs may adequately represent some aspects of the heart failure disease state and, as such, offer a unique contractility assay for studying cell-based treatment mechanisms and developing future cardiac therapies.

Nevertheless, like others in the field, we continue to develop strategies to promote phenotypic maturation of human pluripotent stem cell derived cardiomyocytes and hECTs including improved electrophysiology and contractility,<sup>177</sup> structurally advanced sarcomeres and evidence of T-tubule formation,<sup>178</sup> and the ability to model various forms of hypertrophic and dilated cardiomyopathies.<sup>165,179</sup> Generating physiologic levels of force may be a prerequisite for surgical implantation applications of engineered cardiac tissues;<sup>158</sup> however, for in vitro studies, the current sub-physiologic but cardio-mimetic performance of our hECTs appears suitable for therapeutic screening applications.

## **2.7 Systems Biology Approaches to Study Stem Cell Paracrine Effects on ECC**

As previously reviewed,<sup>120,134</sup> bioinformatics methods have proven valuable for investigating paracrine mechanisms of stem cell therapy, such as angiogenesis, fibrosis, and immune modulation. However, in the specific context of paracrine effects of stem cells on cardiac ECC, the application of computational and systems biology approaches is a relatively nascent field. As discussed below, recent systems biology approaches have shown promise

for: 1) complementing experimental data to better understand non-cardiomyocyte paracrine effects on contractile function; and 2) identifying key paracrine mediators responsible for increases in contractility.

In our previous work,<sup>54</sup> complementary experimental and computational methods were used to study hMSC paracrine-mediated effects on contractility and arrhythmogenicity. The mathematical models could simulate how paracrine signaling affects cardiac cell and tissue physiology (e.g., action potentials and calcium transients) based on calibrating the models with measured effects on cellular physiology and tissue-level fibrosis. One benefit of this approach is that the relative importance of specific effects can be independently controlled and readily delineated in the simulations, which is often challenging in an experimental setting. A second benefit is that because the model is calibrated using data covering a range of hMSC concentrations, the effects of intermediate concentrations can also be simulated. Our model was successful in reproducing paracrine-mediated effects on hECT contraction that were not included in the model calibration process, demonstrating the predictive power of the model. Together, these two approaches, which provide complementary information, can yield greater insights than either strategy used in isolation.

Nevertheless, such phenomenologic simulations cannot be used to infer which components of the secretome are crucial in altering myocyte physiology. Recent advancements in systems biology have enabled linking complex networks of cues (e.g., hMSC microenvironment), signals (e.g., hMSC factors), and responses (e.g., phenotypes of interest). Janes et al. first demonstrated that partial least squares regression (PLSR) analysis is useful for forming relationships between signaling molecules and cell decisions.<sup>180</sup> The PLSR method has been applied to a range of bioanalytics problems;<sup>181-184</sup> recently, the Davis group used PLSR in a pair of studies to form relationships between CPC exosomal miRNA effectors and pro-angiogenic, anti-fibrotic, and anti-hypertrophic responses.<sup>101,152</sup> This method was successful in

predicting various key exosomal miRNAs, though it has yet to be applied in the context of cardiomyocyte ECC.

## **2.8 Integrating Tissue Engineering and Systems Biology Approaches to Identify Novel Cardioactive Factors**

Ranganath et al. first proposed a systematic approach to optimize and harness the hMSC secretion profile by conditioning hMSCs with an array of small molecules, and subsequently characterizing the customized secretomes via high-throughput human cytokine antibody array.<sup>120</sup> In the context of identifying key components of the hMSC secretome responsible for increasing contractility, this method could address the issue of hMSC secretome dependence on microenvironment/preconditioning, but it would not reveal: 1) the key factors responsible for a given contractile phenotype; nor 2) the role of insoluble factors, including exosomes and their cargo, which have been demonstrated to influence contractile function.<sup>54</sup>

We propose utilizing the PLSR method to help identify key hMSC factors responsible for increasing contractility. By collecting sets of quantitative measurements of “input” signaling molecules and “output” metrics of interest across an array of culturing conditions, PLSR can be utilized to predict relationships between the cues, signals, and responses (details of this method are available elsewhere<sup>101,152</sup>). This method is an extension of that proposed by Ranganath et al.,<sup>120</sup> in addition to signals and cues, it would also require responses of interest. Given our stated focus on ECC, we propose utilizing hECTs as an in vitro contractility assay to generate physiologically relevant response data for the PLSR analysis. By testing the contractile function of hECTs supplemented with hMSC-conditioned media from an array of preconditioning environments, PLSR can be applied to systematically reveal relationships between factors identified via protein and miRNA profiling techniques, and functional contractile outputs of hECTs. Such methodology could equally be applied to identify key CPC-secreted ECC-modulating factors. Examples of conditioning environments for these cell types that may alter

their secretome composition and potency include: normoxia versus hypoxia;<sup>101,112</sup> two-dimensional versus three-dimensional substrates,<sup>54</sup> soft versus hard stiffness;<sup>185,186</sup> and homocellular versus heterocellular culture.<sup>54,187</sup>

## 2.9 Conclusions

Recent studies have demonstrated that in addition to classical endothelial cell paracrine modulation of ECC, other resident non-cardiomyocyte heart cells (e.g., physiologic fibroblasts and pathologic myofibroblasts), or even experimental cardiotherapeutic cells (e.g., MSCs and CPCs), are also capable of altering cardiac ECC through indirect paracrine mechanisms. Based on our recent work and the new experimental data herein, we demonstrate that hECTs are a promising contractility assay to further study non-cardiomyocyte paracrine effects on tissue-level contractility. Systems biology approaches can provide complementary information to identify the key stem cell paracrine mediators of ECC and their mechanisms of action. Altogether, integrating tissue engineering and systems biology approaches shows exciting potential for providing novel insight into paracrine mediators of ECC and their underlying mechanisms of action, ultimately leading to improved cell-based therapies for patients with heart disease.

## **2.10 References:**

1. Bers DM. Cardiac excitation-contraction coupling. *Nature*. 2002;415:198-205
2. Lohse MJ, Engelhardt S, Eschenhagen T. What is the role of beta-adrenergic signaling in heart failure? *Circ Res*. 2003;93:896-906
3. Kaumann A, Bartel S, Molenaar P, Sanders L, Burrell K, Vetter D, Hempel P, Karczewski P, Krause EG. Activation of beta2-adrenergic receptors hastens relaxation and mediates phosphorylation of phospholamban, troponin i, and c-protein in ventricular myocardium from patients with terminal heart failure. *Circulation*. 1999;99:65-72
4. Zhao XL, Gutierrez LM, Chang CF, Hosey MM. The alpha 1-subunit of skeletal muscle I-type ca channels is the key target for regulation by a-kinase and protein phosphatase-1c. *Biochem Biophys Res Commun*. 1994;198:166-173
5. Gerhardstein BL, Puri TS, Chien AJ, Hosey MM. Identification of the sites phosphorylated by cyclic amp-dependent protein kinase on the beta 2 subunit of I-type voltage-dependent calcium channels. *Biochemistry*. 1999;38:10361-10370
6. Simmerman HK, Jones LR. Phospholamban: Protein structure, mechanism of action, and role in cardiac function. *Physiol Rev*. 1998;78:921-947
7. Marx SO, Reiken S, Hisamatsu Y, Jayaraman T, Burkhoff D, Rosemblit N, Marks AR. Pka phosphorylation dissociates fkbp12.6 from the calcium release channel (ryanodine receptor): Defective regulation in failing hearts. *Cell*. 2000;101:365-376
8. Sulakhe PV, Vo XT. Regulation of phospholamban and troponin-i phosphorylation in the intact rat cardiomyocytes by adrenergic and cholinergic stimuli: Roles of cyclic nucleotides, calcium, protein kinases and phosphatases and depolarization. *Mol Cell Biochem*. 1995;149-150:103-126
9. Kunst G, Kress KR, Gruen M, Uttenweiler D, Gautel M, Fink RH. Myosin binding protein c, a phosphorylation-dependent force regulator in muscle that controls the attachment of myosin heads by its interaction with myosin s2. *Circ Res*. 2000;86:51-58

10. Pyo RT, Sui J, Dhume A, Palomeque J, Blaxall BC, Diaz G, Tunstead J, Logothetis DE, Hajjar RJ, Schecter AD. Cxcr4 modulates contractility in adult cardiac myocytes. *J Mol Cell Cardiol.* 2006;41:834-844
11. Hare JM. Nitric oxide and excitation-contraction coupling. *J Mol Cell Cardiol.* 2003;35:719-729
12. Massion PB, Feron O, Dessaix C, Balligand JL. Nitric oxide and cardiac function: Ten years after, and continuing. *Circ Res.* 2003;93:388-398
13. Malik ZA, Kott KS, Poe AJ, Kuo T, Chen L, Ferrara KW, Knowlton AA. Cardiac myocyte exosomes: Stability, hsp60, and proteomics. *Am J Physiol Heart Circ Physiol.* 2013;304:H954-965
14. Datta R, Bansal T, Rana S, Datta K, Datta Chaudhuri R, Chawla-Sarkar M, Sarkar S. Myocyte-derived hsp90 modulates collagen upregulation via biphasic activation of stat-3 in fibroblasts during cardiac hypertrophy. *Mol Cell Biol.* 2017;37
15. Garcia NA, Ontoria-Oviedo I, Gonzalez-King H, Diez-Juan A, Sepulveda P. Glucose starvation in cardiomyocytes enhances exosome secretion and promotes angiogenesis in endothelial cells. *PLoS One.* 2015;10:e0138849
16. Sahoo S, Losordo DW. Exosomes and cardiac repair after myocardial infarction. *Circ Res.* 2014;114:333-344
17. Campbell DL, Stamler JS, Strauss HC. Redox modulation of I-type calcium channels in ferret ventricular myocytes. Dual mechanism regulation by nitric oxide and s-nitrosothiols. *J Gen Physiol.* 1996;108:277-293
18. Xu L, Eu JP, Meissner G, Stamler JS. Activation of the cardiac calcium release channel (ryanodine receptor) by poly-s-nitrosylation. *Science.* 1998;279:234-237
19. Han X, Kobzik L, Balligand JL, Kelly RA, Smith TW. Nitric oxide synthase (nos3)-mediated cholinergic modulation of ca<sup>2+</sup> current in adult rabbit atrioventricular nodal cells. *Circ Res.* 1996;78:998-1008

20. Hartzell HC, Fischmeister R. Opposite effects of cyclic gmp and cyclic amp on ca<sub>2+</sub> current in single heart cells. *Nature*. 1986;323:273-275
21. Gallo MP, Ghigo D, Bosia A, Alloatti G, Costamagna C, Penna C, Levi RC. Modulation of guinea-pig cardiac I-type calcium current by nitric oxide synthase inhibitors. *J Physiol*. 1998;506 ( Pt 3):639-651
22. Seddon M, Shah AM, Casadei B. Cardiomyocytes as effectors of nitric oxide signalling. *Cardiovasc Res*. 2007;75:315-326
23. Shah AM, Spurgeon HA, Sollott SJ, Talo A, Lakatta EG. 8-bromo-cgmp reduces the myofilament response to ca<sub>2+</sub> in intact cardiac myocytes. *Circ Res*. 1994;74:970-978
24. Layland J, Li JM, Shah AM. Role of cyclic gmp-dependent protein kinase in the contractile response to exogenous nitric oxide in rat cardiac myocytes. *J Physiol*. 2002;540:457-467
25. Ballard C, Schaffer S. Stimulation of the na+/ca<sub>2+</sub> exchanger by phenylephrine, angiotensin ii and endothelin 1. *J Mol Cell Cardiol*. 1996;28:11-17
26. Yang HT, Sakurai K, Sugawara H, Watanabe T, Norota I, Endoh M. Role of na+/ca<sub>2+</sub> exchange in endothelin-1-induced increases in ca<sub>2+</sub> transient and contractility in rabbit ventricular myocytes: Pharmacological analysis with kb-r7943. *Br J Pharmacol*. 1999;126:1785-1795
27. Aiello EA, Villa-Abrille MC, Dulce RA, Cingolani HE, Perez NG. Endothelin-1 stimulates the na+/ca<sub>2+</sub> exchanger reverse mode through intracellular na+ (na+i)-dependent and na+i-independent pathways. *Hypertension*. 2005;45:288-293
28. Dulce RA, Hurtado C, Ennis IL, Garciarena CD, Alvarez MC, Caldiz C, Pierce GN, Portiansky EL, Chiappe de Cingolani GE, Camilion de Hurtado MC. Endothelin-1 induced hypertrophic effect in neonatal rat cardiomyocytes: Involvement of na+/h<sup>+</sup> and na+/ca<sub>2+</sub> exchangers. *J Mol Cell Cardiol*. 2006;41:807-815

29. Alvarez BV, Perez NG, Ennis IL, Camilion de Hurtado MC, Cingolani HE. Mechanisms underlying the increase in force and ca(2+) transient that follow stretch of cardiac muscle: A possible explanation of the anrep effect. *Circ Res*. 1999;85:716-722
30. Cingolani HE, Ennis IL, Aiello EA, Perez NG. Role of autocrine/paracrine mechanisms in response to myocardial strain. *Pflugers Arch*. 2011;462:29-38
31. Lauer MR, Gunn MD, Clusin WT. Endothelin activates voltage-dependent ca<sup>2+</sup> current by a g protein-dependent mechanism in rabbit cardiac myocytes. *J Physiol*. 1992;448:729-747
32. He JQ, Pi Y, Walker JW, Kamp TJ. Endothelin-1 and photoreleased diacylglycerol increase I-type ca<sup>2+</sup> current by activation of protein kinase c in rat ventricular myocytes. *J Physiol*. 2000;524 Pt 3:807-820
33. Ono K, Tsujimoto G, Sakamoto A, Eto K, Masaki T, Ozaki Y, Satake M. Endothelin-a receptor mediates cardiac inhibition by regulating calcium and potassium currents. *Nature*. 1994;370:301-304
34. Cheng TH, Chang CY, Wei J, Lin CI. Effects of endothelin 1 on calcium and sodium currents in isolated human cardiac myocytes. *Can J Physiol Pharmacol*. 1995;73:1774-1783
35. Kamp TJ, Hell JW. Regulation of cardiac I-type calcium channels by protein kinase a and protein kinase c. *Circ Res*. 2000;87:1095-1102
36. Pi Y, Zhang D, Kemnitz KR, Wang H, Walker JW. Protein kinase c and a sites on troponin i regulate myofilament ca<sup>2+</sup> sensitivity and atpase activity in the mouse myocardium. *J Physiol*. 2003;552:845-857
37. Wang H, Grant JE, Doede CM, Sadayappan S, Robbins J, Walker JW. Pkc-betaII sensitizes cardiac myofilaments to ca<sup>2+</sup> by phosphorylating troponin i on threonine-144. *J Mol Cell Cardiol*. 2006;41:823-833

38. Cuello F, Bardswell SC, Haworth RS, Yin X, Lutz S, Wieland T, Mayr M, Kentish JC, Avkiran M. Protein kinase d selectively targets cardiac troponin i and regulates myofilament ca<sup>2+</sup> sensitivity in ventricular myocytes. *Circ Res*. 2007;100:864-873
39. Cuello F, Bardswell SC, Haworth RS, Ehler E, Sadayappan S, Kentish JC, Avkiran M. Novel role for p90 ribosomal s6 kinase in the regulation of cardiac myofilament phosphorylation. *J Biol Chem*. 2011;286:5300-5310
40. Chen PP, Patel JR, Rybakova IN, Walker JW, Moss RL. Protein kinase a-induced myofilament desensitization to ca(2+) as a result of phosphorylation of cardiac myosin-binding protein c. *J Gen Physiol*. 2010;136:615-627
41. Proven A, Roderick HL, Conway SJ, Berridge MJ, Horton JK, Capper SJ, Bootman MD. Inositol 1,4,5-trisphosphate supports the arrhythmogenic action of endothelin-1 on ventricular cardiac myocytes. *J Cell Sci*. 2006;119:3363-3375
42. Domeier TL, Zima AV, Maxwell JT, Huke S, Mignery GA, Blatter LA. Ip3 receptor-dependent ca<sup>2+</sup> release modulates excitation-contraction coupling in rabbit ventricular myocytes. *Am J Physiol Heart Circ Physiol*. 2008;294:H596-604
43. Harzheim D, Movassagh M, Foo RS, Ritter O, Tashfeen A, Conway SJ, Bootman MD, Roderick HL. Increased insp3rs in the junctional sarcoplasmic reticulum augment ca<sup>2+</sup> transients and arrhythmias associated with cardiac hypertrophy. *Proc Natl Acad Sci U S A*. 2009;106:11406-11411
44. van Wamel AJ, Ruwhof C, van der Valk-Kokshoom LE, Schrier PI, van der Laarse A. The role of angiotensin ii, endothelin-1 and transforming growth factor-beta as autocrine/paracrine mediators of stretch-induced cardiomyocyte hypertrophy. *Mol Cell Biochem*. 2001;218:113-124
45. Gray MO, Long CS, Kalinyak JE, Li HT, Karliner JS. Angiotensin ii stimulates cardiac myocyte hypertrophy via paracrine release of tgf-beta 1 and endothelin-1 from fibroblasts. *Cardiovasc Res*. 1998;40:352-363

46. Pedrotty DM, Klinger RY, Kirkton RD, Bursac N. Cardiac fibroblast paracrine factors alter impulse conduction and ion channel expression of neonatal rat cardiomyocytes. *Cardiovasc Res.* 2009;83:688-697
47. Cartledge JE, Kane C, Dias P, Tesfom M, Clarke L, McKee B, Al Ayoubi S, Chester A, Yacoub MH, Camelliti P, Terracciano CM. Functional crosstalk between cardiac fibroblasts and adult cardiomyocytes by soluble mediators. *Cardiovasc Res.* 2015;105:260-270
48. Liau B, Jackman CP, Li Y, Bursac N. Developmental stage-dependent effects of cardiac fibroblasts on function of stem cell-derived engineered cardiac tissues. *Sci Rep.* 2017;7:42290
49. Bang C, Batkai S, Dangwal S, et al. Cardiac fibroblast-derived microRNA passenger strand-enriched exosomes mediate cardiomyocyte hypertrophy. *J Clin Invest.* 2014;124:2136-2146
50. Maxeiner H, Krehbiehl N, Muller A, Woitasky N, Akinturk H, Muller M, Weigand MA, Abdallah Y, Kasseckert S, Schreckenberg R, Schluter KD, Wenzel S. New insights into paracrine mechanisms of human cardiac progenitor cells. *Eur J Heart Fail.* 2010;12:730-737
51. Askar SF, Ramkisoensing AA, Atsma DE, Schalij MJ, de Vries AA, Pijnappels DA. Engraftment patterns of human adult mesenchymal stem cells expose electrotonic and paracrine proarrhythmic mechanisms in myocardial cell cultures. *Circ Arrhythm Electrophysiol.* 2013;6:380-391
52. DeSantiago J, Bare DJ, Semenov I, Minshall RD, Geenen DL, Wolska BM, Banach K. Excitation-contraction coupling in ventricular myocytes is enhanced by paracrine signaling from mesenchymal stem cells. *J Mol Cell Cardiol.* 2012;52:1249-1256
53. Hwang HJ, Chang W, Song BW, et al. Antiarrhythmic potential of mesenchymal stem cell is modulated by hypoxic environment. *J Am Coll Cardiol.* 2012;60:1698-1706

54. Mayourian J, Cashman TJ, Ceholski DK, Johnson BV, Sachs D, Kaji DA, Sahoo S, Hare JM, Hajjar RJ, Sobie EA, Costa KD. Experimental and computational insight into human mesenchymal stem cell paracrine signaling and heterocellular coupling effects on cardiac contractility and arrhythmogenicity. *Circ Res*. 2017
55. Sattayaprasert P, Nassal DM, Wan X, Deschenes I, Laurita KR. Mesenchymal stem cells suppress cardiac alternans by activation of pi3k mediated nitroso-redox pathway. *J Mol Cell Cardiol*. 2016;98:138-145
56. DeSantiago J, Bare DJ, Banach K. Ischemia/reperfusion injury protection by mesenchymal stem cell derived antioxidant capacity. *Stem Cells Dev*. 2013;22:2497-2507
57. de Jong R, Houtgraaf JH, Samiei S, Boersma E, Duckers HJ. Intracoronary stem cell infusion after acute myocardial infarction: A meta-analysis and update on clinical trials. *Circ Cardiovasc Interv*. 2014;7:156-167
58. Hare JM, Fishman JE, Gerstenblith G, et al. Comparison of allogeneic vs autologous bone marrow-derived mesenchymal stem cells delivered by transendocardial injection in patients with ischemic cardiomyopathy: The poseidon randomized trial. *JAMA*. 2012;308:2369-2379
59. De Hert SG, Gillebert TC, Andries LJ, Brutsaert DL. Role of the endocardial endothelium in the regulation of myocardial function. Physiologic and pathophysiologic implications. *Anesthesiology*. 1993;79:1354-1366
60. Brutsaert DL, De Keulenaer GW, Fransen P, Mohan P, Kaluza GL, Andries LJ, Rouleau JL, Sys SU. The cardiac endothelium: Functional morphology, development, and physiology. *Prog Cardiovasc Dis*. 1996;39:239-262
61. Noireaud J, Andriantsitohaina R. Recent insights in the paracrine modulation of cardiomyocyte contractility by cardiac endothelial cells. *Biomed Res Int*. 2014;2014:923805

62. Shah AM, MacCarthy PA. Paracrine and autocrine effects of nitric oxide on myocardial function. *Pharmacol Ther.* 2000;86:49-86
63. Lewis MJ, Shah AM. *Endothelial modulation of cardiac function.* Australia ; United Kingdom: Harwood Academic; 1997.
64. Massion PB, Balligand JL. Modulation of cardiac contraction, relaxation and rate by the endothelial nitric oxide synthase (enos): Lessons from genetically modified mice. *J Physiol.* 2003;546:63-75
65. Kojda G, Kottenberg K, Nix P, Schluter KD, Piper HM, Noack E. Low increase in cGMP induced by organic nitrates and nitrovasodilators improves contractile response of rat ventricular myocytes. *Circ Res.* 1996;78:91-101
66. Mohan P, Brutsaert DL, Paulus WJ, Sys SU. Myocardial contractile response to nitric oxide and cGMP. *Circulation.* 1996;93:1223-1229
67. Vila-Petroff MG, Younes A, Egan J, Lakatta EG, Sollott SJ. Activation of distinct cAMP-dependent and cGMP-dependent pathways by nitric oxide in cardiac myocytes. *Circ Res.* 1999;84:1020-1031
68. Wegener JW, Godecke A, Schrader J, Nawrath H. Effects of nitric oxide donors on cardiac contractility in wild-type and myoglobin-deficient mice. *Br J Pharmacol.* 2002;136:415-420
69. Paolocci N, Ekelund UE, Isoda T, Ozaki M, Vandegaer K, Georgakopoulos D, Harrison RW, Kass DA, Hare JM. Cyclic GMP-independent inotropic effects of nitric oxide and peroxynitrite donors: Potential role for nitrosylation. *Am J Physiol Heart Circ Physiol.* 2000;279:H1982-1988
70. Chesnais JM, Fischmeister R, Mery PF. Positive and negative inotropic effects of NO donors in atrial and ventricular fibres of the frog heart. *J Physiol.* 1999;518 ( Pt 2):449-461

71. Yasuda S, Coutu P, Sadayappan S, Robbins J, Metzger JM. Cardiac transgenic and gene transfer strategies converge to support an important role for troponin i in regulating relaxation in cardiac myocytes. *Circ Res*. 2007;101:377-386
72. Yanagisawa M, Kurihara H, Kimura S, Tomobe Y, Kobayashi M, Mitsui Y, Yazaki Y, Goto K, Masaki T. A novel potent vasoconstrictor peptide produced by vascular endothelial cells. *Nature*. 1988;332:411-415
73. Endoh M. Signal transduction and ca<sup>2+</sup> signaling in intact myocardium. *J Pharmacol Sci*. 2006;100:525-537
74. Brunner F, Bras-Silva C, Cerdeira AS, Leite-Moreira AF. Cardiovascular endothelins: Essential regulators of cardiovascular homeostasis. *Pharmacol Ther*. 2006;111:508-531
75. Nagasaka T, Izumi M, Hori M, Ozaki H, Karaki H. Positive inotropic effect of endothelin-1 in the neonatal mouse right ventricle. *Eur J Pharmacol*. 2003;472:197-204
76. Drawnel FM, Archer CR, Roderick HL. The role of the paracrine/autocrine mediator endothelin-1 in regulation of cardiac contractility and growth. *Br J Pharmacol*. 2013;168:296-317
77. Lipp P, Laine M, Tovey SC, Burrell KM, Berridge MJ, Li W, Bootman MD. Functional inositol triphosphate receptors that may modulate excitation-contraction coupling in the heart. *Curr Biol*. 2000;10:939-942
78. Camelliti P, Borg TK, Kohl P. Structural and functional characterisation of cardiac fibroblasts. *Cardiovasc Res*. 2005;65:40-51
79. Nag AC. Study of non-muscle cells of the adult mammalian heart: A fine structural analysis and distribution. *Cytobios*. 1980;28:41-61
80. Banerjee I, Yekkala K, Borg TK, Baudino TA. Dynamic interactions between myocytes, fibroblasts, and extracellular matrix. *Ann N Y Acad Sci*. 2006;1080:76-84

81. Pinto AR, Ilinykh A, Ivey MJ, Kuwabara JT, D'Antoni ML, Debuque R, Chandran A, Wang L, Arora K, Rosenthal NA, Tallquist MD. Revisiting cardiac cellular composition. *Circ Res*. 2016;118:400-409
82. de Bakker JM, van Capelle FJ, Janse MJ, Tasseron S, Vermeulen JT, de Jonge N, Lahpor JR. Slow conduction in the infarcted human heart. 'Zigzag' course of activation. *Circulation*. 1993;88:915-926
83. Spach MS, Boineau JP. Microfibrosis produces electrical load variations due to loss of side-to-side cell connections: A major mechanism of structural heart disease arrhythmias. *Pacing Clin Electrophysiol*. 1997;20:397-413
84. Nguyen HX, Kirkton RD, Bursac N. Engineering prokaryotic channels for control of mammalian tissue excitability. *Nat Commun*. 2016;7:13132
85. Ongstad E, Kohl P. Fibroblast-myocyte coupling in the heart: Potential relevance for therapeutic interventions. *J Mol Cell Cardiol*. 2016;91:238-246
86. Mahoney VM, Mezzano V, Morley GE. A review of the literature on cardiac electrical activity between fibroblasts and myocytes. *Prog Biophys Mol Biol*. 2016;120:128-133
87. Long CS, Henrich CJ, Simpson PC. A growth factor for cardiac myocytes is produced by cardiac nonmyocytes. *Cell Regul*. 1991;2:1081-1095
88. Aceto JF, Baker KM. [sar1]angiotensin ii receptor-mediated stimulation of protein synthesis in chick heart cells. *Am J Physiol*. 1990;258:H806-813
89. Harada M, Itoh H, Nakagawa O, Ogawa Y, Miyamoto Y, Kuwahara K, Ogawa E, Igaki T, Yamashita J, Masuda I, Yoshimasa T, Tanaka I, Saito Y, Nakao K. Significance of ventricular myocytes and nonmyocytes interaction during cardiocyte hypertrophy: Evidence for endothelin-1 as a paracrine hypertrophic factor from cardiac nonmyocytes. *Circulation*. 1997;96:3737-3744

90. Ponicke K, Heinroth-Hoffmann I, Becker K, Brodde OE. Trophic effect of angiotensin II in neonatal rat cardiomyocytes: Role of endothelin-1 and non-myocyte cells. *Br J Pharmacol.* 1997;121:118-124
91. Leask A. TGFbeta, cardiac fibroblasts, and the fibrotic response. *Cardiovasc Res.* 2007;74:207-212
92. Rosenkranz S, Flesch M, Amann K, Haeuseler C, Kilter H, Seeland U, Schluter KD, Bohm M. Alterations of beta-adrenergic signaling and cardiac hypertrophy in transgenic mice overexpressing tgf-beta(1). *Am J Physiol Heart Circ Physiol.* 2002;283:H1253-1262
93. Kuwahara K, Saito Y, Harada M, Ishikawa M, Ogawa E, Miyamoto Y, Hamanaka I, Kamitani S, Kajiyama N, Takahashi N, Nakagawa O, Masuda I, Nakao K. Involvement of cardiotrophin-1 in cardiac myocyte-nonmyocyte interactions during hypertrophy of rat cardiac myocytes in vitro. *Circulation.* 1999;100:1116-1124
94. Horio T, Maki T, Kishimoto I, Tokudome T, Okumura H, Yoshihara F, Suga S, Takeo S, Kawano Y, Kangawa K. Production and autocrine/paracrine effects of endogenous insulin-like growth factor-1 in rat cardiac fibroblasts. *Regul Pept.* 2005;124:65-72
95. Guo W, Kamiya K, Yasui K, Kodama I, Toyama J. Paracrine hypertrophic factors from cardiac non-myocyte cells downregulate the transient outward current density and Kv4.2 K<sup>+</sup> channel expression in cultured rat cardiomyocytes. *Cardiovasc Res.* 1999;41:157-165
96. Takeda N, Manabe I, Uchino Y, Eguchi K, Matsumoto S, Nishimura S, Shindo T, Sano M, Otsu K, Snider P, Conway SJ, Nagai R. Cardiac fibroblasts are essential for the adaptive response of the murine heart to pressure overload. *J Clin Invest.* 2010;120:254-265
97. Pellieux C, Foletti A, Peduto G, Aubert JF, Nussberger J, Beermann F, Brunner HR, Pedrazzini T. Dilated cardiomyopathy and impaired cardiac hypertrophic response to angiotensin II in mice lacking fgf-2. *J Clin Invest.* 2001;108:1843-1851

98. Emanueli C, Shearn AI, Angelini GD, Sahoo S. Exosomes and exosomal mirnas in cardiovascular protection and repair. *Vascul Pharmacol.* 2015;71:24-30
99. Barile L, Lionetti V, Cervio E, Matteucci M, Gherghiceanu M, Popescu LM, Torre T, Siclari F, Moccetti T, Vassalli G. Extracellular vesicles from human cardiac progenitor cells inhibit cardiomyocyte apoptosis and improve cardiac function after myocardial infarction. *Cardiovasc Res.* 2014;103:530-541
100. Arslan F, Lai RC, Smeets MB, Akeroyd L, Choo A, Aguor EN, Timmers L, van Rijen HV, Doevedans PA, Pasterkamp G, Lim SK, de Kleijn DP. Mesenchymal stem cell-derived exosomes increase atp levels, decrease oxidative stress and activate pi3k/akt pathway to enhance myocardial viability and prevent adverse remodeling after myocardial ischemia/reperfusion injury. *Stem Cell Res.* 2013;10:301-312
101. Gray WD, French KM, Ghosh-Choudhary S, Maxwell JT, Brown ME, Platt MO, Searles CD, Davis ME. Identification of therapeutic covariant microrna clusters in hypoxia-treated cardiac progenitor cell exosomes using systems biology. *Circ Res.* 2015;116:255-263
102. Sahoo S, Klychko E, Thorne T, Misener S, Schultz KM, Millay M, Ito A, Liu T, Kamide C, Agrawal H, Perlman H, Qin G, Kishore R, Losordo DW. Exosomes from human cd34(+) stem cells mediate their proangiogenic paracrine activity. *Circ Res.* 2011;109:724-728
103. Hart G. Cellular electrophysiology in cardiac hypertrophy and failure. *Cardiovasc Res.* 1994;28:933-946
104. Boyden PA, Jeck CD. Ion channel function in disease. *Cardiovasc Res.* 1995;29:312-318
105. Kaur K, Zarzoso M, Ponce-Balbuena D, Guerrero-Serna G, Hou L, Musa H, Jalife J. Tgf-beta1, released by myofibroblasts, differentially regulates transcription and function of sodium and potassium channels in adult rat ventricular myocytes. *PLoS One.* 2013;8:e55391

106. Trieschmann J, Bettin D, Haustein M, Koster A, Molcanyi M, Halbach M, Hanna M, Fouad M, Brockmeier K, Hescheler J, Pfannkuche K, Hannes T. The interaction between adult cardiac fibroblasts and embryonic stem cell-derived cardiomyocytes leads to proarrhythmic changes in in vitro cocultures. *Stem Cells Int.* 2016;2016:2936126
107. Ramos-Mondragon R, Vega AV, Avila G. Long-term modulation of na<sup>+</sup> and k<sup>+</sup> channels by tgf-beta1 in neonatal rat cardiac myocytes. *Pflugers Arch.* 2011;461:235-247
108. Zhang YE. Non-smad pathways in tgf-beta signaling. *Cell Res.* 2009;19:128-139
109. Monsanto MM, White KS, Kim T, Wang BJ, Fisher K, Ilves K, Khalafalla FG, Casillas A, Broughton K, Mohsin S, Dembitsky WP, Sussman MA. Concurrent isolation of 3 distinct cardiac stem cell populations from a single human heart biopsy. *Circ Res.* 2017;121:113-124
110. Tang J, Shen D, Caranasos TG, Wang Z, Vandergriff AC, Allen TA, Hensley MT, Dinh PU, Cores J, Li TS, Zhang J, Kan Q, Cheng K. Therapeutic microparticles functionalized with biomimetic cardiac stem cell membranes and secretome. *Nat Commun.* 2017;8:13724
111. Tang YL, Zhu W, Cheng M, Chen L, Zhang J, Sun T, Kishore R, Phillips MI, Losordo DW, Qin G. Hypoxic preconditioning enhances the benefit of cardiac progenitor cell therapy for treatment of myocardial infarction by inducing cxcr4 expression. *Circ Res.* 2009;104:1209-1216
112. Agarwal U, George A, Bhutani S, Ghosh-Choudhary S, Maxwell JT, Brown ME, Mehta Y, Platt MO, Liang Y, Sahoo S, Davis ME. Experimental, systems, and computational approaches to understanding the microrna-mediated reparative potential of cardiac progenitor cell-derived exosomes from pediatric patients. *Circ Res.* 2017;120:701-712
113. Bolli R, Chugh AR, D'Amario D, et al. Cardiac stem cells in patients with ischaemic cardiomyopathy (scipio): Initial results of a randomised phase 1 trial. *Lancet.* 2011;378:1847-1857

114. Heldman AW, DiFede DL, Fishman JE, et al. Transendocardial mesenchymal stem cells and mononuclear bone marrow cells for ischemic cardiomyopathy: The tac-hft randomized trial. *JAMA*. 2014;311:62-73
115. Karantalis V, DiFede DL, Gerstenblith G, et al. Autologous mesenchymal stem cells produce concordant improvements in regional function, tissue perfusion, and fibrotic burden when administered to patients undergoing coronary artery bypass grafting: The prospective randomized study of mesenchymal stem cell therapy in patients undergoing cardiac surgery (prometheus) trial. *Circ Res*. 2014;114:1302-1310
116. Karantalis V, Hare JM. Use of mesenchymal stem cells for therapy of cardiac disease. *Circ Res*. 2015;116:1413-1430
117. Liang X, Zhang L, Wang S, Han Q, Zhao RC. Exosomes secreted by mesenchymal stem cells promote endothelial cell angiogenesis by transferring mir-125a. *J Cell Sci*. 2016;129:2182-2189
118. Merino-Gonzalez C, Zuniga FA, Escudero C, Ormazabal V, Reyes C, Nova-Lamperti E, Salomon C, Aguayo C. Mesenchymal stem cell-derived extracellular vesicles promote angiogenesis: Potencial clinical application. *Front Physiol*. 2016;7:24
119. Liu JF, Wang BW, Hung HF, Chang H, Shyu KG. Human mesenchymal stem cells improve myocardial performance in a splenectomized rat model of chronic myocardial infarction. *J Formos Med Assoc*. 2008;107:165-174
120. Ranganath SH, Levy O, Inamdar MS, Karp JM. Harnessing the mesenchymal stem cell secretome for the treatment of cardiovascular disease. *Cell Stem Cell*. 2012;10:244-258
121. Mirotsou M, Jayawardena TM, Schmeckpeper J, Gnechi M, Dzau VJ. Paracrine mechanisms of stem cell reparative and regenerative actions in the heart. *J Mol Cell Cardiol*. 2011;50:280-289
122. Gnechi M, Zhang Z, Ni A, Dzau VJ. Paracrine mechanisms in adult stem cell signaling and therapy. *Circ Res*. 2008;103:1204-1219

123. Eschenhagen T. Beta-adrenergic signaling in heart failure-adapt or die. *Nat Med.* 2008;14:485-487
124. Mureli S, Gans CP, Bare DJ, Geenen DL, Kumar NM, Banach K. Mesenchymal stem cells improve cardiac conduction by upregulation of connexin 43 through paracrine signaling. *Am J Physiol Heart Circ Physiol.* 2013;304:H600-609
125. Chang MG, Tung L, Sekar RB, Chang CY, Cysyk J, Dong P, Marban E, Abraham MR. Proarrhythmic potential of mesenchymal stem cell transplantation revealed in an in vitro coculture model. *Circulation.* 2006;113:1832-1841
126. Beeres SL, Atsma DE, van der Laarse A, Pijnappels DA, van Tuyn J, Fibbe WE, de Vries AA, Ypey DL, van der Wall EE, Schalij MJ. Human adult bone marrow mesenchymal stem cells repair experimental conduction block in rat cardiomyocyte cultures. *J Am Coll Cardiol.* 2005;46:1943-1952
127. Pijnappels DA, Schalij MJ, van Tuyn J, Ypey DL, de Vries AA, van der Wall EE, van der Laarse A, Atsma DE. Progressive increase in conduction velocity across human mesenchymal stem cells is mediated by enhanced electrical coupling. *Cardiovasc Res.* 2006;72:282-291
128. Mayourian J, Savizky RM, Sobie EA, Costa KD. Modeling electrophysiological coupling and fusion between human mesenchymal stem cells and cardiomyocytes. *PLoS Comput Biol.* 2016;12:e1005014
129. Aratyn-Schaus Y, Pasqualini FS, Yuan H, McCain ML, Ye GJ, Sheehy SP, Campbell PH, Parker KK. Coupling primary and stem cell-derived cardiomyocytes in an in vitro model of cardiac cell therapy. *J Cell Biol.* 2016;212:389-397
130. Luo L, Tang J, Nishi K, Yan C, Dinh PU, Cores J, Kudo T, Zhang J, Li TS, Cheng K. Fabrication of synthetic mesenchymal stem cells for the treatment of acute myocardial infarction in mice. *Circ Res.* 2017;120:1768-1775

131. Baglio SR, Rooijers K, Koppers-Lalic D, Verweij FJ, Perez Lanzon M, Zini N, Naaijkens B, Perut F, Niessen HW, Baldini N, Pegtel DM. Human bone marrow- and adipose-mesenchymal stem cells secrete exosomes enriched in distinctive mirna and tRNA species. *Stem Cell Res Ther.* 2015;6:127
132. Teixeira FG, Panchalingam KM, Assuncao-Silva R, Serra SC, Mendes-Pinheiro B, Patrício P, Jung S, Anjo SI, Manadas B, Pinto L, Sousa N, Behie LA, Salgado AJ. Modulation of the mesenchymal stem cell secretome using computer-controlled bioreactors: Impact on neuronal cell proliferation, survival and differentiation. *Sci Rep.* 2016;6:27791
133. Anderson JD, Johansson HJ, Graham CS, et al. Comprehensive proteomic analysis of mesenchymal stem cell exosomes reveals modulation of angiogenesis via nuclear factor-kappab signaling. *Stem Cells.* 2016;34:601-613
134. Kucova Skalnikova H. Proteomic techniques for characterisation of mesenchymal stem cell secretome. *Biochimie.* 2013;95:2196-2211
135. Phinney DG, Di Giuseppe M, Njah J, et al. Mesenchymal stem cells use extracellular vesicles to outsource mitophagy and shuttle microRNAs. *Nat Commun.* 2015;6:8472
136. Park CW, Kim KS, Bae S, Son HK, Myung PK, Hong HJ, Kim H. Cytokine secretion profiling of human mesenchymal stem cells by antibody array. *Int J Stem Cells.* 2009;2:59-68
137. Okumura H, Nagaya N, Itoh T, Okano I, Hino J, Mori K, Tsukamoto Y, Ishibashi-Ueda H, Miwa S, Tambara K, Toyokuni S, Yutani C, Kangawa K. Adrenomedullin infusion attenuates myocardial ischemia/reperfusion injury through the phosphatidylinositol 3-kinase/akt-dependent pathway. *Circulation.* 2004;109:242-248
138. Tao Z, Chen B, Tan X, Zhao Y, Wang L, Zhu T, Cao K, Yang Z, Kan YW, Su H. Coexpression of vegf and angiopoietin-1 promotes angiogenesis and cardiomyocyte

proliferation reduces apoptosis in porcine myocardial infarction (mi) heart. *Proc Natl Acad Sci U S A.* 2011;108:2064-2069

139. Cashman TJ, Gouon-Evans V, Costa KD. Mesenchymal stem cells for cardiac therapy: Practical challenges and potential mechanisms. *Stem Cell Rev.* 2013;9:254-265
140. Urbanek K, Rota M, Cascapera S, et al. Cardiac stem cells possess growth factor-receptor systems that after activation regenerate the infarcted myocardium, improving ventricular function and long-term survival. *Circ Res.* 2005;97:663-673
141. Bujak M, Dobaczewski M, Gonzalez-Quesada C, Xia Y, Leucker T, Zymek P, Veeranna V, Tager AM, Luster AD, Frangogiannis NG. Induction of the cxc chemokine interferon-gamma-inducible protein 10 regulates the reparative response following myocardial infarction. *Circ Res.* 2009;105:973-983
142. Kang K, Ma R, Cai W, Huang W, Paul C, Liang J, Wang Y, Zhao T, Kim HW, Xu M, Millard RW, Wen Z, Wang Y. Exosomes secreted from cxcr4 overexpressing mesenchymal stem cells promote cardioprotection via akt signaling pathway following myocardial infarction. *Stem Cells Int.* 2015;2015:659890
143. Lai RC, Chen TS, Lim SK. Mesenchymal stem cell exosome: A novel stem cell-based therapy for cardiovascular disease. *Regen Med.* 2011;6:481-492
144. Lai RC, Arslan F, Lee MM, Sze NS, Choo A, Chen TS, Salto-Tellez M, Timmers L, Lee CN, El Oakley RM, Pasterkamp G, de Kleijn DP, Lim SK. Exosome secreted by msc reduces myocardial ischemia/reperfusion injury. *Stem Cell Res.* 2010;4:214-222
145. Baglio SR, Pegtel DM, Baldini N. Mesenchymal stem cell secreted vesicles provide novel opportunities in (stem) cell-free therapy. *Front Physiol.* 2012;3:359
146. Nakamura Y, Miyaki S, Ishitobi H, Matsuyama S, Nakasa T, Kamei N, Akimoto T, Higashi Y, Ochi M. Mesenchymal-stem-cell-derived exosomes accelerate skeletal muscle regeneration. *FEBS Lett.* 2015;589:1257-1265

147. Xiao J, Pan Y, Li XH, Yang XY, Feng YL, Tan HH, Jiang L, Feng J, Yu XY. Cardiac progenitor cell-derived exosomes prevent cardiomyocytes apoptosis through exosomal mir-21 by targeting pdcd4. *Cell Death Dis.* 2016;7:e2277
148. Wei C, Li L, Kim IK, Sun P, Gupta S. Nf-kappab mediated mir-21 regulation in cardiomyocytes apoptosis under oxidative stress. *Free Radic Res.* 2014;48:282-291
149. Cheng Y, Liu X, Zhang S, Lin Y, Yang J, Zhang C. Microrna-21 protects against the h(2)o(2)-induced injury on cardiac myocytes via its target gene pdcd4. *J Mol Cell Cardiol.* 2009;47:5-14
150. Soller KJ, Yang J, Veglia G, Bowser MT. Reversal of phospholamban inhibition of the sarco(endo)plasmic reticulum ca<sup>2+</sup>-atpase (serca) using short, protein-interacting rnas and oligonucleotide analogs. *J Biol Chem.* 2016;291:21510-21518
151. Qiao S, Olson JM, Paterson M, Yan Y, Zaja I, Liu Y, Riess ML, Kersten JR, Liang M, Warltier DC, Bosnjak ZJ, Ge ZD. Microrna-21 mediates isoflurane-induced cardioprotection against ischemia-reperfusion injury via akt/nitric oxide synthase/mitochondrial permeability transition pore pathway. *Anesthesiology.* 2015;123:786-798
152. Agarwal U, George A, Bhutani S, Ghosh-Choudhary S, Maxwell JT, Brown ME, Mehta Y, Platt MO, Liang Y, Sahoo S, Davis ME. Experimental, systems and computational approaches to understanding the microrna-mediated reparative potential of cardiac progenitor cell-derived exosomes from pediatric patients. *Circ Res.* 2016
153. Kinnaird T, Stabile E, Burnett MS, Lee CW, Barr S, Fuchs S, Epstein SE. Marrow-derived stromal cells express genes encoding a broad spectrum of arteriogenic cytokines and promote in vitro and in vivo arteriogenesis through paracrine mechanisms. *Circ Res.* 2004;94:678-685
154. Gnechi M, He H, Noiseux N, Liang OD, Zhang L, Morello F, Mu H, Melo LG, Pratt RE, Ingwall JS, Dzau VJ. Evidence supporting paracrine hypothesis for akt-modified

- mesenchymal stem cell-mediated cardiac protection and functional improvement. *Faseb J.* 2006;20:661-669
155. Herrmann JL, Wang Y, Abarbanell AM, Weil BR, Tan J, Meldrum DR. Preconditioning mesenchymal stem cells with transforming growth factor-alpha improves mesenchymal stem cell-mediated cardioprotection. *Shock.* 2010;33:24-30
156. Schaaf S, Shibamiya A, Mewe M, Eder A, Stohr A, Hirt MN, Rau T, Zimmermann WH, Conradi L, Eschenhagen T, Hansen A. Human engineered heart tissue as a versatile tool in basic research and preclinical toxicology. *PLoS One.* 2011;6:e26397
157. Tulloch NL, Muskheli V, Razumova MV, Korte FS, Regnier M, Hauch KD, Pabon L, Reinecke H, Murry CE. Growth of engineered human myocardium with mechanical loading and vascular coculture. *Circ Res.* 2011;109:47-59
158. Zhang D, Shadrin IY, Lam J, Xian HQ, Snodgrass HR, Bursac N. Tissue-engineered cardiac patch for advanced functional maturation of human esc-derived cardiomyocytes. *Biomaterials.* 2013;34:5813-5820
159. Hirt MN, Hansen A, Eschenhagen T. Cardiac tissue engineering: State of the art. *Circ Res.* 2014;114:354-367
160. Liau B, Zhang D, Bursac N. Functional cardiac tissue engineering. *Regen Med.* 2012;7:187-206
161. Ogle BM, Bursac N, Domian I, Huang NF, Menasche P, Murry CE, Pruitt B, Radisic M, Wu JC, Wu SM, Zhang J, Zimmermann WH, Vunjak-Novakovic G. Distilling complexity to advance cardiac tissue engineering. *Sci Transl Med.* 2016;8:342ps313
162. Cashman TJ, Josowitz R, Gelb BD, Li RA, Dubois NC, Costa KD. Construction of defined human engineered cardiac tissues to study mechanisms of cardiac cell therapy. *J Vis Exp.* 2016:e53447

163. Turnbull IC, Karakikes I, Serrao GW, Backeris P, Lee JJ, Xie C, Senyei G, Gordon RE, Li RA, Akar FG, Hajjar RJ, Hulot JS, Costa KD. Advancing functional engineered cardiac tissues toward a preclinical model of human myocardium. *Faseb J.* 2014;28:644-654
164. Serrao GW, Turnbull IC, Ancukiewicz D, Kim DE, Kao E, Cashman TJ, Hadri L, Hajjar RJ, Costa KD. Myocyte-depleted engineered cardiac tissues support therapeutic potential of mesenchymal stem cells. *Tissue Eng Part A.* 2012;18:1322-1333
165. Stillitano F, Turnbull IC, Karakikes I, Nonnenmacher M, Backeris P, Hulot JS, Kranias EG, Hajjar RJ, Costa KD. Genomic correction of familial cardiomyopathy in human engineered cardiac tissues. *Eur Heart J.* 2016;37:3282-3284
166. Niwa N, Nerbonne JM. Molecular determinants of cardiac transient outward potassium current (i<sub>to</sub>) expression and regulation. *J Mol Cell Cardiol.* 2010;48:12-25
167. Peralta AO, John RM, Gaasch WH, Taggart PI, Martin DT, Venditti FJ. The class iii antiarrhythmic effect of sotalol exerts a reverse use-dependent positive inotropic effect in the intact canine heart. *J Am Coll Cardiol.* 2000;36:1404-1410
168. Tande PM, Refsum H. Class iii antiarrhythmic action linked with positive inotropy: Acute electrophysiological and inotropic effects of amiodarone in vitro. *Pharmacol Toxicol.* 1990;66:18-22
169. Hoey A, Amos GJ, Ravens U. Comparison of the action potential prolonging and positive inotropic activity of dpi 201-106 and bdf 9148 in human ventricular myocardium. *J Mol Cell Cardiol.* 1994;26:985-994
170. Bouchard RA, Clark RB, Giles WR. Effects of action potential duration on excitation-contraction coupling in rat ventricular myocytes. Action potential voltage-clamp measurements. *Circ Res.* 1995;76:790-801
171. Allen DG. On the relationship between action potential duration and tension in cat papillary muscle. *Cardiovasc Res.* 1977;11:210-218

172. Wohlfart B. Relationships between peak force, action potential duration and stimulus interval in rabbit myocardium. *Acta Physiol Scand.* 1979;106:395-409
173. Zhu R, Blazeski A, Poon E, Costa KD, Tung L, Boheler KR. Physical developmental cues for the maturation of human pluripotent stem cell-derived cardiomyocytes. *Stem Cell Res Ther.* 2014;5:117
174. Hartman ME, Dai DF, Laflamme MA. Human pluripotent stem cells: Prospects and challenges as a source of cardiomyocytes for in vitro modeling and cell-based cardiac repair. *Adv Drug Deliv Rev.* 2016;96:3-17
175. Rajabi M, Kassiotis C, Razeghi P, Taegtmeyer H. Return to the fetal gene program protects the stressed heart: A strong hypothesis. *Heart Fail Rev.* 2007;12:331-343
176. Selem SM, Kaushal S, Hare JM. Stem cell therapy for pediatric dilated cardiomyopathy. *Curr Cardiol Rep.* 2013;15:369
177. Chen G, Li S, Karakikes I, Ren L, Chow MZ, Chopra A, Keung W, Yan B, Chan CW, Costa KD, Kong CW, Hajjar RJ, Chen CS, Li RA. Phospholamban as a crucial determinant of the inotropic response of human pluripotent stem cell-derived ventricular cardiomyocytes and engineered 3-dimensional tissue constructs. *Circ Arrhythm Electrophysiol.* 2015;8:193-202
178. Kerscher P, Turnbull IC, Hodge AJ, Kim J, Seliktar D, Easley CJ, Costa KD, Lipke EA. Direct hydrogel encapsulation of pluripotent stem cells enables ontomimetic differentiation and growth of engineered human heart tissues. *Biomaterials.* 2016;83:383-395
179. Cashman TJ, Josowitz R, Johnson BV, Gelb BD, Costa KD. Human engineered cardiac tissues created using induced pluripotent stem cells reveal functional characteristics of braf-mediated hypertrophic cardiomyopathy. *PLoS One.* 2016;11:e0146697

180. Janes KA, Kelly JR, Gaudet S, Albeck JG, Sorger PK, Lauffenburger DA. Cue-signal-response analysis of tnf-induced apoptosis by partial least squares regression of dynamic multivariate data. *J Comput Biol.* 2004;11:544-561
181. Janes KA, Albeck JG, Gaudet S, Sorger PK, Lauffenburger DA, Yaffe MB. A systems model of signaling identifies a molecular basis set for cytokine-induced apoptosis. *Science.* 2005;310:1646-1653
182. Miller-Jensen K, Janes KA, Brugge JS, Lauffenburger DA. Common effector processing mediates cell-specific responses to stimuli. *Nature.* 2007;448:604-608
183. Platt MO, Wilder CL, Wells A, Griffith LG, Lauffenburger DA. Multipathway kinase signatures of multipotent stromal cells are predictive for osteogenic differentiation: Tissue-specific stem cells. *Stem Cells.* 2009;27:2804-2814
184. Park KY, Li WA, Platt MO. Patient specific proteolytic activity of monocyte-derived macrophages and osteoclasts predicted with temporal kinase activation states during differentiation. *Integr Biol (Camb).* 2012;4:1459-1469
185. Mosqueira D, Pagliari S, Uto K, et al. Hippo pathway effectors control cardiac progenitor cell fate by acting as dynamic sensors of substrate mechanics and nanostructure. *ACS Nano.* 2014;8:2033-2047
186. Engler AJ, Sen S, Sweeney HL, Discher DE. Matrix elasticity directs stem cell lineage specification. *Cell.* 2006;126:677-689
187. Williams AR, Hatzistergos KE, Addicott B, McCall F, Carvalho D, Suncion V, Morales AR, Da Silva J, Sussman MA, Heldman AW, Hare JM. Enhanced effect of combining human cardiac stem cells and bone marrow mesenchymal stem cells to reduce infarct size and to restore cardiac function after myocardial infarction. *Circulation.* 2013;127:213-223

## **Chapter 2 Supplemental Material**

### **Supplementary Methods**

#### *hECT Tissue Construction*

hECTs were created from differentiated human embryonic stem cells (H7 cell line, NIH Registration #0061) and type-I collagen using methods previously described.<sup>1,2</sup>

#### *hECT Functional Test Metrics*

hECT twitch force and dynamics were assessed; hECT developed force (DF) was measured as the difference between maximum systolic and minimum diastolic force, using beam bending theory as described elsewhere.<sup>3</sup> Beat rate was measured from a sequence of contractions in spontaneously beating hECTs using previously established methods.<sup>4</sup>

#### *hACF/HFF Conditioned Media*

Conditioned media was collected from 10 cm dishes of 50% confluent hACFs or HFFs cultured in serum-free defined media (SFDM) for five days and used within 3 hours of collection.

#### *Functional Assessment of hECTs Treated with hACF/HFF Conditioned Media*

Following 48 hours of tissue compaction, hECTs were cultured in SFDM until day 5. Following spontaneous and 0.5 Hz pacing baseline contractile function testing on day 5, SFDM was replaced with the following treatments: 1) SFDM (Control); 2) fresh hACF conditioned media; or 3) fresh HFF conditioned media. hECTs were cultured an additional 5 days in their respective treatments, after which contractile function was measured and compared to baseline measurements. Spontaneous beat rate and DF were also measured on a daily basis.

*hECT Immunofluorescence:*

hECTs were fixed in 4% paraformaldehyde, and were later frozen and embedded in Tissue-Tek optimal cutting temperature compound (Sakura, Torrance, CA, USA). 10  $\mu$ m sections were stained using either anti-cardiac troponin I (H-170, 1:100; Santa Cruz Biotechnology, Dallas, TX, USA) or anti-sarcoendoplasmic reticulum  $\text{Ca}^{2+}$ -ATPase 2 (MA3-919, 1:100; Invitrogen, Carlsbad, CA, USA), followed by Alexa Fluor 488 secondary antibody (A-11034, 1:200; Invitrogen) or Alexa Fluor 594 secondary antibody (A-11032, 1:200; Invitrogen), respectively. All sections were counterstained with 4',6-diamidino-2-phenylindole (DAPI); images were obtained using a laser-scanning confocal microscope (Leica TCS SP5 DMI; Leica Microsystems, Buffalo Grove, IL, USA) using a 63x oil immersion objective.

*qRT-PCR*

Total RNA was extracted from flash-frozen hECTs using the Quick-RNA MiniPrep kit (Zymo Research, Irvine, CA) after lysis using FastPrep Lysis Beads and Matrix Tubes (MP Products, Santa Ana, CA) and quantified using a NanoDrop 2000 (ThermoFisher, Rockville, MD). Reverse transcription was performed using the iScript cDNA synthesis kit (Biorad Laboratories, Hercules, CA) and quantitative PCR (10 ng cDNA/reaction) was performed using a two-step system with SYBR Advantage qPCR Premix (Clontech Laboratories, Mountain View, CA) on the ABI Prism 7500 Fast Real-Time PCR system (Applied Biosystems, Foster City, CA) according to manufacturer recommendations.

All primers used were human-specific and are shown in the 5' to 3' direction:

Gene	Direction	Sequence (5'→3')
$\beta$ 2M	Forward	GTATGCCTGCCGTGTGAAC
$\beta$ 2M	Reverse	CAAGCAAGCAGAATTGGAA

TNNT2	Forward	AAGAGGCAGACTGAGCGGGAAA
TNNT2	Reverse	AGATGCTCTGCCACAGCTCCTT
$\alpha$ MYHC	Forward	GGAAGACAAGGTCAACAGCCTG
$\alpha$ MYHC	Reverse	TCCAGTTCCGCTTGCTCGCT
$\beta$ MYHC	Forward	GGAGTTCACACGCCTCAAAGAG
$\beta$ MYHC	Reverse	TCCTCAGCATCTGCCAGGTTGT
SERCA2a	Forward	CTGTCCATGTCACTCCACTTCC
SERCA2a	Reverse	AGCGGTTACTCCAGTATTGCAG
CASP3	Forward	TTAATAAAGGTATCCATGGAGAACACT
CASP3	Reverse	TTAGTGATAAAAATAGAGTTCTTGAG
CASP9	Forward	TTCCCAGGTTTGTTCTG
CASP9	Reverse	CCTTCACCGAAACAGCATT
BCL2	Forward	CTGCACCTGACGCCCTTCACC
BCL2	Reverse	CACATGACCCCACCGAACTCAAAGA
BAX	Forward	GGACGAACTGGACAGTAACATGG
BAX	Reverse	GCAAAGTAGAAAAGGGCGACAAC
LTCC	Forward	TGACTATTTGCCAATTGTGTGG
LTCC	Reverse	GCGGAGGTAGGCATTGGG
Cx43	Forward	GGGTTAAGGGAAAGAGCGACC
Cx43	Reverse	CCCCATTGATTTGTTCTGC
Kv4.2	Forward	CCAACCTCAGTCGCATCTACCAC
Kv4.2	Reverse	GCTCTGCATGTAAGCATTGCGC
ANF	Forward	ACAATGCCGTGTCCAACGCAGA
ANF	Reverse	CTTCATTGGCTCACTGAGCAC
Kir2.1	Forward	AACAGTGCAGGAGCCGCTTGT

Kir2.1	Reverse	AGGACGAAAGCCAGGCAGAAGA
Kv11.1	Forward	CATCTGCGTCATGCTCATTGGC
Kv11.1	Reverse	TCTGGTGGAAGCGGATGAACTC
Nav1.5	Forward	CAAGACCTGCTACCACATCGTG
Nav1.5	Reverse	GTCGGCATACTCAAGCAGAACCC

Fold changes in gene expression were determined using the comparative threshold cycle method ( $\Delta\Delta Ct$ ) with normalization to the housekeeping gene beta-2-microglobulin ( $\beta 2M$ ). This experiment was repeated in triplicate.

#### Statistical Testing and Analysis

The descriptive statistics used to present results are specified within each figure. Statistical analyses were performed using Prism 6. Repeated measures analysis of variance (ANOVA), followed by Bonferroni's multiple comparisons test, was used for Figure 4. One-way ANOVA, followed by Scheffe's post-hoc test, was used for multiple pairwise comparisons of unequal group sizes in Figure 5. Differences with a p-value less than 0.05 were considered statistically significant.

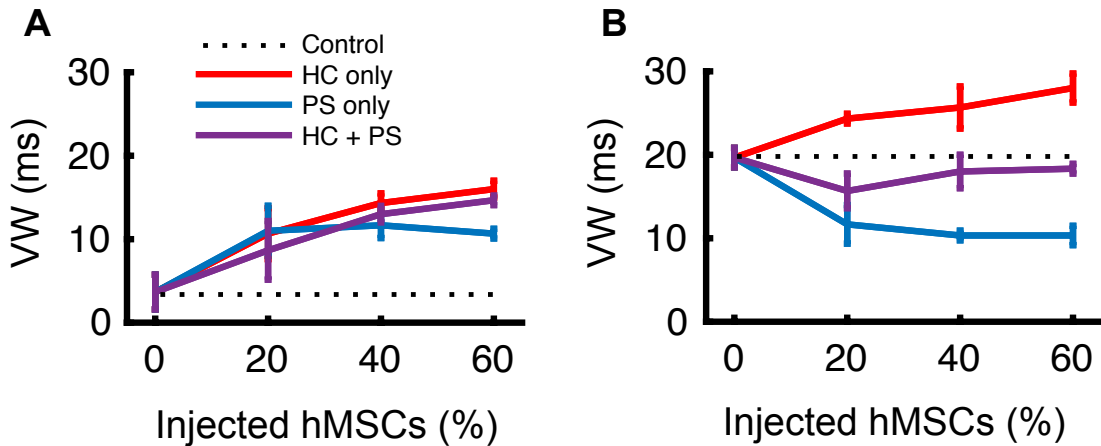


**Figure S1: Simulated Vulnerable Window (VW) Analysis on hMSC-Supplemented Fibrotic Cardiac Tissue.** A VW analysis was performed on low (4%; left panel) and high (40%; right panel) fibroblast-populated cardiac tissue injected with 0% (control), 20%, 40%, or 60% hMSCs at high (16%) engraftment levels ( $n=3$  randomized cell distributions). In low fibrosis (i.e., more representative of myocyte monolayers in vitro), both paracrine signaling (PS) and heterocellular coupling (HC) increases the VW, while in high fibrosis (i.e., more similar to pre-clinical/clinical conditions for hMSC intervention), PS decreases the VW and overcomes potentially pro-arrhythmic HC. Panel B adapted from Mayourian et al.<sup>5</sup> which also provides detailed methods for these in silico simulations. As recommended by White et al.<sup>6</sup>, comparative statistics were not implemented, as p-values are dependent on sample size (which can be arbitrarily high in simulations).

**Supporting References:**

1. Turnbull IC, Karakikes I, Serrao GW, Backeris P, Lee JJ, Xie C, Senyei G, Gordon RE, Li RA, Akar FG, Hajjar RJ, Hulot JS, Costa KD. Advancing functional engineered cardiac tissues toward a preclinical model of human myocardium. *FASEB J.* 2014;28:644-654
2. Cashman TJ, Josowitz R, Gelb BD, Li RA, Dubois NC, Costa KD. Construction of defined human engineered cardiac tissues to study mechanisms of cardiac cell therapy. *J Vis Exp.* 2016:e53447
3. Serrao GW, Turnbull IC, Ancukiewicz D, Kim DE, Kao E, Cashman TJ, Hadri L, Hajjar RJ, Costa KD. Myocyte-depleted engineered cardiac tissues support therapeutic potential of mesenchymal stem cells. *Tissue Eng Part A.* 2012;18:1322-1333
4. Cashman TJ, Josowitz R, Johnson BV, Gelb BD, Costa KD. Human engineered cardiac tissues created using induced pluripotent stem cells reveal functional characteristics of braf-mediated hypertrophic cardiomyopathy. *PLoS One.* 2016;11:e0146697
5. Mayourian J, Cashman TJ, Ceholski DK, Johnson BV, Sachs D, Kaji DA, Sahoo S, Hare JM, Hajjar RJ, Sobie EA, Costa KD. Experimental and computational insight into human mesenchymal stem cell paracrine signaling and heterocellular coupling effects on cardiac contractility and arrhythmogenicity. *Circ Res.* 2017
6. White JW, Rassweiler A, Samhouri JF, Stier AC, White C. Ecologists should not use statistical significance tests to interpret simulation model results. *OIKOS Synthesising Ecology.* 2014;123:385-388

## **Chapter 3: An Introduction to Functional Testing of Healthy and Injured Human Engineered Cardiac Tissues**

*Note: The following chapter is a modified draft of an original article in press in Methods in Molecular Biology:*

Turnbull IC, Mayourian J, Murphy JF, Stillitano F, Ceholski DK, Costa KD. Cardiac Tissue Models of Inherited and Acquired Cardiomyopathies. Methods in Molecular Biology (in press).

ICT and JM conceived the idea, collected the data, and wrote the manuscript. The text within the current chapter reflect JM's contribution to the manuscript.

### **3.1 Abstract**

The lack of biomimetic *in vitro* models of the human heart has posed a critical barrier to progress in the field of modeling cardiac disease. Human engineered cardiac tissues (hECTs)—autonomous, beating structures that recapitulate key aspects of native cardiac muscle physiology—offer an attractive alternative to traditional *in vitro* models. Here we describe the use of hECTs to advance our understanding and modeling of cardiac diseases in order to test therapeutic interventions, with a focus on contractile dysfunction in the setting of acquired forms of cardiomyopathies. Three major procedures are discussed in this chapter: 1) preparation of hECTs from human induced pluripotent stem cell-derived cardiomyocytes (hiPSC-CMs) on single- and multi-tissue bioreactors; 2) data acquisition of hECT contractile function on both of these platforms; and 3) cryo-injury and doxorubicin-induced hECT models of acquired cardiomyopathy.

### **3.2 Introduction**

Non-ischemic dilated cardiomyopathy (NIDCM), which is characterized by ventricular dilation and systolic dysfunction in the absence of coronary artery disease, is a major form of heart failure impacting 1 in 20,000 adults per year in the United States.<sup>1</sup> Inotropic support is a strategy of medical management for NIDCM, but it does not treat the underlying cause. This highlights a critical need to develop novel therapeutic strategies for restoring cardiac performance in NIDCM. Stem cell therapy has emerged as a promising approach to address this problem.<sup>2</sup>

In our hands, human engineered cardiac tissues (hECTs)—capable of recapitulating key aspects of native cardiac muscle physiology<sup>3</sup>—provide a simple yet effective contractility assay to study therapeutic strategies,<sup>4</sup> such as stem cell-based cardiotherapies, in the context of healthy<sup>5</sup> and myocyte-depleted<sup>6</sup> conditions. Nevertheless, to further progress the translational relevance of such findings (and other therapeutic interventions), it is necessary to continue improving hECT models of both ischemic and non-ischemic cardiomyopathy. To this end, in this chapter, we highlight our recent efforts to advance hECT models of NIDCM and ischemic cardiomyopathy.

First, we provide step-by-step instructions on how to create hECTs with our single- and multi-hECT bioreactor platforms using human induced pluripotent stem cell-derived cardiomyocytes (hiPSC-CMs), and subsequently measure their contractile performance. Next, motivated by in vivo animal models of acquired ischemic<sup>7</sup> and non-ischemic<sup>8</sup> cardiomyopathy, we present instructions and original data on cryoinjury- and doxorubicin-induced hECT cardiomyopathy models, respectively.

Many in vitro disease models are evaluated exclusively using molecular and histology analysis. However, a strength of the hECT system is that it also provides a functional phenotype, which can be further analyzed for structural and molecular characteristics as desired.

Altogether, this chapter complements our previous work to further support the use of hECTs as a system to help bridge a gap in traditional experimental models of the heart, in order

to provide new opportunities for advancing our understanding of cardiac disease and therapeutics.

### 3.3 Materials

#### 3.3.1 Cell Collection

1. hiPSCs (see **Notes 1 and 2**)
2. mTeSR<sup>TM</sup> 1
3. 6-well tissue culture treated plates
4. +I media: RPMI 1640 + B-27 Supplement (50X) + 1% penicillin streptomycin.
5. -I media: RPMI 1640 + B-27 Supplement Minus Insulin (50X) + 1% penicillin streptomycin
6. 0.025% trypsin
7. DMEM/F-12 Media, 1:1 Nutrient Mixture
8. CHIR99021 (30 mM stock solution)
9. IWR-1 (10 mM stock solution)
10. 1X phosphate-buffered saline without calcium or magnesium (PBS, pH 7.4), sterile-filtered
11. 15 mL conical tubes
12. 1.5 mL Eppendorf tubes

#### 3.3.2 Tissue Formation

1. 5 mg/ml type-I collagen
2. 1 M NaOH
3. 10X PBS
4. Sterile ultrapure deionized water
5. 10X Minimum Essential Medium (MEM)

6. 0.2 N HEPES pH 9
7. Stem cell-qualified Matrigel
8. Petri dishes 60mm x 15mm style and 100mm x 20mm style.

### 3.3.3 *Bioreactor Construction*

1. Bioreactor design schematics. CAD files and a list of related stock materials related to master mold fabrication are available upon request. See elsewhere<sup>9</sup> for more details (see **Note 3**).
2. Sylgard 184 silicone elastomer kit (polydimethylsiloxane, or PDMS)
3. Alcohol resistant black marker
4. 2% Bovine Serum Albumin (BSA)
5. Silicone vacuum grease
6. Tweezers

### 3.3.4. *Data Acquisition*

1. Laptop
2. GRASS S88X stimulator
3. High-speed camera capable of capturing at least 50 frames per second.
4. Dissecting microscope with sufficient magnification to see both ends of the tissue
5. Carbon rods (required only for single-tissue data acquisition).
6. Carbon plates (required only for multi-tissue data acquisition).
7. Tungsten wire.
8. Plate heater (recommended for experiments where physiologic temperature is desired).
9. Boom microscope stand.
10. Goose neck lamp.

11. Vibration isolation table.
12. Laminar flow hood.
13. Mirror
14. Laboratory Jack x 2 (required only for multi-tissue data acquisition).
15.  $\frac{3}{4}$ " spacers x 4 (required only for multi-tissue data acquisition).
16. LabVIEW (National Instruments, Austin, TX) and MATLAB (Natick, Massachusetts) software. Custom LabVIEW program used for data acquisition, and MATLAB script used for data analysis, are available upon request from the authors.

### 3.4 Methods

#### 3.4.1 Cardiomyocyte differentiation of hiPSCs

1. To start the cardiomyocyte differentiation at 80-90% confluence (see **Note 4**) of hiPSCs in a 6-well plate, replace mTeSR<sup>TM</sup> 1 maintenance media (see **Note 5**) with 2 mL -I media containing CHIR99021 (10  $\mu$ M final concentration) per well.
2. After 24 hours, wash with DMEM/F12 (see **Note 6**) and replace with 2 mL -I media per well.
3. After 48 hours, wash with DMEM/F12 and replace with 2 mL -I media containing IWR-1 (5  $\mu$ M final concentration) per well.
4. After 24 hours, wash with DMEM/F12 and replace with 2 mL -I media containing IWR-1 (5  $\mu$ M final concentration) per well.
5. After 24 hours, wash with DMEM/F12 and replace with 2 mL -I media (without IWR-1) per well.
6. Repeat step 3.1.5.
7. After 24 hours, wash with DMEM/F12 and replace with 2 mL +I media per well.
8. Repeat step 3.1.7 (see **Note 7**) up to days 20-30 of differentiation.

### *3.4.2. Preparing the Single-Tissue Bioreactor*

1. Mark the tip of bioreactor posts with alcohol resistant black marker to facilitate later video tracking.
2. Assemble single-tissue bioreactor with inserts (**Figure 1A**).
3. Sterilize (see **Note 8**).
4. In a laminar flow hood using sterile tweezers, remove the PDMS mold from the autoclave bag. While holding the mold with the tweezers, apply a spare amount of vacuum grease to the bottom of the mold (see **Note 9**) and then place it on the 60 mm dish applying pressure so the mold adheres to the bottom of the dish.
5. Pipette approximately 150 $\mu$ l of 2% BSA into the well of the single-tissue bioreactor, and place in the incubator (37°C and 5% CO<sub>2</sub>) for one hour.
6. Remove the BSA, then rinse by serial washes as follows: 1) add approximately 150 $\mu$ l of 1x PBS 2) remove and repeat; 3) add approximately 150 $\mu$ l of distilled water; and 4) remove and repeat.
7. Aspirate all the liquid from the well and leave the single-tissue bioreactor in the laminar flow hood to air dry.

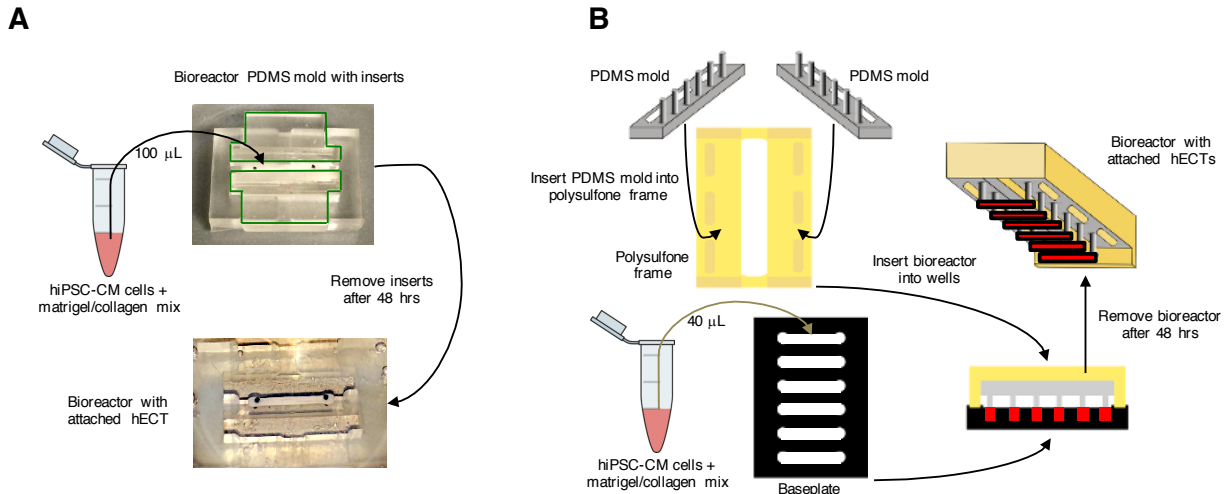


**Figure 1: Overview of hECT Construction.** hECTs are created either with **A)** single-tissue or **B)** multi-tissue bioreactors. For single-tissue bioreactors (**A**), a set volume of the cell/extracellular matrix mix is added to each well of the bioreactor. After two hours of incubation the bioreactor is submerged in culture media for 48 hours. Following hECT compaction, the inserts are slowly removed from the bioreactor. For multi-tissue bioreactors (**B**), a set volume of the cell/extracellular matrix mix is added to each well of the baseplate. Six pairs of bioreactor posts are then submerged into matching baseplate wells for 48 hours. Following hECT compaction, the bioreactor is slowly lifted out of the baseplate with the tissues suspended between pairs of end-posts.

### 3.4.3. Preparing the Multi-Tissue Bioreactor

1. Mark the tip of bioreactor posts with alcohol resistant black marker to facilitate later video tracking.
2. Assemble multi-tissue bioreactor with inserts (**Figure 1C**).
3. Sterilize (see **Note 8**).

### 3.4.4 Collecting hiPSC-CMs from the Monolayer

In our experience an effective time window to harvest the cells for hECT fabrication is between 20-30 days of differentiation, as convenient for experimental planning.

1. On the day of cell harvest, first wash cells with 1X PBS.
2. Add 1 mL 0.025% trypsin per well (see **Notes 10 and 11**).
3. Incubate for 5 minutes at 37°C and 5% CO<sub>2</sub>.
4. Remove cells from each well mechanically using the 0.025% trypsin from each well.
5. Place trypsin/cell mix into 15 mL conical tube, and neutralize with equal amount of cold (4°C) +I media.
6. Centrifuge at 300 x g for 5 min.
7. Aspirate and re-suspend with 10 mL +I media.
8. Count cells using hemocytometer.
9. Centrifuge at 300 x g for 5 min (see **Note 12**).

#### *3.4.5. Preparing the Collagen/Matrigel Mix*

Avoid bubbles throughout each of these steps.

1. Keep all solutions on ice. Keep cells (hiPSC-CM) at room temperature. All volumes listed below are per hECT for the single-tissue bioreactor. For the multi-tissue bioreactor, multiply each volume by 0.4-0.6 (see **Note 13**).
2. Dilute 100.0 µl of 5 mg/ml collagen stock to 3.125 mg/ml with 2.5 µl of 1 M NaOH, 16 µl of 10x PBS and 41.5 µl of sterile ultrapure deionized water (see **Note 14**).
3. Add 20.0 µl of both 10x MEM and 0.2 N HEPES pH 9 to the dilute collagen mixture (previous step) to create the collagen mix.
4. Add stem cell-qualified Matrigel to the collagen mix (0.9 mg/ml final concentration)
5. Store the collagen/Matrigel mix on ice.

### *3.4.6. Forming hECTs on the Single-Tissue Bioreactor*

Avoid bubbles throughout each of these steps. For a schematic summarizing these steps, see

#### **Figure 1A.**

1. Aspirate supernatant from hiPSC-CM pellet.
2. Add 50 µL of collagen-Matrigel mix per million cells (hiPSC-CM) to the cell pellet (see **Note 15**).
3. Add 100 µL hiPSC-CMs + collagen/Matrigel mix into the well of the single-tissue bioreactor, avoid bubbles (see **Note 16**).
4. Discard top lid of 60 mm dish; place 60 mm dish into 100 mm tissue culture treated dish (see **Note 17**).
5. To ensure the cell/collagen mixture does not get dehydrated during gel polymerization, add 1 mL of +I media into the edge of the 60 mm dish, being careful not to drop any media onto the bioreactor.
6. Place into incubator for 2 hours at 37°C and 5% CO<sub>2</sub>, this is sufficient time for the collagen to polymerize.
7. Remove from incubator and place in sterile hood.
8. Slowly add approximately 14 mL +I media into 60 mm dish so that the entire bioreactor is covered with media (see **Note 18**).
9. Return assembly to incubator for 48 hours at 37°C and 5% CO<sub>2</sub>.
10. Remove from incubator and bring to laminar flow hood; using sterile tweezers slowly remove the inserts and exchange media (half volume).
11. Continue half-media exchanges with +I media daily for tissue maintenance.

### *3.4.7 Forming hECTs Using the Multi-Tissue Bioreactor*

Avoid bubbles throughout these steps. For a schematic summary of these steps, see **Figure 1B** (see **Note 3**).

1. Aspirate supernatant from hiPSC-CM pellet.
2. Add 40 µL of collagen-Matrigel mix per million cells (hiPSC-CM) to the cell pellet (see **Note 19**).
3. Place baseplate in 60 mm tissue-culture treated dish.
4. Add 40 µL hiPSC-CMs + collagen/Matrigel mix into each well of the baseplate (see **Note 16**).
5. Insert bioreactor into baseplate (see **Note 20**).
6. Discard top lid of 60 mm dish; place 60 mm dish into 100 mm tissue culture treated dish (see **Note 17**).
7. Add 1 mL of +I media into edge of 60 mm dish to prevent dehydration of the gel.
8. Place into incubator for 2 hours at 37°C and 5% CO<sub>2</sub> for gel to polymerize.
9. Remove from incubator and bring to laminar flow hood.
10. Slowly add 14 mL +I media into 60 mm dish (see **Notes 18 and 21**).
11. Place into incubator for 48 hours at 37°C and 5% CO<sub>2</sub> (see **Note 22**).
12. Remove from incubator; slowly lift bioreactor out of baseplate (see **Note 23**), and place bioreactor into new 60 mm dish with 14 mL +I media.

#### *3.4.8 Data Acquisition for Single-hECT and Multi-hECT Bioreactors*

For a schematic summary of these steps, see **Figure 2**.

1. Set up laminar hood with vibration isolation table, goose neck lamp, boom stand, dissecting microscope and high speed camera. For single-hECT bioreactors, place 60mm dish with bioreactor on top of plate heater, and align microscope to view the hECT from the top (**Figure 2A**). For multi-hECT bioreactor, include the laboratory jack, place ¾"

spacers equally distant from the mirror in the center, place the 100mm dish containing the 60mm dish with the multi-tissue bioreactor carefully on top of the  $\frac{3}{4}$ " spacers, and align the microscope to view the reflection of the multi-tissue bioreactor on the mirror (**Figure 2B,E-F**) (see note **25**). Connect grass stimulator and camera to laptop.

2. Adjust microscope magnification and limit region of interest to have both posts of one hECT in view (**Figure 2C**). Use a binary filter of the image to maximize contrast from posts marked with black marker.
3. Using a custom LabVIEW program (available upon request), record the displacement of both posts simultaneously without electrical stimulation to analyze the spontaneous contractile properties of the hECT.
4. Place carbon rods (or carbon plates) adjacent to the single-tissue (or the multi-tissue) bioreactor, respectively, and connect them to the grass stimulator electrodes (see **Note 25**).
5. Using a custom LabVIEW program, record the displacement of both posts simultaneously with electrical stimulation (see **Note 26**).
6. Measure the post heights and tissue height on the posts by acquiring a side view image of the hECT as in **Figure 2D** (see **Note 27**). For the single tissue bioreactor, place the mirror in the 60mm dish along a long end of the bioreactor. For the multi-tissue bioreactor acquire side view images with the microscope looking directly through the 60mm dish.
7. The data is then processed using a custom MATLAB script (available upon request) to produce the results for the different twitch parameters that are analyzed.

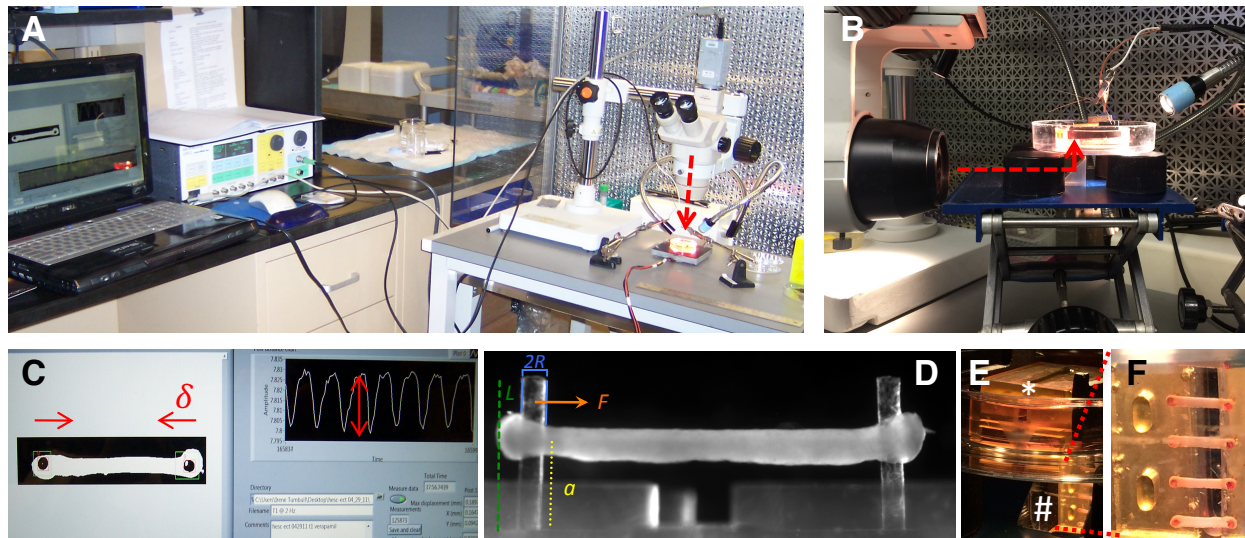


**Figure 2: Overview of hECT data acquisition.** **A)** Set up for data acquisition from hECT on single-tissue bioreactor. Camera viewing path (dotted red line) aligned with top view of hECT. **B)** Set up for data acquisition from hECT multi-tissue bioreactor. Camera viewing path (dotted red line) aligned with mirror. **C)** Screen view during data acquisition, live tracking of inward post-displacement during hECT contraction ( $\delta$ ), with corresponding measurement of the amplitude of each contraction (double headed arrow). **D)** Side view of hECT on single-tissue bioreactor with embedded schematic of the measurements included in the calculation of force. **E)** Multi-tissue bioreactor (\*) with tissues submerged facing the bottom of the dish, and reflected image of hECT on mirror (#) to allow for imaging and data collection without manipulation of the hECT. **F)** Zoomed in view of reflected image of hECT on mirror. Courtesy of Dr. Irene Turnbull.

### 3.4.9 Cryo-injury hECT cardiomyopathy model

For a schematic summary of the steps, see **Figure 3A**. The contractile performance of representative hECTs during this intervention is shown in **Figure 3B**. In this form of acquired ischemic cardiomyopathy, you would expect a decrease in function<sup>7</sup>, consistent with **Figure 3B**.

1. Follow steps described above in **Section 3.4.4** to fabricate the hECTs.

2. Six days post-tissue formation, pace hECTs using methods described above to measure pre-injury baseline function (see **Section 3.4.8**).
3. Remove +I media to fully expose the hECT.
4. Lay a 1.6-mm diameter steel pin frozen in liquid nitrogen on the hECT for 5 seconds. For sham use a room temperature pin.
5. Drip media onto the pin.
6. Remove the pin.
7. Re-suspend hECT in +I media.
8. Place in incubator for 24 hours at 37°C and 5% CO<sub>2</sub>.
9. Pace hECTs using methods described above (see **Section 3.4.8**) to measure short-term post-injury contractile function.
10. Rinse with 1X PBS.
11. Re-suspend hECT in +I media.
12. Place in incubator for 72 hours (or longer as desired) at 37°C and 5% CO<sub>2</sub>.
13. Pace hECTs using methods described above (see **Section 3.4.8**) to monitor long-term post-injury contractile function.

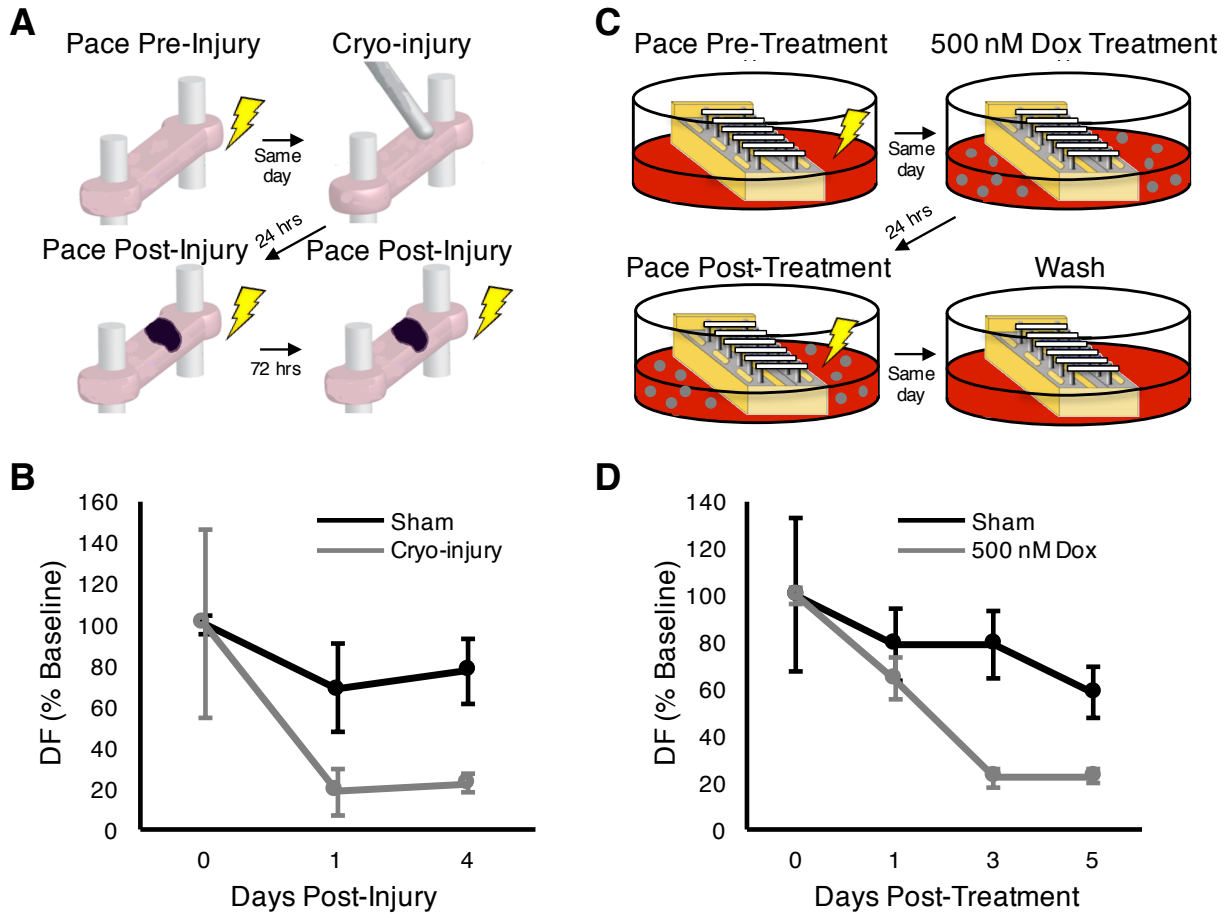


**Figure 3: hECT Models of Acquired Cardiac Disease.** **A)** Overview of cryo-injury method for acquired ischemic cardiomyopathy hECT model. **B)** Effects of cryo-injury model (grey) on hECT developed force (DF) over time (mean $\pm$ SEM, n=2-3). **C)** Overview of doxorubicin (Dox) method for acquired non-ischemic cardiomyopathy hECT model. **D)** Effects of 500 nM Dox (grey) on hECT DF over time (mean $\pm$ SEM, n=4).

#### 3.4.10. Doxorubicin-induced hECT cardiomyopathy model

For a schematic summary of these steps, see **Figure 3C**. The contractile performance of representative hECTs during this intervention is shown in **Figure 3D**. In this form of acquired non-ischemic cardiomyopathy, you would expect a decrease in function<sup>8</sup>, consistent with **Figure 3D** (see **Note 28**).

1. Five days post-tissue formation, pace hECTs using methods described above (see **Section 3.4.8**) to establish pre-dox baseline contractile function.
2. Rinse with 1x PBS.
3. Transfer bioreactor to new 60 mm dish with +I media containing 500 nM doxorubicin.
4. Place in incubator for 24 hours at 37°C and 5% CO<sub>2</sub>.
5. Pace hECTs using methods described above (see **Section 3.4.8**) to measure short-term post-dox contractile function.
6. Rinse with 1x PBS.
7. Transfer bioreactor to new 60 mm dish with +I media.
8. Place in incubator for 48 hours at 37°C and 5% CO<sub>2</sub>.
9. Pace hECTs using methods described above (see **Section 3.4.8**) to monitor long-term post-dox contractile function.
10. Repeat steps 6 through 9 as needed for longer term studies.

### 3.5 Notes

1. The SKiPS-31.3 line was used. This line was generated from dermal fibroblasts from a healthy 45-year-old male volunteer with no symptoms of cardiovascular disease.<sup>10</sup>
2. Differentiations work best using hiPSCs between passages 30-70.
3. As shown in **Figure 1B**, the baseplate design has been adjusted from our previous work;<sup>9</sup> rather than a “dog bone”-shaped channel, the width has been increased to create a more rectangular channel for improved tissue adhesion to the flexible end-posts.
4. Confluence greatly affects differentiation efficiency.
5. E8 media can also be used for maintenance.
6. Washing away dead cells with DMEM/F12 helps improve differentiation efficiency.
7. At this stage of differentiation, changing media every 48 hours (with 4 mL per well), rather than every 24 hours (with 2 mL per well), is also a viable option. After day 10 of differentiation, it is not necessary to wash with DMEM:F12.
8. The PDMS molds can withstand sterilization cycles in a steam autoclave up to 121°C.
9. The vacuum grease helps to adhere the mold to the bottom of the culture dish, so that in later steps, when the dish is filled with media, the single-tissue bioreactor will remain submerged. Avoid applying vacuum grease on the center of the mold because that will interfere with visualization of the tissue using an inverted microscope.
10. TrypLE Express can also be used for dissociation.
11. For poor differentiations, it is possible to improve hiPSC-CM purity by mechanically removing only the top layer of cells with the dissociation reagent and without incubation proceed to **Step 3.4.2.5**.
12. Working with 1.5-mL Eppendorf tubes is preferred when making hECTs; cells should be re-suspended in 1 mL of +I media post-centrifugation/aspiration and transferred to an Eppendorf tube. Centrifugation is then repeated at 300 x g for 5 min.

13. Using 0.4-0.6 scaling factors have proven successful in our hands. Scaling factor is dependent on desired amount of matrigel/collagen mix to be used per tissue. See **Note 19.**
14. Avoid bubbles.
15. On average, one well from a six-well plate yields enough hiPSC-CM to fabricate one tissue using a single-tissue bioreactor.
16. To account for pipette error (and to help avoid bubbles), add 10% more of the cell/extracellular mix into the pipette.
17. Be sure that if you have relevant information on the lid, transcribe that information to the lid of the 100mm dish. It also helps to label the bottom of the dish to keep record of the bioreactor inside the dish.
18. To improve compaction, add DMEM containing 10% Neonatal Bovine Serum, 1% penicillin-streptomycin and 0.2% Amphotericin B instead of +I for the first 24 to 48 hours.
19. Using 40-60  $\mu$ L matrigel/collagen mix per tissue has proven successful in our hands.
20. Confirm that bioreactor posts are submerged into the wells, but are not bent from touching the bottom or edges of the well.
21. May need to add more +I media to confirm that all hECTs are fully submerged into media.
22. Check on compaction; if compaction progressing slower than expected it is okay to leave bioreactor in baseplate for an additional 24 hours, on the other hand remove earlier if tissue compaction appears accelerated.
23. This method has been updated since previous work<sup>9</sup>. While holding the baseplate at the bottom of the 60 mm dish, the bioreactor is slowly lifted vertically out of the baseplate into a new 60 mm dish with 14 mL +I media.
24. The multi-tissue bioreactor is maintained in culture and tested with the hECT facing the bottom of the dish; the reflected image on the mirror allows visualizing the tissue without requiring any direct manipulation.

25. To aid in connecting the carbon rods/plates to the grass stimulator electrodes, the electrodes can be fitted with alligator clips soldered to the end of the electrodes; tungsten wire can be looped tightly around the carbon rods/plates; lastly, clasp loose end of each tungsten wire with the alligator clips.
26. The protocol to follow for electrical stimulation should be determined per the experiment. We typically pace the hECT starting at low frequency (0.25Hz), and then record hECT contractions (post displacement) at different frequencies using 0.25-Hz increments.
27. The beam bending equation  $F = \frac{3\pi E R^4}{2a^2(3L-a)} \delta$  is used to calculate the force (F) (**Figure 2C-D**). Post length (L) and tissue height along the posts (a) are measured using a side view image of the hECT; the post displacement ( $\delta$ ) is measured during data acquisition using LabVIEW. The radius (R) and Young's modulus (E) are only required to be measured once upon fabrication of a bioreactor, and thereafter the values remain constant. Developed Force (DF) is the difference between the maximum and minimum force during each twitch.
28. In our experience, the adverse effect of doxorubicin on hECT contractile function is dependent on the initial developed force. For desired level of force reduction titrate doxorubicin between 0.25 to 2.0  $\mu$ M, administered for no longer than 48 hours.

### **3.6. References**

1. Towbin JA, Lowe AM, Colan SD, Sleeper LA, Orav EJ, Clunie S, Messere J, Cox GF, Lurie PR, Hsu D, Canter C, Wilkinson JD, Lipshultz SE. Incidence, causes, and outcomes of dilated cardiomyopathy in children. *JAMA*. 2006;296:1867-1876
2. Mushtaq M, DiFede DL, Golpanian S, Khan A, Gomes SA, Mendizabal A, Heldman AW, Hare JM. Rationale and design of the percutaneous stem cell injection delivery effects on neomyogenesis in dilated cardiomyopathy (the poseidon-dcm study): A phase i/ii, randomized pilot study of the comparative safety and efficacy of transendocardial injection of autologous mesenchymal stem cell vs. Allogeneic mesenchymal stem cells in patients with non-ischemic dilated cardiomyopathy. *J Cardiovasc Transl Res*. 2014;7:769-780
3. Turnbull IC, Karakikes I, Serrao GW, Backeris P, Lee JJ, Xie C, Senyei G, Gordon RE, Li RA, Akar FG, Hajjar RJ, Hulot JS, Costa KD. Advancing functional engineered cardiac tissues toward a preclinical model of human myocardium. *FASEB J*. 2014;28:644-654
4. Mayourian J, Ceholski DK, Gonzalez DM, Cashman TJ, Sahoo S, Hajjar RJ, Costa KD. Physiologic, pathologic, and therapeutic paracrine modulation of cardiac excitation-contraction coupling. *Circ Res*. 2017;in press
5. Mayourian J, Cashman TJ, Ceholski DK, Johnson BV, Sachs D, Kaji DA, Sahoo S, Hare JM, Hajjar RJ, Sobie EA, Costa KD. Experimental and computational insight into human mesenchymal stem cell paracrine signaling and heterocellular coupling effects on cardiac contractility and arrhythmogenicity. *Circ Res*. 2017;121:411-423
6. Serrao GW, Turnbull IC, Ancukiewicz D, Kim DE, Kao E, Cashman TJ, Hadri L, Hajjar RJ, Costa KD. Myocyte-depleted engineered cardiac tissues support therapeutic potential of mesenchymal stem cells. *Tissue Eng Part A*. 2012;18:1322-1333
7. Strungs EG, Ongstad EL, O'Quinn MP, Palatinus JA, Jourdan LJ, Gourdie RG. Cryoinjury models of the adult and neonatal mouse heart for studies of scarring and regeneration. *Methods Mol Biol*. 2013;1037:343-353

8. Toyoda Y, Okada M, Kashem MA. A canine model of dilated cardiomyopathy induced by repetitive intracoronary doxorubicin administration. *J Thorac Cardiovasc Surg.* 1998;115:1367-1373
9. Cashman TJ, Josowitz R, Gelb BD, Li RA, Dubois NC, Costa KD. Construction of defined human engineered cardiac tissues to study mechanisms of cardiac cell therapy. *J Vis Exp.* 2016:e53447
10. Karakikes I, Senyei GD, Hansen J, Kong CW, Azeloglu EU, Stillitano F, Lieu DK, Wang J, Ren L, Hulot JS, Iyengar R, Li RA, Hajjar RJ. Small molecule-mediated directed differentiation of human embryonic stem cells toward ventricular cardiomyocytes. *Stem Cells Transl Med.* 2014;3:18-31

## **Chapter 4: An Introduction to Computational Modeling of Cardiac Electrophysiology and Arrhythmogenicity**

*Note: The following chapter is a modified draft of an original first-author article in press in Methods in Molecular Biology:*

Mayourian J, Sobie EA, Costa KD. An Introduction to Computational Modeling of Cardiac Electrophysiology and Arrhythmogenicity. Methods in Molecular Biology (in press).

JM conceived the idea and wrote the manuscript.

#### **4.1 Abstract**

Mathematical modeling is a powerful tool to study the complex and orchestrated biological process of cardiac electrical activity. By integrating experimental data from key components of cardiac electrophysiology, systems biology simulations can complement empirical findings, provide quantitative insight into physiological and pathophysiological mechanisms of action, and guide new hypotheses to better understand this complex biological system to develop novel cardiotherapeutic approaches. In this chapter, we briefly introduce *in silico* methods to describe the dynamics of physiological and pathophysiological single-cell and tissue-level cardiac electrophysiology. Using a “bottom-up” approach, we first describe the basis of ion channel mathematical models. Next, we discuss how the net flux of ions through such channels leads to changes in transmembrane voltage during cardiomyocyte action potentials. By applying these fundamentals, we describe how action potentials propagate in models of cardiac tissue. In addition, we provide case studies simulating single-cell and tissue-level arrhythmogenesis, as well as promising approaches to circumvent or overcome such adverse events. Overall, basic concepts and tools are discussed in this chapter as an accessible introduction to non-mathematicians to facilitate an understanding of electrophysiological modeling studies and communication with dry lab colleagues and collaborators.

## 4.2 Introduction

### 4.2.1 Why Do We Need Mathematical Models in Basic and Translational Research?

Biological processes exhibit different layers of complexity that obscure the interpretation of experimental findings. First, many biological phenomena are nonlinear, whereby small changes in one system component can lead to large changes in overall behavior. Second, biological processes are multiscale, which means that the translation of behavior from one spatial scale (e.g. the cell) to another (e.g. the organ) is not always straightforward. Such complexity forces experimentalists to utilize a simplified representation, or a model, of a given system in order to address a biological question. Independent of one's biological interests, three fundamental questions are commonly asked<sup>1</sup>: 1) what mechanisms regulate my biological process? 2) how do my findings translate in a multi-scale context? and 3) how can I extract meaningful biological information from my big data set? Each of these issues can be addressed with computational methods.

Experimentalists utilize conceptual models to develop causal relationships; computational models use mathematical equations to describe such relationships. Both types of models help build intuition, contextualize data, and generate hypotheses<sup>1</sup>. Together, these two approaches provide complementary information and can yield greater insights than either strategy used in isolation.<sup>2,3</sup>

A typical flowchart to incorporate mathematical modeling into an experimental study involves a well-defined research question, model development/refinement, and experimental validation, leading to refined hypotheses or answers to biological questions (**Figure 1**). In this chapter, we discuss methods to incorporate mathematical modeling into experimental cardiac electrophysiology under healthy and diseased conditions.

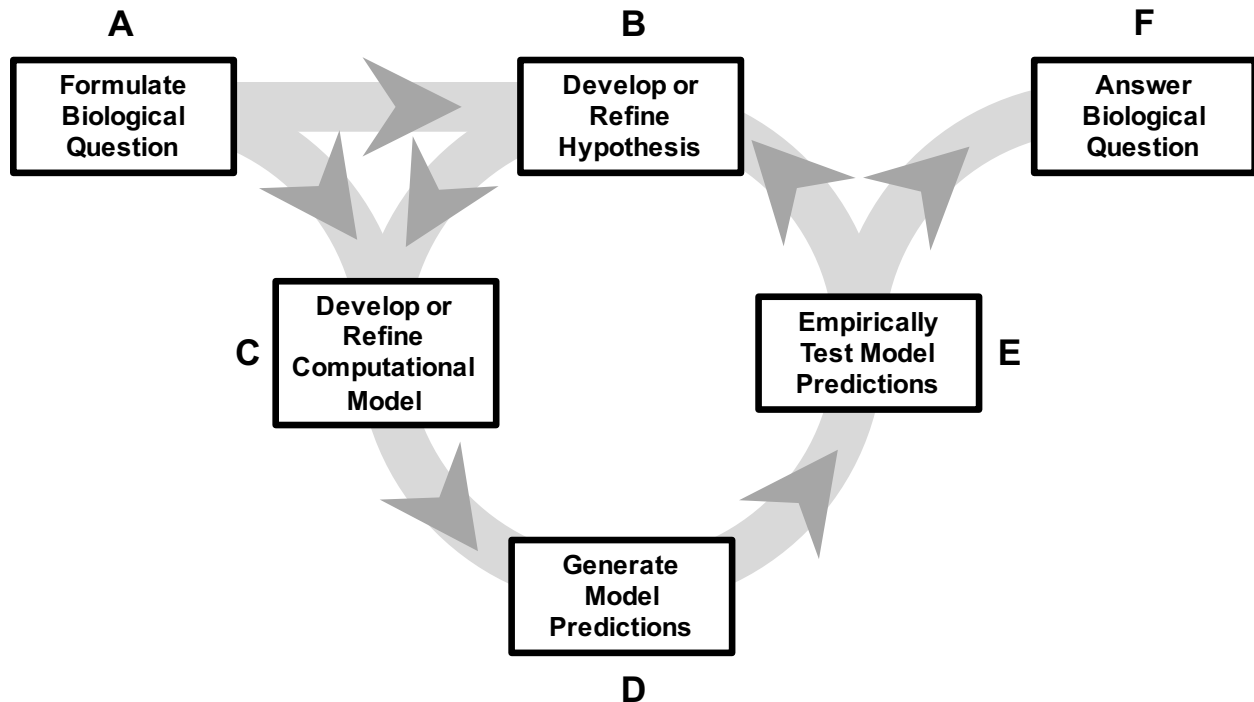


**Figure 1: Typical flowchart for incorporating mathematical modeling into an experimental study to answer biological questions.** (A) Well-defined research questions lead to (B) the development of hypotheses and (C) appropriate modeling approaches. Iterating through (D) model development, fine-tuning, and (E) experimental validation can lead to refined hypotheses (B) or answers to biological questions (F). Figure redrawn from elsewhere.<sup>1</sup>

#### 4.2.2 Multi-Scale Characteristics of Cardiac Electrophysiology Models and Their Applications

Like other biological processes, cardiac electrophysiology has complex nonlinear and multi-scale characteristics (**Figure 2**). By integrating experimental data from key components of cardiac electrophysiology, systems biology simulations can complement empirical findings, provide quantitative insight into physiological and pathophysiological mechanisms of action, and guide new hypotheses to better understand this complex biological system and develop novel cardiotherapeutic approaches.

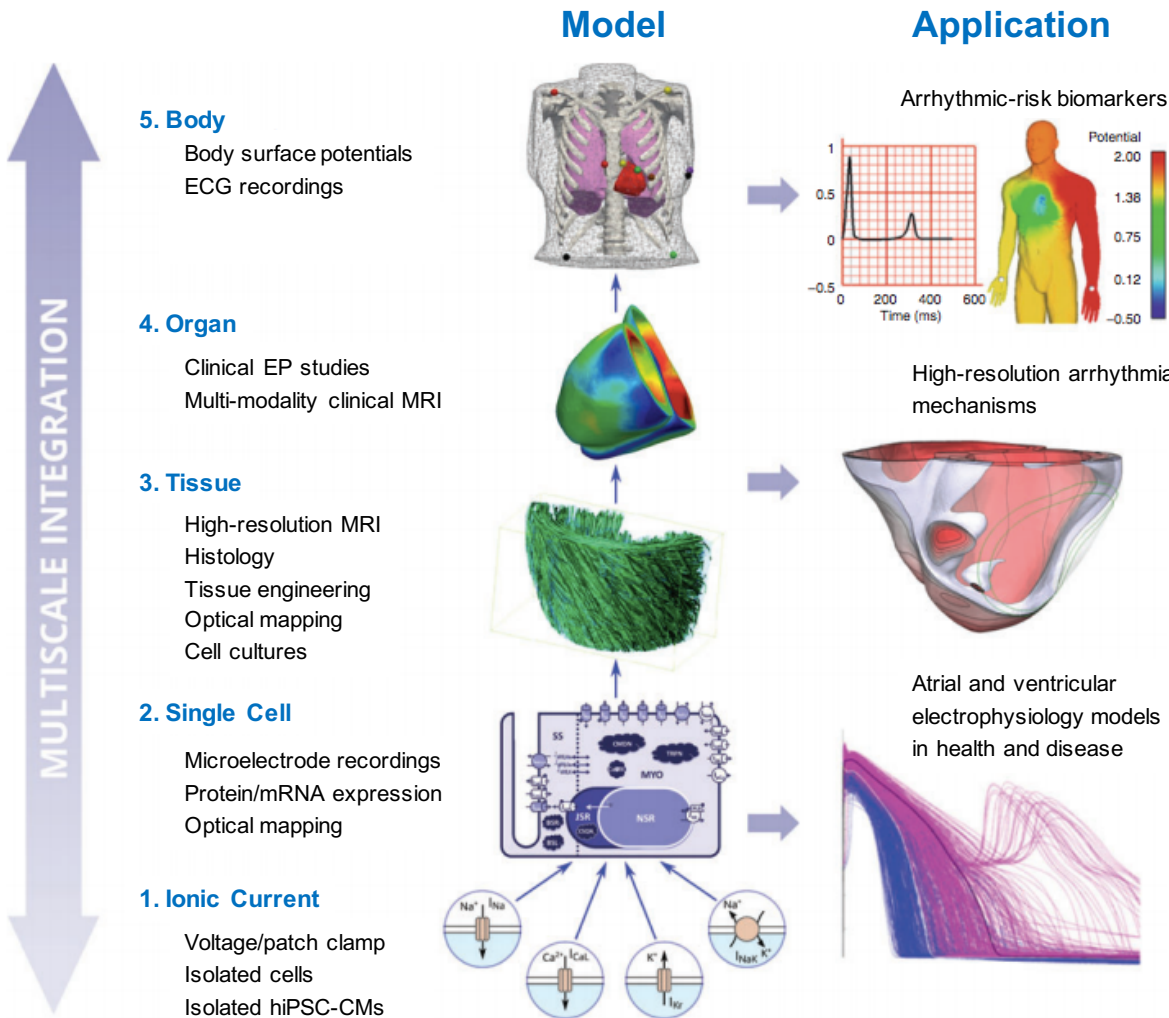


**Figure 2: Multi-scale integration of experimental data into mathematical models to predict healthy and diseased cardiac electrophysiology.** From bottom to top: 1) voltage/patch clamp data is used to develop models of cardiac ion channels; 2) the net effects of all cardiac ion channels/pumps/etc. are used for single-cell cardiomyocyte models; together, these models can be perturbed to simulate physiologic and pathophysiologic single-cell electrophysiology. 3-5) tissue-, organ-, and body-level simulations utilize image-based anatomical models; incorporating single-cell models with electrical excitation through tissue allows for higher-order predictions of arrhythmia. The right panel provides *in silico* applications for each respective scale. Figure adapted from elsewhere<sup>4</sup> with permission.

Fine-tuned movements of ions into and out of the cardiomyocyte are at the core of cardiac electrophysiology. Individual cardiomyocytes have distinct ion channels, each with their own kinetics and properties that regulate the magnitude and rate of ions fluxing into and out of the cell (**Figure 2, item 1**). The activity of a given ion channel can be successfully mathematically modeled with sufficient voltage clamp data obtained by measuring ion channel activity while holding a cell's transmembrane voltage for a set amount of time at a range of values (for more details, see **Section 4.2.1**). Tireless efforts and collaborations between experimentalists and dry lab colleagues have led to models of each key ion moving through compartments of the cardiomyocyte. By accounting for the net effects of all key ion channels/pumps/exchangers in cardiomyocytes, mathematical modelers have been successful in simulating whole-cell electrophysiology (**Figure 2, item 2**; for more details see **Section 4.2.2**). Experimentally, cellular electrophysiology can be assessed via single cell imaging and microelectrodes, whereas tissue-level measurements are commonly made with electrode arrays and optical mapping. Higher-order models can be subsequently developed by accounting for electrical excitation through image-based anatomical representations of tissue comprised of *in silico* single-cell models (**Figure 2, items 3-5**).

Throughout this chapter, we sequentially demonstrate that each order of model—from ion currents to whole-cell to tissue-level—has its own individual utility and contributes to modeling and predicting specific types of physiology and pathophysiology (**Figure 2, right panel**).

#### 4.2.3 Chapter Overview

In the remainder of this chapter, we briefly introduce *in silico* methods to describe the dynamics of physiological and pathophysiological single-cell and tissue-level cardiac electrophysiology (**Figure 2, items 1-3**), aiming to provide a primer that will enable non-mathematicians to better communicate with computational modeling colleagues and understand

the related scientific literature. Following a brief review of the basics of human ventricular cardiomyocyte electrophysiology (**Section 4.1.4**), we adopt a “bottom-up” approach that starts by describing the basis of ion channel mathematical models (**Section 4.2.1**). Next, we discuss how the net flux of ions through key channels leads to changes in transmembrane voltage during cardiomyocyte action potentials (**Section 4.2.2**). By applying these fundamentals, we describe how action potentials propagate in models of cardiac tissue (**Section 4.2.3**). Finally, for each of these latter sections, we also provide case studies and applications of simulating single-cell and tissue-level electrophysiological pathology (**Sections 4.3.1** and **4.3.2**, respectively).

### **4.3 Brief Overview of Adult Human Cardiomyocyte Electrophysiological Properties**

As a reference for the non-electrophysiologist, we first provide a brief overview on cardiomyocyte electrophysiology. As illustrated in **Figure 3**, the human adult ventricular cardiomyocyte (hCM) has five phases of the cardiac action potential: 0) upstroke; 1) early repolarization notch; 2) plateau; 3) late repolarization; and 4) diastole. Specific ion channels dominate each of these respective phases: 0) sodium current; 1) transient outward potassium current; 2) L-type calcium current; 3) rapid and slow delayed rectifier potassium currents; and 4) inward rectifier potassium current. **Figure 3** illustrates how these channels contribute to the action potential, and when they are active during the ventricular action potential.

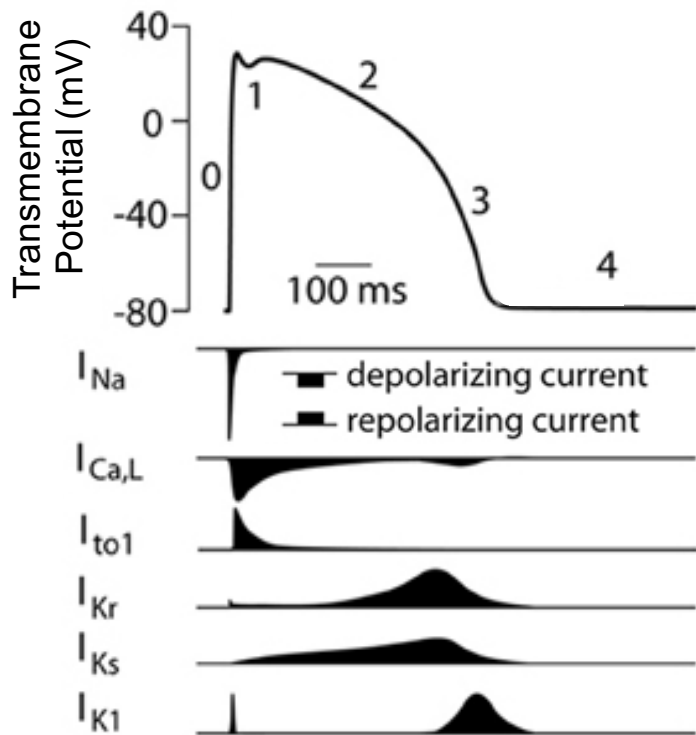


**Figure 3: Overview of cardiomyocyte action potential electrophysiology.** Human adult ventricular cardiomyocytes have distinct action potential waveforms with unique underlying ion current contributions. Phases 0 to 4 of an excited adult ventricular cardiomyocyte action potential (looking at transmembrane potential over time) correspond to upstroke (mainly due to the sodium current,  $I_{Na}$ ), early repolarization notch (mainly due to transient outward  $K^+$  current type 1,  $I_{to1}$ ), plateau (mainly due to L-type calcium current,  $I_{Ca,L}$ ), late repolarization (mainly due rapid and slow delayed rectifier  $K^+$  currents,  $I_{Kr}$  and  $I_{Ks}$ , as well as the inward rectifier  $K^+$  current,  $I_{K1}$ ), and diastole (mainly due to  $I_{K1}$  and others not shown), respectively. Adapted from elsewhere<sup>5</sup> with permission.

Myocytes from different regions of the heart (e.g. atria compared with ventricles) contain different ionic current constituents, and, as a result, exhibit different action potential shapes. Similarly, important differences in ion channels and action potential waveforms are observed between mature adult human cardiomyocytes and human stem cell-derived cardiomyocytes

(hiPSC-CMs) that are often used in the experimental setting. More specifically, hiPSC-CMs have prominent funny currents, or pacemaker currents, which contribute to hiPSC-CM automaticity that is not evident in adult ventricular myocytes (**Figure 3**).<sup>6</sup> Mathematical models can describe these differences, and even help predict how findings from hiPSC-CMs may translate to healthy and diseased adult ventricular myocytes.<sup>3</sup> Below, we describe how to mathematically model individual families of ion currents; specifically, we use the hERG rapid delayed rectifier K<sup>+</sup> current (I<sub>Kr</sub>) as a case example.

#### 4.4 Methods

##### 4.4.1 How to Model Ion Channel Activity

Cellular electrophysiology depends on the movement of sodium, potassium, calcium, and other ions across semi-permeable cellular and intracellular membranes. However, the lipid bilayer has an extremely high resistance that acts as an electrical insulator; transmembrane ion channels allow for the flux of specific ions across cell membranes.<sup>7</sup>

Ions flow through an ion channel down an electrochemical gradient—that is, ion flux is influenced by both diffusional and electric field forces. When ion x's movement in one direction of a channel due to diffusion is equal and opposite to the rate of movement due to the electric field, equilibrium is achieved. This occurs when the transmembrane voltage ( $V_m$ ), defined by present-day convention as intracellular minus extracellular voltage, is equal to the Nernst equilibrium potential ( $E_x$ ) that can be calculated using an equation derived by the physical chemist and Nobel Laureate, Walther Nernst in the late 19<sup>th</sup> century:

$$E_x = \frac{RT}{zF} \ln \left( \frac{[x_o]}{[x_i]} \right) \quad (1)$$

That is, for an ion with a known charge  $z$  at constant temperature  $T$ ,  $E_x$  increases in magnitude when the disparity between intracellular and extracellular concentration ( $[x_i]$  and  $[x_o]$ , respectively) of a given ion  $x$  increases. Note that  $R$  and  $F$  are the ideal gas and Faraday's

constants, respectively. Mathematical modelers can therefore keep track of intracellular and extracellular concentrations of ions to calculate  $E_x$  over time. Using the present-day convention,  $E_x$  is positive if the extracellular concentration of an ion is greater, and negative if the intracellular concentration of an ion is greater.

When deviating from equilibrium, the net driving force of ion  $x$  outward (based on convention) can be defined as ( $V_m - E_x$ ). If  $V_m > E_x$ , the outward diffusion forces (e.g.,  $K^+$  is higher intracellularly than extracellularly) outweigh inward electric forces, leading to a net flux of a given ion out of the cell through its channel (this is common in several cardiomyocyte  $K^+$  ion channels, as  $E_K$  is approximately -90 mV, and a cardiomyocyte's  $V_m$  ranges from approximately -90 mV to +40 mV). Conversely, if  $V_m < E_x$ , the inward diffusion forces (e.g.,  $Na^+$  is higher extracellularly than intracellularly) outweigh outward electric forces, leading to a net flux of a given ion into the cell through its channel (this is common in the cardiomyocyte  $Na^+$  ion channel, which leads to Phase 0 depolarization as in **Figure 3**).

Using this framework, the current  $I$  of ion  $x$  is proportional to the electrochemical driving force ( $V_m - E_x$ ), with the proportionality coefficient  $g_x$ , defined as the conductance, or the ability of electrical charge to flow through the ion channel. The conductance is generally not modeled as a constant, but rather simulated to account for the average number of channels within a cell membrane that are open at a particular time.

Macroscopically, the number of open voltage gated channels changes over time in response to  $V_m$ . Computational electrophysiologists describe these changes mathematically using macroscopic channel kinetic equations. In a simple case, a channel can be modeled as switching between active and inactive states using first-order rate processes. The average percent of open channels ( $x_1$ ) over time can therefore be described by two variables: 1) its steady state value,  $x_{1,\infty}$ , the average percent of open channels over a sufficiently extended period of time; and 2) its time constant,  $\tau_{x1}$ , defining how quickly  $x_1$  approaches  $x_{1,\infty}$ . Based on

these definitions,  $x_{1,\infty}$  ranges between 0 and 1, where it increases at higher transmembrane voltages. Mathematically,  $x_1$  obeys the differential equation:

$$\frac{dx_1}{dt} = \frac{x_{1,\infty} - x_1}{\tau_{x1}} \quad (2)$$

That is, the instantaneous change in  $x_1$  is such that it approaches  $x_{1,\infty}$  (i.e., if  $x_1$  is less than  $x_{1,\infty}$ , there is a positive instantaneous change in  $x_1$  to approach its steady-state value  $x_{1,\infty}$ ; on the other hand, if  $x_1$  is greater than  $x_{1,\infty}$ , there is a negative instantaneous change in  $x_1$  to approach its steady-state value  $x_{1,\infty}$ ) at a rate proportional to  $1/\tau_{x1}$  (i.e., the smaller the  $\tau_{x1}$ , the faster it will approach the steady-state value). Importantly, both  $x_{1,\infty}$  and  $\tau_{x1}$  are functions of transmembrane voltage, as we will discuss in **Figure 4**. Numerical methods are used to update  $x_1$  values over time, thereby simulating the temporal evolution of ion channel gating at a given voltage, by: 1) discretizing changes in time (e.g., time increments of 0.0025 ms); 2) calculating the right hand side of the differential equation—recall that  $x_{1,\infty}$  and  $\tau_{x1}$  are functions of transmembrane voltage, so this value must be known; 3) multiplying the values from the previous two steps; 4) adding step 3 to the previous value of  $x_1$ ; and 5) repeating steps 1-4.

In more complex cases, a channel can again switch between open and closed states; however, in addition, it can also be inactivated—or blocked—by unique subunits of a channel, adding another layer of complexity. The switch between the two states—inactivated or not inactivated—can be modeled using similar first-order rate processes. However, the steady-state values typically decrease, rather than increase, at higher transmembrane voltages. Nevertheless, the same differential equation typically applies to model inactivation.

This approach was utilized by Tong et al. to model the hERG delayed rectifier current ( $I_{Kr}$ ).<sup>8</sup> To formulate such a model, it is necessary to develop relationships between the transmembrane voltage and steady-state activation, activation time constant, steady-state inactivation, and inactivation time constant. This was done by Tong et al.<sup>8</sup> by extracting data

from full length hERG clones expressed in different expression systems,<sup>9-12</sup> as shown in **Figure 4A-D**, respectively.

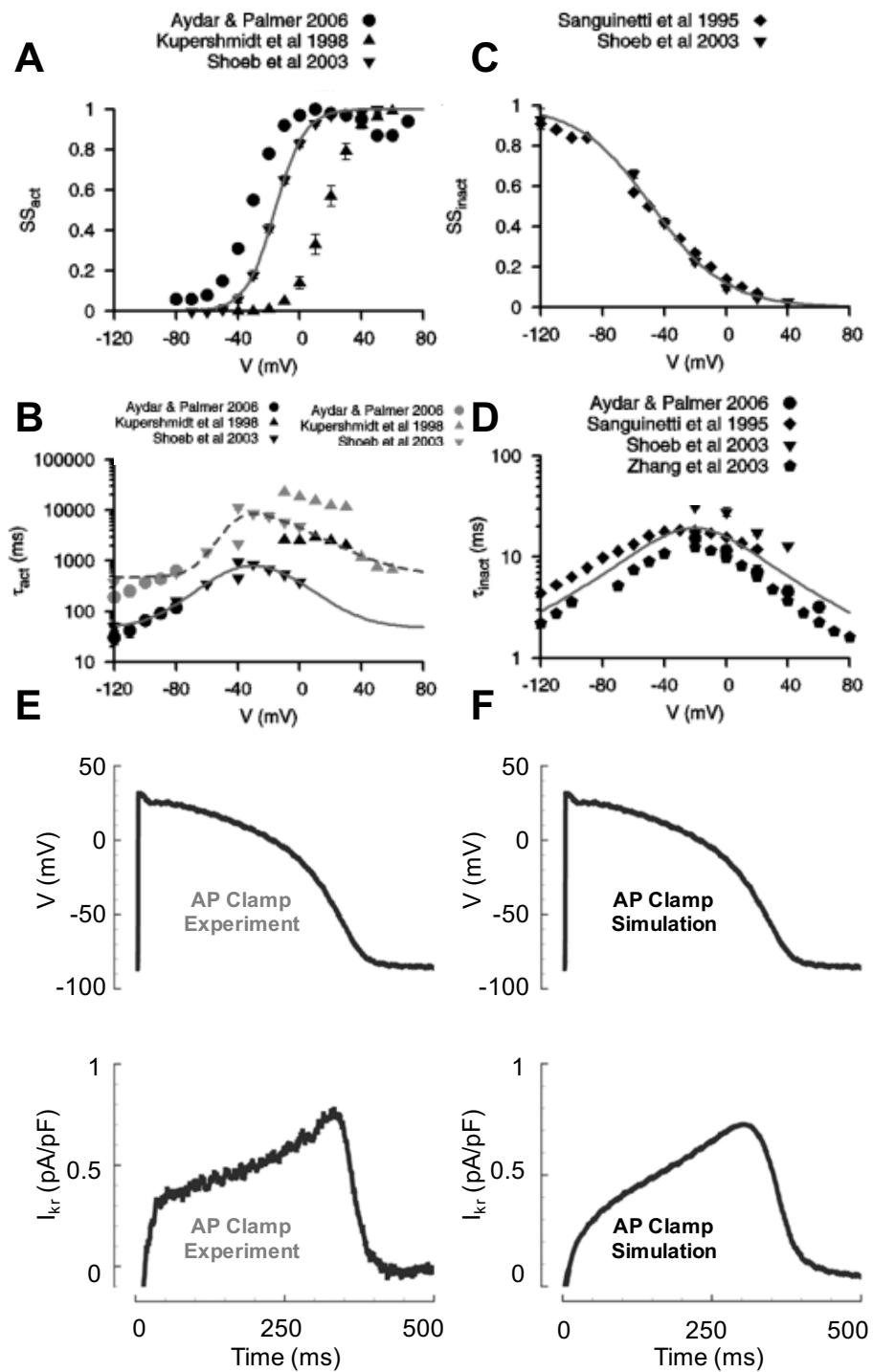


**Figure 4: Modeling the hERG rapid delayed rectifier ion channel.** Tong et al.<sup>8</sup> developed a model of the hERG delayed rectifier channel by determining relationships between the transmembrane voltage ( $V$ ) and (A) steady-state activation ( $ss_{act}$ ), (B) activation time constant ( $\tau_{act}$ ), (C) steady-state inactivation ( $ss_{inact}$ ), and (D) inactivation time constant ( $\tau_{inact}$ ) using data from full length hERG clones expressed in different expression systems.<sup>9-12</sup> Lines represent best fit equations to experimental data points. Note two different activation gates were incorporated into the Tong et al.<sup>8</sup> hERG model by using the same steady-state activation equations from Panel (A), each with different activation time constants  $\tau_{hn1}$  and  $\tau_{hn2}$  from Panel (C). (E-F) Other models (e.g., O'Hara et al.<sup>13</sup>) have been developed to better reflect the hERG delayed rectifier ( $I_{K_r}$ ) current contribution during an adult human cardiomyocyte action potential. Panels (A) through (D) adapted from elsewhere<sup>8</sup> with permission. Panels (E) through (F) adapted from elsewhere<sup>13</sup> with permission.

The theory behind gating kinetics motivates the use of the sigmoidal-shaped function to relate voltage and steady-state variables, as shown in **Figures 4A and 4C**. On the other hand, normal distribution-shaped functions (as in **Figures 4B and 4D**) or exponential decay-shaped functions (not shown) are commonly used to relate voltage and time constants. The parameters within each equation are typically found through algorithms to minimize the error between the function outputs and experimental data points. Both activation and inactivation variables obey the differential Equation 2 previously shown; in this case, the resulting conductance ( $g_{hERG}$ ) was defined as the product of the maximum conductance constant, activation variables (each a function of time and voltage, as previously described), and the inactivation variable (a function of time and voltage, as previously described), which can be inserted into the hERG ion current equation,  $I_{hERG} = g_{hERG}(V_m - E_K)$ .

More sophisticated models have been developed to refine the hERG model specifically for its contributions to the cardiomyocyte action potential. For example, using a similar methodology to what was described herein, O'Hara et al.<sup>13</sup> developed a more complex, but more cardiomyocyte-specific, representation of the delayed rectifier potassium current. As shown in **Figures 4E** and **4F**, it is highly representative of experimental hERG activity throughout the cardiac action potential.

In the next section, we demonstrate how O'Hara et al.<sup>13</sup> used their hERG model (and other key action potential ion channel/pump models) to simulate whole-cardiomyocyte action potentials. While other human ventricular models have been successfully developed,<sup>14-16</sup> we focus on the O'Hara et al. model<sup>13</sup> for its current use as an in silico component of the Comprehensive in vitro Proarrhythmia Assay (CiPA) initiative, which we describe further in **Section 3.1**.<sup>17</sup>

#### *4.4.2 How to Model Whole-Cardiomyocyte Electrophysiology*

As outlined in **Section 4.1.4**, several key ion channels are active at different phases of the cardiac action potential. Each of these channels can be modeled using the framework described in **Section 4.2.1**, with slight modifications to account for unique properties of each channel. The net flux of ions ( $I_{total}$ ) through key channels (for a schematic of all channels/pumps/etc. involved in the O'Hara et al. human adult cardiomyocyte model, see **Figure 5A**)<sup>13</sup> leads to changes in transmembrane potential ( $V_m$ ) over time, obeying the following differential equation:

$$\frac{dV_m}{dt} = -\frac{I_{total} + I_{stim}}{C_m} \quad (3)$$

where  $C_m$  is the constant capacitance of the cell (proportional to cell size) and  $I_{stim}$  is the artificial stimulus provided in the simulation (adult ventricular myocytes do not excite on their own, thus requiring artificial activation in the model). Note that the negative term in front of the right hand

side of the equation is due to the present-day convention of current previously described. Similar to the differential Equation (2), numerical methods can be used to update  $V_m$  values over time (allowing for simulations of the transmembrane voltage over time) by: 1) discretizing changes in time (e.g., time increments of 0.0025 ms); 2) calculating the right hand side of the differential equation (recall each ion channel has its own gates, so for each gate, the numerical methods for solving respective gating differential equation (**Section 4.2.1**) must be used); 3) multiplying the values from the previous two steps; 4) adding step 3 to the previous value of  $V_m$ ; and 5) repeating steps 1-4.

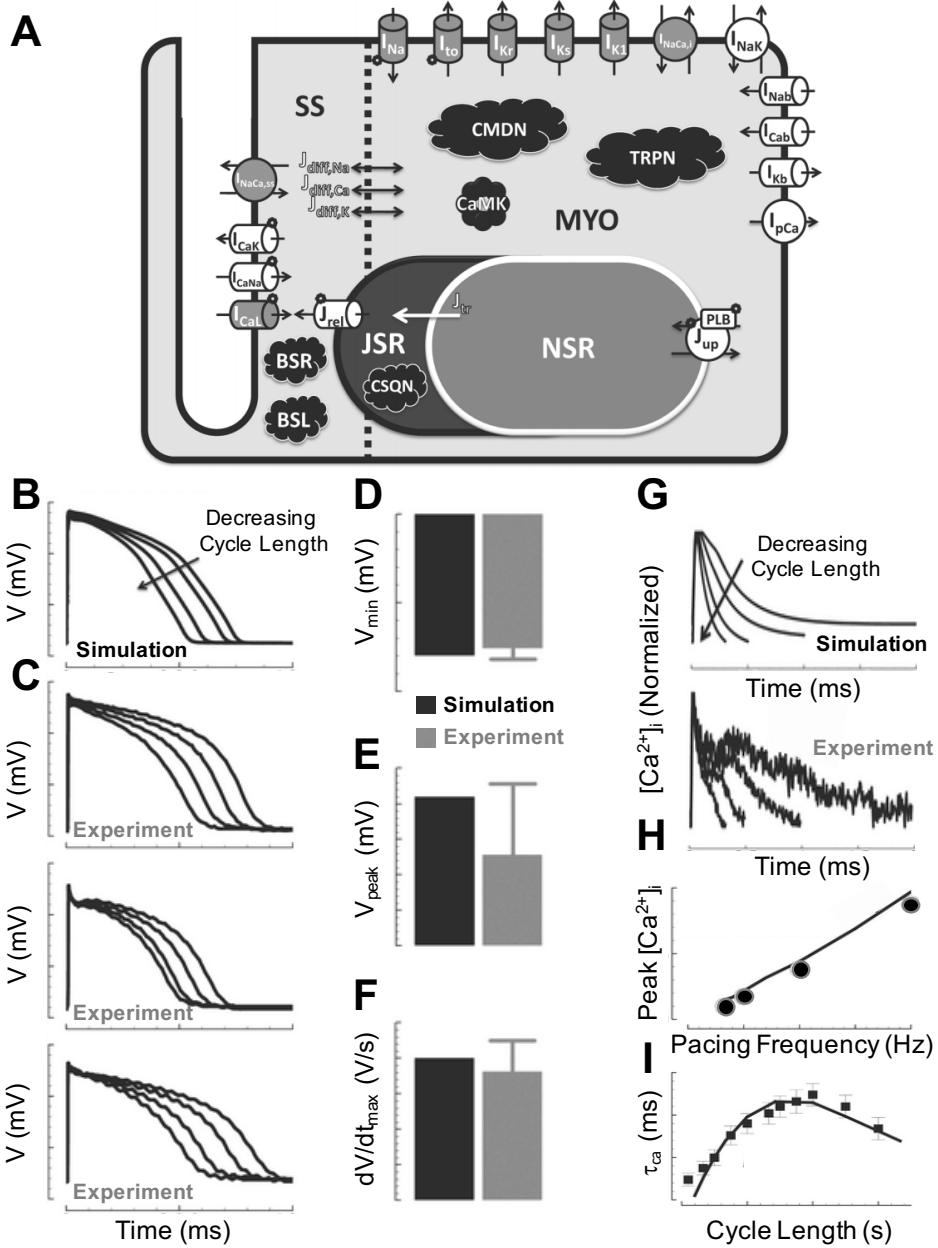


**Figure 5: Modeling the human adult cardiomyocyte action potential.** (A) Schematic of the types of ion channels/pumps/exchangers modeled; the net effects of these channels/pumps/exchangers in their given compartment are used to model whole cell electrophysiology. Four main compartments are accounted for, including: 1) bulk myoplasm (myo), 2) junctional sarcoplasmic reticulum (JSR), 3) network sarcoplasmic reticulum (NSR), and 4) subspace (SS); for details, see elsewhere.<sup>13</sup> Comparison of the (B) simulated and (C)

three select experimental adult cardiomyocyte action potentials during electrical pacing with varying cycle length (inverse of frequency). **(D-F)** Comparison of simulated and experimental characteristics of the action potential, including resting membrane potential ( $V_{min}$ ), peak voltage ( $V_{peak}$ ), and maximum rate of voltage increase ( $dV/dt_{max}$ ), respectively. **(G)** By accounting for net fluxes of calcium into and out of each key cellular compartment, O'Hara et al.<sup>13</sup> could also simulate intracellular calcium ( $[Ca^{2+}]_i$ ) over the duration of the action potential (top); comparison to experimental  $[Ca^{2+}]_i$  transients (bottom). **(H-I)** Comparison of simulated and experimental characteristics of the calcium transient, including peak  $[Ca^{2+}]_i$  and decay time constant ( $\tau_{ca}$ ), respectively. Adapted from elsewhere<sup>13</sup> with permission.

By doing so, the O'Hara et al. model<sup>13</sup> was able to successfully simulate adult cardiomyocyte action potentials (**Figure 5B**) that look remarkably similar to experimental action potentials from three select adult cardiomyocytes (**Figure 5C**) and was within experimental variability for several characteristics of the action potential, including resting membrane potential, peak voltage, and maximum rate of voltage increase (**Figure 5D-F**). Furthermore, by accounting for net fluxes of calcium into and out of four key cellular compartments—such as bulk myoplasm (myo), junctional sarcoplasmic reticulum (JSR), network sarcoplasmic reticulum (NSR), and subspace (SS)—the O'Hara et al. model<sup>13</sup> could also simulate intracellular calcium (in myo) over the duration of the action potential, which was also remarkably similar to experimental calcium transients characteristics (**Figure 5G-I**).

#### 4.4.3 How to Model Cardiac Tissue Strands

Myocardium is made up of individual cardiomyocytes connected by intercalated disks, embedded within the extracellular matrix; in the context of cardiac tissue electrophysiology, gap junctions play a key role by allowing for intercellular propagation of action potentials throughout the myocardial tissue. To simulate tissue-level electrophysiology, mathematical modelers

extend the single-cell model (**Section 4.2.2**) by accounting for ion flow through gap junctions between neighboring cells. **Figure 6** illustrates this method and the resultant simulations in the simplest tissue case—a one-dimensional strand of myocytes, also referred to as a “cable model”.

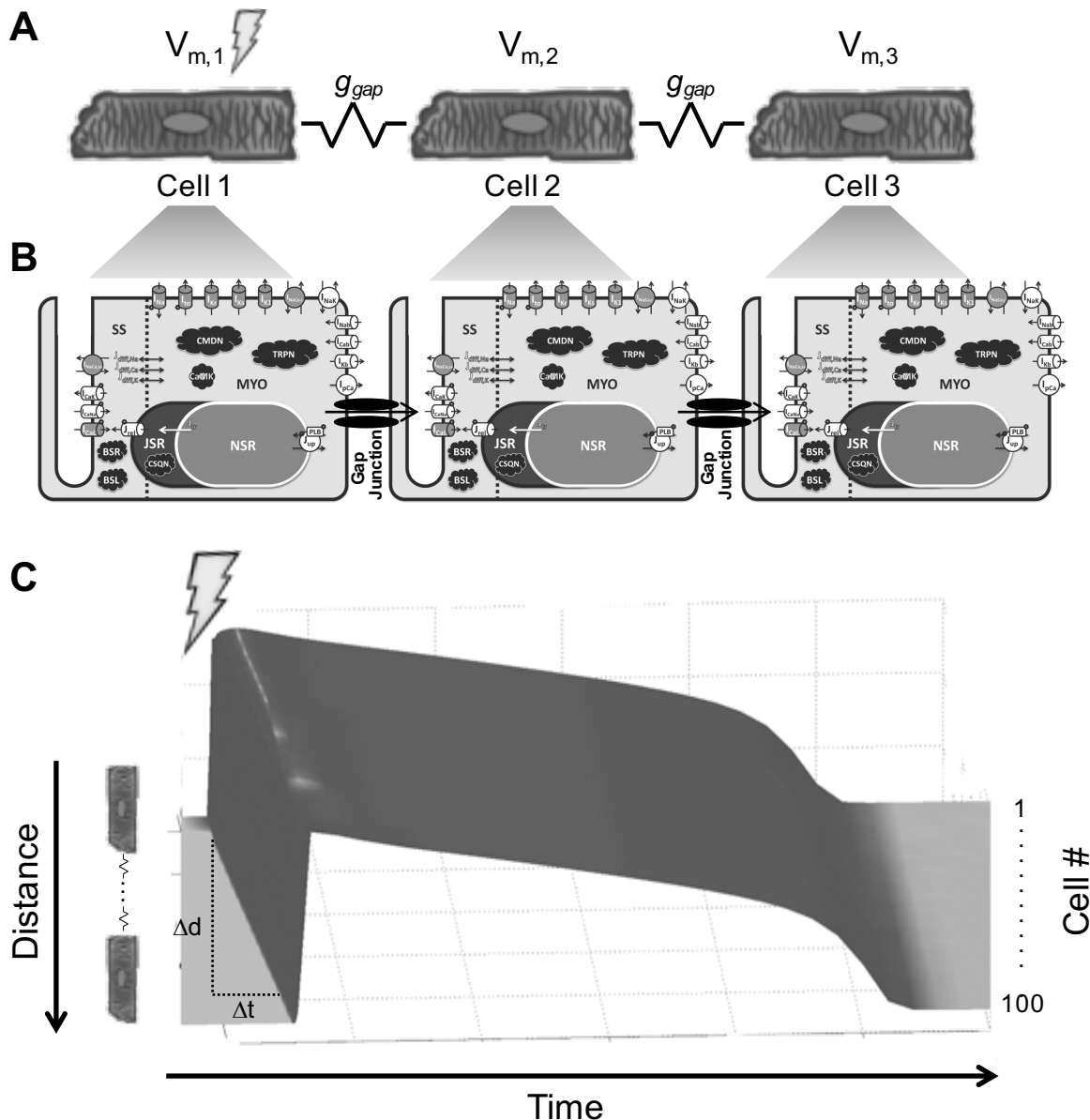


**Figure 6: Modeling Action Potential Propagation in a 1-Dimensional Tissue Strand. (A)**  
Schematic of action potential propagation when cells are coupled to each other—cell 1 is

excited, leading to depolarization;  $V_{m,1}$  therefore has a higher voltage than neighboring cell 2, driving cation flux from cell 1 to cell 2, and so forth. **(B)** This can be represented with electrophysiological models, where each cell has its own whole-cell model (e.g., O'Hara et al. cell model<sup>13</sup>), and ions flow down the electrochemical gradient through gap junctional channels with constant conductance,  $g_{gap}$ . **(C)** Simulation results of action potentials propagating from excited cell 1 to cell 100. The speed of propagation from one cell to the next can be calculated by the conduction velocity ( $\Delta d/\Delta t$ ). Panel **(B)** adapted from elsewhere<sup>13</sup> with permission. Panel **(C)** adapted from elsewhere<sup>18</sup> with permission.

In this example, cells are connected end-to-end through gap junctions. Gap junctions contain proteins called connexins, and these form channels that connect the intracellular spaces of two adjacent myocytes. As a result of the connexin proteins, gap junctions allow the flow of electrical charge (i.e., they are conductive). To this end, flow between two cells can be modeled analogously to an ion channel. Just as there was an electrochemical driving force ( $V_m - E_x$ ) for a single-cell's ion channel, there is a driving force through a gap junction between cells 1 and 2 of ( $V_{m,1} - V_{m,2}$ ); if cell 1 has a higher voltage than neighboring cell 2 (i.e.,  $V_{m,1} > V_{m,2}$ ), then cation flux is driven from cell 1 to cell 2 (**Figure 6A**). This gets scaled by the constant gap junctional conductance,  $g_{gap}$ , to compute the gap junctional current. Keep in mind, each cell has its own electrophysiological properties that can be described by whole-cell models (**Figure 6B**). Altogether, each cell within the tissue strand can be mathematically approximated as:

$$\frac{\Delta V_{m,cell\ n}}{\Delta t} = - \frac{I_{total,n} + I_{stim,n} + g_{gap}(V_n - V_{n-1}) + g_{gap}(V_n - V_{n+1})}{c_m} \quad (4)$$

where, for a given cell  $n$  with transmembrane voltage  $V_{m, cell\ n}$ , the change in voltage over time can be approximated as single-cell changes (from  $I_{total,n}$  and  $I_{stim,n}$ ), in addition to the fluxes through gap junctions to neighboring cells to the left ( $g_{gap}(V_{m,n} - V_{m,n-1})$ ) and right ( $g_{gap}(V_{m,n} - V_{m,n+1})$ ) of cell  $n$ . Yet again, as an extension to the whole-cell calculations (**Section 4.2.2**), numerical

methods can be used to update voltage values of all cells in a tissue over time by: 1) discretizing changes in time; 2) calculating the right hand side of the differential equation (recall each cell has its own voltage and channels, so for each cell's gates—which are dependent on voltage—the numerical methods used to solve each gating differential equation (**Section 4.2.1**) must be implemented); 3) multiplying the values from the previous two steps; 4) adding step 3 to the previous value of  $V_m$  for each cell; and 5) repeating steps 1-4. Note that  $I_{stim}$  does not necessarily need to excite all cells at once, as we discuss below.

**Figure 6C** illustrates simulation results of action potentials propagating from cell 1 (the only excited cell) to cell 100 connected in series. Note a delay in activation from cell-to-cell, which reflects the intrinsic resistance to ionic flux through the gap junctions. A typical metric used to characterize this delay is called the conduction velocity (CV); the greater the conduction velocity, the less the delay. Measuring the difference in time of activation between a cell near the beginning of the strand and the end of the strand (defined as  $\Delta t$ ) and the spatial distance between these two cells (defined as  $\Delta d$ ), conduction velocity is calculated as  $CV = \Delta d / \Delta t$  (**Figure 7C**). Physiologic CV along the fiber direction in healthy adult human myocardium can decrease appreciably in the setting of fibrosis or other pathologies or interventions that diminish the integrity or expression level of gap junction proteins, leading to irregular heart beats. Therefore, CV is recognized as a valuable metric when attempting to predict myocardial arrhythmic potential.

## 4.5 Applications of Cardiac Electrophysiology Models

### 4.5.1 Applications of Single-Cell Models: Predicting Torsadogenic Drugs

In this section, we provide an example of the utility and promise of computational approaches to model whole-cell electrophysiological pathology and emerging drug toxicity screening technologies.

Torsades de Pointes (TdP) is a rare but lethal form of polymorphic ventricular tachycardia.<sup>19</sup> In addition to congenital long QT syndrome, anti-arrhythmic and non-cardiac drugs have been implicated in causing TdP.<sup>20</sup> Drug-induced TdP is a leading cause of drug relabeling or withdrawal from the market, second only to drug-induced hepatotoxicity;<sup>21,22</sup> this has led to the establishment of regulatory cardiotoxicity testing<sup>23-25</sup>—including in vitro measurements on hERG current inhibition, animal model QT assays, and clinical examination of QT interval in healthy volunteers—that is both expensive and of limited predictive value for subsequent clinical trials.<sup>26,27</sup> Given early drug development attrition rates of 80-90% and only 10% commercial success<sup>28,29</sup> with development costs on the order of two to three billion dollars,<sup>30</sup> it is of great interest for pharmaceutical companies to economically and effectively screen whether a drug under development is likely to be torsadogenic.<sup>31</sup>

Recent work has demonstrated the promise of integrating systematic simulations with machine learning to successfully predict pharmacological toxicity.<sup>32</sup> Lancaster and Sobie<sup>32</sup> simulated the individual effects of a panel of 86 drugs on cardiomyocyte action potential and calcium transient metrics by incorporating each of their empirical inhibitory effects on hERG delayed rectifier K<sup>+</sup> channel, L-type calcium channel, and sodium channel activity (**Figure 7A**). This was accomplished by scaling the maximum conductance as a function of the half-maximal inhibitory concentration (IC<sub>50</sub>) value, and the effective free therapeutic plasma concentration (EFTPC).

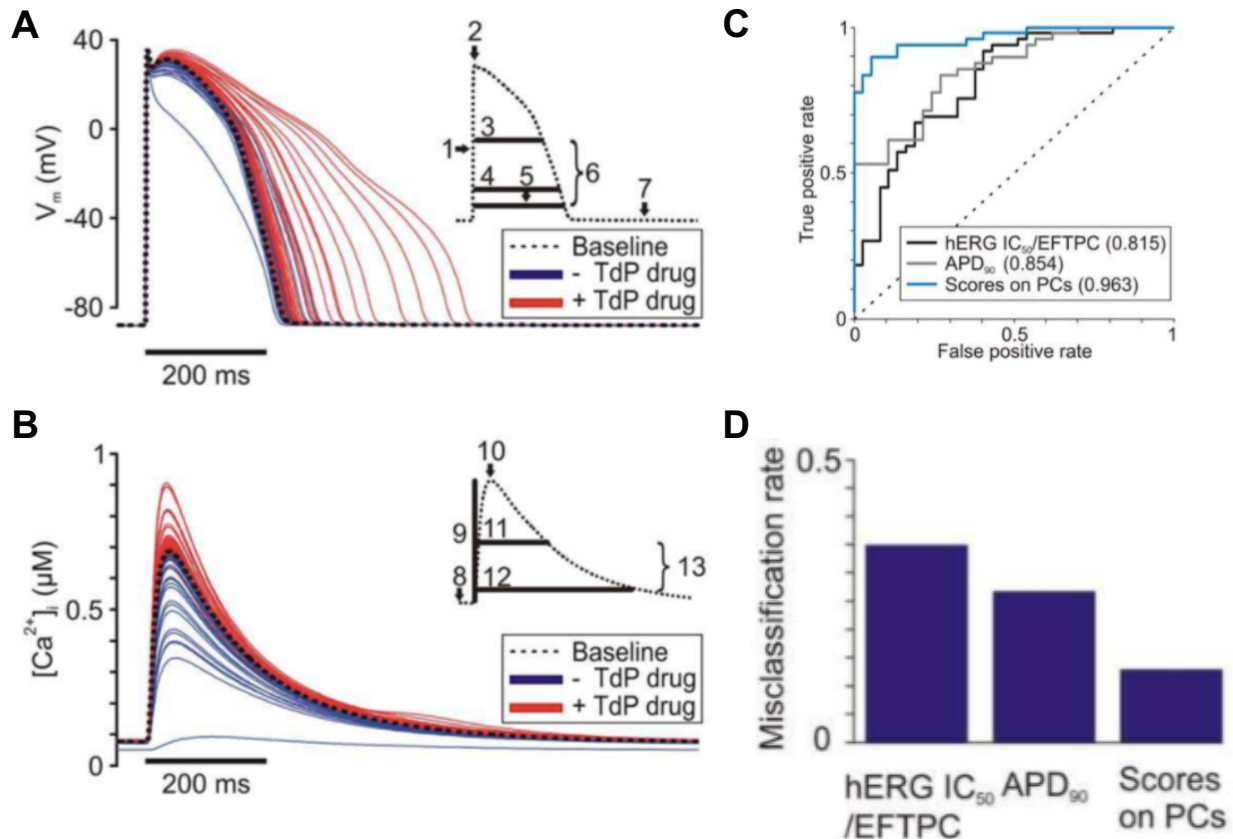


**Figure 7: Using Single-Cell Models to Predict Drug-Induced Arrhythmias.** By simulating effects of 86 drugs on 13 metrics (inset) from human adult ventricular myocyte (A) action potentials and (B) calcium transients, Lancaster and Sobie<sup>32</sup> were able to classify drugs as torsadogenic or non-torsadogenic with superior (C) sensitivity and specificity and (D) misclassification rates compared to conventional methods (e.g., using IC<sub>50</sub> values from hERG channel inhibition assays (hERG IC<sub>50</sub>/EFTPC), or from simulations of action potential duration alone (APD<sub>90</sub>)). Figure adapted from elsewhere<sup>32</sup> with permission.

By inputting the simulated effects of each drug on 13 action potential (Figure 7A) and calcium transient (Figure 7B) metrics into a support vector machine (SVM) learning algorithm (SVM divides the input metrics into two regions—e.g., torsadogenic and non-torsadogenic—separated by a linear boundary), Lancaster and Sobie<sup>32</sup> were able to classify drugs as

torsadogenic or non-torsadogenic with superior sensitivity and specificity (**Figure 7C**) and misclassification rates (**Figure 7D**) in comparison to conventional methods (e.g., using IC<sub>50</sub> values from hERG channel inhibition assays (hERG IC<sub>50</sub>/EFTPC), or from simulations of action potential duration alone (APD<sub>90</sub>)).

These promising quantitative systems pharmacology approaches are gaining attraction; currently, in silico modeling of human ventricular electrical activity is an integral part of the CiPA initiative to detect and avoid drug-induced TdP for new drugs seeking regulatory approval from the Food and Drug Administration (FDA).<sup>17</sup>

#### *4.5.2 Applications of Tissue-Level Models: Predicting Stem Cell Effects on Electrical Properties of Fibrotic Heart Tissue*

In this final section, we provide an example of using computational approaches to model tissue-level electrophysiology pathology and therapeutic interventions.

Human bone marrow-derived mesenchymal stem cells (hMSCs) are an emerging approach to treat heart failure.<sup>33</sup> To date, clinical benefits of hMSC therapy have achieved statistical significance, but remain modest in effect and not long lasting,<sup>34-37</sup> representing an opportunity for improvement. A better understanding of underlying cardioactive mechanisms could help optimize future hMSC-based therapies. These mechanisms involve anti-fibrotic and ion channel remodeling effects of hMSC paracrine signaling, as well as direct hMSC-myocyte heterocellular coupling.<sup>38</sup>

In our recent study,<sup>38</sup> in silico findings provided insights that help resolve disparate reports of potential pro-arrhythmic risks of hMSCs *in vitro*<sup>39</sup> that contradict *in vivo* reports of hMSCs having no effect<sup>40</sup> or even favorable cardioprotective effects<sup>37</sup> on arrhythmogenesis in pre-clinical animal studies and clinical trials. To do so, we extended 1-dimensional tissue strands to 2-dimensional tissue sheets (**Figure 8A**), with cells coupled end-to-end in the x direction, as well as side-to-side in the y direction. Heterogeneous cell populations comprised

of cardiac myocytes and fibroblasts were used to simulate cardiac tissue with either low levels or high levels of fibrosis. The former is more representative of *in vitro* cell culture with minimal fibrosis, whereas the latter represents *in vivo* models where hMSCs are used therapeutically post-myocardial infarction. Note that myocyte-myocyte gap junctional conductances are higher than myocyte-fibroblast gap junctions (i.e., there is more resistance in myocyte-fibroblast coupling), leading to slower CV when adding fibrosis into cardiac tissue simulations.

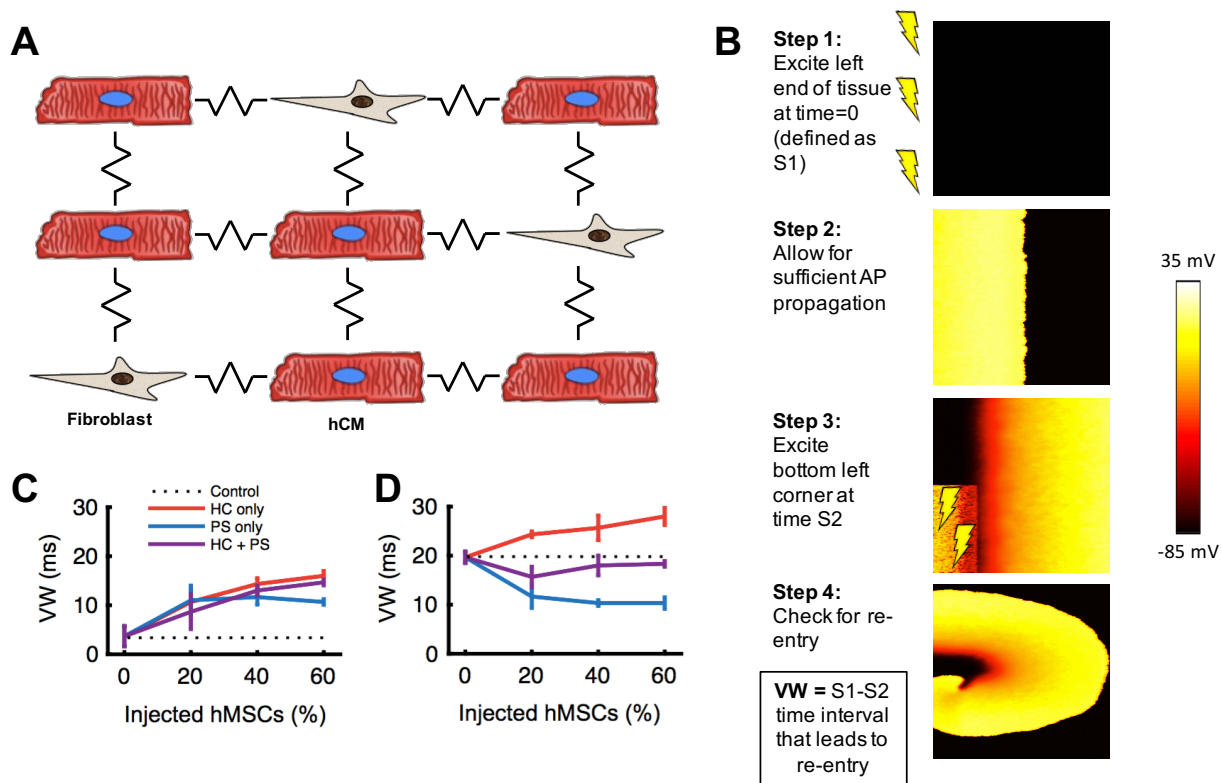


**Figure 8: Modeling hMSC electrophysiological effects on 2-D fibrotic cardiac tissue. (A)** Schematic of two-dimensional cell-cell coupling between human adult ventricular myocytes (hCMs) and fibroblasts. In this case, action potentials can propagate both in the x and y directions, rather than just along one dimension as in **Figure 6**. **(B)** Steps for performing two-dimensional vulnerable window (VW) analysis by observing electrical wavefront propagation patterns in a 5x5-cm square region of simulated cardiac tissue. VWs of **(C)** low fibrotic and **(D)**

high fibrotic cardiac tissue with varying levels of human mesenchymal stem cell heterocellular coupling (HC) and/or paracrine signaling (PS) interventions. Panel (**B**) adapted from elsewhere<sup>41</sup> with permission. Panels (**C**) and (**D**) adapted from elsewhere<sup>3</sup> with permission.

Slowed conduction could lead to arrhythmogenesis, warranting a systematic method to test arrhythmic responses. In the context of cardiac tissue, a metric called the vulnerable window (VW) is often used.<sup>38</sup> A typical protocol for VW analysis is shown in **Figure 8B**; a higher VW corresponds to a higher risk of arrhythmogenesis.

In simulations more closely representing healthy myocyte monolayers (**Figure 8C**), both hMSC paracrine signaling (PS) and heterocellular coupling (HC) are predicted to increase arrhythmogenicity compared to hMSC-free control conditions. However, in VW simulations of highly fibrotic cardiac tissue (**Figure 8D**), hMSC paracrine signaling-only conditions were predicted to be anti-arrhythmic by decreasing VW compared to control, whereas HC between hMSCs and cardiomyocytes caused the VW to increase.<sup>38</sup> VW analyses further predicted that hMSC supplementation (involving both PS and HC mechanisms) did not adversely impact fibrotic cardiac tissue arrhythmogenesis, and may even be anti-arrhythmogenic.<sup>38</sup> These simulations could help explain why hMSCs are often reported as safe<sup>40</sup> or even anti-arrhythmic<sup>37</sup> in clinical trials where paracrine effects are present despite low cell engraftment.

#### **4.6 References:**

1. Yang JH, Saucerman JJ. Computational models reduce complexity and accelerate insight into cardiac signaling networks. *Circ Res*. 2011;108:85-97
2. Mayourian J, Ceholski DK, Gonzalez DM, Cashman TJ, Sahoo S, Hajjar RJ, Costa KD. Physiologic, pathologic, and therapeutic paracrine modulation of cardiac excitation-contraction coupling. *Circ Res*. 2017;in press
3. Mayourian J, Cashman TJ, Ceholski DK, Johnson BV, Sachs D, Kaji DA, Sahoo S, Hare JM, Hajjar RJ, Sobie EA, Costa KD. Experimental and computational insight into human mesenchymal stem cell paracrine signaling and heterocellular coupling effects on cardiac contractility and arrhythmogenicity. *Circ Res*. 2017;121:411-423
4. Rodriguez B, Carusi A, Abi-Gerges N, et al. Human-based approaches to pharmacology and cardiology: An interdisciplinary and intersectorial workshop. *Europace*. 2016;18:1287-1298
5. Hoekstra M, Mummery CL, Wilde AA, Bezzina CR, Verkerk AO. Induced pluripotent stem cell derived cardiomyocytes as models for cardiac arrhythmias. *Front Physiol*. 2012;3:346
6. Karakikes I, Ameen M, Termglinchan V, Wu JC. Human induced pluripotent stem cell-derived cardiomyocytes: Insights into molecular, cellular, and functional phenotypes. *Circ Res*. 2015;117:80-88
7. Plonsey R, Barr RC. *Bioelectricity : A quantitative approach*. New York, NY: Springer; 2007.
8. Tong WC, Tribe RM, Smith R, Taggart MJ. Computational modeling reveals key contributions of kcnq and herg currents to the malleability of uterine action potentials underpinning labor. *PLoS One*. 2014;9:e114034

9. Sanguinetti MC, Jiang C, Curran ME, Keating MT. A mechanistic link between an inherited and an acquired cardiac arrhythmia: Herg encodes the ikr potassium channel. *Cell*. 1995;81:299-307
10. Shoeb F, Malykhina AP, Akbarali HI. Cloning and functional characterization of the smooth muscle ether-a-go-go-related gene k<sup>+</sup> channel. Potential role of a conserved amino acid substitution in the s4 region. *J Biol Chem*. 2003;278:2503-2514
11. Kupershmidt S, Snyders DJ, Raes A, Roden DM. A k<sup>+</sup> channel splice variant common in human heart lacks a c-terminal domain required for expression of rapidly activating delayed rectifier current. *J Biol Chem*. 1998;273:27231-27235
12. Zhang S, Kehl SJ, Fedida D. Modulation of human ether-a-go-go-related k<sup>+</sup> (herg) channel inactivation by cs+ and k<sup>+</sup>. *J Physiol*. 2003;548:691-702
13. O'Hara T, Virag L, Varro A, Rudy Y. Simulation of the undiseased human cardiac ventricular action potential: Model formulation and experimental validation. *PLoS Comput Biol*. 2011;7:e1002061
14. Grandi E, Pasqualini FS, Bers DM. A novel computational model of the human ventricular action potential and ca transient. *J Mol Cell Cardiol*. 2010;48:112-121
15. ten Tusscher KH, Noble D, Noble PJ, Panfilov AV. A model for human ventricular tissue. *Am J Physiol Heart Circ Physiol*. 2004;286:H1573-1589
16. ten Tusscher KH, Panfilov AV. Alternans and spiral breakup in a human ventricular tissue model. *Am J Physiol Heart Circ Physiol*. 2006;291:H1088-1100
17. Colatsky T, Fermini B, Gintant G, Pierson JB, Sager P, Sekino Y, Strauss DG, Stockbridge N. The comprehensive in vitro proarrhythmia assay (cipa) initiative - update on progress. *J Pharmacol Toxicol Methods*. 2016;81:15-20
18. Yang PC, Kurokawa J, Furukawa T, Clancy CE. Acute effects of sex steroid hormones on susceptibility to cardiac arrhythmias: A simulation study. *PLoS Comput Biol*. 2010;6:e1000658

19. Sauer AJ, Newton-Cheh C. Clinical and genetic determinants of torsade de pointes risk. *Circulation*. 2012;125:1684-1694
20. Yap YG, Camm AJ. Drug induced qt prolongation and torsades de pointes. *Heart*. 2003;89:1363-1372
21. Shah RR. Drug-induced qt interval prolongation: Does ethnicity of the thorough qt study population matter? *Br J Clin Pharmacol*. 2013;75:347-358
22. Shah RR. Can pharmacogenetics help rescue drugs withdrawn from the market? *Pharmacogenomics*. 2006;7:889-908
23. Fermini B, Hancox JC, Abi-Gerges N, et al. A new perspective in the field of cardiac safety testing through the comprehensive in vitro proarrhythmia assay paradigm. *J Biomol Screen*. 2016;21:1-11
24. Caverio I, Crumb W. Ich s7b draft guideline on the non-clinical strategy for testing delayed cardiac repolarisation risk of drugs: A critical analysis. *Expert Opin Drug Saf*. 2005;4:509-530
25. Shah RR. Drugs, qtc interval prolongation and final ich e14 guideline : An important milestone with challenges ahead. *Drug Saf*. 2005;28:1009-1028
26. Redfern WS, Carlsson L, Davis AS, Lynch WG, MacKenzie I, Palethorpe S, Siegl PK, Strang I, Sullivan AT, Wallis R, Camm AJ, Hammond TG. Relationships between preclinical cardiac electrophysiology, clinical qt interval prolongation and torsade de pointes for a broad range of drugs: Evidence for a provisional safety margin in drug development. *Cardiovasc Res*. 2003;58:32-45
27. Gintant G. An evaluation of herg current assay performance: Translating preclinical safety studies to clinical qt prolongation. *Pharmacol Ther*. 2011;129:109-119
28. Fermini B, Fossa AA. The impact of drug-induced qt interval prolongation on drug discovery and development. *Nat Rev Drug Discov*. 2003;2:439-447

29. Shah RR. Drug-induced prolongation of the qt interval: Regulatory dilemmas and implications for approval and labelling of a new chemical entity. *Fundam Clin Pharmacol.* 2002;16:147-156
30. Avorn J. The \$2.6 billion pill--methodologic and policy considerations. *N Engl J Med.* 2015;372:1877-1879
31. Gintant G, Fermini B, Stockbridge N, Strauss D. The evolving roles of human ipsc-derived cardiomyocytes in drug safety and discovery. *Cell Stem Cell.* 2017;21:14-17
32. Lancaster MC, Sobie EA. Improved prediction of drug-induced torsades de pointes through simulations of dynamics and machine learning algorithms. *Clin Pharmacol Ther.* 2016;100:371-379
33. Karantalis V, Hare JM. Use of mesenchymal stem cells for therapy of cardiac disease. *Circ Res.* 2015;116:1413-1430
34. Karantalis V, DiFede DL, Gerstenblith G, et al. Autologous mesenchymal stem cells produce concordant improvements in regional function, tissue perfusion, and fibrotic burden when administered to patients undergoing coronary artery bypass grafting: The prospective randomized study of mesenchymal stem cell therapy in patients undergoing cardiac surgery (prometheus) trial. *Circ Res.* 2014;114:1302-1310
35. Heldman AW, DiFede DL, Fishman JE, et al. Transendocardial mesenchymal stem cells and mononuclear bone marrow cells for ischemic cardiomyopathy: The tac-hft randomized trial. *JAMA.* 2014;311:62-73
36. Meyer GP, Wollert KC, Lotz J, Pirr J, Rager U, Lippolt P, Hahn A, Fichtner S, Schaefer A, Arseniev L, Ganser A, Drexler H. Intracoronary bone marrow cell transfer after myocardial infarction: 5-year follow-up from the randomized-controlled boost trial. *Eur Heart J.* 2009;30:2978-2984
37. Hare JM, Fishman JE, Gerstenblith G, et al. Comparison of allogeneic vs autologous bone marrow-derived mesenchymal stem cells delivered by transendocardial injection in

patients with ischemic cardiomyopathy: The poseidon randomized trial. *JAMA*. 2012;308:2369-2379

38. Mayourian J, Cashman TJ, Ceholski DK, Johnson BV, Sachs D, Kaji DA, Sahoo S, Hare JM, Hajjar RJ, Sobie EA, Costa KD. Experimental and computational insight into human mesenchymal stem cell paracrine signaling and heterocellular coupling effects on cardiac contractility and arrhythmogenicity. *Circ Res*. 2017
39. Chang MG, Tung L, Sekar RB, Chang CY, Cysyk J, Dong P, Marban E, Abraham MR. Proarrhythmic potential of mesenchymal stem cell transplantation revealed in an in vitro coculture model. *Circulation*. 2006;113:1832-1841
40. de Jong R, Houtgraaf JH, Samiei S, Boersma E, Duckers HJ. Intracoronary stem cell infusion after acute myocardial infarction: A meta-analysis and update on clinical trials. *Circ Cardiovasc Interv*. 2014;7:156-167
41. Mayourian J, Savizky RM, Sobie EA, Costa KD. Modeling electrophysiological coupling and fusion between human mesenchymal stem cells and cardiomyocytes. *PLoS Comput Biol*. 2016;12:e1005014

## **Chapter 5: Modeling Electrophysiological Coupling and Fusion between Human Mesenchymal Stem Cells and Cardiomyocytes**

*Note: The following chapter is a modified draft of an original first-author research article published in PLoS Computational Biology:*

Mayourian J, Savizky RM, Sobie EA, Costa KD. Modeling Electrophysiological Coupling and Fusion between Human Mesenchymal Stem Cells and Cardiomyocytes. PLoS Comput Biol. 2016;12(7):e1005014. doi:10.1371/journal.pcbi.1005014

JM conceived the idea, collected and analyzed the data, and wrote the manuscript. The current PLoS Computational Biology license states, "you as the author agree that anyone can reuse your article in whole or part for any purpose, for free, even for commercial purposes. Anyone may copy, distribute, or reuse the content as long as the author and original source are properly cited."

The manuscript was selected as an Editor's pick in stem cell research, and the cover of the July 2016 issue:

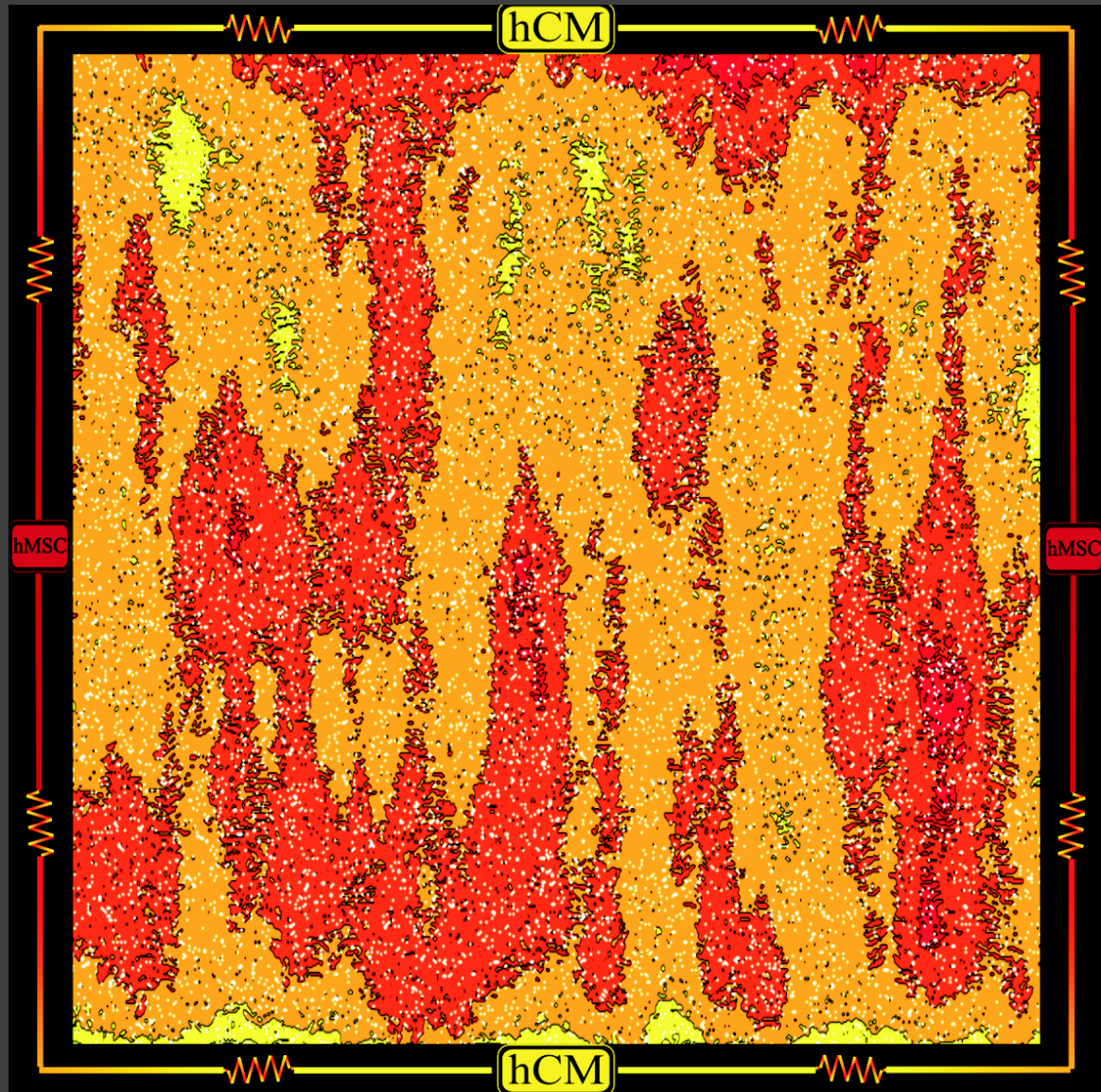


PUBLIC LIBRARY of SCIENCE | ploscompbiol.org | Volume 12 | Issue 7 | July 2016

**PLOS**

**COMPUTATIONAL  
BIOLOGY**

Published in association with the International Society for Computational Biology



## 5.1 Abstract

Human mesenchymal stem cell (hMSC) delivery has demonstrated promise in preclinical and clinical trials for myocardial infarction therapy; however, broad acceptance is hindered by limited understanding of hMSC-human cardiomyocyte (hCM) interactions. To better understand the electrophysiological consequences of direct heterocellular connections between hMSCs and hCMs, three original mathematical models were developed, representing an experimentally verified triad of hMSC families with distinct functional ion channel currents. The arrhythmogenic risk of such direct electrical interactions in the setting of healthy adult myocardium was predicted by coupling and fusing these hMSC models to the published ten Tusscher midcardial hCM model. Substantial variations in action potential waveform—such as decreased action potential duration (APD) and plateau height—were found when hCMs were coupled to the two hMSC models expressing functional delayed rectifier-like human ether à-go-go K<sup>+</sup> channel 1 (hEAG1); the effects were exacerbated for fused hMSC-hCM hybrid cells. The third family of hMSCs (Type C), absent of hEAG1 activity, led to smaller single-cell action potential alterations during coupling and fusion, translating to longer tissue-level mean action potential wavelength. In a simulated 2-D monolayer of cardiac tissue, re-entry vulnerability with low (5%) hMSC insertion was approximately eight-fold lower with Type C hMSCs compared to hEAG1-functional hMSCs. A 20% decrease in APD dispersion by Type C hMSCs compared to hEAG1-active hMSCs supports the claim of reduced arrhythmogenic potential of this cell type with low hMSC insertion. However, at moderate (15%) and high (25%) hMSC insertion, the vulnerable window increased independent of hMSC type. In summary, this study provides novel electrophysiological models of hMSCs, predicts possible arrhythmogenic effects of hMSCs when directly coupled to healthy hCMs, and proposes that isolating a subset of hMSCs absent of hEAG1 activity may offer increased safety as a cell delivery cardiotherapy at low levels of hMSC-hCM coupling.

## **5.2 Author Summary**

Myocardial infarction—better known as a heart attack—strikes on average every 43 seconds in America. An emerging approach to treat myocardial infarction patients involves the delivery of human mesenchymal stem cells (hMSCs) to the damaged heart. While clinical trials of this therapeutic approach have yet to report adverse effects on heart electrical rhythm, such consequences have been implicated in simpler experimental systems and thus remain a concern. In this study, we utilized mathematical modeling to simulate electrical interactions arising from direct coupling between hMSCs and human heart cells to develop insight into the possible adverse effects of this therapeutic approach on human heart electrical activity, and to assess a novel strategy for reducing some potential risks of this therapy. We developed the first mathematical models of electrical activity of three families of hMSCs based on published experimental data, and integrated these with previously established mathematical models of human heart cell electrical activity. Our computer simulations demonstrated that one particular family of hMSCs minimized the disturbances in cardiac electrical activity both at the single-cell and tissue levels, suggesting that isolating this specific sub-population of hMSCs for myocardial delivery could potentially increase the safety of future hMSC-based heart therapies.

### **5.3 Introduction**

Ischemic heart disease, which results from reduced coronary flow of oxygenated blood, is a leading cause of myocardial infarction and heart failure. This insufficient oxygenation results in the death of cardiomyocytes, which are normally incapable of substantial regeneration. Therefore, despite tremendous advancements in pharmacological and interventional therapeutic approaches, ischemic heart disease continues to be responsible for nearly 1 out of 6 deaths in the United States.<sup>1,2</sup> This has motivated novel cardiotherapeutic strategies to repair and regenerate heart muscle, including human mesenchymal stem cell (hMSC) therapy, the method of interest in this study.

In clinical trials for treating myocardial infarction, the delivery of autologous bone marrow derived hMSCs has demonstrated improved ventricular ejection, enhanced angiogenesis, decreased fibrosis and scar size, and minimal immune response.<sup>3</sup> However, the benefits have often been modest and transient,<sup>4,5</sup> underscoring a need to better understand and exploit the underlying mechanisms by which hMSCs interact with human cardiomyocytes (hCMs).<sup>6</sup> This limited mechanistic knowledge further makes it difficult to ensure long-term stability, with seamless structural and functional integration into the host tissue.<sup>7-9</sup> Therefore, deeper investigation into the mechanisms of how hMSCs impact cardiac function is necessary.

Proposed hMSC-hCM interactions predominantly include: reprogramming of host hCMs, transdifferentiation of hMSCs into hCMs, paracrine signaling, electrophysiological coupling, and cellular fusion.<sup>6,10</sup> Indirect paracrine signaling through the release of largely unidentified soluble factors is thought to play an important role;<sup>6,11</sup> however, hMSCs have also exhibited functional direct electrical interactions with cardiomyocytes both in vitro and in vivo,<sup>10,12-17</sup> motivating ongoing investigations of the electrophysiological coupling and cellular fusion mechanisms. In particular, Valiunas et al. showed that hMSCs form connexin 43-mediated gap junctions between each other and with acutely isolated canine cardiomyocytes, suggesting the ability to form heterocellular electrical networks.<sup>15</sup> Later in vitro studies showed that such electrical

connections can be functional and potentially arrhythmogenic, as co-culturing murine cardiomyocytes with greater than 10 percent of hMSCs decreased conduction velocity (CV) and predisposed re-entrant arrhythmias.<sup>16</sup> Pro-arrhythmic characteristics were also detected *in vivo*, where pigs receiving intravenous injections of mesenchymal stem cells had decreased effective refractory periods.<sup>17</sup> Moreover, Shadrin et al. recently reported a 25–40% incidence of hybrid cell formation of hMSCs and neonatal rat ventricular myocytes through cell fusion.<sup>10</sup> However, species-specific effects can limit the clinical relevance of such animal and *in vitro* studies, and similarly controlled experiments are difficult to perform in human patients. While hMSC therapy clinical trials are yet to report arrhythmogenicity,<sup>18</sup> such adverse effects remain a concern. Therefore, in this study, it was of interest to assess the electrophysiological safety of various levels of direct hMSC-hCM electrical interactions under healthy conditions,<sup>18</sup> and to predict methods of improving the safety of this therapy.

Mathematical modeling is a powerful tool that can simulate direct intercellular electrical interactions between hMSCs and hCMs. Electrophysiological models have been established to describe hCMs,<sup>19-21</sup> as well as their interactions with other resident heart cells,<sup>22-25</sup> but never before with hMSCs. Therefore, in this study, the various types of currents experimentally characterized in hMSCs<sup>26-29</sup> were mathematically modeled to simulate an empirically classified triad of hMSC families distinguished by their respective functional ion channels: Type A) delayed rectifier-like hEAG1 and calcium activated potassium currents; Type B) delayed rectifier-like hEAG1, calcium activated potassium, tetrodotoxin (TTX)-sensitive sodium, and L-type calcium currents; and Type C) calcium activated potassium and transient outward currents.<sup>26,28</sup> The empirical distinction of these three hMSC families was originally reported by Li et al.<sup>26</sup> based on patch clamp measurements of bone marrow-derived hMSCs obtained commercially and maintained in monolayer culture. We then simulated the electrical activity of hMSCs coupled to healthy hCMs, and interpreted the model findings within the context of prior

in vitro and in vivo experiments to identify possible opportunities to minimize arrhythmic potential in future hMSC-based cell delivery cardiotherapies.

## 5.4 Methods

### 5.4.1 hMSC Model Development

The hMSC transmembrane voltage can be modeled as:

$$\frac{dV}{dt} = -\frac{1}{C_m}(I_{stim} + I_{tot,i}) \quad (1)$$

where  $V$  is voltage,  $t$  is time,  $C_m$  is the cell capacitance,  $I_{stim}$  is a stimulus current, and  $I_{tot,i}$  is the total transmembrane ionic current of Type  $i$  hMSCs (where  $i = A, B, \text{ or } C$ ). The total transmembrane ionic current for Types A, B, and C hMSCs are given by Equations 2, 3, and 4, respectively:

$$I_{tot,A} = I_{KCa} + I_{dr} + I_{L,A} \quad (2)$$

$$I_{tot,B} = I_{KCa} + I_{dr} + I_{LCa} + I_{Na} + I_{L,B} \quad (3)$$

$$I_{tot,C} = I_{KCa} + I_{to} + I_{L,C} \quad (4)$$

where  $I_{KCa}$  is the calcium activated potassium current,  $I_{dr}$  is the delayed rectifier-like hEAG1 current,  $I_{L,i}$  is the leakage current for hMSC Type  $i$  (where  $i = A, B, \text{ or } C$ ),  $I_{LCa}$  is the L-type calcium current,  $I_{Na}$  is the TTX-sensitive sodium current, and  $I_{to}$  is the transient outward current.

### 5.4.2 Modeling hMSC Ionic Currents

To describe each type of hMSC ionic current, either Hodgkin-Huxley-like or Markovian-like approaches were taken. Parameters for these models were fit to published experimental hMSC data using numerical methods described in Supplementary Text. Parameters used in this study can be found in Tables A-G of Supplementary Text.

#### 5.4.3 Calcium activated potassium channel current.

To describe hMSC  $I_{\text{KCa}}$  encoded by the KCNMA1 gene,<sup>26</sup> we modified the Gerstner et al.<sup>30</sup> persistent model, such that:

$$I_{\text{KCa}} = G_{\text{KCa}}x(V - E_K) \quad (5)$$

where  $G_{\text{KCa}}$  is the maximum conductance of the channel,  $V$  is the membrane potential,  $E_K$  is the potassium Nernst potential, and  $x$  is an activation variable. The voltage- and intracellular calcium concentration-dependent activation kinetics of  $I_{\text{KCa}}$  described by Gerstner et al.<sup>30</sup> was simplified by assuming constant intracellular calcium concentration. The activation parameters in this model were fit to values derived from hMSC  $I_{\text{KCa}}$  experimental data reported by Li et al.<sup>26</sup> Figure 1A shows the simulated steady-state current-voltage ( $I$ - $V$ ) relationship together with mean experimental data. A simulation of a 300 ms voltage clamp experiment is shown in Figure 1B (voltage clamp protocol inset), demonstrating the time-dependent behavior of this current. Figure S1 shows the steady-state activation and time constant curves used in the model with corresponding values derived from experimental data.<sup>26</sup> The resulting formulas and fitted model parameters to fully describe  $I_{\text{KCa}}$  are shown in Table B of Supplementary Text.

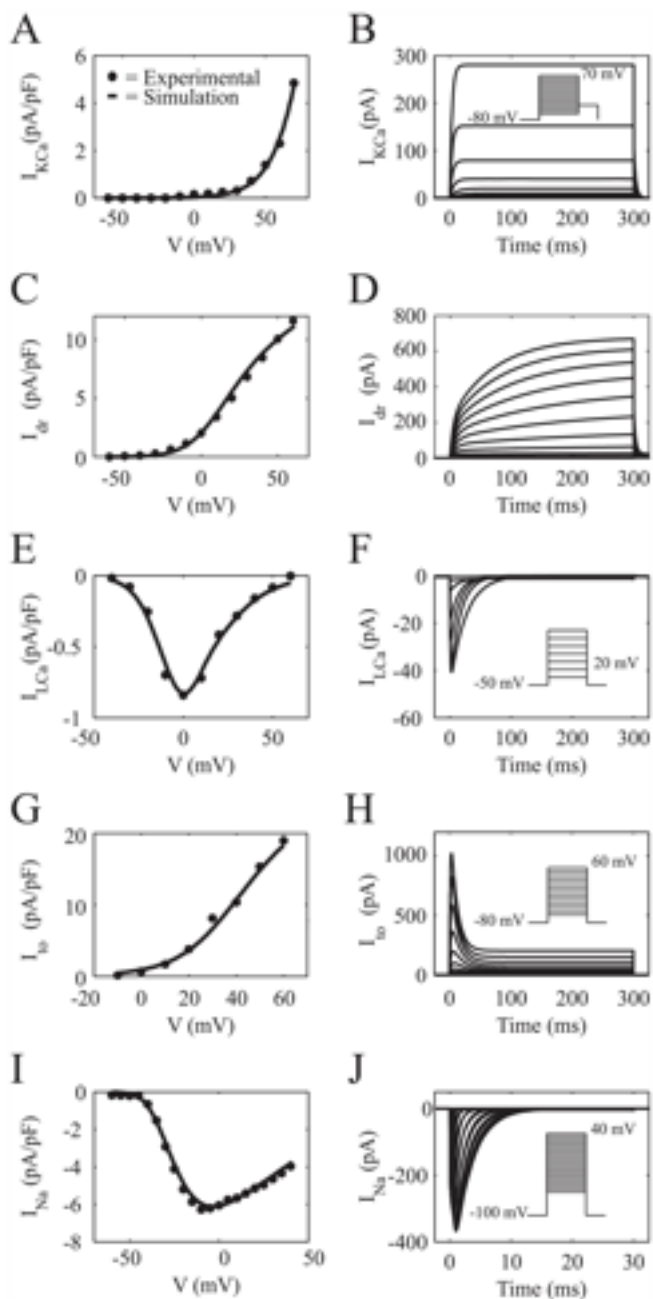


**Figure 1:  $I$ - $V$  and Voltage Clamp Simulations of hMSC Currents.** Comparison of experimental and fitted  $I$ - $V$  curves for hMSC channels, and the resulting voltage clamp simulations. (A) Fitted  $I$ - $V$  curve for  $I_{KCa}$  together with mean experimental data from Li et al.<sup>26</sup> (B) Simulated voltage clamp experiment of  $I_{KCa}$  (voltage step protocol inset). (C) Theoretical  $I$ - $V$  curve for  $I_{dr}$  and its fit to mean experimental data.<sup>26</sup> (D) In silico voltage clamp experiment of  $I_{dr}$  (voltage step protocol shown in inset of Figure 3C). (E) A comparison of fitted theoretical and

mean experimental *I*-*V* curve data<sup>26</sup> for  $I_{LCa}$ . (**F**) Voltage clamp simulation for  $I_{LCa}$  (voltage step protocol inset). Comparisons between fitted theoretical and experimental *I*-*V* data<sup>26</sup> for  $I_{to}$  and  $I_{Na}$  are shown in (**G**) and (**I**), respectively. Voltage clamp simulations for  $I_{to}$  and  $I_{Na}$  are shown in (**H**) and (**J**), respectively (voltage step protocols inset).

#### 5.4.4 Delayed rectifier potassium channel current

The hMSC  $I_{dr}$  encoded by the hEAG1 gene<sup>26</sup> is also persistent. Interestingly, one of its sub-families, the hEAG-related gene,<sup>31</sup> is responsible for the rapid repolarization of the cardiac action potential.<sup>32</sup> To model this channel, we modified Silverman's two voltage-sensor transition model (Figure 2),<sup>33,34</sup> with one closed state (C1), one intermediate state (C2), and one open state ( $y$ ):

$$\frac{dC_1}{dt} = \delta C_2 - \gamma C_1 \quad (6)$$

$$\frac{dC_2}{dt} = \gamma C_1 + \beta y - (\alpha + \delta) C_2 \quad (7)$$

$$\frac{dy}{dt} = \alpha C_2 - \beta y \quad (8)$$

where  $\alpha$ ,  $\beta$ ,  $\gamma$ , and  $\delta$  are voltage-dependent rate functions. The resulting  $I_{dr}$  model is:

$$I_{dr} = G_{dr}y(V - E_k) \quad (9)$$

where  $G_{dr}$  is the maximum conductance of the channel,  $y$  is the activation variable, and  $E_k$  is the potassium Nernst potential. The activation parameters in this model were fit to values derived from experimental hMSC  $I_{dr}$  data from Li et al.<sup>26</sup> The fitted *I*-*V* relationship and the corresponding mean experimental data are shown in Figure 1C. A simulation of a 300 ms voltage clamp experiment is shown in Figure 1D (voltage clamp protocol shown in Figure 3C inset), providing insight into the transient behavior of this current. Figure S2 shows the steady-state activation

curve and time constant curves, in agreement with empirical results by Li et al.<sup>26</sup> The resulting formulas and fitted model parameters to fully describe  $I_{dr}$  are shown in Table C of S1 Text.

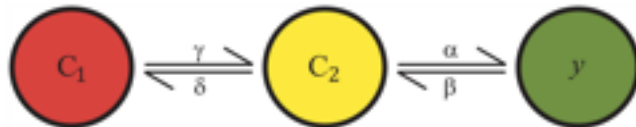


**Figure 2: Voltage-Sensor Transition Model for the Delayed Rectifier Current.** To model  $I_{dr}$ , a modified version of Silverman's two voltage-sensor transition Markovian-like model<sup>33,34</sup> was used. As shown, there is one closed state ( $C_1$ ), one intermediate state ( $C_2$ ), and one open state ( $y$ ). Each state has its own voltage-dependent rate functions (i.e.,  $\alpha$ ,  $\beta$ ,  $\gamma$ , and  $\delta$ ).

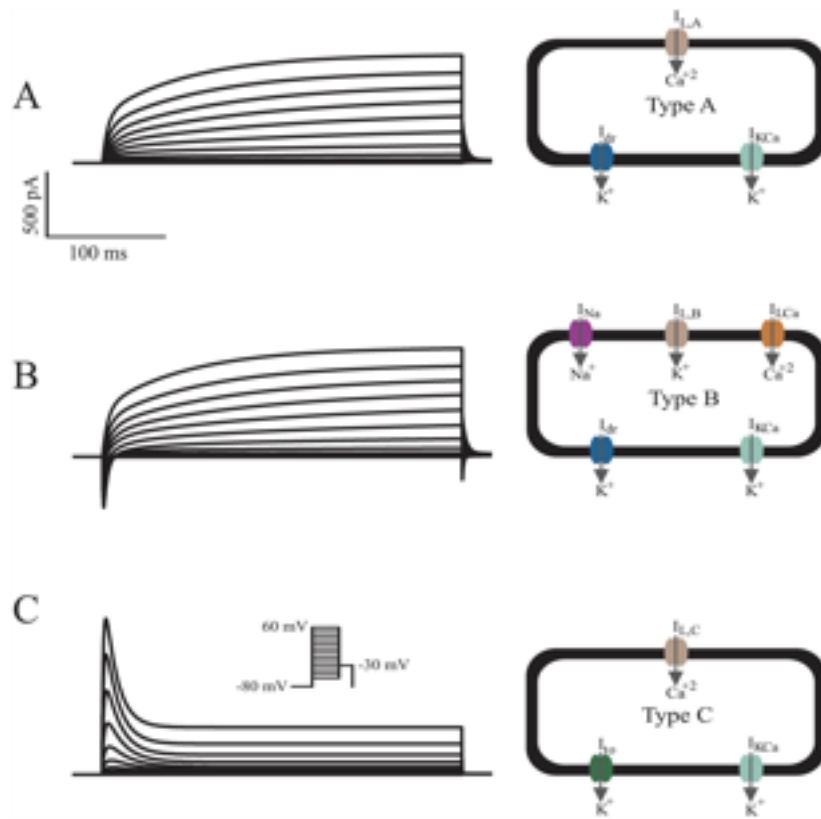


**Figure 3: Total Current Simulations of the Triad of hMSC Families.** The whole-cell models developed in this study were validated by simulating  $I_{tot,A}$ ,  $I_{tot,B}$ , and  $I_{tot,C}$ , as shown in (A), (B), and (C), respectively. Schematics of functional currents for each cell type are shown to the right

of each simulation. The voltage protocol for each cell type is inset in (C). The simulations generally agree with the magnitude and behavior of representative experimental data,<sup>26</sup> and thus were used to predict the direct electrical interactions between hMSCs and hCMs.

#### 5.4.5 *L*-type calcium current

The hMSC  $I_{LCa}$  encoded by the CACNA1C gene<sup>26</sup> is also found with hCMs, where it is responsible for the plateau phase of the cardiac action potential. The driving force of  $I_{LCa}$  was described by the Goldman-Hodgkin-Katz equation<sup>35</sup> to account for the large Ca+2concentration gradient across the cell membrane.<sup>30,36</sup> Therefore,  $I_{LCa}$  was defined as:

$$I_{LCa} = G_{LCa}df4 \frac{VF^2}{RT} \frac{[Ca_i^{+2}]e^{2VF/RT} - \phi[Ca_o^{+2}]}{e^{2VF/RT} - 1} \quad (10)$$

where  $G_{LCa}$  is the maximum conductance,  $F$  is Faraday's constant,  $\phi$  is the partition coefficient, and  $d$  and  $f$  are activation and inactivation gate variables, respectively. The Goldman-Hodgkin-Katz equation was simplified in this study by assuming constant intracellular and extracellular calcium concentrations. Each gate is described by Hodgkin-Huxley-type differential equations.<sup>37</sup> Both steady-state  $d$  and  $f$  functions, as well as their respective time constants, were fit to values derived from experimental hMSC  $I_{LCa}$  data from Li et al.<sup>26</sup> The fitted peak  $I$ - $V$  relationship is in agreement with mean experimental data, as shown in Figure 1E. A simulation of a 300 ms voltage clamp experiment is shown in Figure 1F (voltage clamp protocol inset), demonstrating the transient behavior of this current. Figure S3 shows the steady-state activation curve, steady-state inactivation curve, and the time constants used in the model together with values derived from experimental data.<sup>26</sup> The resulting formulas and fitted model parameters to fully describe  $I_{LCa}$  are shown in Table D of Supplementary Text.

#### 5.4.6 Transient outward potassium channel current

Similar to the transient outward current of human atrial myocytes and Purkinje fiber cells,<sup>38,39</sup> the hMSC ( $I_{\text{to}}$ ) encoded by Kv4.2 and Kv1.4 genes displays both ephemeral and sustained currents [26]. Transient outward current is also found with hCMs, where it contributes to the notch of the cardiac action potential. To account for both the transient and sustained currents within the hMSC model, a modified version of the Nygren et al. model<sup>40</sup> was used:

$$I_{\text{to}} = G_{\text{to}}r_s(V - E_K) + G_{\text{to,sus}}r_{\text{sus}}(V - E_K) \quad (11)$$

where  $G_{\text{to}}$  and  $G_{\text{to,sus}}$  are the maximum conductances of the transient and sustained portions of the channel, respectively.  $r$  and  $s$  are activation and inactivation variables of the transient behavior, respectively, and  $r_{\text{sus}}$  is the activation variable of the sustained behavior. Each gate is described by Hodgkin-Huxley-type equations.<sup>37</sup> Steady-state functions and their respective time constants were fit to values derived from experimental hMSC  $I_{\text{to}}$  data from Li et al.<sup>26</sup> The fitted peak  $I$ - $V$  relationship is in agreement with experimental data, as shown in Figure 1G. A simulation of a 300 ms voltage clamp experiment is shown in Figure 1H (voltage clamp protocol inset), demonstrating the transient behavior of this current. Figure S4 shows the steady-state activation curves ( $r_{\infty}$  and  $r_{\text{sus}}$ ), the steady-state inactivation curve, and the time constants used in the model together with values derived from experimental data.<sup>26</sup> The fitted formulas to fully describe  $I_{\text{to}}$  are shown in Table E of Supplementary Text.

#### 5.4.7 TTX-sensitive sodium channel current

A modified version of the Hodgkin-Huxley two gates formula<sup>30,37,41</sup> was used to describe the hMSC  $I_{\text{Na}}$  encoded by the hNE-Na gene,<sup>26</sup> such that:

$$I_{\text{Na}} = G_{\text{Na}}m^3h(V - E_{\text{Na}}) \quad (12)$$

where  $G_{\text{Na}}$  is the maximum sodium conductance,  $m$  is an activation gate,  $h$  is an inactivation gate, and  $E_{\text{Na}}$  is the sodium Nernst potential. Steady-state  $m$  and  $h$  functions, and their

respective time constants were fit to values derived from experimental hMSC  $I_{\text{Na}}$  data from Li et al.<sup>26</sup> The fitted peak  $I$ - $V$  relationship is compared to mean experimental data, as shown in Figure 1I. A simulation of a 30 ms voltage clamp experiment is shown in Figure 1J (voltage clamp protocol inset), demonstrating the transient behavior of this current. Figure S5 shows the steady-state activation curve, steady-state inactivation curve, and the time constants used in the model and its comparison to values derived from experimental data.<sup>26</sup> The fitted formulas to fully describe  $I_{\text{Na}}$  are shown in Table F of Supplementary Text.

#### *5.4.8 Leakage channel current*

The leakage channel current constitutes all ions crossing the cell membrane that are not accounted for,<sup>42</sup> using:

$$I_{\text{L},i} = G_{\text{L},i}(V - E_{\text{L},i}) \quad (13)$$

where  $I_{\text{L},i}$  is the leakage current for Type  $i$  hMSCs,  $G_{\text{L},i}$  is the conductance of the leakage channel for Type  $i$  hMSCs, and  $E_{\text{L},i}$  is the leakage reversal potential for Type  $i$  hMSC (where  $i = \text{A, B, or C}$ ). For each type of hMSC, different leakage conductance and reversal potential values were used to satisfy its resting membrane potential (RMP) at approximately -35 mV.<sup>9,26,27</sup> A simulation demonstrating the resting potential lies at -35 mV is shown in Figure S6. The formulas to describe the leakage currents are shown in Table G of Supplementary Text.

#### *5.4.9 Ion channel assumptions*

Most patch clamp studies are conducted at room temperature (21°C to 22°C).<sup>26,27</sup> The Nernst potential, which is dependent on temperature, was therefore extrapolated to normal body temperature (37°C, or 310 K). For the purposes of this study, it is also assumed the hMSC extracellular and intracellular sodium, potassium, and calcium concentrations are constant both

in hMSC-hCM coupling and fusion. Finally, it is assumed that no other ionic current plays a significant role in the electrical activity of hMSCs.

#### 5.4.10 hMSC-hCM Single-Cell Interactions

The hMSC models were coupled to the ten Tusscher endocardial, midcardial, and epicardial healthy hCM models of the ventricular action potential<sup>20</sup> using established cell-cell coupling equations:<sup>22</sup>

$$\frac{dV_{\text{hCM}}}{dt} = -\frac{1}{C_{m,\text{hCM}}} [I_{\text{tot,hCM}} + I_{\text{stim}} + I_{\text{gap,hCM}}] \quad (14)$$

$$\frac{dV_{\text{hMSC}}}{dt} = -\frac{1}{C_{m,\text{hMSC}}} [I_{\text{tot,hMSC}} + I_{\text{stim}} + I_{\text{gap,hMSC}}] \quad (15)$$

such that:

$$I_{\text{gap,hCM}} = f_{\text{hMSC}} G_{\text{gap}} (V_{\text{hCM}} - V_{\text{hMSC}}) \quad (16)$$

$$I_{\text{gap,hMSC}} = G_{\text{gap}} (V_{\text{hMSC}} - V_{\text{hCM}}) \quad (17)$$

and:

$$f_{\text{hMSC}} = \frac{\%_{\text{hMSC}}}{100 - \%_{\text{hMSC}}} \quad (18)$$

where  $I_{\text{gap}}$  is the gap junction current between hMSCs and hCMs,  $G_{\text{gap}}$  is the gap junction conductance, % hMSC is the percentage of hMSCs in a homogeneously distributed hMSC-hCM population, and  $V_j$ ,  $C_{m,j}$ , and  $I_{\text{tot},j}$  are the voltage, capacitance, and total current of cell type  $j$  (where  $j = \text{hCM}$  or  $\text{hMSC}$ ), respectively. The single-cell coupling simulations were performed in a homogeneously distributed hMSC-hCM population ranging from 0% (control) to 80% hMSCs, with basic cycle lengths of 1000 ms. Simulations were run until steady-state was achieved. The characteristics of interest, action potential duration (APD) and plateau height ( $V_{APD/2}$ ), were defined as time to 90% repolarization and  $V(t = APD/2)$ , respectively. All

simulations were written in MATLAB (The MathWorks, Natick MA) and numerically integrated using a stiff ordinary differential equation solver (ode15s).

#### *5.4.11 Modeling passive hMSC-hCM coupling*

To model passive hMSCs and their effects on hCMs,  $I_{\text{tot,hMSC}}$  was set equal to zero in Equation 15.

#### *5.4.12 Modeling hMSC-hCM fusion*

The hMSC models were fused to the midcardial ten Tusscher healthy hCM electrophysiological models by combining respective  $I_{\text{tot}}$  and  $C_m$  terms, such that:

$$\frac{dV_{\text{fused}}}{dt} = -\frac{1}{C_{m,\text{hCM}} + f_{\text{hMSC}} C_{m,\text{hMSC}}} [I_{\text{tot,hCM}} + f_{\text{hMSC}} I_{\text{tot,hMSC}} + I_{\text{stim}}] \quad (19)$$

where  $V_{\text{fused}}$  is the voltage of the fused cell. To validate this method of modeling cell fusion, we compared our simulations results to the limiting case of cell coupling where  $G_{\text{gap}} \rightarrow \infty$ , which should theoretically converge to the same answer. This was confirmed in Figure S7 APD restitution curve protocol.

A standard S1–S2 APD restitution protocol<sup>20</sup> was performed at the single-cell level on hCMs with 0% hMSC coupling (control), as well as low (5%), moderate (15%), and high (25%) percentages of coupled hMSCs. Briefly, 10 S1 stimuli were applied at a basic cycle length of 600 ms, followed by a single S2 stimulus at a certain diastolic interval (DI) after the last action potential generated.

#### *5.4.13 Modeling hMSC-hCM Coupling at the Tissue Level*

##### *5.4.13.1 Two dimensional cardiac tissue sheet configuration*

For the vulnerable window (VW) analysis, a single layer tissue model was used, composed of hCMs and hMSCs. Specifically, a 5 cm × 5 cm two-dimensional midcardial cardiac

tissue sheet was simulated, with randomly inserted hMSCs comprising either 0%, 5%, 15%, or 25% of the total cell population (Figure S8). Three random configurations (i.e.,  $n = 3$ ) were tested for each percentage of hMSC insertion; the mean and standard deviation of VW are reported. A schematic summarizing the geometry, mesh size, and key node characteristics is shown in Figure S8. Each node executed either the midcardial hCM model membrane kinetics<sup>20</sup> or the selected hMSC membrane kinetics, such that:

$$\frac{\partial V}{\partial t} = -\frac{I_{\text{tot},k} + I_{\text{stim}}}{C_{m,k}} + D_{k,x} \frac{\partial^2 V}{\partial x^2} + D_{k,y} \frac{\partial^2 V}{\partial y^2} \quad (20)$$

for:

$$D_{k,x} = \frac{1}{\rho_{k,x} S_{k,x} C'_{m,k}} \quad (21)$$

where  $C'_{m,k}$  is the cell capacitance per unit surface area of cell type  $k$ ,  $S_{k,x}$  is the surface-to-volume ratio of cell type  $k$  in the  $x$  direction, and  $\rho_{k,x}$  is the effective cellular resistivity of cell type  $k$  in the  $x$  direction (where  $k = \text{hCM}$  or  $\text{hMSC}$ ).

Midcardial hCM electrical activity was simulated with the ten Tusscher midcardial model,<sup>20</sup> while hMSC electrical activity was simulated with the models herein. Euclidian geometry was selected, with  $\Delta x = \Delta y = 0.01$  cm, and  $\Delta t = 0.01$  ms. Neumann-type boundary conditions were implemented to solve the partial differential equations. As performed elsewhere,<sup>43</sup> anisotropy was modeled as  $D_{k,x} = 4D_{k,y}$ . Relevant parameters for the development of these simulations can be found in Table A of Supplementary Text. All tissue simulations were written and executed in Python.

#### 5.4.13.2 Stimulation protocol and vulnerable window assessment

A cross-field stimulation protocol was applied, as described elsewhere.<sup>43,44</sup> Briefly, after achieving steady-state conditions, two S1 stimuli were applied at the left end of the tissue with a basic cycle length of 1000 ms. An S2 stimulation was applied 300–500 ms after the second S1

stimulus, at 1 ms increments, at the bottom left corner of the tissue (1.25 cm wide × 2.5 cm high). For each tissue model, the VW was defined as the range of S1–S2 intervals that led to at least one spiral wave rotation.

#### *5.4.13.3 APD dispersion analysis*

A modified version of an established APD dispersion analysis<sup>45</sup> was used on the 5 cm × 5 cm two-dimensional midcardial cardiac tissue sheets described above. APD was calculated after the second S1 stimulus, with a basic cycle length of 1000 ms. APD dispersion,  $\zeta$ , was defined as:

$$\zeta = \sqrt{\frac{1}{N} \sum_{i=1}^N (APD_i - \overline{APD})^2} \quad (22)$$

where  $i$  is an hCM grid point,  $N$  is the total number of hCM grid points, and  $\overline{APD}$  is the mean APD of hCMs in the tissue. Mean and standard deviation of APD dispersion of three random tissue sheet configurations ( $n = 3$ ) are reported for each type of hMSC inserted at 5%, 15%, and 25% of the total cell population.

#### *5.4.13.4 Conduction velocity restitution curve protocol*

A standard S1–S2 CV restitution protocol<sup>20</sup> was simulated for a 1 cm × 1 cm two-dimensional midcardial cardiac tissue monolayer with properties analogous to the larger 5 cm × 5 cm tissue models described above. Briefly, two S1 stimuli were applied at varying DIs, and resultant CVs were measured after the second S1 stimulus. CV was measured in the x direction along each row of tissue nodes; mean and standard deviation of CV across the 100 rows is reported.

#### *5.4.14 Sensitivity Analysis*

To quantify the impact of each hMSC parameter on the hCM APD, an established multivariable regression analysis was performed.<sup>46,47</sup> In 300 trials for each hMSC model, we randomly varied hMSC maximum conductance parameters and time constant parameters by a log-normally distributed pseudorandom scale factor with a standard deviation of 10%, as described elsewhere.<sup>48</sup> hMSCs were coupled to midcardial hCMs in a 1:1 ratio in this analysis. From the changes in the model APD outputs (**Y**) and parameters (**X**), a linear approximation can be made to find the normalized parameter sensitivity vector (**B**), such that  $\mathbf{Y} \approx \mathbf{XB}$ . Therefore, a positive or negative sign of B (i.e., an element of **B**) indicates a positive or negative correlation between the parameter of interest and APD, respectively. Furthermore, the magnitude of B indicates the sensitivity of the APD to the parameter of interest. To better demonstrate the sensitivity of the APD output to each hMSC cell type, **B** was scaled by  $\sigma_{APD}$ , the standard deviation of the APDs for each set of 300 trials for a respective hMSC cell type.

## 5.5 Results

In this study, three hMSC electrophysiology models were developed based on published experimental data. These three models were subsequently used to develop insight into hMSC-hCM electrical interactions.

### 5.5.1 hMSC Electrophysiology Model

Three novel electrophysiological models were developed for the triad of hMSC families based on empirical data.<sup>26</sup> After successfully modeling each type of current expressed in hMSCs (Figure 1), it was necessary to validate the whole-cell models by simulating  $I_{tot,A}$ ,  $I_{tot,B}$ , and  $I_{tot,C}$ . Total current whole-cell voltage-clamp simulations of Types A, B, and C hMSCs are shown in Figure 3, along with schematics of functional currents for each cell type.<sup>26</sup> Like experimental recordings,<sup>26</sup> our simulation had a conditioning potential of -80 mV, followed by 10 mV voltage steps for 300 ms between -60 mV and 60 mV, and a final holding potential of -30

mV. Overall, fitting individual currents (Figure 1) allowed for ample reconstruction of representative whole cell electrical activity. The simulations for Types A and B hMSCs, both of which possess delayed rectifier-like channel activity, generally agree with the magnitude and behavior of experimental total currents for a wide range of voltage contours.<sup>26</sup> As demonstrated by Li et al.,  $I_{dr}$  at a potential of 60 mV has a standard deviation of approximately 90 pA, and the activation time constant for  $I_{dr}$  at a holding potential of -80 mV has a substantial standard deviation of approximately 25 ms.<sup>26</sup> Since these deviations affect the amplitude and activation kinetics of Types A and B hMSCs, we performed a sensitivity analysis to determine the impact of these parameters on hCM APD (see Sensitivity Analysis below for details). Type C hMSCs, absent of functional hEAG1 expression, also reproduced the magnitude and form of the experimental voltage-clamp experiments characterizing this hMSC family's electrophysiological behavior.<sup>26</sup> Therefore, we used each of these hMSC models to predict the direct electrical interactions between hMSCs and hCMs.

### *5.5.2 Simulations of hCM-hMSC Coupling and Fusion*

The three models developed in this study were each coupled and fused to hCMs to better understand direct cell-cell electrical interactions during hMSC cardiotherapies.

### *5.5.3 Cell coupling and fusion effects on action potential waveform.*

Figure 4 shows the qualitative effects of coupling and fusing midcardial myocytes to each type of hMSC model in 1:1 hMSC-hCM populations (i.e., 50% hMSCs). Types A and B hMSCs expressing functional hEAG1 noticeably shortened the plateau phase, initiated repolarization sooner, and thus distinctively decreased APD when coupling 1:1 with hCMs (Figure 4A and 4B, respectively). Fusing hCMs with Types A and B hMSCs exacerbated APD shortening and lowered the phase 2 plateau voltage compared to the hCM-only control, demonstrating the capability for these mesenchymal cell types to act as major electrical sinks.

These effects were evident predominantly during phase 3 of the cardiac action potential, where  $I_{K1}$ ,  $I_{Kr}$ , and  $I_{Ks}$  are most influential (Figure S9). By contrast, Type C hMSCs absent of delayed rectifier-like hEAG1 currents caused minimal disturbance of the hCM action potential, whether coupled or fused at the 1:1 cell ratio (Figure 4C). To develop an empirically-relevant representation of the impact of hMSCs on APD, a mixed population of hMSCs based on their approximate prevalence<sup>26</sup> was coupled 1:1 to hCMs. As shown in Figure 4D, the mixed population of hMSCs demonstrated similar effects as Types A and B hMSCs. This suggests the relatively benign effects of Type C hMSCs on hCM electrophysiology may be obscured in practice by the other more prevalent hMSC cell types, as only about 8% of hMSCs were characterized as Type C in vitro.<sup>26</sup> Similar trends were evident for coupling between hMSCs and either endocardial or epicardial myocytes, where Type C hMSCs resulted in the least deviation in action potential waveform from the hCM-only control condition (Figures S10 and S11, respectively).

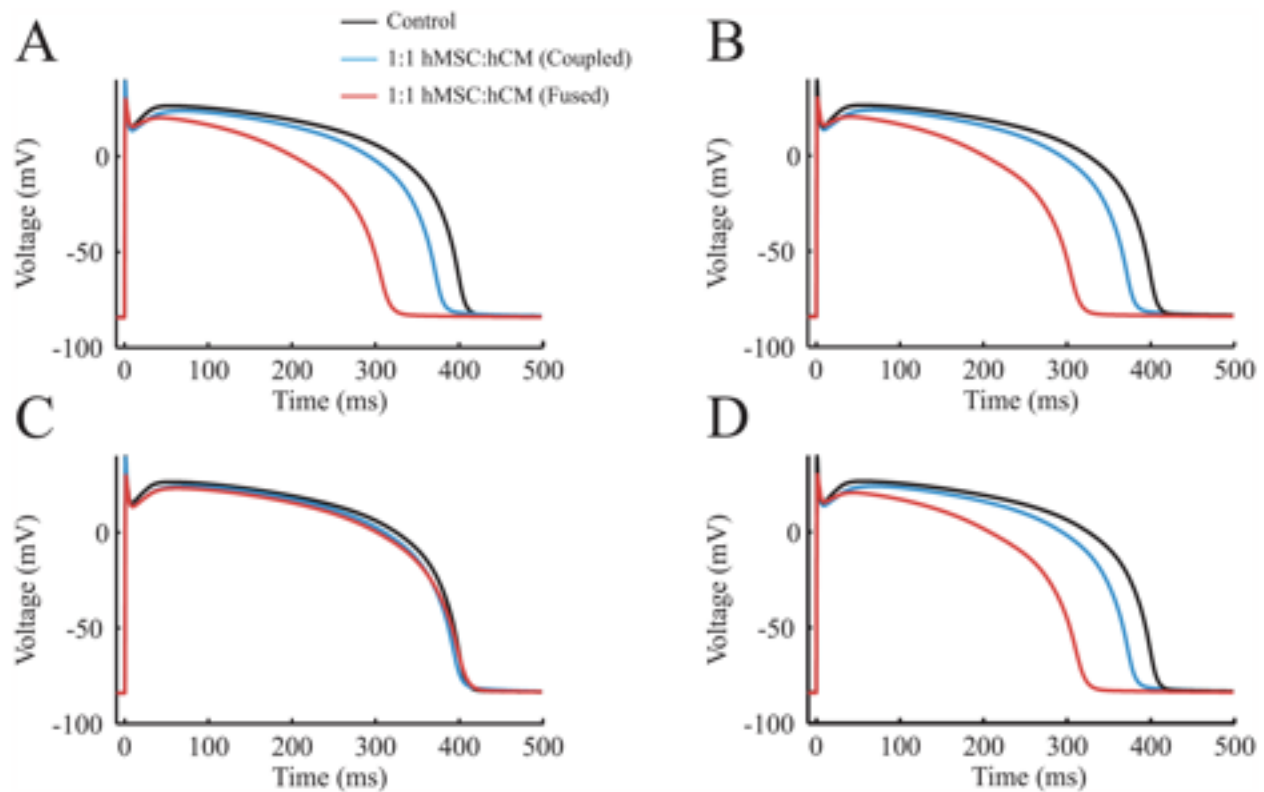


**Figure 4: Effects of Direct hMSC-hCM Electrophysiological Interactions on hCM Action**

**Potential.** The three hMSC models developed in this study were coupled or fused to midcardial hCM electrophysiological models at a 1:1 cell ratio. **(A)** Type A hMSCs coupled and fused to hCMs resulted in a decrease in hCM APD. **(B)** Type B hMSCs coupled and fused to hCMs resulted in a similar effect. **(C)** Type C hMSCs, absent of delayed rectifier-like hEAG1 channel activity, had a noticeably smaller effect on hCM action potential. **(D)** A mixed population of hMSCs (i.e., Types A, B, and C hMSCs weighted based on the approximate prevalence of 63%, 29%, and 8% in vitro, respectively<sup>26</sup>) coupled and fused to hCMs resulted in a similar effect as Types A and B hMSCs, because only a small portion of hMSCs are Type C.<sup>26</sup>

To more clearly demonstrate how the type of hMSC dictates effects on hCM action potential waveform, we quantified the effects of different percentages of hMSCs in a homogeneously distributed hMSC-hCM population in terms of APD,  $V_{APD/2}$ , and RMP (Figure 5).

As previously observed, coupling hCMs with Type A and B hMSCs with functional delayed rectifier-like hEAG1 channels results in larger deviations in APD compared to Type C hMSCs (Figure 5A, left). Coupling Types A and B hMSCs to hCMs 1:1 (i.e., hMSCs are 50% of the total cell population) decreases midcardial APD by greater than 26 ms, compared to less than 6 ms for Type C hMSCs absent of delayed rectifier-like hEAG1 activity (Figure 5A, left). The effects of Types A and B hMSCs on single hCM APD were exacerbated by cellular fusion (Figure 5A, right). These trends were also evident with action potential plateau height (Figure 5B). By contrast, RMP changed by less than 1 mV in both cellular coupling and fusion conditions (Figure 5C), independent of the hMSC type. In general, it is evident that Type C hMSCs counterbalance the potential passive and electrical sinking natures of hMSCs. This unique cell type consistently results in the least deviation from the action potential of control hCMs. These observations motivated further exploration of why Type C hMSCs act differently, and the interplay between passivity and electrical sinking.

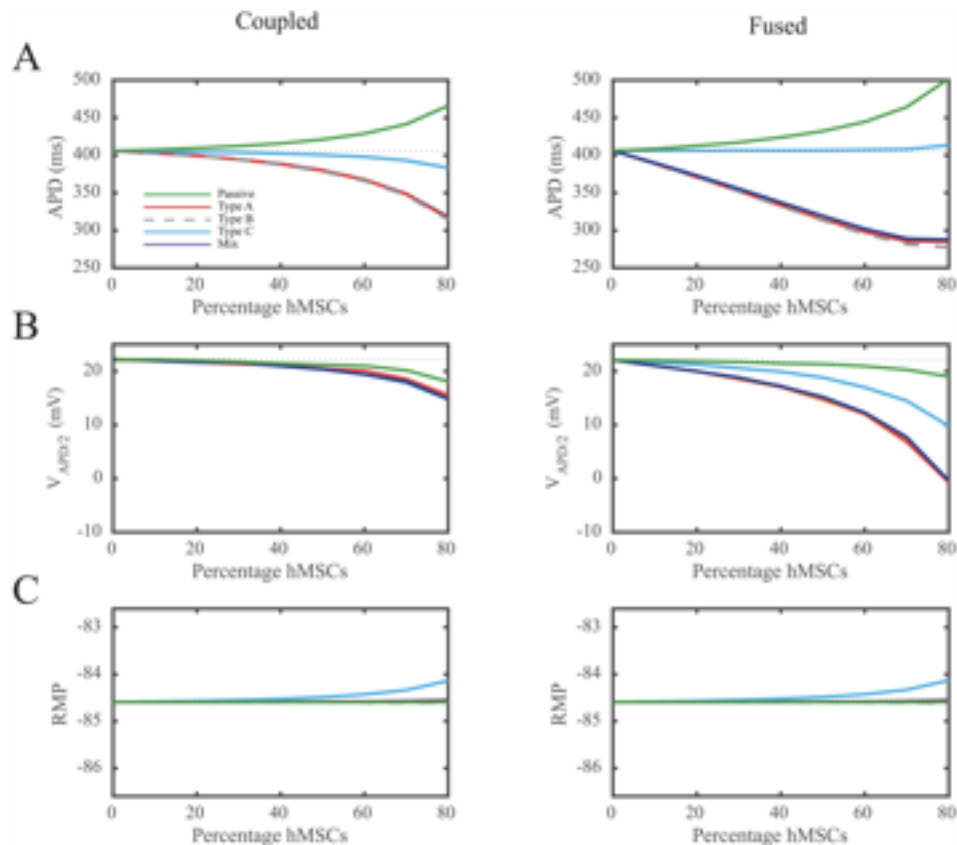


**Figure 5: Quantification of hCM Action Potential Waveform Following Direct hMSC-hCM Electrical Interactions.** To further explore the effects of each family of hMSC, we quantified the relationship between (A) APD, (B)  $V_{APD/2}$ , (C) RMP, and the percentage of coupled (left panel) or fused (right panel) hMSCs in a homogeneously distributed hMSC-hCM population. hMSCs were coupled or fused to midcardial hCMs in an hMSC-hCM population ranging from 0% (control) to 80% hMSCs at 10% increments. These effects were compared to hCMs coupled to a passive R-C circuit-like hMSC cell. In general, Type C hMSCs resulted in the least variation in hCM APD and  $V_{APD/2}$ . The dotted lines represent the control condition of hCMs with no hMSC coupling or fusion.

hMSCs were coupled to midcardial hCMs in a 1:1 ratio to further study the overall electrical source and sink behavior of each type of hMSC and its role in altering hCM action potentials (Figure 6A). In this configuration, we examined the dependence of hMSC membrane potential and gap current (Figure 6B and 6C, respectively) on the hMSC type, which ultimately influences the hCM action potential. As shown in Figure 6B, the membrane potential of types A and B hMSCs were lower than both type C and passive hMSCs throughout an action potential. As a result, they demonstrated a larger sinking gap current than hMSCs absent of delayed rectifier current activity throughout phase 2 of the action potential, leading to shortened hCM APDs. Type C hMSCs had a membrane potential that was intermediate between passive and delayed rectifier-acting hMSCs (Figure 6B), corresponding to a favorable gap current (Figure 6C) and minimal effects on the coupled hCM APD. In general, lower hMSC membrane potentials led to larger sinking effects and therefore shorter APDs. To identify the culprits of lower hMSC membrane potentials and thus larger sinking effects, we further examined outward currents of each hMSC cell type.

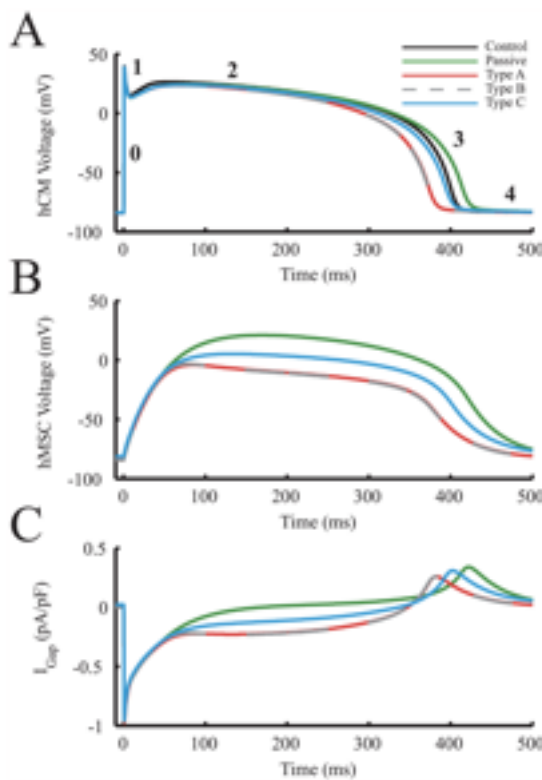


**Figure 6: hMSCs Act as Electrical Sources and Sinks in hCM APD Variations.** hMSCs were coupled to midcardial hCMs in a 1:1 ratio to examine how hMSC membrane potential and gap current affected the hCM action potential. **(A)** Effects of coupling each type of hMSC on hCM action potentials, compared to hCM-only control. Phases 1 through 4 of the cardiac action potential are labeled for reference. **(B)** hMSC transmembrane voltage throughout an hCM action potential. **(C)** The resulting gap currents between hMSCs and hCMs due to differences in voltage between cell types.  $I_{\text{Gap}}$  was defined as current flowing from the hMSC to the hCM (i.e.,  $I_{\text{Gap,hCM}}$ ).

The main hMSC outward currents potentially triggering an earlier initiation of phases 3 and 4 of hCM action potentials were examined in the same 1:1 hMSC:hCM ratio (Figure 7). Specifically,  $I_{\text{KCa}}$ ,  $I_{\text{dr}}$ , and  $I_{\text{to}}$  were examined (Figure 7A, 7B and 7C, respectively). During an hCM action potential, the delayed-rectifier like current of Types A and B hMSCs had the highest outward current magnitude and area under the curve; this resulted in the largest electrical sinking effects by restraining the depolarization of hMSCs in synchrony with hCMs. The peak

hEAG1 current ( $I_{dr}$ ) was two-fold greater than the maximum magnitude of  $I_{to}$ , and nearly twenty-fold greater than the maximum magnitude of  $I_{KCa}$ . The greater net outward current of Types A and B hMSCs resists these hMSCs from approaching the transmembrane voltage of hCMs, thus resulting in an overall larger sinking effect. To confirm the substantial role of hEAG1 outward currents in shortening APD, a quantitative sensitivity analysis was performed.

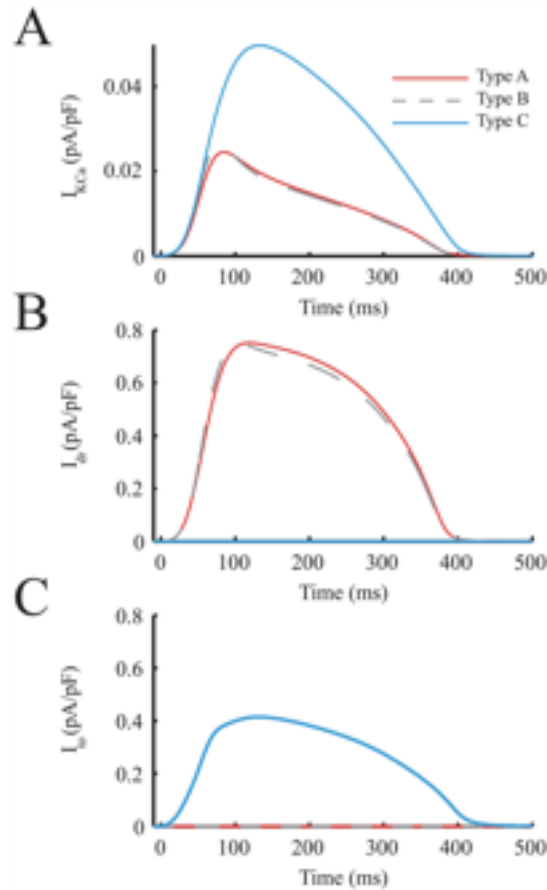


**Figure 7: Key hMSC Outward Currents Involved in Electrical Sinking.** The main hMSC outward currents involved in a faster initiation of phases 3 and 4 of hCM action potentials were examined. The hMSC currents analyzed were: (A)  $I_{KCa}$ , (B)  $I_{dr}$ , and (C)  $I_{to}$ . During an hCM action potential,  $I_{dr}$  had the largest magnitude and area under the curve, which resulted in the greatest electrical sink effects.

#### 5.5.4 Sensitivity analysis

A sensitivity analysis was performed for Types A, B, and C hMSCs in 1:1 ratios with midcardial hCMs to confirm the role of hEAG1 currents, and to develop insight into how sensitive hCM action potentials are to direct hMSC-hCM coupling (Figure 8). Coefficients of determination of 0.99, 0.99, and 0.98 (for Types A, B, and C hMSCs, respectively) demonstrate the accuracy of using these linear approximations to develop a relationship between input parameters and output APD. hCM APD was negatively correlated and highly sensitive to Types A and B hMSC  $G_{\text{junction}}$ , verifying the large sinking effects of these cell types (Figure 8A and 8B). This sensitivity was amplified by a negative correlation with  $G_{\text{dr}}$  and its activating parameters ( $\alpha$  and  $\gamma$ ), and a positive correlation with its inactivating parameters ( $\beta$  and  $\delta$ ), demonstrating the influential role of hEAG1 currents on APD. The variations of these parameters were almost exclusively responsible for the more than two-fold greater  $\sigma_{\text{APD}}$  compared to Type C hMSCs ( $\sigma_{\text{APD}}$  values indicated in Figure 8). Therefore, hEAG1 activity is indeed the leading cause of sinking effects of hMSCs, and results in larger deviations in APD versus Type C hMSCs.

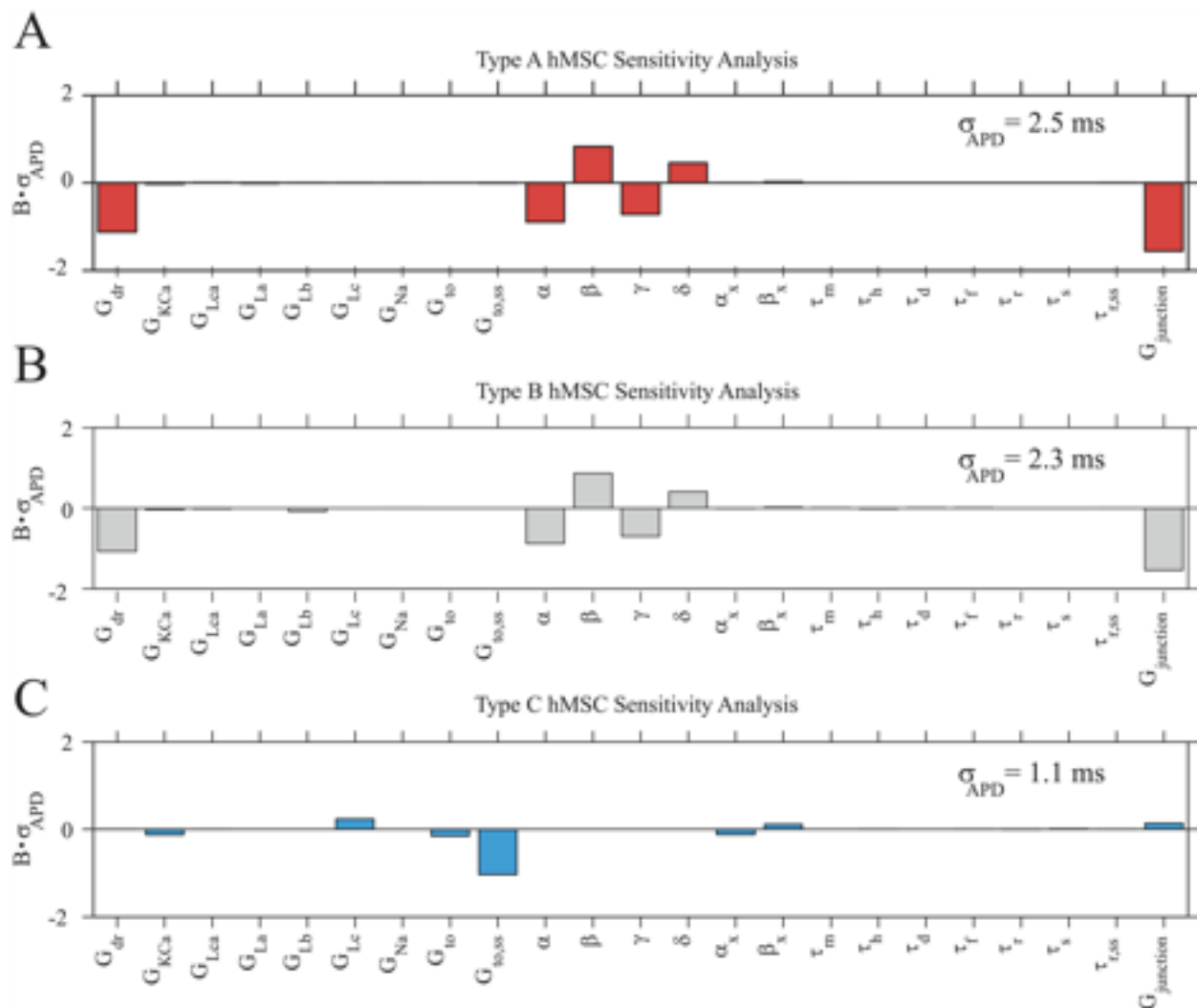


**Figure 8: hCM APD Sensitivity to hMSC Current Parameters.** A sensitivity analysis based on 300 trials per cell type was performed to develop insight into the correlation between hCM APD and current parameters of (A) Type A hMSCs, (B) Type B hMSCs, and (C) Type C hMSCs, each at a 1:1 ratio with midcardial hCMs. hCM APD was most sensitive to Types A and B hMSC gap junctional conductance ( $G_{\text{junction}}$ ) and delayed-rectifier current parameters ( $G_{dr}$ ,  $\alpha$ ,  $\beta$ ,  $\gamma$ , and  $\delta$ ). hCM APD was less sensitive to Type C hMSC  $G_{\text{junction}}$ , demonstrating that this cell type's effects are less disruptive to the APD of coupled hCMs and caused less APD variability (i.e., lowest value of  $\sigma_{APD}$ , as noted in each panel). The normalized parameter sensitivity vector,  $\mathbf{B}$ , was scaled by  $\sigma_{APD}$  to better illustrate the sensitivity of the APD output to each hMSC cell type.

This sensitivity analysis also gives insight into how well controlled the process of direct hMSC-hCM coupling can be in affecting hCM APD. The larger  $\sigma_{APD}$  for both Types A and B hMSC sensitivity analyses suggest that transplanted cells with delayed rectifier-like currents may be less consistent in their effects on hCM APD. Furthermore, as previously described, the activation kinetics of hEAG1 currents are highly variable.<sup>26</sup> Therefore, this large variability, coupled with the high sensitivity of APD to these channel parameters, could be detrimental in controlling hMSC electrical effects in a cardiac implant setting. hCM APD is also sensitive to Types A and B  $G_{junction}$ , which is itself intrinsically variable,<sup>15</sup> further contributing to poor electrical stability. Overall, Type C hMSCs appear to induce the least variations in hCM APD.

#### *5.5.5 Vulnerable Window Analysis*

To understand the arrhythmogenic effects of direct hMSC-hCM coupling at the tissue level, a VW analysis was performed on a single layer, anisotropic 5 cm × 5 cm 2-D midcardial tissue with 0% hMSCs (healthy control), 5%, 15%, or 25% randomly inserted hMSCs repeated for three different configurations per condition (see Figure 9A for sample re-entry simulations at selected S1–S2 intervals).

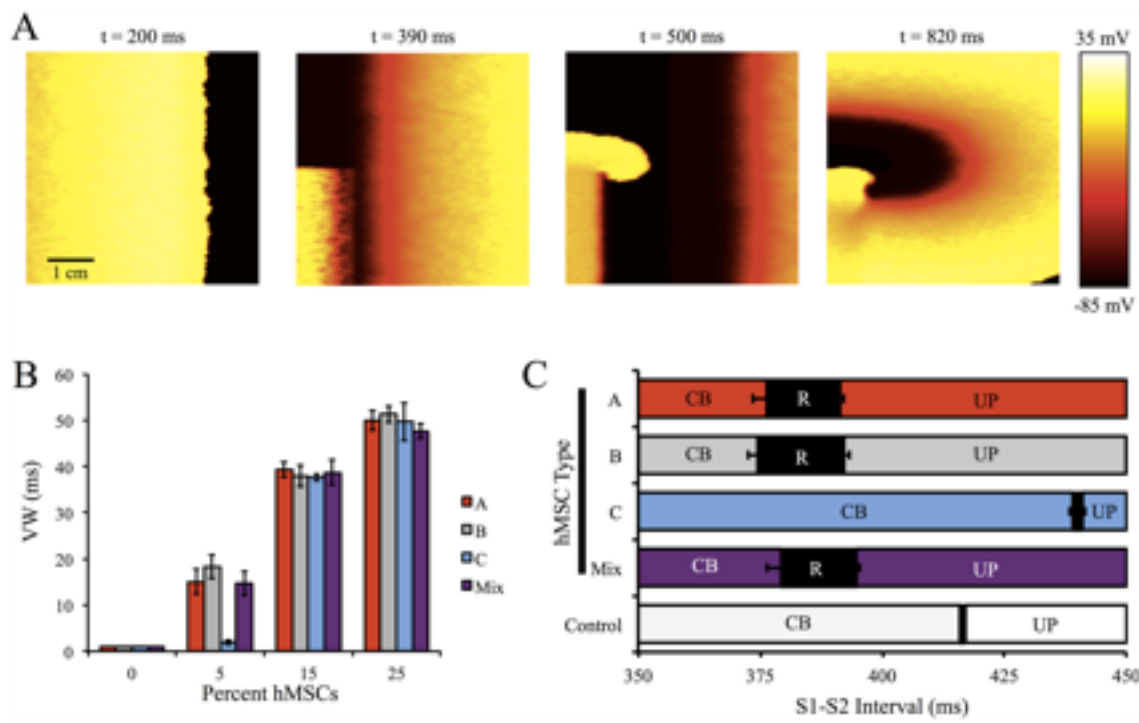


**Figure 9: VW Analysis on Cardiac Tissue With Randomly Inserted hMSCs.** A VW analysis was performed to better understand the pro-arrhythmic potential of hMSC insertion in cardiac tissue. **(A)** Selected frames from a representative simulation of an S1–S2 interval of 380 ms that led to re-entry with 25% Type A hMSC random insertion into 2-D cardiac tissue. **(B)** The VWs for tissues with 0% (control), 5%, 15%, and 25% random insertion of hMSCs; at low levels of hMSC insertion, Type C hMSCs lead to the smallest increase in VW compared to control. **(C)** Analysis of S1–S2 intervals leading to conduction block (CB), re-entry (R), or uninterrupted propagation (UP) with 5% hMSC insertion. Error bars represent standard deviation based on three tissue configurations per condition.

As shown in Figure 9B, VWs lengthened with increasing percent of inserted hMSCs. Interestingly, at low (5%) insertion levels, VWs were dependent on the type of coupled hMSCs (Figure 9B); inserting hMSCs with delayed rectifier-like activity (i.e. Types A, B, and mixed populations of hMSCs) led to substantially larger VWs (approximately 15 to 20 ms) compared to Type C hMSCs ( $VW = 2.0 \pm 0.5$  ms,  $n = 3$ ). At greater levels of hMSC insertion (i.e., 15% and

25%), VWs were nearly independent of the type of coupled hMSCs, and VWs exceeding 50 ms were observed. The S1–S2 intervals that led to re-entry for each hMSC type at low levels of insertion are shown in Figure 9C. As expected, the shifts in S1–S2 intervals leading to re-entry depended on the different mean tissue APDs (Figure S12).

#### 5.5.6 Dispersion of Refractoriness and Restitution Analysis

Various modeling studies have demonstrated APD dispersion may influence re-entry,<sup>45,49</sup> while APD restitution slope, the range of DIs for APD restitution slopes greater than 1, and CV restitution slope are key factors in restitution-induced instability.<sup>20,50-53</sup> Figure 10 illustrates the effects of the percentage and types of hMSCs on each of these arrhythmogenic factors.

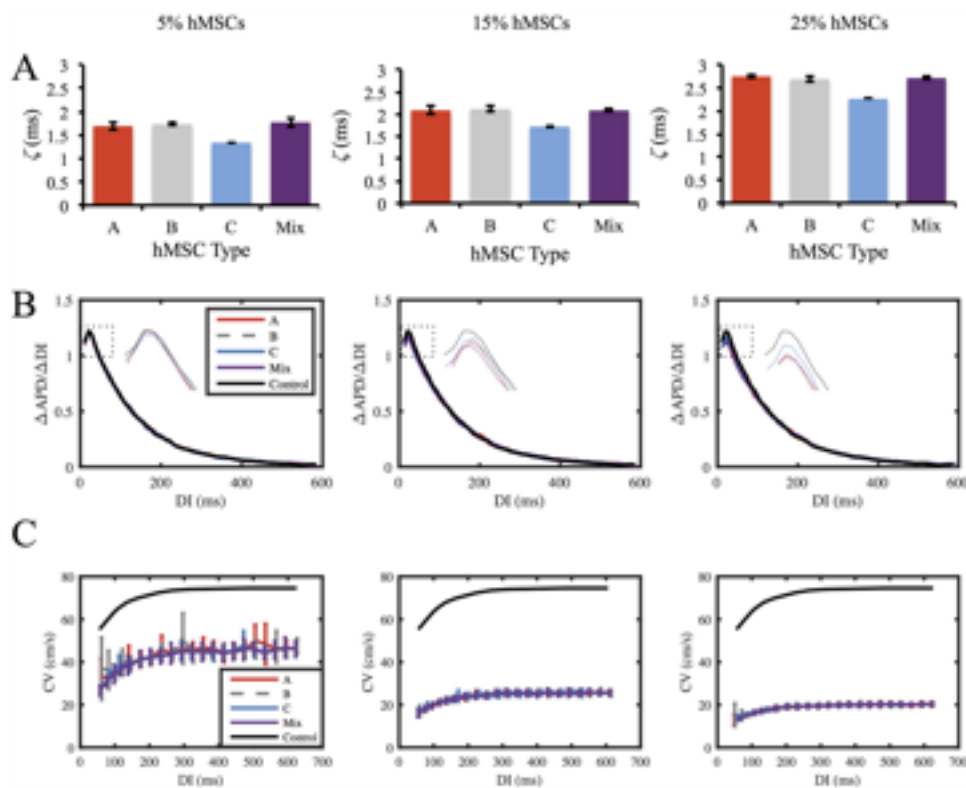


**Figure 10: hMSC Effects on Dispersion of Refractoriness and Restitution Curves.** Effects of the types of hMSCs coupled, as well as the percentage of hMSCs coupled, on dispersion of refractoriness and restitution curves were examined. **(A)** APD dispersion ( $\zeta$ ) was lowest for Type

C hMSCs. APD dispersion increased with higher percentages of coupled hMSCs. (B) APD restitution slopes, as well as the range of DIs for slopes greater than 1, decreased with hMSC percentage. Inset plot shows expanded region of APD restitution slopes greater than 1. (C) CV restitution curves were independent of hMSC type. As the percentage of inserted hMSCs increased, the maximum CV decreased.

As expected, APD dispersion ( $\zeta$ ) increased with greater levels of hMSC insertion for all hMSC types (Figure 10A). However, APD dispersion was approximately 21%, 18%, and 17% lower for Type C hMSCs compared to hMSCs with delayed rectifier-like activity at 5%, 15%, and 25% hMSC insertion, respectively (Figure 10A). Figure S12 shows APD maps for cardiac tissues with 5% hMSC insertion.

APD restitution slopes, as well as the range of DIs for slopes greater than 1, were slightly decreased following coupling with each hMSC type (Figure 10B; for raw APD restitution curves, see Figure S13). Even at 25% hMSC insertion, the shift in maximum APD restitution slope was less than 10% (Figure 10B). CV restitution slopes markedly decreased following hMSC insertion, by as much as 71% at 25% hMSC insertion (Figure 10C). The coupling effects on CV restitution slopes were predominately dependent on percentage of hMSC inserted, rather than the type of hMSC (Figure 10C). Altogether, this dispersion of refractoriness and restitution analysis supports the claim that increased arrhythmogenic potential of inserted stem cells is minimized by Type C hMSCs at low levels of hMSC insertion, as VW and APD dispersion are lowest for this cell type, without adversely affecting APD and CV restitution slopes in comparison to delayed rectifier-like hMSCs.

## 5.6 Discussion

Our study provides insight into hMSC electrical activity, and the electrophysiological effects when directly coupling hMSCs to hCMs at both the single-cell and the tissue level. This

computational analysis allowed us to hypothesize an electrophysiology-based approach for improved hMSC-based cardiotherapies, which has not been suggested elsewhere. We first developed three novel hMSC electrophysiology models based on a published empirical triad of hMSC families having distinct ion channel currents: Type A)  $I_{dr}$  and  $I_{KCa}$ ; Type B)  $I_{dr}$ ,  $I_{KCa}$ ,  $I_{Na}$ , and  $I_{LCa}$ ; and Type C)  $I_{KCa}$  and  $I_{to}$ .<sup>26,28</sup> Subsequently, each hMSC model type was coupled to an adult ventricular hCM electrophysiology model to better understand the direct interactions of these cell types. The computational analysis led us to find that: 1) our model simulations are consistent with a range of empirical findings; 2) hMSC-hCM direct coupling can increase vulnerability to re-entry; and 3) vulnerability to re-entry can be minimized using Type C hMSCs at low levels of stem cell insertion.

#### *5.6.1 Comparison of Model Results to Empirical Findings*

The ability of our computational models to reproduce empirical electrical hMSC and hMSC-hCM co-culture findings supports the validity of our results. As previously described, fitting individual currents (Figure 1) allowed reconstruction of representative whole cell voltage-clamp data by Li et al. (Figure 3).<sup>26</sup> This enabled us to simulate hMSC-hCM coupling to develop insight into direct electrical effects of co-culturing these two cell types.

The complex hMSC-hCM interactome, which also includes paracrine signaling,<sup>6,11</sup> makes it empirically infeasible to isolate direct electrophysiological coupling effects on APD. For example, Askar et al. have previously shown that the hMSC secretome alone significantly increases neonatal rat cardiomyocyte APD and significantly decreases Cav1.2 and Kv4.3 levels,<sup>54</sup> while DeSantiago et al. demonstrated the hMSC paracrine factors stimulate the L-type calcium channel current and calcium transient activity in mouse ventricular myocytes.<sup>55</sup> Furthermore, Askar et al. found the paracrine effects on APD to be dose-dependent.<sup>54</sup> Several studies<sup>13,16,54</sup> demonstrate that hMSC co-culture does not lead to APD shortening in vitro, whereas our model studies suggest direct hMSC-hCM coupling alone would tend to shorten

APD. Therefore, we hypothesize that in the experimental setting, hMSC-mediated paracrine effects may overshadow the model-predicted APD shortening effects of direct heterocellular coupling.

Furthermore, the hMSC secretome reportedly alters atrial myocyte conduction,<sup>56</sup> but does not significantly affect the conduction of ventricular myocytes,<sup>54</sup> making it reasonable to compare our model results to empirical conduction and VW findings. Studies have shown that sufficient hMSC supplementation decreases CV and CV restitution slopes,<sup>16,54</sup> consistent with our simulations. Specifically, Chang et al. observed co-culturing cardiomyocytes with greater than 10 percent of hMSCs decreased CV and the CV restitution slope.<sup>16</sup> Moreover, sufficient hMSC supplementation increased inducibility of re-entry,<sup>16</sup> which was also shown in our simulations (Figure 9). Based on our direct coupling-only simulations reproducing empirical co-culture conduction and VW findings, we hypothesize that in the experimental setting, hMSC-mediated paracrine effects on hCM conduction do not counteract the effects of direct heterocellular coupling demonstrated in this study, emphasizing the importance of understanding and minimizing the potential sources of hMSC-related arrhythmogenicity.

### *5.6.2 Mechanistic Insights into hMSC-hCM Coupling*

Despite their non-excitable nature, hMSCs express gap junction proteins<sup>15</sup> and are therefore capable of influencing hCM action potentials. Furthermore, these effects cannot be presumed to be simply passive, as shown in Figures 5 and 6A. In the case of a passive cell, there is a consistent increase in hCM APD. The relatively large capacitance of hMSCs (approximately 60 pF,<sup>26</sup> compared to 6.3 pF for cardiac fibroblasts<sup>22</sup>) makes this effect substantial, resulting in increases in APD of approximately 50 ms with a population of 80% passive hMSCs with midcardial hCMs.

These passive effects were not duplicated once the cells expressed their respective ionic currents. Unlike passive hMSCs, Types A and B hMSCs decreased APD independent of

hCM cell type. For example, the APDs of midcardial hCMs shortened by approximately 88 ms with a population of 80% Type A or B hMSCs. This effect was exacerbated in cellular fusion, where midcardial hCM APD was shortened by approximately 120 ms. During an hCM action potential, the peak hEAG1 current was two-fold greater than the maximum magnitude of  $I_{to}$ , and nearly twenty-fold greater than the maximum magnitude of  $I_{KCa}$ . The larger outward current of Types A and B hMSCs resists hMSCs from approaching the transmembrane voltage of hCMs, resulting in an overall larger sinking effect that shortens phase 2 of the cardiac action potential, and initiates phases 3 and 4 of repolarization earlier. Such drastic changes in the action potential waveform could be possible *in vivo* if the delivered stem cells cluster in regions of the heart,<sup>57</sup> such that hMSCs outnumber hCMs locally. This would be of even greater concern if the high incidence of cell fusion reported *in vitro*<sup>10</sup> were also found to occur *in vivo* as suggested by recent animal studies.<sup>58</sup> The implications of action potential variations include pathological electrical and mechanical states.

### *5.6.3 Potential Pathophysiological Consequences of hMSC-hCM Coupling*

Overall, our simulations suggest hMSC-hCM coupling: 1) alters action potential waveform at the single-cell and tissue level; 2) increases dispersion of APDs at the tissue levels; and 3) substantially decreases CV. Shortening of APDs by Types A and B hMSCs could have notable electrophysiological implications in the heart. Studies have shown that shortening of APDs could induce ventricular tachycardias, suggesting Types A and B hMSCs may be capable of pro-arrhythmic electrical remodeling.<sup>17,59,60</sup> Furthermore, one signature of ischemic patients is a loss of epicardial action potential dome, resulting in ST-segment elevation.<sup>61</sup> hMSC direct coupling to hCMs could exaggerate these effects by clustering in the epicardium and acting as an electrical sink, thus becoming pro-arrhythmic.

Substantial decreases in APD due to Types A and B hMSCs could also portend altered  $Ca^{2+}$  transients in the hCM, resulting in decreased inotropy.<sup>62-67</sup> Such alterations could directly

impact left-ventricular pressure development,<sup>22</sup> which is of particular concern for myocardial infarction patients who already suffer decreases in ejection fraction, preload, stroke work, rate of pressure development, and overall mechanical efficiency.<sup>68</sup>

The large variability in electrical activity of Types A and B hMSCs presents another potential source of arrhythmogenicity. hCM APD was negatively correlated and highly sensitive to Types A and B hMSC  $G_{\text{junction}}$  (Figure 8A and 8B). This gap conductance has been shown empirically to be highly variable with a coefficient of variation of 87%.<sup>15</sup> The potentially irregular actions of Types A and B hMSCs are further amplified by the fact that hEAG1 activation kinetics are also highly variable, with a coefficient of variation of approximately 35%.<sup>26</sup> Since there is a highly negative correlation between hCM APD and numerous  $I_{\text{dr}}$  components (e.g., its activating parameters and  $G_{\text{dr}}$ ), and a highly positive correlation with its inactivating parameters, hMSCs with delayed rectifier-like currents are likely to be unpredictable in their direct effects on hCM APD. This is exacerbated by the fact that hMSC insertion leads to increased APD dispersion in a dose-dependent manner, which could unfavorably alter VWs and electrical stability.<sup>45,49</sup>

Decreased CV caused by hMSC supplementation (Figure 10C) is an established source of re-entrant loops,<sup>16</sup> making hMSC-hCM direct coupling potentially arrhythmogenic. Chang et al. showed the potential of re-entrant arrhythmias in vitro was dependent on hMSC supplementation,<sup>16</sup> which was confirmed in our simulations (Figure 9B). The decrease in CV is more drastic with increased hMSC supplementation (Figure 10C), which may occur if hMSCs cluster in a localized region, resulting in an increased probability for re-entry. Decreased CV also plays a significant role in ischemic patients. Specifically, ischemic patients also have signatures of transmural conduction slowing, resulting in ST-segment elevation and T-wave inversion.<sup>61</sup> These abnormalities may be exacerbated by the decreased CV effects of hMSC insertion.

#### *5.6.4 Implications of Findings for Future Cardiotherapies*

Current hMSC cardiotherapies involve implementation of electrically-unspecified hMSCs. As a result, Types A and B hMSCs, which reportedly account for a majority of hMSCs,<sup>26</sup> will tend to dominate the electrical interactions with hCMs. This was seen in Figures 4 and 5, where the mixed population of hMSCs acted almost indistinguishably from Types A and B hMSCs. This model study suggests that the isolation of Type C hMSCs, absent of delayed rectifier-like currents, may offer superior effectiveness and safety as a cell-based cardiotherapy at low levels of hMSC insertion by minimizing VWs and action potential waveform perturbations compared to other hMSC types. Type C hMSCs exhibited unique electrical activity that was intermediate between the passive and delayed rectifier-functioning hMSCs, resulting in a favorable gap current. The equilibrating source-sink actions within the Type C hMSC gap currents resulted in smaller deviations in the APD (Figures 4 and 5), corresponding to longer action potential wavelengths at the tissue level following hMSC insertion (Table H of Supplementary Text), which we hypothesize contributed to this cell type having the smallest VW at low levels of hMSC insertion (Figure 9B and 9C). This suggests a decreased likelihood of the potential adverse electrical effects previously described.

It is also important to note that overall at the tissue level, the VW increased at greater levels of hMSC-hCM direct coupling, and became independent of hMSC type at moderate and high levels of hMSC insertion. Previous findings suggest the hMSC-hCM interactome involves not only intrinsic, direct cell-cell coupling, but also indirect paracrine signaling through the release of largely unidentified soluble factors and exosome nanovesicles.<sup>6,11</sup> Harnessing and delivering the key components of the hMSC secretome while circumventing the potentially pro-arrhythmic effects of direct cell-cell coupling may offer a superior cardiac therapy in the future.

### *5.6.5 Limitations and Future Work*

We note several limitations of the hMSC models developed. As previously discussed, the activation time constant for  $I_{dr}$  at a holding potential of -80 mV has a coefficient of variation of approximately 35%.<sup>26</sup> This variability affects the output APD, as suggested by the sensitivity analysis, demonstrating the necessity for further empirical investigation into the kinetics of hMSC  $I_{dr}$ . We also assumed that only a triad of families of hMSCs exist, but there may be more; for instance, it has been reported that ion channel expression varies with cell cycle progression,<sup>69-71</sup> which may contribute to the variable electrical families and activities of hMSCs. However, the limited understanding of this behavior in the context of hMSCs motivated us to focus only on the three previously characterized hMSC families. We also assume constant ionic concentrations across the hMSC cell membrane. Currently, there is not enough experimental data to sufficiently model intracellular calcium levels in hMSCs. Our sensitivity analysis demonstrates that APD is not highly influenced by channels that are largely affected by these variations (e.g.,  $I_{KCa}$ ), justifying this assumption. Collecting more electrophysiological data on carrier proteins within hMSCs<sup>29</sup> would encourage incorporating transient behavior of ionic concentrations into our models.

A second limitation was that we assumed healthy hCMs in order to develop insight into the arrhythmogenic effects of hMSC insertion into healthy cardiac tissue, effectively performing an *in silico* Phase I clinical trial. However, we did not consider the effects of microfibrosis or random microscale obstacles.<sup>24,72-77</sup> Each of these effects was purposely not considered in this study, as hMSC paracrine effects are expected to have a major impact on these changes.<sup>78-81</sup> The simulations performed in this study provide a framework for future investigation into each of these factors.

Therapeutic hMSCs can disperse to both healthy and ischemic regions of the heart, motivating investigation of the effects of hMSC coupling with ischemic hCMs. This healthy hCM-only assumption made it appropriate to model local cardiac behavior (i.e., 5 cm × 5 cm

heterogeneous anisotropic tissue) rather than whole heart behavior. Studying the effects of various spatial distributions of hMSCs using a fully three-dimensional anatomically detailed model of the heart could represent an area for future investigation building on the electrophysiology models developed herein.

A fourth limitation was that we did not model other factors that may influence electrical instability, such as short-term cardiac memory and intracellular calcium dynamics.<sup>20,82-84</sup> Instead, we prioritized other established factors of instability (e.g. APD dispersion, APD restitution slopes, CV restitution slopes), and found several advantages of Type C hMSCs compared to the other mesenchymal stem cell families.

Finally, we assumed no interplay between paracrine signaling and electrophysiological coupling. However, it was recently shown that paracrine signaling can cause upregulation of Cx43 and increase intercellular conduction in atrial myocytes,<sup>56</sup> as well as alter ion channel activity in ventricular myocytes.<sup>54</sup> We neglected paracrine mechanisms in our models, so investigating this time-dependent interaction would require further study.

Based on these limitations, areas for future work include: 1) improving the models based on advancements in empirical data on hMSC electrophysiology; 2) considering the effects of microfibrosis or random microscale obstacles in combination with hMSC anti-fibrotic paracrine effects; 3) examining the electrical and electromechanical effects of hMSC models coupled with ischemic hCM models;<sup>85</sup> 4) modeling the interplay between electrophysiological effects and paracrine signaling in the hMSC-hCM interactome; and 5) empirically confirming our simulations, demonstrating that Type C hMSCs minimize the impact on APD and reduce the VW at low levels of hMSC insertion, offering a potential strategy for improving the safety of cardiac cell therapies.

In conclusion, our study provides novel electrophysiological models of hMSCs that reproduce key experimental measurements from patch clamp studies, identifies mechanisms underlying the arrhythmogenic effects of hMSCs coupled to hCMs via gap junctions,

underscores the electrical effects associated with hMSC-hCM fusion, and establishes the possibility of isolating a specific sub-population of hMSCs absent of hEAG1 delayed rectifier-like channel activity for minimizing the arrhythmogenic risk of future hMSC-based cell delivery cardioterapies using low levels of hMSC coupling.

## **5.7 References**

1. Schulman IH, Hare JM. Key developments in stem cell therapy in cardiology. *Regenerative medicine*. 2012 Nov;7(6 Suppl):17–24.
2. Go AS, Mozaffarian D, Roger VL, Benjamin EJ, Berry JD, Blaha MJ, et al. Heart disease and stroke statistics—2014 update: a report from the american heart association. *Circulation*. 2014 Jan;129(3):e28–e292.
3. Karantalis V, DiFede DL, Gerstenblith G, Pham S, Symes J, Zambrano JP, et al. Autologous mesenchymal stem cells produce concordant improvements in regional function, tissue perfusion, and fibrotic burden when administered to patients undergoing coronary artery bypass grafting: The Prospective Randomized Study of Mesenchymal Stem Cell Therapy in Patients Undergoing Cardiac Surgery (PROMETHEUS) trial. *Circulation research*. 2014 Apr;114(8):1302–1310.
4. Schaefer A, Zwadlo C, Fuchs M, Meyer GP, Lippolt P, Wollert KC, et al. Long-term effects of intracoronary bone marrow cell transfer on diastolic function in patients after acute myocardial infarction: 5-year results from the randomized-controlled BOOST trial—an echocardiographic study. *European journal of echocardiography: the journal of the working group on echocardiography of the european society of cardiology*. 2010 Mar;11(2):165–171.
5. Heldman AW, DiFede DL, Fishman JE, Zambrano JP, Trachtenberg BH, Karantalis V, et al. Transendocardial mesenchymal stem cells and mononuclear bone marrow cells for ischemic cardiomyopathy: the TAC-HFT randomized trial. *The journal of the american medical association*. 2014 Jan;311(1):62–73.
6. Cashman TJ, Gouon-Evans V, Costa KD. Mesenchymal stem cells for cardiac therapy: practical challenges and potential mechanisms. *Stem cell reviews*. 2013 Jun;9(3):254–265.

7. Segers VF, Lee RT. Stem-cell therapy for cardiac disease. *Nature*. 2008 Feb;451(7181):937–942.
8. Almeida SO, Skelton RJ, Adigopula S, Ardehali R. Arrhythmia in stem cell transplantation. *Cardiac electrophysiology clinics*. 2015 Jun;7(2):357–370.
9. Smit NW, Coronel R. Stem cells can form gap junctions with cardiac myocytes and exert pro-arrhythmic effects. *Frontiers in physiology*. 2014 Oct;5:419.
10. Shadrin IY, Yoon W, Li L, Shepherd N, Bursac N. Rapid fusion between mesenchymal stem cells and cardiomyocytes yields electrically active, non-contractile hybrid cells. *Scientific reports*. 2015 Jul;5:12043.
11. Ranganath SH, Levy O, Inamdar MS, Karp JM. Harnessing the mesenchymal stem cell secretome for the treatment of cardiovascular disease. *Cell stem cell*. 2012 Mar;10(3):244–258.
12. Beeres SL, Atsma DE, van der Laarse A, Pijnappels DA, van Tuyn J, Fibbe WE, et al. Human adult bone marrow mesenchymal stem cells repair experimental conduction block in rat cardiomyocyte cultures. *Journal of the american college of cardiology*. 2005 Nov;46(10):1943–1952.
13. Pijnappels DA, Schalij MJ, van Tuyn J, Ypey DL, de Vries AAF, van der Wall EE, et al. Progressive increase in conduction velocity across human mesenchymal stem cells is mediated by enhanced electrical coupling. *Cardiovascular research*. 2006 Nov;72(2):282–291.
14. Pak HN, Qayyum M, Kim DT, Hamabe A, Miyauchi Y, Lill MC, et al. Mesenchymal stem cell injection induces cardiac nerve sprouting and increased tenascin expression in a swine model of myocardial infarction. *Journal of cardiovascular electrophysiology*. 2003 Aug;14(8):841–848.

15. Valiunas V, Doronin S, Valiuniene L, Potapova I, Zuckerman J, Walcott B, et al. Human mesenchymal stem cells make cardiac connexins and form functional gap junctions. *The journal of physiology*. 2004 Mar;555(Pt 3):617–626.
16. Chang MG, Tung L, Sekar RB, Chang CY, Cysyk J, Dong P, et al. Proarrhythmic potential of mesenchymal stem cell transplantation revealed in an in vitro coculture model. *Circulation*. 2006 Apr;113(15):1832–1841.
17. Price MJ, Chou CC, Frantzen M, Miyamoto T, Kar S, Lee S, et al. Intravenous mesenchymal stem cell therapy early after reperfused acute myocardial infarction improves left ventricular function and alters electrophysiologic properties. *International journal of cardiology*. 2006 Aug;111(2):231–239.
18. Karantalis V, Hare JM. Use of mesenchymal stem cells for therapy of cardiac disease. *Circulation research*. 2015 Apr;116(8):1413–1430.
19. ten Tusscher KH, Noble D, Noble PJ, Panfilov AV. A model for human ventricular tissue. *American journal of physiology—heart and circulatory physiology*. 2004 Apr;286(4):H1573–H1589.
20. ten Tusscher KH, Panfilov AV. Cell model for efficient simulation of wave propagation in human ventricular tissue under normal and pathological conditions. *Physics in medicine and biology*. 2006 Dec;51(23):6141–6156.
21. O'Hara T, Virág L, Varró A, Rudy Y. Simulation of the undiseased human cardiac ventricular action potential: model formulation and experimental validation. *PLoS computational biology*. 2011 May;7(5):e1002061. pmid:21637795
22. MacCannell KA, Bazzazi H, Chilton L, Shibukawa Y, Clark RB, Giles WR. A mathematical model of electrotonic interactions between ventricular myocytes and fibroblasts. *Biophysical journal*. 2007 Jun;92(11):4121–4132.

23. Sachse FB, Moreno AP, Abildskov JA. Electrophysiological modeling of fibroblasts and their interaction with myocytes. *Annals of biomedical engineering*. 2008 Jan;36(1):41–56.
24. Jacquemet V, Henriquez CS. Loading effect of fibroblast-myocyte coupling on resting potential, impulse propagation, and repolarization: insights from a microstructure model. *American journal of physiology Heart and circulatory physiology*. 2008 May;294(5):H2040–H2052.
25. Xie Y, Garfinkel A, Camelliti P, Kohl P, Weiss JN, Qu Z. Effects of fibroblast-myocyte coupling on cardiac conduction and vulnerability to reentry: A computational study. *Heart rhythm: the official journal of the Heart Rhythm Society*. 2009 Nov;6(11):1641–1649.
26. Li GR, Sun H, Deng X, Lau CP. Characterization of ionic currents in human mesenchymal stem cells from bone marrow. *Stem cells (Dayton, Ohio)*. 2005 Mar;23(3):371–382.
27. Heubach JF, Graf EM, Leutheuser J, Bock M, Balana B, Zahanich I, et al. Electrophysiological properties of human mesenchymal stem cells. *The journal of physiology*. 2004 Feb;554(Pt 3):659–672.
28. Li GR, Deng XL. Functional ion channels in stem cells. *World journal of stem cells*. 2011 Mar;3(3):19–24.
29. Kawano S, Otsu K, Shoji S. Calcium oscillations regulated by sodium-calcium exchanger and plasma membrane calcium pump induce fluctuations of membrane currents and potentials in human mesenchymal stem cells. *Cell calcium*. 2003 Aug;34(2):145–56. pmid:12810056
30. Wolfram G, Kistler WM. Spiking neuron models: Single neurons, populations, plasticity. Cambridge university press; 2002.

31. Schlichter LC, Jiang J, Wang J, Newell EW, Tsui FWL, Lam D. Regulation of hERG and hEAG channels by Src and by SHP-1 tyrosine phosphatase via an ITIM region in the cyclic nucleotide binding domain. *PLoS one*. 2014 Feb;9(2):e90024.
32. Sanguinetti MC, Tristani-Firouzi M. hERG potassium channels and cardiac arrhythmia. *Nature*. 2006 Mar;440(7083):463–469.
33. Silverman WR, Roux B, Papazian DM. Structural basis of two-stage voltage-dependent activation in K<sup>+</sup> channels. *Proceedings of the national academy of sciences of the United States of America*. 2003 Mar;100(5):2935–2940.
34. Rudy Y, Silva JR. Computational biology in the study of cardiac ion channels and cell electrophysiology. *Quarterly reviews of biophysics*. 2006 Feb;39(1):57–116.
35. Hille B. *Ion channels of excitable membranes*. Mass.; 2001.
36. Koch C, Segev I. *Methods in neuronal modeling: from ions to networks*. MIT Press; 1998.
37. Hodgkin AL, Huxley AF. A quantitative description of membrane current and its application to conduction and excitation in nerve. *The journal of physiology*. 1952 Aug;117(4):500–544.
38. Stewart P, Aslanidi OV, Noble D, Noble PJ, Boyett MR, Zhang H. Mathematical models of the electrical action potential of Purkinje fibre cells. *Philosophical transactions A: mathematical, physical, and engineering sciences*. 2009 Jun;367(1896):2225–2255.
39. Wang Z, Fermini B, Nattel S. Sustained depolarization-induced outward current in human atrial myocytes. Evidence for a novel delayed rectifier K<sup>+</sup> current similar to Kv1.5 cloned channel currents. *Circulation research*. 1993 Dec;73(6):1061–1076.
40. Nygren A, Fiset C, Firek L, Clark JW, Lindblad DS, Clark RB, et al. Mathematical model of an adult human atrial cell: the role of K<sup>+</sup> currents in repolarization. *Circulation research*. 1998 Jan;82(1):63–81.

41. Beeler GW, Reuter H. Reconstruction of the action potential of ventricular myocardial fibres. *The journal of physiology*. 1977 Jun;268(1):177–210.
42. Plonsey R, Barr RC. Bioelectricity: A Quantitative Approach. Springer; 2007.
43. Gomez JF, Cardona K, Martinez L, Saiz J, Trenor B. Electrophysiological and structural remodeling in heart failure modulate arrhythmogenesis. 2D simulation study. *PloS one*. 2014 Jul;9(7):e103273.
44. Greisas A, Zlochiver S. Modulation of spiral-wave dynamics and spontaneous activity in a fibroblast/myocyte heterocellular tissue—a computational study. *IEEE transactions on bio-medical engineering*. 2012 May;59(5):1398–1407. \
45. Qu Z, Garfinkel A, Chen PS, Weiss JN. Mechanisms of discordant alternans and induction of reentry in simulated cardiac tissue. *Circulation*. 2000 Oct;102(14):1664–1670
46. Sobie EA. Parameter sensitivity analysis in electrophysiological models using multivariable regression. *Biophysical journal*. 2009 Feb;96(4):1264–1274.
47. Sarkar AX, Sobie EA. Regression analysis for constraining free parameters in electrophysiological models of cardiac cells. *PLoS computational biology*. 2010 Sep;6(9):e1000914.
48. Cummins MA, Dalal PJ, Bugana M, Severi S, Sobie EA. Comprehensive analyses of ventricular myocyte models identify targets exhibiting favorable rate dependence. *PLoS computational biology*. 2014 Mar;10(3):e1003543.
49. Clayton RH, Holden AV. Dispersion of cardiac action potential duration and the initiation of re-entry: a computational study. *Biomedical engineering online*. 2005 Feb;4:11.
50. Cao JM, Qu Z, Kim YH, Wu TJ, Garfinkel A, Weiss JN, et al. Spatiotemporal heterogeneity in the induction of ventricular fibrillation by rapid pacing: importance of cardiac restitution properties. *Circulation research*. 1999 Jun;84(11):1318–1331.

51. Cytrynbaum E, Keener JP. Stability conditions for the traveling pulse: Modifying the restitution hypothesis. *Chaos (Woodbury, NY)*. 2002 Sep;12(3):788–799.
52. Echebarria B, Karma A. Instability and spatiotemporal dynamics of alternans in paced cardiac tissue. *Physical review letters*. 2002 May;88(20):208101.
53. Qu Z, Weiss JN, Garfinkel A. Cardiac electrical restitution properties and stability of reentrant spiral waves: a simulation study. *The American journal of physiology*. 1999 Jan;276(1 Pt 2):H269–H283.
54. Askar SFA, Ramkisoensing AA, Atsma DE, Schalij MJ, de Vries AAF, Pijnappels DA. Engraftment patterns of human adult mesenchymal stem cells expose electrotonic and paracrine proarrhythmic mechanisms in myocardial cell cultures. *Circulation Arrhythmia and electrophysiology*. 2013 Apr;6(2):380–391.
55. DeSantiago J, Bare DJ, Semenov I, Minshall RD, Geenen DL, Wolska BM, et al. Excitation-contraction coupling in ventricular myocytes is enhanced by paracrine signaling from mesenchymal stem cells. *Journal of molecular and cellular cardiology*. 2012 Jun;52(6):1249–1256.
56. Mureli S, Gans CP, Bare DJ, Geenen DL, Kumar NM, Banach K. Mesenchymal stem cells improve cardiac conduction by upregulation of connexin 43 through paracrine signaling. *American journal of physiology: heart and circulatory physiology*. 2013 Feb;304(4):H600–H609.
57. Vela DC, Silva GV, Assad JA, Sousa AL, Coulter S, Fernandes MR, et al. Histopathological study of healing after allogenic mesenchymal stem cell delivery in myocardial infarction in dogs. *The journal of histochemistry and cytochemistry: official journal of the histochemistry society*. 2009 Feb;57(2):167–176.
58. Freeman BT, Kouris NA, Ogle BM. Tracking fusion of human mesenchymal stem cells after transplantation to the heart. *Stem cells translational medicine*. 2015 Jun;4(6):685–694.

59. Kuo CS, Munakata K, Reddy CP, Surawicz B. Characteristics and possible mechanism of ventricular arrhythmia dependent on the dispersion of action potential durations. *Circulation*. 1983 Jun;67(6):1356–1367.
60. Bode F, Karasik P, Katus HA, Franz MR. Upstream stimulation versus downstream stimulation: arrhythmogenesis based on repolarization dispersion in the human heart. *Journal of the american college of cardiology*. 2002 Aug;40(4):731–736.
61. Di Diego JM, Antzelevitch C. Cellular basis for ST-segment changes observed during ischemia. *Journal of electrocardiology*. 2003;36 Suppl:1–5.
62. Bouchard RA, Clark RB, Giles WR. Effects of action potential duration on excitation-contraction coupling in rat ventricular myocytes. Action potential voltage-clamp measurements. *Circulation research*. 1995 May;76(5):790–801.
63. Wood EH, Heppner RL, Weidmann S. Inotropic effects of electric currents. *Circulation research*. 1969 Mar;24(3):409–445.
64. Morad M, Goldman Y. Excitation-contraction coupling in heart muscle: membrane control of development of tension. *Progress in biophysics and molecular biology*. 1973;27:257–313.
65. Allen DG. On the relationship between action potential duration and tension in cat papillary muscle. *Cardiovascular research*. 1977 May;11(3):210–218.
66. Wohlfart B. Relationships between peak force, action potential duration and stimulus interval in rabbit myocardium. *Acta physiologica Scandinavica*. 1979 Aug;106(4):395–409.
67. Schouten VJ. The negative correlation between action potential duration and force of contraction during restitution in rat myocardium. *Journal of molecular and cellular cardiology*. 1986 Oct;18(10):1033–1045.

68. Angeli FS, Shapiro M, Amabile N, Orcino G, Smith CS, Tacy T, et al. Left ventricular remodeling after myocardial infarction: characterization of a swine model on beta-blocker therapy. *Comparative medicine*. 2009 Jun;59(3):272–279.
69. Ouadid-Ahidouch H, Le Bourhis X, Roudbaraki M, Toillon RA, Delcourt P, Prevarskaya N. Changes in the K<sup>+</sup> current-density of MCF-7 cells during progression through the cell cycle: possible involvement of a h-ether a-gogo K<sup>+</sup> channel. *Receptors and channels*. 2001;7(5):345–356.
70. MacFarlane SN, Sontheimer H. Changes in ion channel expression accompany cell cycle progression of spinal cord astrocytes. *Glia*. 2000 Mar;30(1):39–48.
71. Ouadid-Ahidouch H, Roudbaraki M, Ahidouch A, Delcourt P, Prevarskaya N. Cell-cycle-dependent expression of the large Ca<sup>2+</sup>-activated K<sup>+</sup> channels in breast cancer cells. *Biochemical and biophysical research communications*. 2004 Mar;316(1):244–251.
72. Bub G, Shrier A, Glass L. Spiral wave generation in heterogeneous excitable media. *Physical review letters*. 2002 Feb;88(5):058101.
73. Hooks DA, Tomlinson KA, Marsden SG, LeGrice IJ, Smaill BH, Pullan AJ, et al. Cardiac microstructure: implications for electrical propagation and defibrillation in the heart. *Circulation research*. 2002 Aug;91(4):331–338.
74. Tanaka K, Zlochiver S, Vikstrom KL, Yamazaki M, Moreno J, Klos M, et al. Spatial distribution of fibrosis governs fibrillation wave dynamics in the posterior left atrium during heart failure. *Circulation research*. 2007 Oct;101(8):839–847.
75. ten Tusscher KHWJ, Panfilov AV. Influence of nonexcitable cells on spiral breakup in two-dimensional and three-dimensional excitable media. *Physical review E, Statistical, nonlinear, and soft matter physics*. 2003 Dec;68(6 Pt 1):062902.
76. Ten Tusscher KHWJ, Panfilov AV. Influence of diffuse fibrosis on wave propagation in human ventricular tissue. *Europace: European pacing, arrhythmias, and cardiac electrophysiology: journal of the working groups on cardiac pacing, arrhythmias, and*

cardiac cellular electrophysiology of the European Society of Cardiology. 2007 Nov;9 Suppl 6:vi38–vi45.

77. Turner I, L-H Huang C, Saumarez RC. Numerical simulation of paced electrogram fractionation: relating clinical observations to changes in fibrosis and action potential duration. *Journal of cardiovascular electrophysiology*. 2005 Feb;16(2):151–161.
78. Li L, Zhang Y, Li Y, Yu B, Xu Y, Zhao S, et al. Mesenchymal stem cell transplantation attenuates cardiac fibrosis associated with isoproterenol-induced global heart failure. *Transplant international: official journal of the European Society for Organ Transplantation*. 2008 Dec;21(12):1181–1189.
79. Wang D, Zhang F, Shen W, Chen M, Yang B, Zhang Y, et al. Mesenchymal stem cell injection ameliorates the inducibility of ventricular arrhythmias after myocardial infarction in rats. *International journal of cardiology*. 2011 Nov;152(3):314–320.
80. Mao Q, Lin CX, Liang XL, Gao JS, Xu B. Mesenchymal stem cells overexpressing integrin-linked kinase attenuate cardiac fibroblast proliferation and collagen synthesis through paracrine actions. *Molecular medicine reports*. 2013 May;7(5):1617–1623.
81. Kawamura M, Miyagawa S, Fukushima S, Saito A, Toda K, Daimon T, et al. Xenotransplantation of Bone Marrow-Derived Human Mesenchymal Stem Cell Sheets Attenuates Left Ventricular Remodeling in a Porcine Ischemic Cardiomyopathy Model. *Tissue engineering Part A*. 2015 Aug;21(15–16):2272–2280.
82. Cherry EM, Fenton FH. Suppression of alternans and conduction blocks despite steep APD restitution: electrotonic, memory, and conduction velocity restitution effects. *American journal of physiology Heart and circulatory physiology*. 2004 Jun;286(6):H2332–H2341.
83. Pruvot EJ, Katra RP, Rosenbaum DS, Laurita KR. Role of calcium cycling versus restitution in the mechanism of repolarization alternans. *Circulation research*. 2004 Apr;94(8):1083–1090.

84. Shimizu W, Antzelevitch C. Cellular basis for long QT, transmural dispersion of repolarization, and torsade de pointes in the long QT syndrome. *Journal of electrocardiology*. 1999;32 Suppl:177–184.
85. Rodríguez B, Trayanova N, Noble D. Modeling cardiac ischemia. *Annals of the New York academy of sciences*. 2006 Oct;1080:395–414. pmid:17132797

## Chapter 5 Supplemental Material

### Supplementary Methods

#### Handling Experimental Data for hMSC Model Development:

Published experimental hMSC electrophysiology data from Li et al.<sup>1</sup> was digitized to develop the hMSC model. Mean I-V  $I_{KCa}$  curve data from Figure 4B of Li et al.<sup>1</sup> was defined as the difference between control and 100 nM Iberiotoxin conditions. Mean I-V  $I_{dr}$  curve data from Figure 6B of Li et al.<sup>1</sup> was defined as control values. Mean I-V  $I_{LCa}$  curve data from Figure 3C of Li et al.<sup>1</sup> was defined as control values. I-V  $I_{to}$  curve data from Figure 5A of Li et al.<sup>1</sup> was defined as the difference between control and 4-AP conditions. Mean I-V  $I_{Na}$  curve data from Figure 2C of Li et al.<sup>1</sup> was defined as control values. Mean  $I_{dr}$  activation data was taken as control values from Figure 6D of Li et al.<sup>1</sup> Mean  $I_{to}$  inactivation data was taken from Figure 5B of Li et al.<sup>1</sup> All other activation and inactivation data were derived from respective I-V plots and voltage-clamp data of Li et al.<sup>1</sup> Activation parameters were derived from voltage-clamp data, and were defined as time to reach 63% of the maximum current. Inactivation parameters were derived from voltage-clamp data, and were defined as time to reach  $I_{\text{steady-state}} + 0.37*(I_{\max} - I_{\text{steady-state}})$ , such that time was greater than time of maximum current.

#### Computational Methods for hMSC Model Development:

Due to the form of ionic channel equations, both an ordinary differential equation solver and a nonlinear optimization programming algorithm were necessary to fit the hMSC ion channel data. The “ode15s” and “fmincon” MATLAB functions were used as the ordinary differential equation solver and nonlinear optimization programming algorithm, respectively. The ion channel equations with fitted model parameters are given in Tables B-G of S1 Text.

Modeling hMSC Cellular Resistivity:

Empirical data was unavailable for the cellular resistivity of an hMSC. Therefore, the cellular resistivity of an hMSC ( $\rho_{hMSC}$ ) was calculated by extending the hCM single-channel gap conductance and cellular resistivity relationship<sup>2,3</sup> to the hMSC cell single-channel gap conductance.<sup>4</sup> This inverse relationship, as described elsewhere,<sup>2,3</sup> is:

$$\rho_{hMSC} g_{gap} = \frac{\pi r_c^2}{L_{gap}}$$

where  $g_{gap}$  is the single channel conductance,  $r_c$  is the channel radius, and  $L_{gap}$  is the length of the gap junction. The length and radius of the hMSC-hCM and hMSC-hMSC gap junctions were assumed to be the same as the hCM-hCM gap junction.

**Supplementary Methods References:**

1. Li GR, Sun H, Deng X, Lau CP. Characterization of ionic currents in human mesenchymal stem cells from bone marrow. *Stem cells* (Dayton, Ohio). 2005 Mar;23(3):371–382.
2. Jongsma HJ and Wilders R. Gap junctions in cardiovascular disease. *Circulation Research*, 86(12):1193–7, Jun 2006.
3. Jongsma HJ and Wilders R. Limitations of the dual voltage clamp method in assaying conductance and kinetics of gap junction channels. *Biophysical Journal*, 63(4):942–953, Oct 1992.
4. Valiunas V, Doronin S, Valiuniene L, Potapova I, Zuckerman J, Walcott B, et al. Human mesenchymal stem cells make cardiac connexins and form functional gap junctions. *The journal of physiology*. 2004 Mar;555(Pt 3):617–626

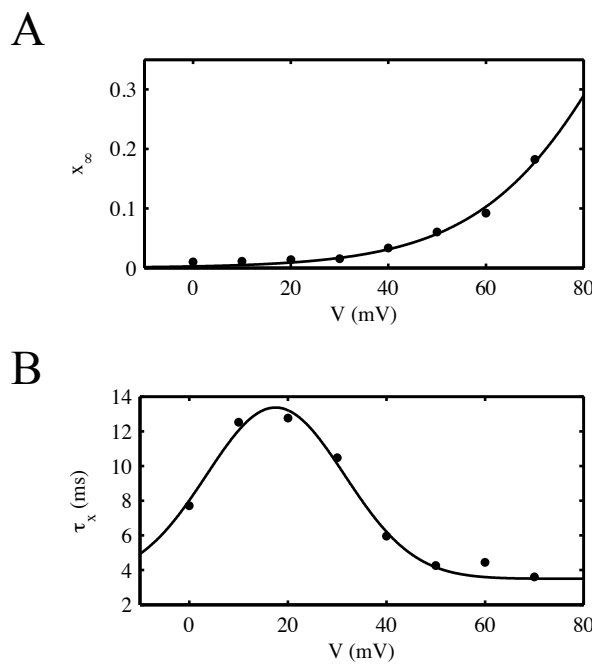


**Fig S1:  $I_{KCa}$  Steady-State Activation and Time Constant Curves:** (A) Steady-state activation curve for  $I_{KCa}$  together with values derived from mean I-V experimental data.<sup>1</sup> (B) Time constant curve for  $I_{KCa}$  together with values derived from experimental voltage clamp data.<sup>1</sup>

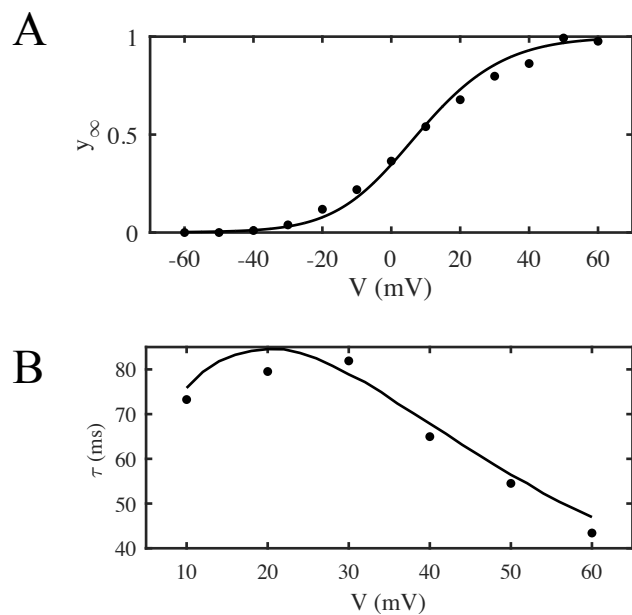


**Fig S2:  $I_{dr}$  Data Fitting Curves:** (A) Steady-state activation curve for  $I_{dr}$  together with values derived from I-V experimental data.<sup>1</sup> (B) Time constant curve for  $I_{dr}$  together with values derived from voltage-clamp data.<sup>1</sup>

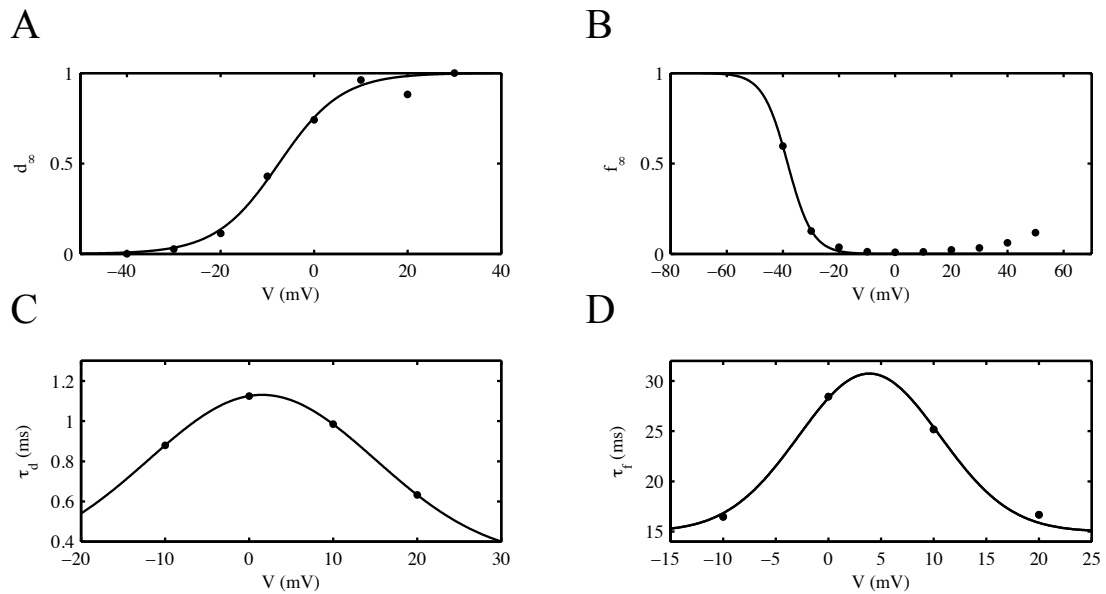


**Fig S3:  $I_{LCa}$  Steady-State Functions and Time Constant Curves:** Steady-state (A) activation and (B) inactivation curves for  $I_{LCa}$  together with values derived from mean I-V experimental data.<sup>1</sup> Time constant (C) activation and (D) inactivation curves for  $I_{LCa}$  together with values derived from voltage-clamp data.<sup>1</sup>

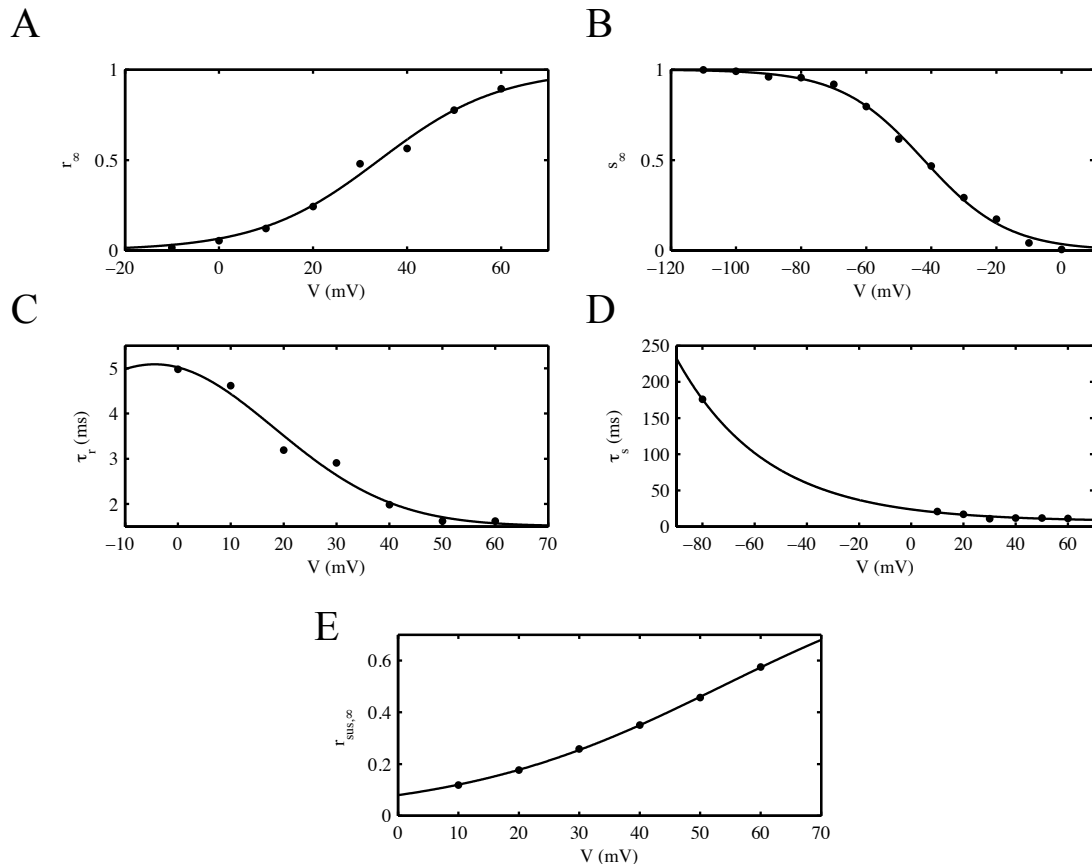


**Fig S4:  $I_{to}$  Steady-State Functions and Time Constant Curves:** Steady-state (A) activation and (B) inactivation curves for  $I_{to}$  together with values derived from voltage-clamp and inactivation experimental data, respectively.<sup>1</sup> Time constant (C) activation and (D) inactivation curves for  $I_{to}$  together with values derived from voltage-clamp data.<sup>1</sup> (E) Steady-state activation curve for  $I_{to}$  sustained currents together with values derived from voltage-clamp data.<sup>1</sup> Sustained current activation time constants were assumed to be 10 times faster than the transient current activation time constants.

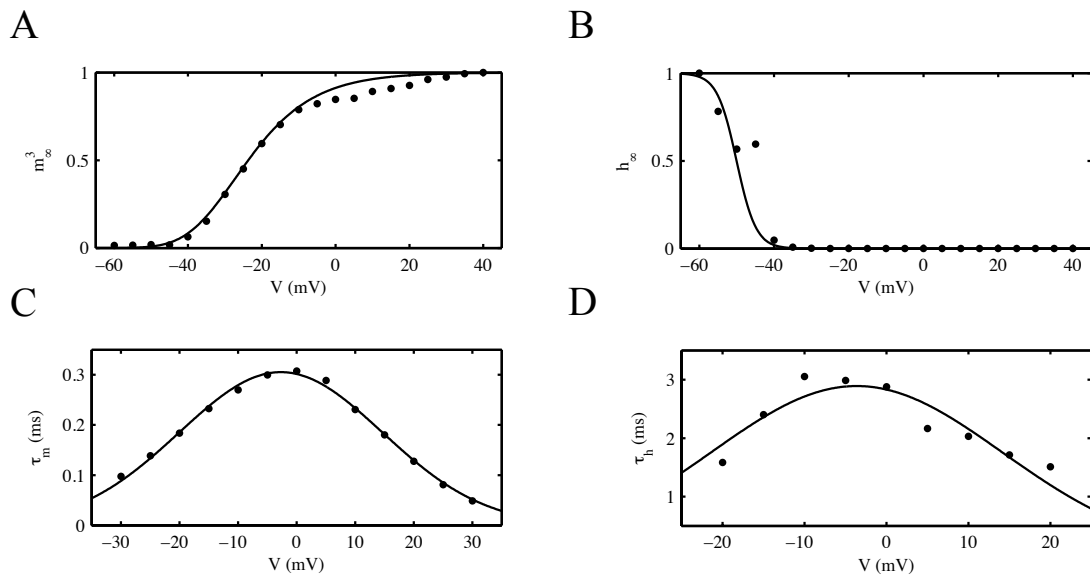


**Fig S5:  $I_{Na}$  Steady-State Functions and Time Constant Curves:** Steady-state (A) activation and (B) inactivation curves for  $I_{Na}$  together with values derived from I-V data.<sup>1</sup> Time constant (C) activation and (D) inactivation curves for  $I_{Na}$  together with values derived from voltage-clamp data.<sup>1</sup>

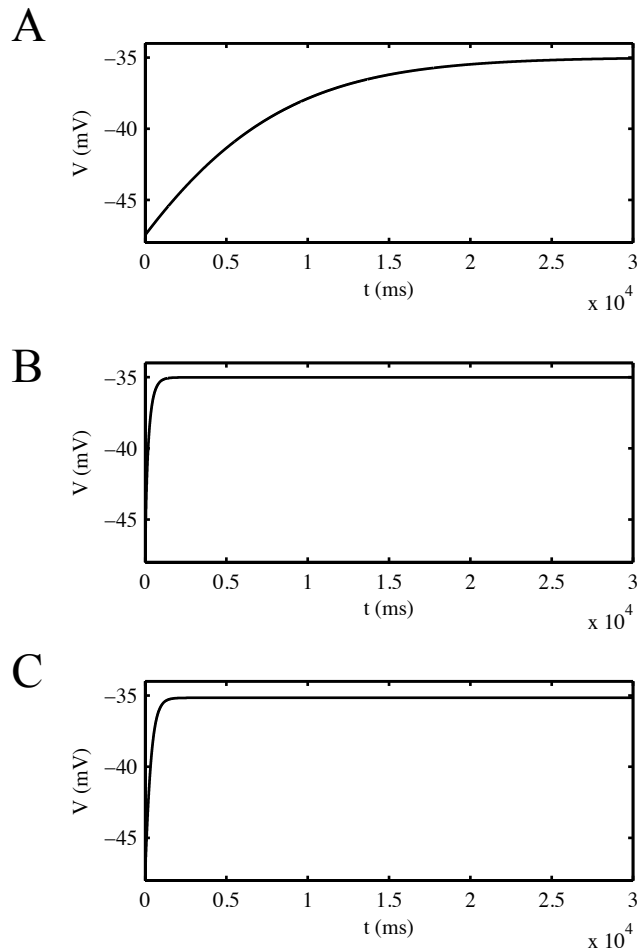


**Fig S6: Confirming the Resting Membrane Potential of Each hMSC Model:** Types A (A), B (B), and C (C) hMSCs received a current pulse at  $t = 0$  ms to determine their respective resting membrane potentials. Different leakage conductance and reversal potential values were used for each hMSC to satisfy resting membrane potentials at  $\sim -35$  mV, within the range of empirical data.<sup>1</sup>

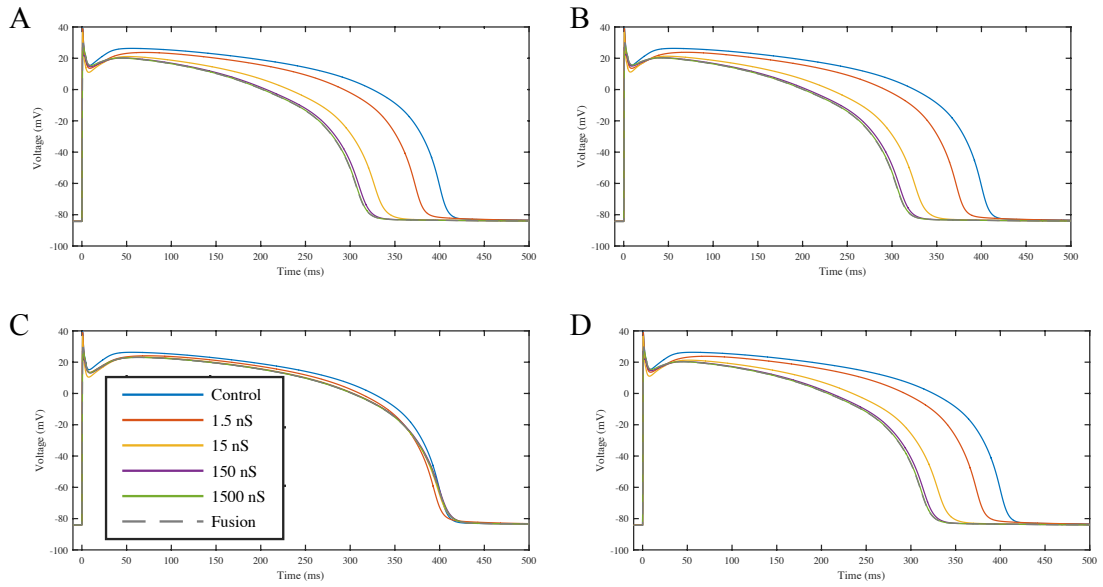


**Fig S7: Confirming the hMSC-hCM Fusion Model:** To validate the method of modeling cell fusion described in this paper, we compared 1:1 hMSC:hCM simulation results for control ( $G_{\text{gap}} = 0$  nS, blue line), standard gap conductance ( $G_{\text{gap}} = 1.5$  nS, red line), and increasing  $G_{\text{gap}}$  (15 nS, 150 nS, 1500 nS; yellow, purple, green, respectively) which converge to the case of cell fusion ( $G_{\text{gap}} \rightarrow \infty$ ) as  $G_{\text{gap}} \rightarrow \infty$ . These two answers converged to the same answers for (A) types A, (B) B, (C) C, and (D) mixed population of hMSCs based on approximate prevalence *in vitro*.<sup>1</sup>

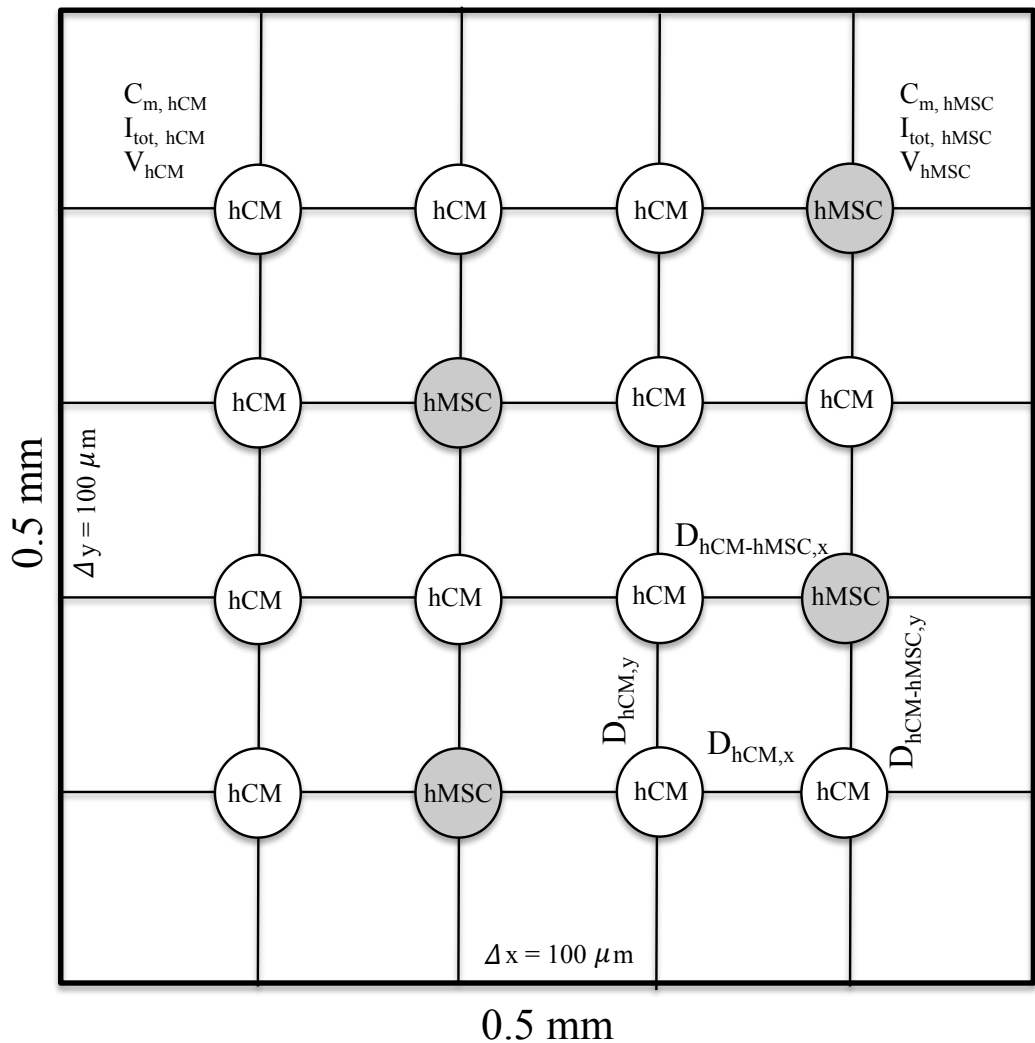


**Fig S8: Configuration of the Heterogeneous Anisotropic hMSC-hCM 2-D Tissue:** A sample 0.5 mm by 0.5 mm section of the monolayer two-dimensional cardiac tissues used in this study.  $V$ ,  $I_{tot}$ , and  $C_m$  represent the voltage, total ionic current, and capacitance used at each node. The diffusion coefficient between hMSCs and their neighboring nodes was  $D_{hCM-hMSC}$ , while the diffusion coefficient between neighboring hCMs was  $D_{hCM}$ . To create anisotropic conditions,  $D_{hCM,x}$  and  $D_{hCM-hMSC,x}$  were four times  $D_{hCM,y}$  and  $D_{hCM-hMSC,y}$ , respectively.

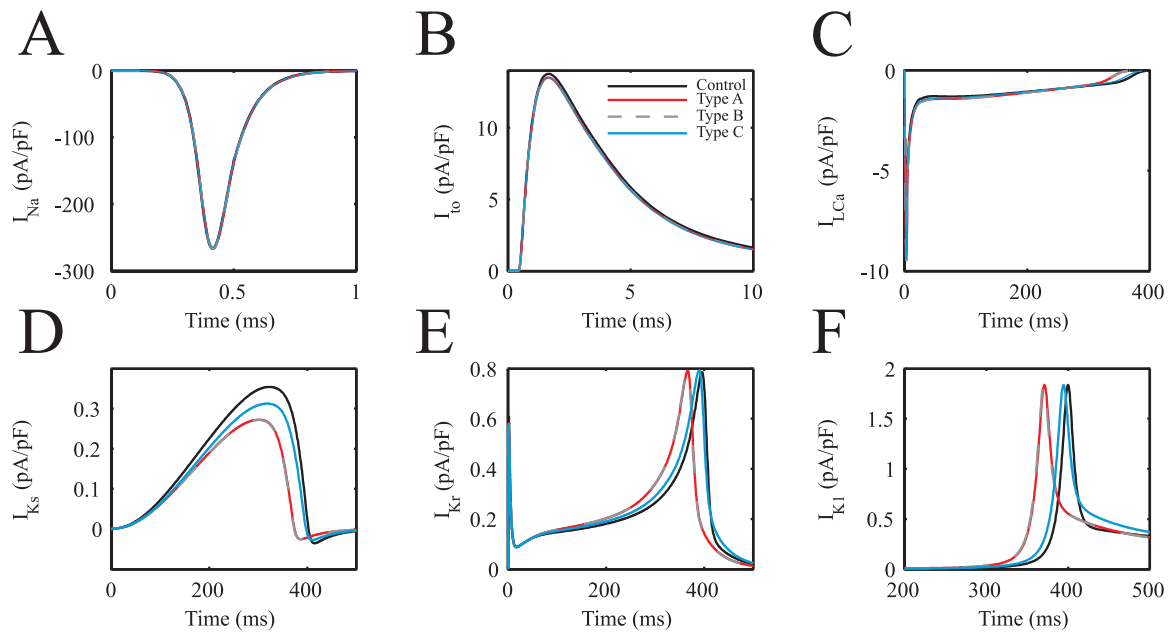


**Fig S9: Underlying Effects of hMSCs on hCM Ionic Currents During an Action Potential:**

hMSCs were coupled to midcardial hCMs in a 1:1 ratio to better understand the underlying effects of each type of hMSC. The hCM ionic currents analyzed include: (A)  $I_{Na}$ , (B)  $I_{fo}$ , (C)  $I_{LCa}$ , (D)  $I_{Ks}$ , (E)  $I_{Kr}$ , and (F)  $I_{K1}$ . The largest effects occurred during phases 2, 3, and 4 of action potentials, when outward potassium currents govern repolarization. hEAG1-functional hMSCs resulted in the earliest initiation of phases 3 and 4.

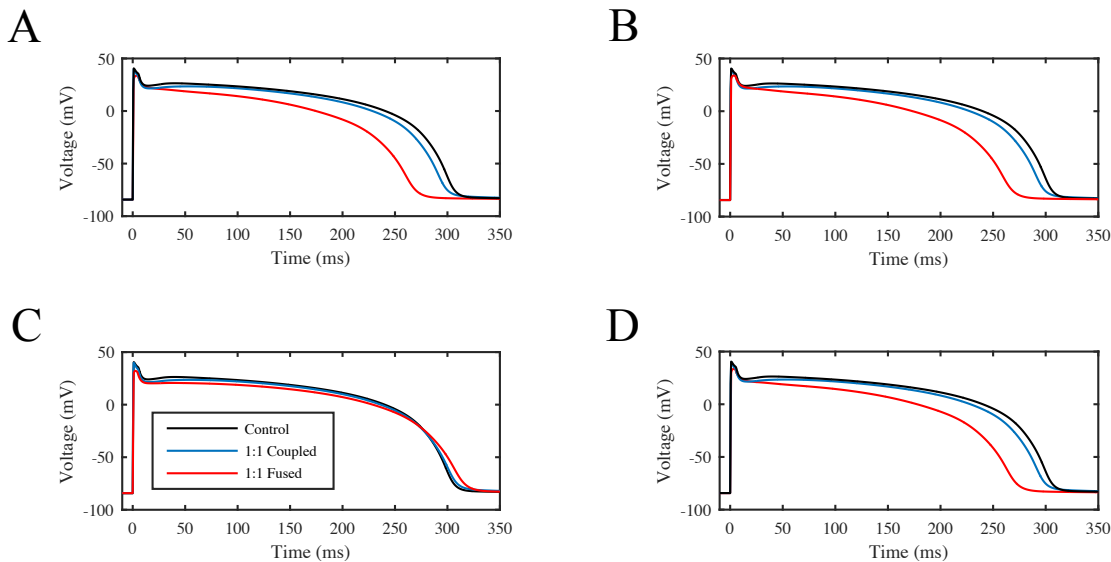


**Fig S10: Effects of hMSC Coupling and Fusion on Endocardial hCMs:** The three hMSC models developed in this study were coupled and fused to endocardial hCM electrophysiological models 1:1 to develop insight into how these two cell types interact. (A) Type A hMSCs were coupled and fused to endocardial hCMs, resulting in a significant decrease in endocardial hCM APD. (B) Type B hMSCs were coupled and fused to endocardial hCMs, resulting in a similar effect as with the type A hMSCs. (C) Type C hMSCs, absent of delayed rectifier-like hEAG1 channel activity, had a noticeably smaller effect on endocardial hCM APD. (D) A mixed population of hMSCs (i.e., all three families of hMSCs weighted based on their approximate prevalence in vitro) were coupled and fused to endocardial hCMs, resulting in similar effects as types A and B hMSCs.

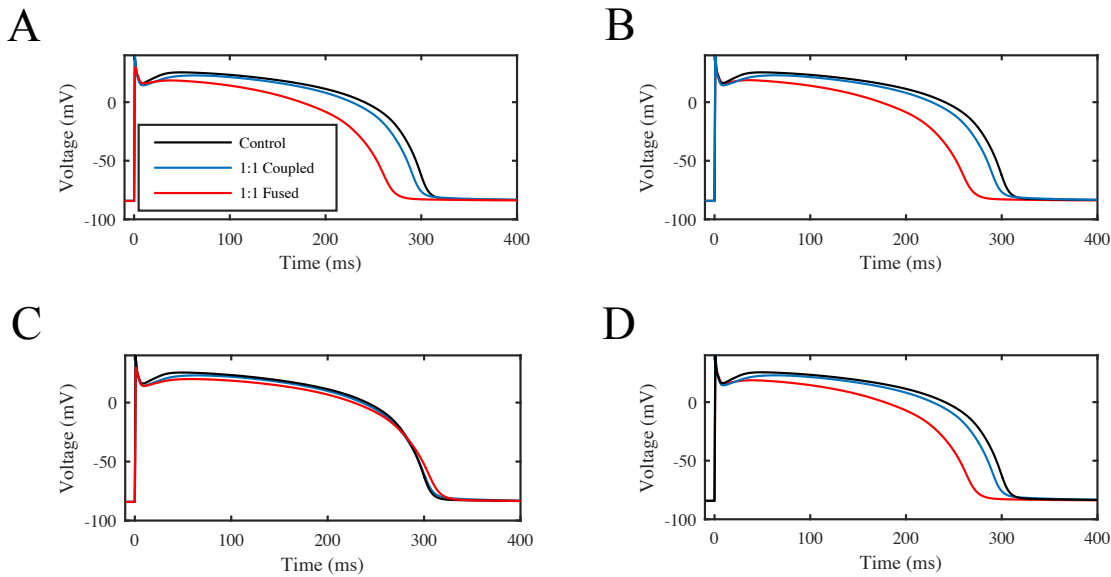


**Fig S11: Effects of hMSC Coupling and Fusion on Epicardial hCMs:** The three hMSC models developed in this study were coupled and fused to epicardial hCM electrophysiological models 1:1 to develop insight into how these two cell types interact. (A) Type A hMSCs were coupled and fused to epicardial hCMs, resulting in a significant decrease in epicardial hCM APD. (B) Type B hMSCs were coupled and fused to epicardial hCMs, resulting in a similar effect as with the type A hMSCs. (C) Type C hMSCs, absent of delayed rectifier-like hEAG1 channel activity, had a noticeably smaller effect on epicardial hCM APD. (D) A mixed population of hMSCs (i.e., all three families of hMSCs weighted based on their approximate prevalence in vitro) were coupled and fused to epicardial hCMs, resulting in similar effects as types A and B hMSCs.

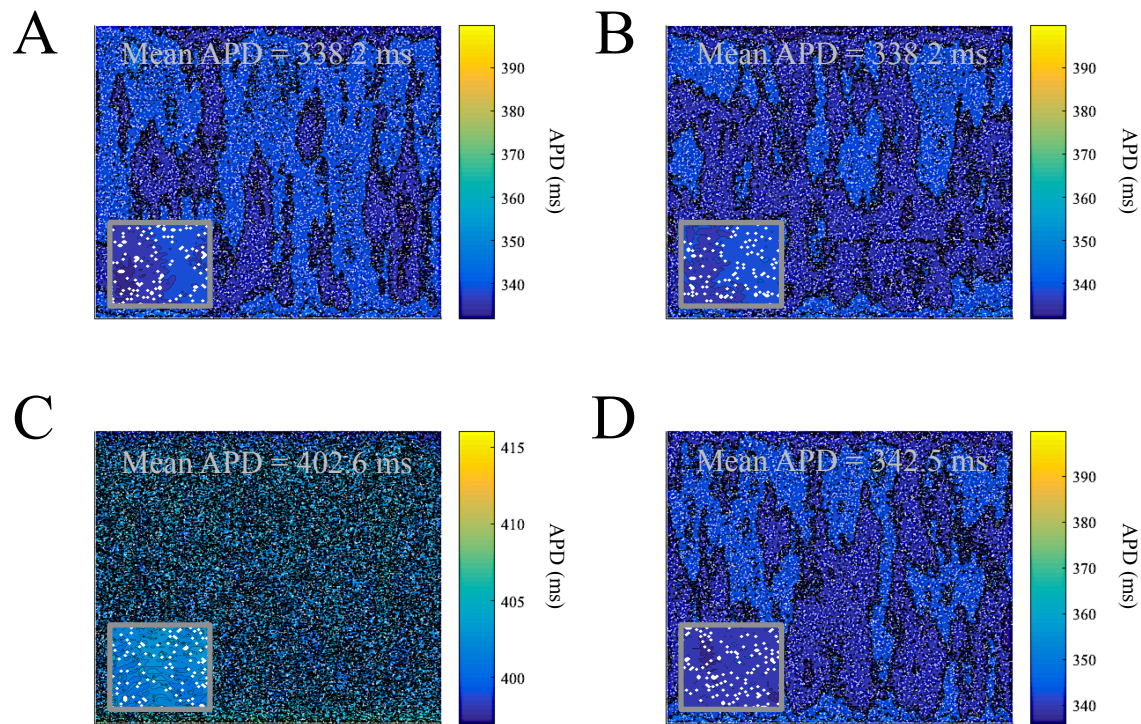


**Fig S12: APD Map of Cardiac Tissue With 5% hMSCs Inserted:** APD maps for cardiac tissue with 5% of types (A) A, (B) B, (C) C, and (D) mixed populations of hMSCs based on approximate prevalence in vitro. Top inset shows the mean APD of the tissue, and bottom left inset shows a 10x zoom on the center of the tissue. White dots represent the random locations of hMSCs.

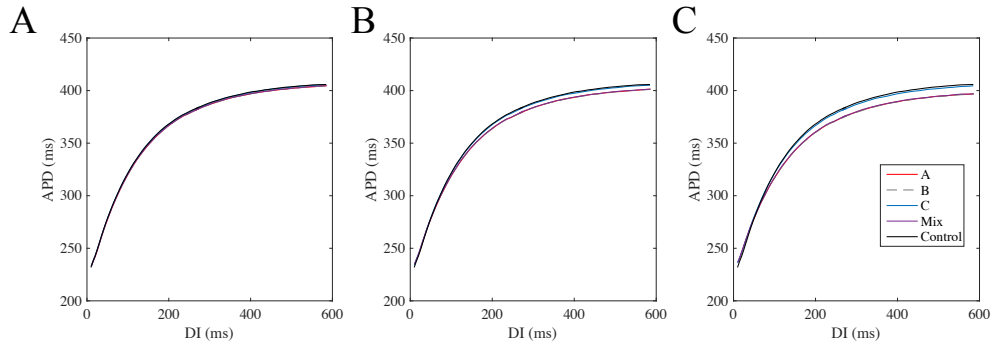


**Fig S13: Restitution Curves Following 5%, 15%, and 25% hMSC-hCM Coupling:** APD restitution slopes when coupling (A) 5%, (B) 15%, and (C) 25% hMSCs were examined for insight into electrical instability. At 5% hMSC coupling, there were indistinguishable effects on the APD restitution curve. At higher hMSC coupling, each type of hMSC slightly reduced the maximum APD restitution slope compared to the control (0% hMSC) condition.

**Supplementary Figure References:**

1. Li GR, Sun H, Deng X, Lau CP. Characterization of ionic currents in human mesenchymal stem cells from bone marrow. *Stem cells* (Dayton, Ohio). 2005 Mar;23(3):371–382.

**Table A: Parameter Values For Modeling hMSCs**

Parameter	Definition	Value	Reference
$R$	Gas Constant	8.314 J/mol/K	[1]
$T$	Temperature	310 K	[2]
$F$	Faraday Constant	96.485 C/mmol	[1]
$C_{m,hMSC}$	Cell Capacitance	59.7 pF	[3]
$C'_{m,hMSC}$	Specific Cell Capacitance	1 $\mu$ F/cm <sup>2</sup>	[3]
$S_{hMSC,x}$	Specific Area	2.262 $\mu$ m <sup>-1</sup>	[4]
$\rho_{hMSC,x}$	Cellular Resistivity	330 $\Omega$ ·cm	[3-6]
$G_{gap}$	Gap Conductance	1.5 nS	[5]
$g_{gap}$	Single-Channel Gap Conductance	50 pS	[5]
$[K_i^+]$	Intracellular Potassium Concentration	140 mM	[2]
$[Na_i^+]$	Intracellular Sodium Concentration	5 mM	[2]
$[Ca_i^{+2}]$	Intracellular Calcium Concentration	100 nM	[2]
$[K_o^+]$	Extracellular Potassium Concentration	5.4 mM	[2]
$[Na_o^+]$	Extracellular Sodium Concentration	140 mM	[2]
$[Ca_o^{+2}]$	Extracellular Calcium Concentration	2 mM	[2]

**Table B: IKCa Formulations**

---

---

Fitted Calcium Activated Potassium Channel Equations

---

$$I_{\text{KCa}} = 10.0x(V - E_{\text{K}})$$

$$\frac{dx}{dt} = \frac{x_{\infty} - x}{\tau_x}$$

$$x_{\infty} = \frac{1}{1 + e^{\frac{V - 94.1}{-15.8}}}$$

$$\tau_x = 9.9e^{-(\frac{V - 17.5}{19.8})^2} + 3.5$$

$$\alpha_x = \frac{x_{\infty}}{\tau_x}$$

$$\beta_x = \frac{1 - x_{\infty}}{\tau_x}$$

$$E_K = \frac{RT}{F} \ln \frac{[K_o^+]}{[K_i^+]}$$

**Table C: Idr Formulation**

---

Fitted Delayed Rectifier Potassium Channel Equations

---

$$I_{\text{dr}} = 4.6y(V - E_k)$$

$$\frac{dC_1}{dt} = \delta C_2 - \gamma C_1$$

$$\frac{dC_2}{dt} = \gamma C_1 + \beta y - (\alpha + \delta) C_2$$

$$\frac{dy}{dt} = \alpha C_2 - \beta y$$

$$\alpha = \frac{0.45}{1 + 15.9e^{-\frac{V+30.7}{36.7}}}$$

$$\beta = 0.0315e^{-\frac{V-10}{18.2}}$$

$$\gamma = \frac{0.025}{1 + 27.9e^{\frac{V+36.7}{-26.7}}} + \frac{1.71e^{\frac{-(V+84.0)^2}{390.3}}}{1 + e^{\frac{V+140.0}{10.0}}}$$

$$\delta = 0.0072e^{\frac{V-80}{68.2}} + \frac{36.936e^{\frac{-(V+120.5)^2}{614.3}}}{1 + e^{\frac{V+140.0}{10.0}}}$$

$$E_K = \frac{RT}{F} \ln \frac{[K_o^+]}{[K_i^+]}$$


---

**Table D: ILCa Formulations**

---

Fitted L-type Calcium Channel Equations

---

$$I_{\text{LCa}} = 9.5df \frac{VF^2}{RT} \frac{[\text{Ca}_i^{+2}]e^{2VF/RT} - 0.341[\text{Ca}_o^{+2}]}{e^{2VF/RT} - 1}$$

$$\frac{dd}{dt} = \frac{d_\infty - d}{\tau_d}$$

$$\frac{df}{dt} = \frac{f_\infty - f}{\tau_f}$$

$$d_\infty = \frac{1}{1 + e^{\frac{V + 7.5}{-6.7}}}$$

$$f_\infty = \frac{1}{1 + e^{\frac{V + 38.3}{4.4}}}$$

$$\tau_d = 0.8e^{-(\frac{V - 1.6}{19.0})^2} + 0.3$$

$$\tau_f = 15.7e^{-(\frac{V - 3.9}{9.5})^2} + 15$$

---

**Table E: Ito Formulations**

---

Fitted Transient Outward Potassium Channel Equations

---

$$I_{\text{to}} = 10.5rs(V - E_K) + 2.4r_{\text{sus}}(V - E_K)$$

$$\frac{dr}{dt} = \frac{r_\infty - r}{\tau_r}$$

$$\frac{ds}{dt} = \frac{s_\infty - s}{\tau_s}$$

$$r_\infty = \frac{1}{1+e^{\frac{V-34.1}{-12.9}}}$$

$$s_\infty = \frac{1}{1+e^{\frac{V+42.3}{12.9}}}$$

$$r_{\text{sus},\infty} = \frac{1}{1+e^{\frac{V-53.5}{-21.9}}}$$

$$\tau_r = 3.6e^{-(\frac{V+4.4}{32.0})^2} + 1.5$$

$$\tau_s = 19.4e^{-(\frac{V+5.4}{34.5})} + 7.2$$

$$\tau_{r,\text{sus}} = 0.1\tau_r$$

$$E_K = \frac{RT}{F} \ln \frac{[K_o^+]}{[K_i^+]}$$

---

**Table F: INa Formulations**

---

Fitted Sodium Channel Equations

---

$$I_{Na} = 7.0m^3h(V - E_{Na})$$

$$\frac{dm}{dt} = \frac{d_\infty - m}{\tau_m}$$

$$\frac{dh}{dt} = \frac{f_\infty - h}{\tau_h}$$

$$m_\infty = \frac{1}{(1+e^{\frac{V+47.7}{-11.4}})^2}$$

$$h_\infty = \frac{1}{(1+e^{\frac{V+50.1}{2.6}})^2}$$

$$\tau_m = 0.3e^{-(\frac{V+2.7}{24.5})^2}$$

$$\tau_h = 2.9e^{-(\frac{V+3.6}{25.2})^2}$$

---

$$E_{Na} = \frac{RT}{F} \ln \frac{[Na_o^+]}{[Na_i^+]}$$

**Table G: IL Formulations**

---

Fitted Leakage Current Equations

---

$$I_{La} = 0.00073(V - E_{Ca})$$

$$I_{Lb} = 0.03(V - E_K)$$

$$I_{Lc} = 0.0195(V - E_{Ca})$$

$$E_{Ca} = \frac{RT}{2F} \ln \frac{[Ca_o^+]}{[Ca_i^+]}$$

$$E_K = \frac{RT}{F} \ln \frac{[K_o^+]}{[K_i^+]}$$

---

**Table H: Cardiac Sheet Wavelengths with 5%, 15%, and 25% hMSC Insertion**

$\lambda = \text{APD} \times \text{CV}$			
hMSC Type	$\lambda_{5\% \text{ hMSC}} \text{ (cm)}$	$\lambda_{15\% \text{ hMSC}} \text{ (cm)}$	$\lambda_{25\% \text{ hMSC}} \text{ (cm)}$
A	15.6	8.2	6.3
B	15.6	8.2	6.3
C	18.6	10.4	8.2
Mix	15.8	8.3	6.4

### **Supplementary Tables References:**

1. Mohr P, Taylor BN, and Newell D. Codata recommended values of the fundamental physical constants: 2006. *Rev. Mod. Phys.*, 80:633–730, June 2006.
2. Bard Ermentrout G. Passive cell models: *Comp neuroscience*.
3. Li GR, Sun H, Deng X, and Lau CP. Characterization of ionic currents in human mesenchymal stem cells from bone marrow. *Stem Cells*, 23(3):371–82, March 2005.
4. Docheva D, Padula D, Popov C, Mutschler W, Clausen-Schaumann H, and Schieker M. Researching into the cellular shape, volume and elasticity of mesenchymal stem cells, osteoblasts and osteosarcoma cells by atomic force microscopy. *J. Cell. Mol. Med.*, 12(2):537–52, April 2008.
5. Valiunas V, Doronin S, Valiuniene L, Potapova I, Zuckerman J, Walcott B, Robinson RB, Rosen MR, Brink PR, and Cohen IS. Human mesenchymal stem cells make cardiac connexins and form functional gap junctions. *J. Physiol.*, 555(3):617–626, Feb 2004.
6. Jongsma HJ and Wilders R. Limitations of the dual voltage clamp method in assaying conductance and kinetics of gap junction channels. *Biophysical Journal*, 63(4):942–953, Oct 1992.

**Chapter 6: Experimental and Computational Insight into Human Mesenchymal Stem Cell  
Paracrine Signaling and Heterocellular Coupling Effects on Cardiac Contractility and  
Arrhythmogenicity**

*Note: The following chapter is a modified draft of an original first-author research article published in Circulation Research:*

Mayourian J, Cashman TJ, Ceholski DK, Johnson BV, Sachs D, Kaji DA, Sahoo S, Hare JM, Hajjar RJ, Sobie EA, Costa KD. Experimental and Computational Insight into Human Mesenchymal Stem Cell Paracrine Signaling and Heterocellular Coupling Effects on Cardiac Contractility and Arrhythmogenicity. *Circulation Research*. 2017;121(4),411-423.

JM conceived the idea, collected and analyzed the computational and tissue engineering functional data (other than Figure 4), and wrote the manuscript. The current *Circulation Research* CTA states, "authors may use parts of the work (eg, tables, figures) in subsequent works without requesting permission from the AHA."

The manuscript was selected as an Editor's pick.

## 6.1 Abstract

**Rationale:** Myocardial delivery of human mesenchymal stem cells (hMSCs) is an emerging therapy for treating the failing heart. However, the relative effects of hMSC-mediated heterocellular coupling (HC) and paracrine signaling (PS) on human cardiac contractility and arrhythmogenicity remain unresolved.

**Objective:** To better understand hMSC PS and HC effects on human cardiac contractility and arrhythmogenicity by integrating experimental and computational approaches.

**Methods and Results:** Extending our previous hMSC-cardiomyocyte HC computational model, we incorporated experimentally calibrated hMSC PS effects on cardiomyocyte L-type calcium channel/SERCA activity and cardiac tissue fibrosis. Excitation-contraction simulations of hMSC PS-only and combined HC+PS effects on human cardiomyocytes were representative of human engineered cardiac tissue (hECT) contractile function measurements under matched experimental treatments. Model simulations and hECTs both demonstrated hMSC-mediated effects were most pronounced under PS-only conditions, where developed force increased approximately 4-fold compared to non-hMSC-supplemented controls during physiologic 1-Hz pacing. Simulations predicted contractility of isolated healthy and ischemic adult human cardiomyocytes would be minimally sensitive to hMSC HC, driven primarily by PS. Dominance of hMSC PS was also revealed in simulations of fibrotic cardiac tissue, where hMSC PS protected from potential pro-arrhythmic effects of HC at various levels of engraftment. Finally, to study the nature of the hMSC paracrine effects on contractility, proteomic analysis of hECT/hMSC conditioned media predicted activation of PI3K/Akt signaling, a recognized target of both soluble and exosomal fractions of the hMSC secretome. Treating hECTs with exosome-enriched, but not exosome-depleted, fractions of the hMSC secretome recapitulated the effects

observed with hMSC conditioned media on hECT developed force and expression of calcium handling genes (e.g., SERCA2a, L-type calcium channel).

**Conclusions:** Collectively, this integrated experimental and computational study helps unravel relative hMSC PS and HC effects on human cardiac contractility and arrhythmogenicity, and provides novel insight into the role of exosomes in hMSC paracrine-mediated effects on contractility.

## **6.2 Novelty and Significance**

### ***What Is Known?***

- Delivery of human mesenchymal stem cells (hMSC) offers a promising therapy for heart repair.
- The hMSC-cardiomyocyte interactome involves both paracrine signaling (PS) and heterocellular coupling (HC) mechanisms.
- Understanding the contributions of PS and HC mechanisms to cardiac contractility and arrhythmogenicity would help optimize the therapeutic potential of hMSCs.

### ***What New Information Does This Article Contribute?***

- Complementary experimental and computational approaches reveal distinct PS and HC effects of hMSCs on cardiac contractility and arrhythmogenicity.
- Functional and molecular data support a key role of exosomes in hMSC paracrine-mediated increase of cardiac contractility.
- Novel in silico insights help resolve disparate reports of potential pro-arrhythmic risks of hMSCs in vitro versus anti-arrhythmic benefits of hMSCs in vivo.

The exciting promise of emerging hMSC cardiotherapies motivates a systematic investigation into underlying mechanisms of action, aiming to minimize potential risks and maximize therapeutic benefits. In this study, computational and experimental approaches were combined to distinguish the effects of hMSC PS and HC on cardiac contractility and arrhythmogenicity. Based on a newly developed mathematical model and human engineered cardiac tissue (hECT) measurements, hMSC-mediated effects on cardiac contractility were most pronounced under PS-only conditions. Simulations of fibrotic cardiac tissue revealed hMSC PS protected from potentially pro-arrhythmic effects of HC, providing novel insight into the discrepancy between in vitro and pre-clinical/clinical findings. We further show that exosomes likely play a key role in hMSC paracrine-mediated effects on hECT contractility and expression of calcium handling

genes. Together, this integrated experimental and computational approach provides an improved understanding of the relative effects of hMSC PS and HC on cardiac contractility and arrhythmogenicity, with evidence supporting the cardioactive potency of hMSC exosomes. Our findings motivate further investigation of how hMSC exosomes and their molecular cargo may yield increased cardiac contractility *in vivo*, ultimately maximizing the safety and efficacy of hMSC-based cardiac therapies.

### 6.3 Introduction

Cardiovascular disease remains a leading cause of morbidity and mortality worldwide.<sup>1</sup> Substantial evidence from *in vitro*,<sup>2,3</sup> pre-clinical,<sup>4-7</sup> and clinical studies<sup>8-10</sup> supports bone marrow-derived human mesenchymal stem cells (hMSCs) as a promising cardio-reparative approach.<sup>11</sup> However, in several clinical trials, stem cell delivery benefits have been modest and transient,<sup>8,9,12,13</sup> representing an opportunity for improvement.<sup>14</sup> Therefore, to optimize future hMSC-based therapies, it is essential to better understand the underlying hMSC-cardiac interactome.

It has been theorized that hMSCs reduce cardiac fibrosis<sup>15</sup> and enhance angiogenesis<sup>16</sup> largely through paracrine signaling (PS) mechanisms.<sup>17,18</sup> Moreover, recent studies have demonstrated that hMSC PS can modulate cardiomyocyte ion channel/pump activity.<sup>19-21</sup> For example, DeSantiago et al. observed that hMSC-conditioned media increased L-type calcium channel (LTCC) current and sarco/endoplasmic reticulum calcium-ATPase (SERCA) activity in mouse ventricular myocytes, yielding an increase in the calcium transient amplitude and an acceleration of the calcium transient decay.<sup>20</sup> Askar et al. later observed that hMSC paracrine conditioned media prolonged action potential duration of neonatal rat cardiomyocytes in a dose-dependent manner.<sup>19</sup>

On the other hand, hMSCs have been shown to form gap junctions with cardiomyocytes,<sup>22</sup> leading to direct heterocellular coupling (HC) and spontaneous fusion<sup>23</sup> that can influence cardiomyocyte electrophysiology. Indeed, our recent computational modeling study demonstrated that if one considers HC mechanisms alone (i.e., neglecting PS), hMSCs would impact cardiac electrophysiology via shortened action potential and decreased conduction velocity, which could potentially increase vulnerability to re-entry.<sup>24</sup>

Taken together, hMSC HC and PS mechanisms each have the potential to modulate single-cell cardiomyocyte action potential and calcium handling waveforms, as well as tissue-level conduction, constituting well-established determinants of excitation-contraction coupling

and arrhythmogenicity in myocardium. However, the relative contributions of hMSC-mediated HC and PS mechanisms on these components of human cardiac function have yet to be established, reflecting challenges with isolating these effects in experimental preparations.

In this study, we utilize both mathematical modeling and three-dimensional human engineered cardiac tissues (hECTs) to better understand hMSC PS and HC effects on human cardiac contractility and arrhythmogenicity. First, we build on our previously established hMSC-cardiomyocyte HC computational model<sup>24</sup> to also experimentally calibrate<sup>25,26</sup> hMSC PS effects on single-cell cardiomyocyte ion channel/pump activity and tissue-level fibrosis. Next, we validate this mathematical model using hECTs under matched experimental hMSC-mediated HC and PS treatments. Finally, we perform proteomic analysis of hECT/hMSC conditioned media and subsequent functional testing/molecular characterization of hECTs treated with exosomes-depleted and exosomes-enriched fractions of the hMSC secretome to provide insight into key hMSC paracrine factors and their potential mechanisms of action.

## 6.4 Methods

An expanded Methods section describing all computational and experimental procedures and protocols is available in the Supplement.

## 6.5 Results

### 6.5.1 Multi-Species Parameter Sensitivity Analysis Reveals Key hMSC PS-Modulators of Cardiomyocyte Action Potential and Calcium Handling Metrics

To build on our previous hMSC-cardiomyocyte HC model<sup>24</sup> by incorporating select hMSC PS effects on single-cell cardiomyocyte ion channel/pump activity, we first performed unbiased hierarchical clustering on a multi-species parameter sensitivity analysis of empirically-determined hMSC PS modulators of action potential and calcium handling behavior—namely

the LTCC,<sup>20</sup> SERCA,<sup>20</sup> and transient outward current<sup>19</sup> (coefficients of determination shown in Table S1).

From this sensitivity analysis and subsequent hierarchical clustering, action potential metrics were most sensitive to LTCC activity, while calcium handling metrics were highly sensitive to SERCA activity (Figure S1). No metric was most influenced by transient outward current perturbation, the least experimentally studied effect; hMSC PS effects on transient outward current were therefore neglected in subsequent models.

### *6.5.2 Experimental Calibration of the hMSC PS Model*

hMSC PS has been reported to affect single-cell ion channel/pump activity,<sup>19,20</sup> as well as to favorably remodel fibrotic cardiac tissue.<sup>21,27-33</sup> The pro-arrhythmic effects of increased fibrosis are well recognized,<sup>34-36</sup> so including anti-fibrotic effects of hMSC PS was a priority in developing a tissue-level model. To develop a model of PS anti-fibrotic effects, we performed an extensive literature search to see if we could uncover a relationship across studies and species between hMSC delivery levels and anti-fibrotic effects.<sup>21,27-33</sup> To compare between species, hMSC delivery levels in each study were normalized to the approximate number of left ventricular myocytes in that species. Interestingly, when we normalized data across nine studies, we found a nearly linear relationship between anti-fibrotic effects and hMSC delivery within a range of approximately 20-60% hMSCs (Figure S2). This consistency between studies allowed us to confidently and easily incorporate anti-fibrotic effects into the tissue level model to test for arrhythmogenicity.

Incorporating the effects of hMSC PS on single-cell ion channel/pump activity was not straightforward, as limited dose-response data were available in the literature for characterizing the single-cell responses of LTCC and SERCA activity to varying doses of hMSC paracrine factors. Given this uncertainty, and the fact that dose-response relationships will vary between experiments, we adopted an established method<sup>25,26</sup> and calibrated a population of models by

closely matching simulation outputs to corresponding experimental recordings for different species at three hMSC PS dosages (Figure 1). The resultant population of models would therefore effectively represent hMSC PS effects on cardiomyocyte action potential and calcium transient across a range of hMSC dosages.

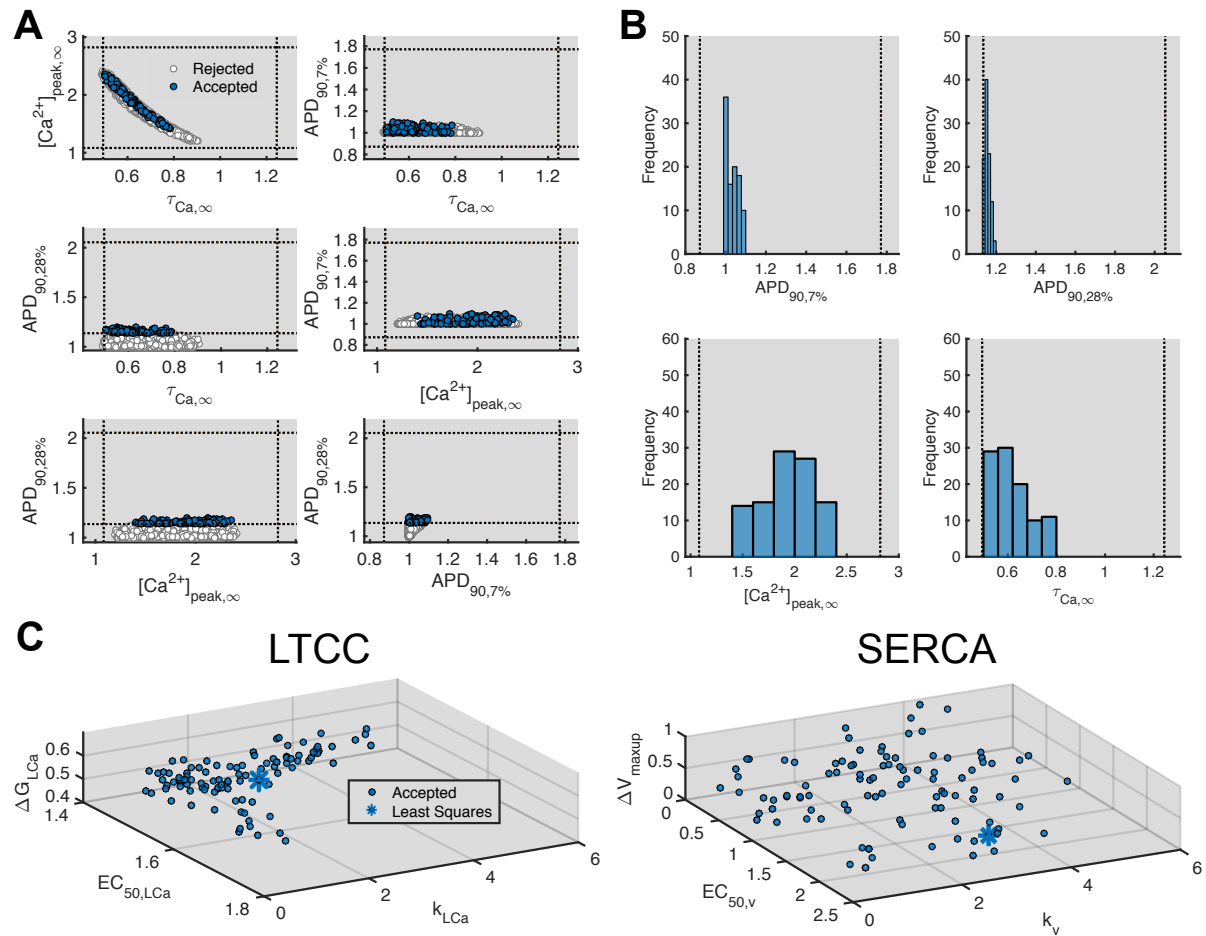


**Figure 1: Experimentally Calibrating hMSC PS Effects.** hMSC PS effects on LTCC and SERCA activity were experimentally calibrated. **(A)** Scatter plots of the initial population (white dots) filtered (blue dots) to be within one standard deviation (boxed region) of action potential duration to 90% repolarization ( $APD_{90}$ ), calcium transient duration at 50% decay ( $\tau_{Ca}$ ), and diastolic-subtracted calcium transient amplitude ( $[Ca^{2+}]_{peak}$ ) metrics across various experimental

species and hMSC dosages (7%, 28%, or saturated ( $\infty$ ))). **(B)** Histograms illustrating distributions of the output simulation metrics resulting from the accepted population of calibrated models. **(C)** Accepted sets of calibrated model parameters of hMSC PS dose response curves (see Online Data Supplement for details). Non-standard abbreviations:  $\Delta G_{LCa}$  and  $\Delta V_{max\ up}$  denote maximum saturated effects of hMSC PS on LTCC and SERCA activity, respectively;  $k_{LCa}$  and  $k_V$  denote respective Hill coefficients;  $EC_{50,LCa}$  and  $EC_{50,V}$  denote respective half maximum effective concentrations. Asterisk point in panel C denotes the least squares calibrated model defined in the Online Data Supplement.

We generated a large initial population of 2,500 model variants with randomly chosen parameter sets within physiologically and empirically relevant bounds (Table S2). In contrast with previous studies,<sup>25,26</sup> however, the parameters varied were not maximal conductances but rather parameters that controlled the sensitivity of myocytes to PS and the maximal effects caused by saturating PS (see Supplementary Methods). The initial population was then filtered to retain only select models (Figure 1A; blue dots) that were consistent (i.e., within one standard deviation) with all experimentally observed data ranges (Figure 1A; within boxed region) of hMSC PS dose-dependent effects on action potential and calcium transient metrics<sup>19,20</sup> (Figure 1A). This calibration process reduced the initial population to 100 accepted model parameter sets. The histograms in Figure 1B illustrate the distribution of output simulation metrics resulting from the range of accepted model parameters. Figure 1C shows the distribution of parameters used to model PS effects on LTCC current (left) and SERCA activity (right) for the population of 100 accepted models. In contrast to the latter, the former case is constrained (Figure 1C) with a relationship between the Hill coefficient and the half-maximal dose concentration.

In addition to our previously established model of hMSC-myocyte HC through gap junctions,<sup>24</sup> this computational model now also includes hMSC PS effects on cardiomyocyte

LTCC and SERCA activity, as well as hMSC PS anti-fibrotic effects. To our knowledge, this is the most comprehensive model capable of reproducing a majority of the non-vasculature-related effects of hMSCs on cardiomyocyte action potential, calcium transient, and excitation-contraction metrics, as further examined below.

#### *6.5.3 hMSC PS and HC Effects on Action Potential and Calcium Handling Behavior*

First, we simulated the effects of hMSC HC-only, hMSC PS-only, and hMSC HC+PS mechanisms on the cardiomyocyte action potential and calcium transient at 100% hMSC supplementation per myocyte (i.e., 1:1 hMSC-cardiomyocyte ratio) for multiple cardiomyocyte species (Figure 2), representing the high end of hMSC:myocyte ratios used in prior in vitro co-culture studies.<sup>20</sup> hMSC PS was modeled using the least squares model (Figure 1C and Table S3). As shown in the Figure S3, our model can be readily adapted to incorporate time-dependent paracrine effects, such as in vitro data from DeSantiago et al.<sup>20</sup> Nevertheless, the remainder of this modeling study uses steady-state solutions to examine longer-term PS effects, which is more relevant to our hECT experiments.

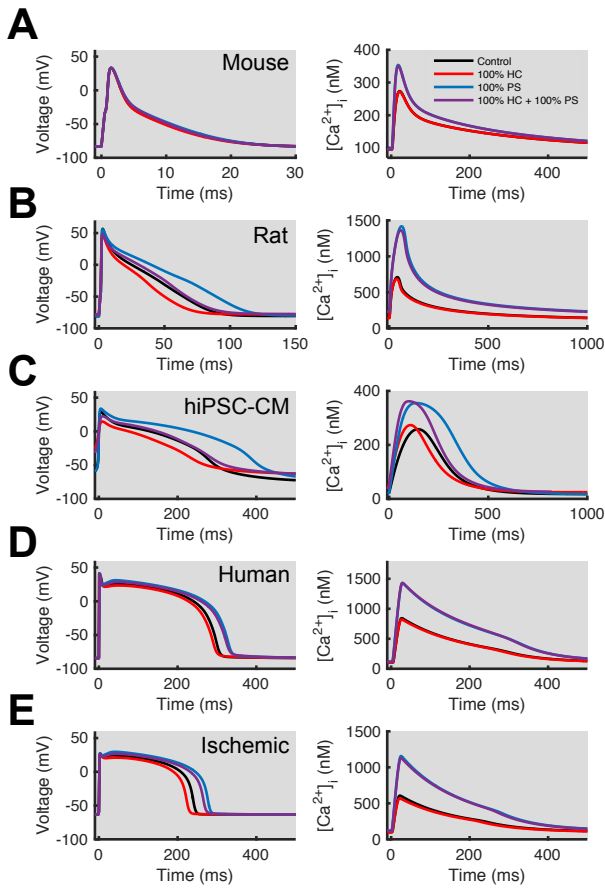


**Figure 2: hMSC PS and HC Effects on Multi-Species Cardiomyocyte Action Potential and Calcium Transient.** The effects of hMSC HC-only (red), hMSC PS-only (blue), and hMSC HC+PS (purple) were simulated on (A) mouse, (B) rat, (C) human induced pluripotent stem cell-derived cardiomyocyte (hiPSC-CM), (D) healthy, and (E) ischemic human adult cardiomyocyte action potential (left) and calcium transient (right) at 100% hMSC supplementation per myocyte, compared to unsupplemented controls (black).

Across all cell types, HC tends to decrease action potential duration to 90% repolarization ( $APD_{90}$ ), whereas PS increases  $APD_{90}$  and calcium transient amplitude, although the magnitude of the effect is cell-type and hMSC dose-dependent (Figure 2 and Figures S4-S5). As enforced in our process of calibrating model populations to experimental data (Figure 1), all simulated dose-dependent effects of hMSC PS-only mechanisms of myocyte action

potential and calcium transient metrics were within one standard deviation of published data for a range of experimental conditions and cardiomyocyte species. Furthermore, we observed that simulated dose-dependent effects of combined hMSC HC+PS mechanisms on myocyte action potential and calcium transient metrics were also consistent with published data. For example, Askar et al.<sup>19</sup> demonstrated that APD<sub>90</sub> increases, while Chang et al.<sup>37</sup> reported no significant effect, for rat myocytes co-cultured approximately 4:1 with hMSCs (i.e., ~25% hMSC dose). Our simulations predicted a modest prolongation of APD<sub>90</sub> under matched conditions (Online Figure IV), intermediate between these findings. Our simulations were also consistent with calcium transient measurements in mouse ventricular cardiomyocytes,<sup>20</sup> where the effects on peak calcium transient and calcium transient decay rate with hMSC HC+PS treatment were not significantly different compared to the hMSC PS-only condition (Figure 2A and Figure S5).

The consistency of our findings with various experimental trends<sup>19,20,37</sup> motivated further validation of simulated hMSC HC and PS effects on cardiac contractile function by comparing to experiments performed with three-dimensional hECTs. Interestingly, the various cardiomyocyte models predicted that human induced pluripotent stem cell-derived cardiomyocytes (hiPSC-CMs)—similar to those used in our hECTs—showed the greatest distinction between hMSC HC+PS and PS-only effects on the action potential and calcium transient (Figure 2C). We therefore hypothesized that hECTs may be well suited to empirically delineate the effects of hMSC HC and PS on contractility.

#### *6.5.4 Counteracting Effects of hMSC PS and HC on hECT Contractility*

Our custom bioreactor system<sup>38</sup> facilitates simultaneous culture of six hECTs that are each comprised of either un-supplemented (-hMSC) or 10% hMSC-supplemented (+hMSC) cellular composition. hMSCs were employed from lots used in recently published clinical trials.<sup>9,13</sup> Prior to using the hMSCs, their tri-lineage potential was confirmed, as shown in Figure S6.

Using this custom bioreactor system, we studied four different experimental groups as illustrated in Figure 3A: 1) hECTs without co-cultured hMSCs (-hMSC; black), 2) hECTs with co-cultured hMSCs (+hMSC; purple), or 3) and 4) alternating +hMSC and -hMSC hECTs in a shared paracrine media bath (red and blue, respectively). Note that equalizing the total number of hECTs in each bioreactor avoids inequalities in total metabolic demand that could introduce a confounding factor; however, this results in a final sample size for the shared media groups being about half that for the +hMSC and -hMSC groups. These four groups correspond to model conditions of approximately: 1) 0% HC + 0% PS; 2) 10% HC + 10% PS; 3) 10% HC + 5% PS; and 4) 0% HC + 5% PS hMSC treatment interventions, respectively. Images of hECTs on the bioreactor and example twitch force measurements are shown in Figures 3B and 3E, respectively. After functional assessment, selected hECTs were fixed, sectioned, and stained for cardiac-troponin-T, revealing similar myofibrillar structures for both -hMSC (Figure 3F) and +hMSC (Figure 3G) tissues. Based on hECT cross-sectional area (Figure 3C-D), hMSC PS alone caused tissue compaction comparable to having hMSCs co-cultured within the tissue; furthermore, there was no significant difference in resting (diastolic) force between all groups (data not shown), suggesting similar passive tissue stiffness. Finally, hMSCs are known to mechanically couple to myocytes.<sup>39</sup> Altogether, this suggests differences in contractile properties of hECT experimental groups largely reflect underlying cardiomyocyte contractility.

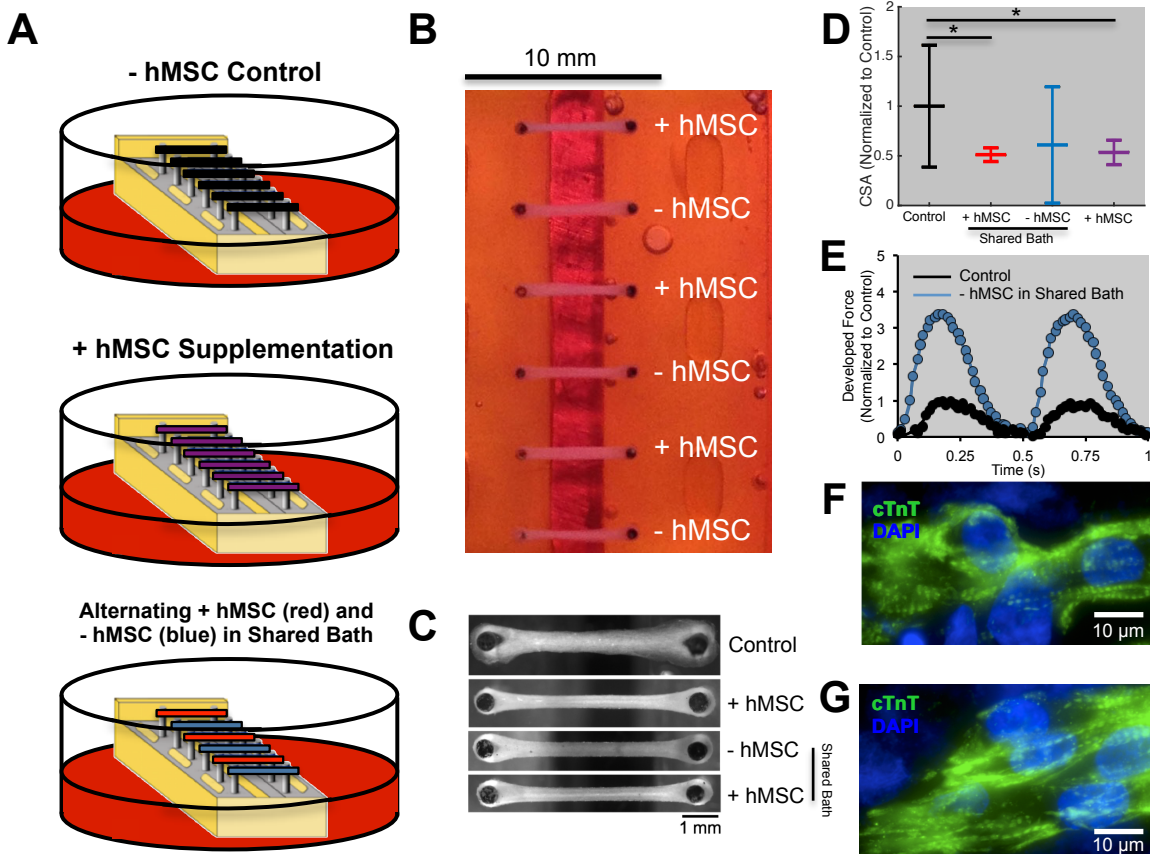


**Figure 3: Schematic and Structure of hECTs in the Bioreactor.** (A) Schematic of the four experimental hECT groups tested. (B-C) Sample images of hECTs on the bioreactor (scale bars inset). (D) Cross-sectional area (CSA) for each hECT group ( $n=10-22$ ) normalized to control. (E) Sample force measurements of control and -hMSC (shared bath) intervention conditions normalized to control. Sarcomeric organization and alignment in both (F) -hMSC and (G) +hMSC hECTs stained with cardiac troponin-T (cTnT, green) and DAPI (blue). \*  $p<0.05$ .

To test the predictive power of our calibrated population of models, we simulated excitation-contraction behavior of hiPSC-CMs subjected to experimentally calibrated hMSC PS (Figure 1) and HC (Figure S7) mechanisms, and compared the simulation results to developed force (DF), maximum rate of contraction ( $+dF/dt$ ), and maximum rate of relaxation ( $-dF/dt$ )

measurements of hECT contractile function under matched experimental hMSC-mediated treatments (Figure 4).

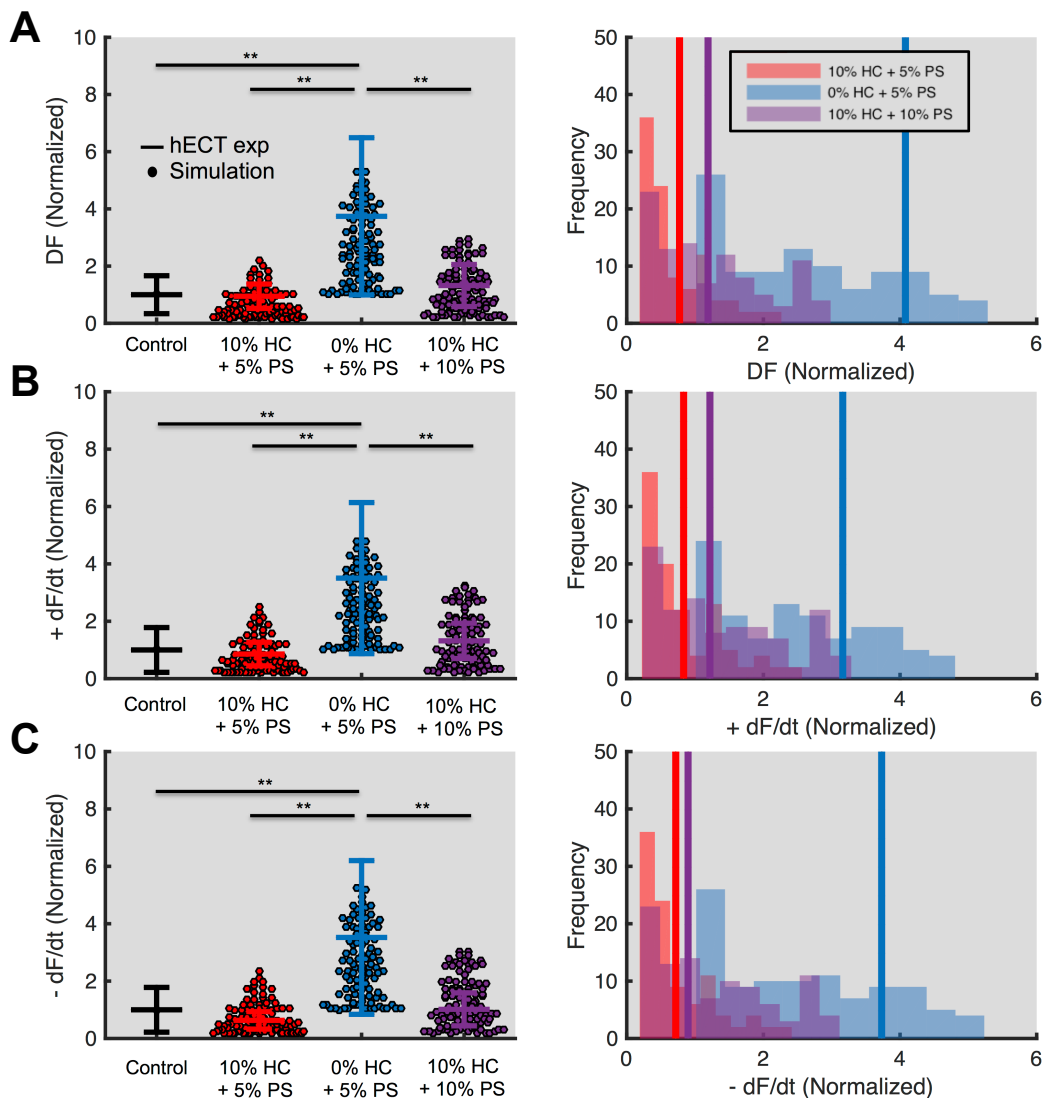


**Figure 4: Model Comparison with hECT Measurements Under hMSC HC and PS**

**Interventions.** Comparison of control (n=22), 10% HC + 5% PS (n=11), 0% HC + 5% PS (n=10), and 10% HC + 10% PS (n=17) hECT measurements (mean +/- standard deviation; legend with “hECT exp” represents empirical hECT data) to simulations (circles) of all 100 accepted models in the calibration population for **(A)** DF, **(B)** +dF/dt, and **(C)** -dF/dt. All data are

normalized to control. \*\* $p<0.01$  based on ANOVA of hECT experiments. Right panel shows histograms of simulation output distributions for each contractility metric; color-coded vertical lines indicate corresponding experimental median values.

Simulations of the experimentally calibrated population of PS-only (0% HC + 5% PS) and combined HC+PS (10% HC + 5% PS and 10% HC + 10% PS) effects of hMSCs on hiPSC-CMs were representative of contractile function measurements of hECTs under matched experimental hMSC-mediated treatments (Figure 4). In fact, 63%, 63%, and 61% of simulations fell within one standard deviation of the experimental mean for DF,  $+dF/dt$ , and  $-dF/dt$ , respectively. The median of each experimental condition was squarely within the range of simulation outputs (Figure 4; right panels). Medians of simulation outputs differed from corresponding experimental medians by a range of -41% to +15%. Coincidentally, the population simulations also recapitulated the variability seen in the experimental measurements; the greatest variability was seen in the 0% HC + 5% PS group, and the least in the 10% HC + 5% PS group.

Both model simulations and hECTs demonstrated that the most pronounced hMSC-mediated effects on contractile function were under PS-only conditions (0% HC + 5% PS), where DF significantly increased by approximately 4-fold on average relative to non-hMSC-supplemented controls during physiologic 1-Hz pacing (Figure 4A). Similarly,  $\pm dF/dt$  were significantly increased by PS-only conditions, and diminished by HC (Figure 4B-C).

To explore how the apparent counteracting effects of hMSC HC and PS on immature stem cell-derived cardiomyocyte contractility demonstrated both empirically and in silico (Figure 4) translates to mature human cardiomyocytes, we modeled the sensitivity of contractile function of hiPSC-CMs (Figure 5A), healthy human adult cardiomyocytes (Figure 5B), and ischemic human adult cardiomyocytes (Figure 5C) to the least squares calibrated model (Online Table III)

with perturbations about a mean hMSC treatment condition of 10% HC and 10% PS. Coefficients of determination can be found in Table S4.

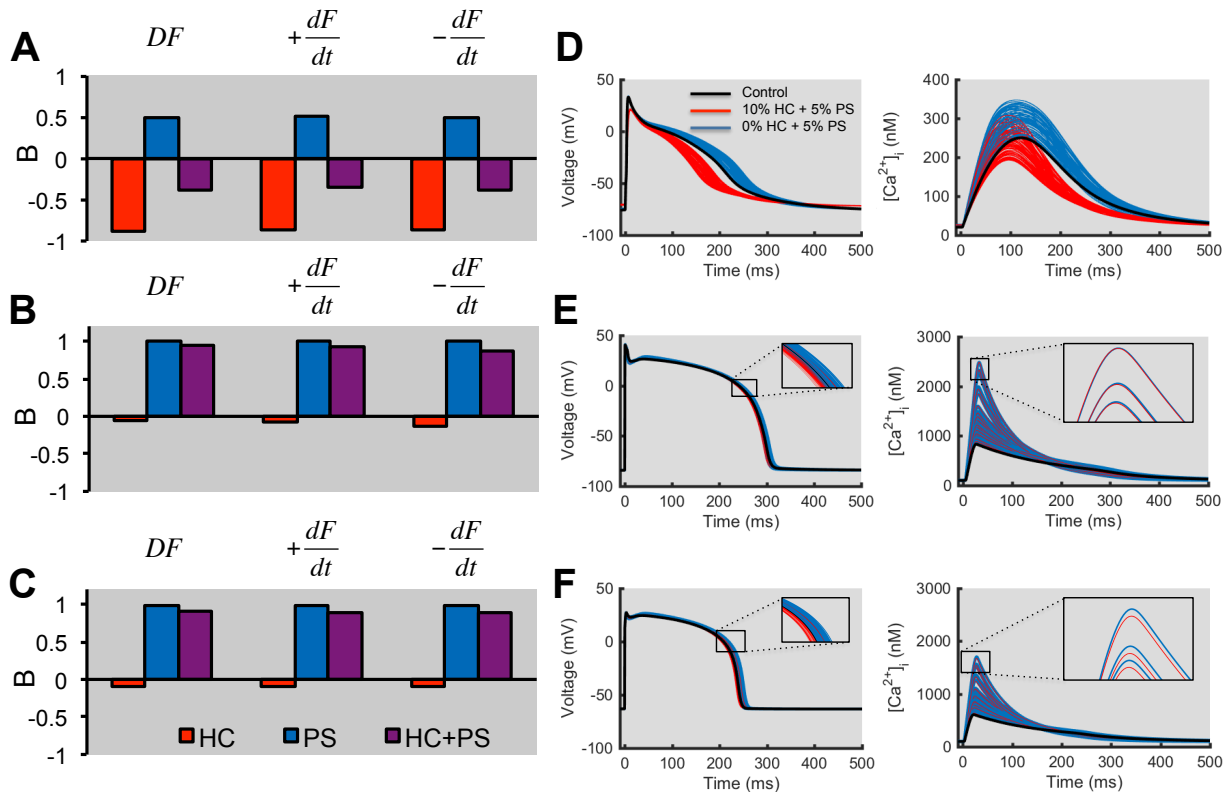


**Figure 5: Simulated hMSC HC and PS Effects on Contractile Function of Derived and Adult Human Cardiomyocytes.** A contractile function sensitivity analysis was performed for (A) hiPSC-CM, (B) healthy human adult cardiomyocyte, and (C) ischemic human adult cardiomyocyte models, with hMSC HC and PS as inputs, and DF,  $+dF/dt$ , and  $-dF/dt$  as outputs. The net sensitivity (HC+PS; purple) to hMSC supplementation is defined as the sum of the sensitivity, B, of hMSC HC (red) and PS (blue) mechanisms individually. Single cell action potential and calcium transient simulations of (D) derived and mature (E) healthy and (F) ischemic human cardiomyocytes across all 100 accepted calibration models under 10% HC + 5% PS (red) and 0% HC + 5% PS (blue) interventions versus untreated controls (black).

Consistent with above findings (Figure 4), these low levels of hMSC PS and HC treatment (relative to Figure 2 conditions) are predicted to have counteracting effects on contractile metrics such as DF and  $\pm dF/dt$  for hiPSC-CMs (Figure 5A), such that increases in contractile metrics would be most pronounced under hMSC PS-only conditions. The sensitivity analysis in Figure 5 implies there is a positive correlation between hMSC PS dosages and more pronounced effects on DF and  $\pm dF/dt$  for all cell types. Interestingly, DF sensitivity to HC was minimal in healthy and ischemic human adult cardiomyocytes (Figures 5B-C); this likely reflects the larger size and higher ion channel density of adult cardiomyocytes, which makes them less susceptible to consequences of direct coupling with non-contractile hMSCs, so that PS effects dominate. Simulations using all 100 accepted calibration models under 10% HC + 5% PS and 0% HC + 5% PS interventions confirmed these findings, as pronounced HC effects on the action potential and calcium transient were predicted for immature hiPSC-CMs, but not adult cardiomyocytes (Figures 5D-F). By contrast, hMSC PS was more potent than HC, and was predicted in some cases to restore calcium transients of ischemic myocytes to healthy cell levels (Figure 5F). Taken together, these findings demonstrate the dominant role of hMSC PS mechanisms on adult cardiomyocyte contractile function relative to HC.

#### *6.5.5 hMSC PS Protects from HC Effects on Arrhythmogenicity*

Using our models of hMSC PS and HC single-cell and tissue-level effects, we analyzed how various empirically relevant levels of hMSC delivery and engraftment affect the vulnerable window (VW) for re-entry in moderate and high diffuse fibrotic cardiac tissue (Figure 6). In this analysis, increases and decreases in VW (compared with 0% hMSCs) can be considered pro-arrhythmic and anti-arrhythmic, respectively (see Supplementary Methods for details).

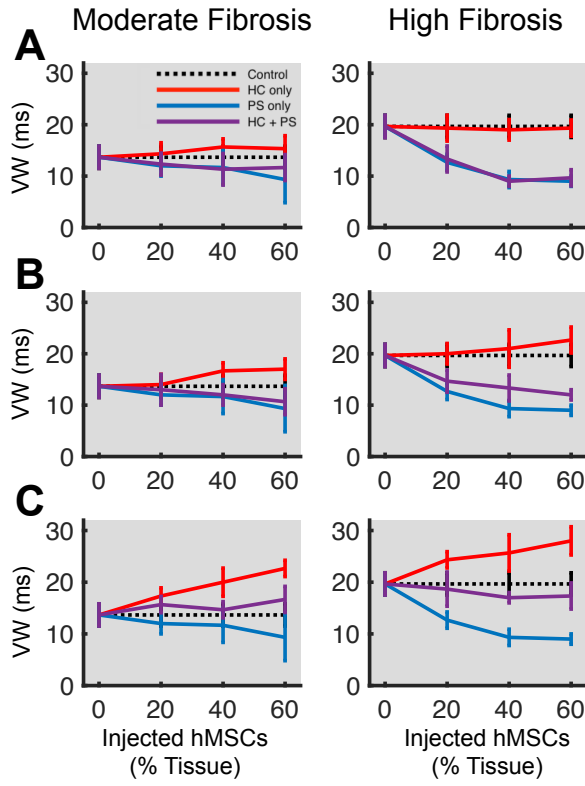


**Figure 6: Simulated Vulnerable Window Analysis on hMSC-Supplemented Fibrotic Cardiac Tissue.** A VW analysis was performed on moderate (21%; left panel) and high (40%; right panel) fibroblast-populated cardiac tissue injected with 0% (control), 20%, 40%, or 60% hMSCs at (A) low (1%), (B) moderate (4.5%), and (C) high (16%) engraftment levels ( $n=3$  randomized cell distributions). In all cases, the PS-only conditions decreased VW, minimizing arrhythmogenicity. As recommended by White et al.<sup>40</sup>, comparative statistics were not implemented, as p-values are dependent on sample size (which can be arbitrarily high in simulations).

Counteracting PS and HC effects of hMSCs were revealed in the VW analysis of tissue-level arrhythmogenicity in simulated cardiac tissue with moderate (21%) and high (40%) diffuse fibrosis (Figure 6). With increasing levels of hMSC delivery and engraftment, the HC-only conditions led to increases in VW for moderate and high fibrosis compared to control. On the

other hand, in all cases, the PS-only conditions decreased VW compared to control, thus minimizing arrhythmogenic risk in an hMSC dose-dependent manner. Spontaneous beat rate variability measurements in hECTs—a proposed surrogate of arrhythmogenicity<sup>41,42</sup>—with low-level hMSC HC and PS interventions qualitatively support these trends (Figure S8).

Importantly, by simulating a range of pre-clinically and clinically relevant percentages of hMSC injection and engraftment, our simulations predict that the combined effects of hMSC HC and PS mechanisms (i.e., HC+PS condition) will cause intermediate effects on VW, predominantly leading to beneficial decreases in VW. In only one case (moderate fibrosis at high engraftment) there was a slight increase in the VW compared to control, suggesting that low levels of engraftment commonly found clinically may in fact be advantageous. Overall, our simulated VW analysis may help explain why hMSCs are reported to have either no effect,<sup>14</sup> or favorable protective effects,<sup>13</sup> on arrhythmogenesis in clinical trials, despite the potential electrophysiological risk of hMSC-cardiomyocyte coupling.

#### *6.5.6 Proteomic Analysis of Experimental Culture Media*

To explore the nature of the observed hMSC paracrine-mediated increase of hECT contractility, we first performed a protein microarray on serum-free defined media (SFDM) collected from each experimental condition in Figure 3A, representative of the soluble factors released cumulatively by hECT cellular constituents. As expected, samples collected from each hECT culture media group predominantly up-regulated protein expression levels relative to mean values of serum-free defined media control (Figure 7A). Importantly, the two hECT culture conditions with hMSC intervention clustered together in a principal component (PC) analysis (Figure 7B), supporting a consistent paracrine effect by hMSCs in both groups.

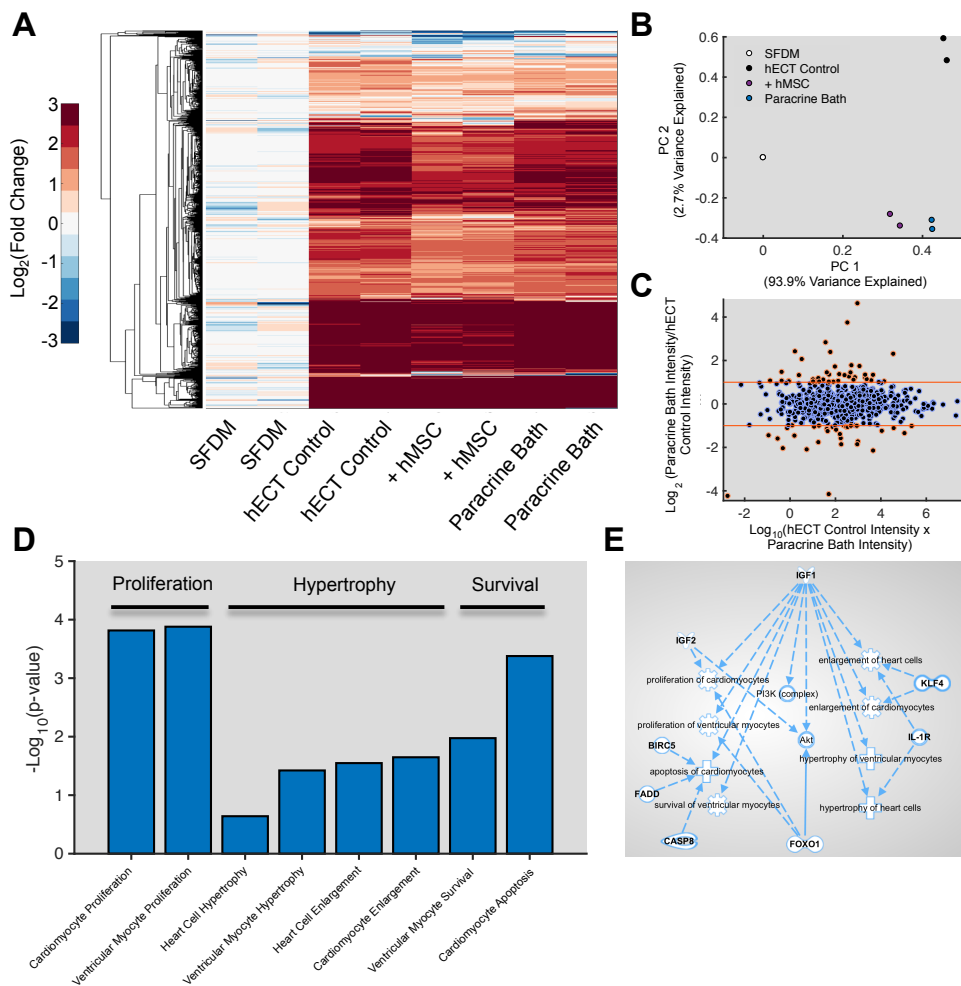


**Figure 7: Proteomic Analysis of hECT Conditioned Media.** Visualization of protein microarray data via (A) heatmap and (B) principal component (PC) analysis. Heatmap values (run in duplicate) are relative to mean values of serum-free defined media (SFDM) control. (C) Bland-Altman plot of mean differentially expressed proteins in paracrine media bath relative to hMSC-unsupplemented hECT control media (2-fold threshold). (D) Cardiac-specific pathway functions significantly modulated by up-regulated soluble proteins. (E) Soluble factors involved in modulating cardiac-specific pathways.

Next, we examined the mean fold-change of soluble proteins in the shared paracrine media bath relative to the hMSC-unsupplemented hECT control media, yielding 39 and 31

factors that were up-regulated and down-regulated at least two-fold, respectively (Figure 7C; black dots with red outline located outside the red lines). Using Ingenuity Pathway Analysis (IPA®) software, functional analyses on the up-regulated proteins significantly modulated cardiac cell-specific pathways (Figure 7D), as well as expected immune-related and pro-angiogenic pathways (Table S5).

Of the 39 up-regulated factors, 8 are linked to at least one of the cardiac cell-specific pathways (Table S6), three of which activate the PI3K/Akt signaling cascade previously hypothesized as the mechanism for hMSC paracrine-mediated effects on contractility (Figure 7E).<sup>20</sup>

#### *6.5.7 Exosomes Play a Key Role in Mesenchymal Stem Cell-Mediated Increase of hECT Contractile Function*

Cardioactive hMSC exosomes have also been shown to modulate myocyte PI3K/Akt signaling,<sup>43,44</sup> motivating us to test whether the exosomes-depleted and/or exosomes-enriched fractions of the hMSC secretome may be responsible for the hMSC paracrine-mediated increase of hECT contractility.

First, we confirmed via confocal microscopy that hMSC exosomes are taken up by the cardiomyocytes and fibroblasts that constitute our hECTs (Figure S9). Next, we tested the role of exosomes-depleted and exosomes-enriched fractions (both confirmed via dynamic light scattering analysis; see Figure S10) of the hMSC secretome on hECT contractile performance by replacing hECT SFDM media with the following treatments following baseline contractile function testing on day 5: 1) SFDM (Control); 2) hMSC conditioned media (hMSC CdM); 3) SFDM enriched with hMSC exosomes (hMSC exo); or 4) hMSC exosomes-depleted conditioned media (hMSC exo-depl). hECTs were cultured an additional 5 days, and then DF was measured post-treatment and was compared to baseline measurements.

As shown in Figure 8A, the Control group DF was unchanged relative to pre-treatment baseline, whereas the hMSC CdM treatment led to statistically significant increases in DF, thus confirming our findings in Figure 4 that hMSC PS was indeed responsible for increasing hECT contractility. Importantly, we further observed that the hMSC exo treatment group yielded a statistically significant increase in hECT DF similar to hMSC CdM, whereas the hMSC exo-depl group was not significantly different from baseline.

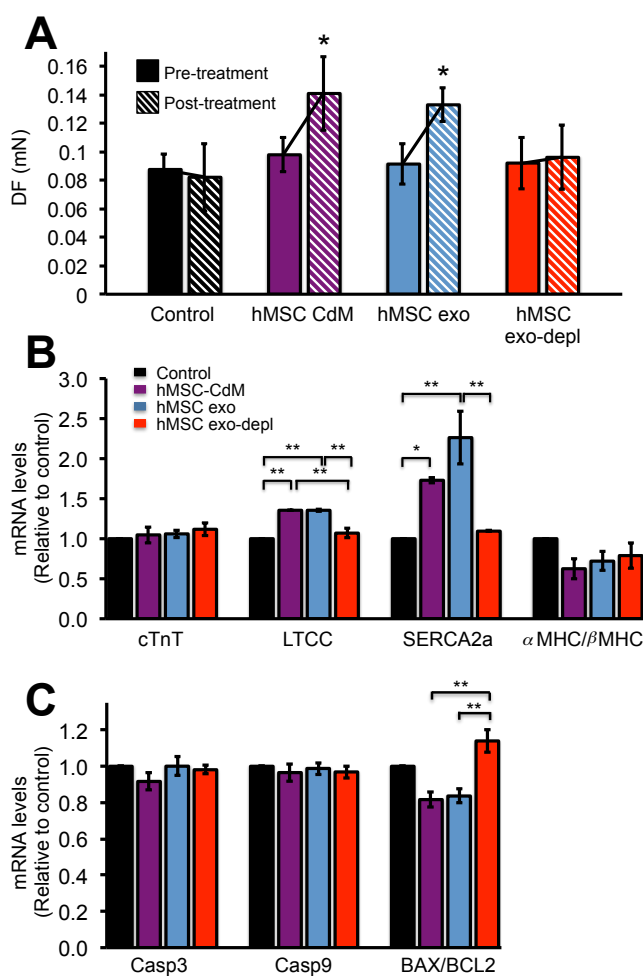


**Figure 8. Effects of hMSC Exosomes on hECT Function and mRNA Levels. (A)** Contractility assay shows hECT DF during 0.5-Hz pacing (mean $\pm$ SEM, n=4-7) at pre-treatment (day 5) and 5-days post-treatment with SFDM, hMSC CdM, hMSC exo, and hMSC exo-depl (see text for

details). \* $p<0.05$ ; p-values from paired t-tests. hECTs from each group ( $n=3$ ) were snap-frozen for qRT-PCR on day 10, where expression of (**B**) cardiac-specific, calcium handling, and (**C**) apoptotic genes were studied. \* $p<0.05$ , \*\* $p<0.01$ ; p-values from one-way ANOVA with post-hoc Tukey test. Non-standard abbreviations: cardiac troponin T (cTnT); L-type calcium channel (LTCC); sarco/endoplasmic reticulum calcium-ATPase (SERCA2a); myosin heavy chain (MHC), caspase-3 (Casp3); caspase-9 (Casp9); B-cell lymphoma 2 (BCL2); BCL2-associated X protein (BAX).

These functional findings were corroborated by hECT molecular characterization. Following five days of treatment as above, hECTs were snap-frozen for prospective qRT-PCR of cardiac-specific, calcium handling, and apoptosis genes. Cardiac troponin T, the ratio of  $\alpha$ -myosin heavy chain to  $\beta$ -myosin heavy chain, and caspase-3/9 mRNA levels were consistent among all groups; on the other hand, mRNA levels of SERCA2a and LTCC—known to be regulated by PI3K/Akt signaling<sup>20</sup>—significantly increased for hECTs treated with hMSC CdM and hMSC exo (Figure 8B), while the BAX/BCL2 ratio, an apoptosis marker,<sup>45</sup> significantly decreased relative to the hMSC exo-depl group (Figure 8C). Together, these findings indicate a key role of exosomes in the paracrine-mediated effects of hMSCs on cardiac contractility.

## 6.6 Discussion

Understanding the therapeutic influence of hMSC HC and PS mechanisms has important implications for their clinical utility. If HC between hMSCs and myocytes is essential for improving cardiac function, then future work should focus on methods to optimize delivery, retention, and integration with host myocardium. On the other hand, if select PS factors secreted by hMSCs are primarily responsible for desired functional benefits, those factors could be identified, isolated, and implemented as a therapy independent of the hMSCs, potentially circumventing some challenges with delivering live biologics. Alternatively, both effects might be

required to optimize the phenotypic and clinical benefits of cellular therapy; our model could facilitate the rational design of cell therapies in the future to achieve desired outcomes.

Herein, we utilized mathematical modeling and three-dimensional hECT experiments to delineate effects of hMSC PS and HC on human cardiac contractility and arrhythmogenicity. This study provides: 1) the first experimental measurements distinguishing the PS and HC effects of hMSC supplementation on contractile function of human stem cell-derived engineered cardiac tissue; 2) a comprehensive mathematical model capable of reproducing a majority of reported effects of hMSCs on cardiomyocyte action potential, calcium transient, and excitation-contraction metrics, allowing for direct comparisons between different species, maturity, and disease conditions; 3) new insight into the discrepancy of why clinical trials of hMSC therapy report either no arrhythmogenic effect or even an anti-arrhythmic effect, whereas hMSCs have been considered pro-arrhythmic in vitro; 4) protein microarray analysis of hECT-conditioned media suggesting PI3K/Akt signaling activation; and 5) functional and molecular data supporting a key role of exosomes in hMSC paracrine-mediated increase of hECT contractility.

#### *6.6.1 Motivation for Model Development*

In our previous computational modeling work,<sup>24</sup> we predicted that HC of human cardiomyocytes with an hMSC electrophysiological model can lead to action potential shortening at the single-cell level, as well as decreased conduction velocity and increased vulnerability to re-entry in simulated 2-D cardiac monolayer tissue absent of fibroblasts. Such tissue-level simulations reproduced several metrics in empirical monolayer studies of arrhythmogenicity;<sup>37</sup> however, the model could not explain effects of hMSC co-culture on single-cell action potential duration and calcium handling as reported by multiple investigators.<sup>19,20,37</sup> Furthermore, our model could not explain pre-clinical and clinical observations, where hMSC delivery to the heart had no significant effect—or even favorable protective benefits—on the arrhythmogenicity of fibrotic cardiac tissue.<sup>13,14,21,46</sup> These discrepancies made it clear that some

other mechanism of hMSC interaction with the myocardium, neglected in our original computational model, must be responsible for the inconsistencies with experimental data.

Extensive literature suggests hMSC PS mechanisms can have a profound effect on cardiac single-cell and tissue-level function;<sup>19,20,21,27-33</sup> we therefore decided to focus our modeling efforts on these PS effects.

#### *6.6.2 Experimental Calibration of the hMSC PS Model*

Computational studies typically involve model development representing the average behavior of a population. However, important information is lost both experimentally and theoretically when the underlying variability is ignored, ultimately limiting the extrapolation of results at a population level. In this study, we integrate experimental measurements with mathematical modeling to calibrate a population of hMSC PS effects on ion channel/pump activity across various hMSC PS dosages representative of physiological variability and several cardiac cell types commonly used in the literature. We then examine this model in the context of experimentally measured contractility of hECTs following hMSC intervention.

Our approach builds on previous studies that show the importance of modeling intersubject variability in biology.<sup>25,26,47</sup> Previous cardiac electrophysiology modeling studies of variability have constructed populations of cardiac cell models by directly adjusting model conductance and kinetic parameters.<sup>25,26</sup> We expanded on this approach by simulating variability in dose-response curve parameters that effectively describe hMSC PS effects on cardiomyocyte model conductances across a wide range of prescribed treatments.

#### *6.6.3 Model is Representative of Empirical Data*

As enforced in our process of calibrating model populations to experimental data (Figure 1), all simulated dose-dependent effects of hMSC PS-only mechanisms of myocyte action potential and calcium transient metrics were within one standard deviation of published data for

a range of experimental conditions and cardiomyocyte species. Importantly, our model was also consistent with published hMSC HC+PS effects on single cells, as well as a wide range of original hECT contractility data that were not used in the model calibration process. Furthermore, our simulations of time-dependent paracrine effects of hMSCs in vitro demonstrate the model's versatility to incorporate clinically relevant time-course data as it becomes available in the future.

Our model was also consistent with reported hMSC-mediated effects on tissue-level arrhythmogenicity. In VW simulations, the hMSC PS-only conditions were anti-arrhythmic compared to control, consistent with a preclinical study on a rat myocardial infarction model, where hMSC paracrine factors were anti-arrhythmic, suppressed fibrosis, and restored conduction.<sup>21</sup> Furthermore, our model trends are consistent with our original hECT data on spontaneous beat rate variability—a proposed surrogate of arrhythmogenicity.<sup>41,42</sup> Most importantly, VW analyses predicted that hMSC supplementation (involving hMSC PS+HC mechanisms) did not adversely impact arrhythmogenesis, and may even be anti-arrhythmogenic under some conditions; such findings may help explain why hMSCs are mainly reported to have either no effect,<sup>14</sup> or favorable protective effects,<sup>13</sup> on arrhythmogenesis in clinical trials.

#### *6.6.4 Nature of the hMSC Paracrine-Mediated Increase of hECT Contractility*

Previously, Desantiago et al. demonstrated hMSC paracrine-mediated enhancement of mouse ventricular myocyte excitation-contraction coupling via the PI3K/Akt signaling cascade.<sup>20</sup> Several soluble factors from our protein microarray are known to modulate this PI3K/Akt signaling cascade; however, cardioactive hMSC exosomes have also been shown to modulate myocyte PI3K/Akt signaling,<sup>43,44</sup> motivating us to comprehensively test whether the exosomes-depleted and/or exosomes-enriched fractions of the hMSC secretome are responsible for the hMSC paracrine-mediated increase of hECT contractility.

Our functional testing and molecular characterization of hECTs treated with exosomes-enriched or exosomes-depleted fractions of the hMSC secretome suggest that exosomes play a key role in the hMSC paracrine-mediated increase of contractility. Given the avascular nature of our hECTs, these findings suggest exosomes can augment contractility via mechanisms other than previously established neovascularization.<sup>48</sup> Importantly, we show mRNA levels of SERCA2a and LTCC—known to be regulated by PI3K/Akt signaling<sup>20</sup>—significantly increased for hECTs treated with hMSC CdM and hMSC exo, which: 1) supports inclusion of these factors in our model development; and 2) motivates future work investigating the interplay between hMSC exosomes, their cargo, and this signaling cascade for improving contractility.

#### *6.6.5 Limitations and Future Work*

Several limitations of the study should be noted. First, there was limited experimental data available for modeling hMSC PS ion channel/pump activity, as well as anti-fibrotic dose-response curves. This led us to neglect the least influential current modulated by hMSC PS (i.e. transient outward current), and to predict dose-response values using an established experimental calibration algorithm.<sup>25,26</sup> Nevertheless, the ability of the model to reproduce a variety of experimental findings justified utilizing the model to make predictions about hMSC HC and PS effects on cardiac function. The model will be further strengthened as more data become available for experimental calibration.

Second, our VW analyses were performed with 2-D diffuse fibrotic tissue, with active fibroblasts assumed to be the same size as cardiomyocytes, and without the electrical remodeling that typically accompanies diseased conditions. Other types of fibrosis could have also been considered, including patchy, interstitial, and compact—the most representative of diseased infarcted heart in hMSC therapy.<sup>49</sup> However, it is believed that ischemic heart disease arrhythmogenicity is not primarily due to macroscopic compact fibrotic scars, but by scars surrounded by a border zone, where diffuse fibrosis coexists with patchy and interstitial

fibrosis.<sup>49</sup> Similarly, our VW analyses focused on a diffuse random distribution of hMSCs; other localized cell distribution patterns could affect the VW differently. Although more advanced models could hypothetically be developed to incorporate realistic anatomical features and fibrosis/hMSC distribution, our model is computationally efficient, yet still provides qualitative insight into hMSC PS and HC effects on contractility and arrhythmogenicity.

Third, the simplified hECT model system does not fully represent native human myocardium. However, the controlled biocomplexity allows for isolation of hMSC-mediated effects on myocyte contractility independent of immunomodulatory, neurohumoral, neovascular, and other mechanisms that may obscure *in vivo* findings. This also facilitates comparing tissue-level contractility in stem cell-derived hECTs with *in silico* single-cell hiPSC-CM excitation-contraction under matched hMSC treatment conditions, as: 1) hMSC PS alone caused tissue compaction comparable to having hMSCs co-cultured within the tissue; and 2) there was no significant difference in diastolic force between all groups, a surrogate of tissue stiffness, even though hMSCs mechanically couple to myocytes *in vitro*.<sup>39</sup> To help account for the different output measures, we focused on fold changes in treatment groups relative to control (Figure 4), where the model closely reproduced empirical tissue-level findings.

Based on our findings, crucial future work should include testing translation of hMSC PS effects on contractile function to hECT models of heart disease, and further studying the role of hMSC exosomes and their molecular cargo that may be responsible for increased contractility *in vivo*. Such research efforts could ultimately lead to improved hMSC-based cardiac therapy.

## 6.7 Conclusions

In summary, this integrated experimental and computational study provides an improved understanding of the relative effects of hMSC PS and HC on cardiac contractility and arrhythmogenicity. Importantly, we provide new insight into the discrepancy of why recent clinical trials report either no arrhythmogenic risk or even an anti-arrhythmic benefit of hMSC

therapy, whereas hMSCs have been shown to be pro-arrhythmic in vitro. Finally, we perform proteomic analysis of hECT/hMSC conditioned media and subsequent functional testing/molecular characterization of hECTs treated with exosomes-depleted and exosomes-enriched fractions of the hMSC secretome, which provides novel insight into the role of exosomes in hMSC paracrine-mediated effects on contractility.

## **6.8 References**

1. Mozaffarian D, Benjamin EJ, Go AS, et al. Heart disease and stroke statistics--2015 update: A report from the american heart association. *Circulation*. 2015;131:e29-322
2. Gnechi M, He H, Liang OD, Melo LG, Morello F, Mu H, Noiseux N, Zhang L, Pratt RE, Ingwall JS, Dzau VJ. Paracrine action accounts for marked protection of ischemic heart by akt-modified mesenchymal stem cells. *Nat Med*. 2005;11:367-368
3. Herrmann JL, Wang Y, Abarbanell AM, Weil BR, Tan J, Meldrum DR. Preconditioning mesenchymal stem cells with transforming growth factor-alpha improves mesenchymal stem cell-mediated cardioprotection. *Shock*. 2010;33:24-30
4. Schuleri KH, Feigenbaum GS, Centola M, et al. Autologous mesenchymal stem cells produce reverse remodelling in chronic ischaemic cardiomyopathy. *Eur Heart J*. 2009;30:2722-2732
5. Hatzistergos KE, Quevedo H, Oskouei BN, et al. Bone marrow mesenchymal stem cells stimulate cardiac stem cell proliferation and differentiation. *Circ Res*. 2010;107:913-922
6. Amado LC, Saliaris AP, Schuleri KH, et al. Cardiac repair with intramyocardial injection of allogeneic mesenchymal stem cells after myocardial infarction. *Proc Natl Acad Sci U S A*. 2005;102:11474-11479
7. Amado LC, Schuleri KH, Saliaris AP, Boyle AJ, Helm R, Oskouei B, Centola M, Eneboe V, Young R, Lima JA, Lardo AC, Heldman AW, Hare JM. Multimodality noninvasive imaging demonstrates in vivo cardiac regeneration after mesenchymal stem cell therapy. *J Am Coll Cardiol*. 2006;48:2116-2124
8. Karantalis V, DiFede DL, Gerstenblith G, et al. Autologous mesenchymal stem cells produce concordant improvements in regional function, tissue perfusion, and fibrotic burden when administered to patients undergoing coronary artery bypass grafting: The prospective randomized study of mesenchymal stem cell therapy in patients undergoing cardiac surgery (prometheus) trial. *Circ Res*. 2014;114:1302-1310

9. Heldman AW, DiFede DL, Fishman JE, et al. Transendocardial mesenchymal stem cells and mononuclear bone marrow cells for ischemic cardiomyopathy: The tac-hft randomized trial. *JAMA*. 2014;311:62-73
10. Hare JM, Traverse JH, Henry TD, Dib N, Strumpf RK, Schulman SP, Gerstenblith G, DeMaria AN, Denktas AE, Gammon RS, Hermiller JB, Jr., Reisman MA, Schaer GL, Sherman W. A randomized, double-blind, placebo-controlled, dose-escalation study of intravenous adult human mesenchymal stem cells (prochymal) after acute myocardial infarction. *J Am Coll Cardiol*. 2009;54:2277-2286
11. Karantalis V, Hare JM. Use of mesenchymal stem cells for therapy of cardiac disease. *Circ Res*. 2015;116:1413-1430
12. Meyer GP, Wollert KC, Lotz J, Pirr J, Rager U, Lippolt P, Hahn A, Fichtner S, Schaefer A, Arseniev L, Ganser A, Drexler H. Intracoronary bone marrow cell transfer after myocardial infarction: 5-year follow-up from the randomized-controlled boost trial. *Eur Heart J*. 2009;30:2978-2984
13. Hare JM, Fishman JE, Gerstenblith G, et al. Comparison of allogeneic vs autologous bone marrow-derived mesenchymal stem cells delivered by transendocardial injection in patients with ischemic cardiomyopathy: The poseidon randomized trial. *JAMA*. 2012;308:2369-2379
14. de Jong R, Houtgraaf JH, Samiei S, Boersma E, Duckers HJ. Intracoronary stem cell infusion after acute myocardial infarction: A meta-analysis and update on clinical trials. *Circ Cardiovasc Interv*. 2014;7:156-167
15. Molina EJ, Palma J, Gupta D, Torres D, Gaughan JP, Houser S, Macha M. Reverse remodeling is associated with changes in extracellular matrix proteases and tissue inhibitors after mesenchymal stem cell (msc) treatment of pressure overload hypertrophy. *J Tissue Eng Regen Med*. 2009;3:85-91

16. Tao H, Han Z, Han ZC, Li Z. Proangiogenic features of mesenchymal stem cells and their therapeutic applications. *Stem Cells Int.* 2016;2016:1314709
17. Cashman TJ, Gouon-Evans V, Costa KD. Mesenchymal stem cells for cardiac therapy: Practical challenges and potential mechanisms. *Stem Cell Rev.* 2013;9:254-265
18. Ranganath SH, Levy O, Inamdar MS, Karp JM. Harnessing the mesenchymal stem cell secretome for the treatment of cardiovascular disease. *Cell Stem Cell.* 2012;10:244-258
19. Askar SF, Ramkisoensing AA, Atsma DE, Schalij MJ, de Vries AA, Pijnappels DA. Engraftment patterns of human adult mesenchymal stem cells expose electrotonic and paracrine proarrhythmic mechanisms in myocardial cell cultures. *Circ Arrhythm Electrophysiol.* 2013;6:380-391
20. DeSantiago J, Bare DJ, Semenov I, Minshall RD, Geenen DL, Wolska BM, Banach K. Excitation-contraction coupling in ventricular myocytes is enhanced by paracrine signaling from mesenchymal stem cells. *J Mol Cell Cardiol.* 2012;52:1249-1256
21. Hwang HJ, Chang W, Song BW, et al. Antiarrhythmic potential of mesenchymal stem cell is modulated by hypoxic environment. *J Am Coll Cardiol.* 2012;60:1698-1706
22. Valiunas V, Doronin S, Valiuniene L, Potapova I, Zuckerman J, Walcott B, Robinson RB, Rosen MR, Brink PR, Cohen IS. Human mesenchymal stem cells make cardiac connexins and form functional gap junctions. *J Physiol.* 2004;555:617-626
23. Shadrin IY, Yoon W, Li L, Shepherd N, Bursac N. Rapid fusion between mesenchymal stem cells and cardiomyocytes yields electrically active, non-contractile hybrid cells. *Sci Rep.* 2015;5:12043
24. Mayourian J, Savizky RM, Sobie EA, Costa KD. Modeling electrophysiological coupling and fusion between human mesenchymal stem cells and cardiomyocytes. *PLoS Comput Biol.* 2016;12:e1005014
25. Britton OJ, Bueno-Orovio A, Van Ammel K, Lu HR, Towart R, Gallacher DJ, Rodriguez B. Experimentally calibrated population of models predicts and explains intersubject

- variability in cardiac cellular electrophysiology. *Proc Natl Acad Sci U S A.* 2013;110:E2098-2105
26. Zhou X, Bueno-Orovio A, Orini M, Hanson B, Hayward M, Taggart P, Lambiase PD, Burrage K, Rodriguez B. In vivo and in silico investigation into mechanisms of frequency dependence of repolarization alternans in human ventricular cardiomyocytes. *Circ Res.* 2016;118:266-278
  27. Wang D, Zhang F, Shen W, Chen M, Yang B, Zhang Y, Cao K. Mesenchymal stem cell injection ameliorates the inducibility of ventricular arrhythmias after myocardial infarction in rats. *Int J Cardiol.* 2011;152:314-320
  28. Tang YL, Tang Y, Zhang YC, Qian K, Shen L, Phillips MI. Improved graft mesenchymal stem cell survival in ischemic heart with a hypoxia-regulated heme oxygenase-1 vector. *J Am Coll Cardiol.* 2005;46:1339-1350
  29. Citro L, Naidu S, Hassan F, Kuppusamy ML, Kuppusamy P, Angelos MG, Khan M. Comparison of human induced pluripotent stem-cell derived cardiomyocytes with human mesenchymal stem cells following acute myocardial infarction. *PLoS One.* 2014;9:e116281
  30. Richardson JD, Bertaso AG, Psaltis PJ, Frost L, Carbone A, Paton S, Nelson AJ, Wong DT, Worthley MI, Gronthos S, Zannettino AC, Worthley SG. Impact of timing and dose of mesenchymal stromal cell therapy in a preclinical model of acute myocardial infarction. *J Card Fail.* 2013;19:342-353
  31. Liu JF, Wang BW, Hung HF, Chang H, Shyu KG. Human mesenchymal stem cells improve myocardial performance in a splenectomized rat model of chronic myocardial infarction. *J Formos Med Assoc.* 2008;107:165-174
  32. Iso Y, Spees JL, Serrano C, Bakondi B, Pochampally R, Song YH, Sobel BE, Delafontaine P, Prockop DJ. Multipotent human stromal cells improve cardiac function

after myocardial infarction in mice without long-term engraftment. *Biochem Biophys Res Commun.* 2007;354:700-706

33. Mathieu E, Lamirault G, Toquet C, Lhommet P, Rederstorff E, Source S, Biteau K, Hulin P, Forest V, Weiss P, Guicheux J, Lemarchand P. Intramyocardial delivery of mesenchymal stem cell-seeded hydrogel preserves cardiac function and attenuates ventricular remodeling after myocardial infarction. *PLoS One.* 2012;7:e51991
34. Kazbanov IV, ten Tusscher KH, Panfilov AV. Effects of heterogeneous diffuse fibrosis on arrhythmia dynamics and mechanism. *Sci Rep.* 2016;6:20835
35. Gomez JF, Cardona K, Martinez L, Saiz J, Trenor B. Electrophysiological and structural remodeling in heart failure modulate arrhythmogenesis. 2d simulation study. *PLoS One.* 2014;9:e103273
36. de Jong S, van Veen TA, van Rijen HV, de Bakker JM. Fibrosis and cardiac arrhythmias. *J Cardiovasc Pharmacol.* 2011;57:630-638
37. Chang MG, Tung L, Sekar RB, Chang CY, Cysyk J, Dong P, Marban E, Abraham MR. Proarrhythmic potential of mesenchymal stem cell transplantation revealed in an in vitro coculture model. *Circulation.* 2006;113:1832-1841
38. Cashman TJ, Josowitz R, Gelb BD, Li RA, Dubois NC, Costa KD. Construction of defined human engineered cardiac tissues to study mechanisms of cardiac cell therapy. *J Vis Exp.* 2016:e53447
39. Pedrotty DM, Klinger RY, Badie N, Hinds S, Kardashian A, Bursac N. Structural coupling of cardiomyocytes and noncardiomyocytes: Quantitative comparisons using a novel micropatterned cell pair assay. *Am J Physiol Heart Circ Physiol.* 2008;295:H390-400
40. White JW, Rassweiler A, Samhouri JF, Stier AC, White C. Ecologists should not use statistical significance tests to interpret simulation model results. *OIKOS Synthesising Ecology.* 2014;123:385-388

41. Cashman TJ, Josowitz R, Johnson BV, Gelb BD, Costa KD. Human engineered cardiac tissues created using induced pluripotent stem cells reveal functional characteristics of braf-mediated hypertrophic cardiomyopathy. *PLoS One*. 2016;11:e0146697
42. Schaaf S, Shibamiya A, Mewe M, Eder A, Stohr A, Hirt MN, Rau T, Zimmermann WH, Conradi L, Eschenhagen T, Hansen A. Human engineered heart tissue as a versatile tool in basic research and preclinical toxicology. *PLoS One*. 2011;6:e26397
43. Kang K, Ma R, Cai W, Huang W, Paul C, Liang J, Wang Y, Zhao T, Kim HW, Xu M, Millard RW, Wen Z, Wang Y. Exosomes secreted from cxcr4 overexpressing mesenchymal stem cells promote cardioprotection via akt signaling pathway following myocardial infarction. *Stem Cells Int*. 2015;2015:659890
44. Arslan F, Lai RC, Smeets MB, Akeroyd L, Choo A, Aguor EN, Timmers L, van Rijen HV, Doevedans PA, Pasterkamp G, Lim SK, de Kleijn DP. Mesenchymal stem cell-derived exosomes increase atp levels, decrease oxidative stress and activate pi3k/akt pathway to enhance myocardial viability and prevent adverse remodeling after myocardial ischemia/reperfusion injury. *Stem Cell Res*. 2013;10:301-312
45. Del Poeta G, Venditti A, Del Principe MI, Maurillo L, Buccisano F, Tamburini A, Cox MC, Franchi A, Bruno A, Mazzone C, Panetta P, Suppo G, Masi M, Amadori S. Amount of spontaneous apoptosis detected by bax/bcl-2 ratio predicts outcome in acute myeloid leukemia (aml). *Blood*. 2003;101:2125-2131
46. Ramireddy A, Brodt CR, Mendizabal AM, DiFede DL, Healy C, Goyal V, Alansari Y, Coffey JO, Viles-Gonzalez JF, Heldman AW, Goldberger JJ, Myerburg RJ, Hare JM, Mitrani RD. Effects of transendocardial stem cell injection on ventricular proarrhythmia in patients with ischemic cardiomyopathy: Results from the poseidon and tac-hft trials. *Stem Cells Transl Med*. 2017;6:1366-1372
47. Sarkar AX, Christini DJ, Sobie EA. Exploiting mathematical models to illuminate electrophysiological variability between individuals. *J Physiol*. 2012;590:2555-2567

48. Teng X, Chen L, Chen W, Yang J, Yang Z, Shen Z. Mesenchymal stem cell-derived exosomes improve the microenvironment of infarcted myocardium contributing to angiogenesis and anti-inflammation. *Cell Physiol Biochem*. 2015;37:2415-2424
49. Nguyen TP, Qu Z, Weiss JN. Cardiac fibrosis and arrhythmogenesis: The road to repair is paved with perils. *J Mol Cell Cardiol*. 2014;70:83-91

## **Chapter 6 Supplementary Material**

### **Detailed Methods**

#### *Single-Cell Cardiomyocyte Electrophysiology Models*

Multiple single-cell endocardial cardiomyocyte electrophysiological models were utilized in this study, including the: Bondarenko et al. mouse ventricular myocyte model;<sup>1</sup> Devenyi et al. rat cardiomyocyte model;<sup>2</sup> Paci et al. human induced pluripotent stem cell-derived ventricular-like cardiomyocyte model;<sup>3</sup> ten Tusscher et al. human healthy cardiomyocyte model;<sup>4</sup> and Weiss et al. human ischemic cardiomyocyte model.<sup>5</sup> All single-cell models were numerically integrated with MATLAB's (The MathWorks, Natick MA) stiff ordinary differential equation solver (ode15s) until steady state was achieved.

#### *Parameter Sensitivity Analysis*

An established multivariable regression analysis was performed;<sup>6-8</sup> briefly, we randomly varied input parameters of interest in 300 trials by a normally distributed pseudorandom scale factor with a coefficient of variation of 10%. From the changes in the model outputs and input parameters, a linear approximation was made to find the normalized parameter sensitivity vector.

#### *Hierarchical Clustering Analysis*

Briefly, hierarchical clustering was performed on our multi-species parameter sensitivity analysis vector elements with a Euclidean distance metric and average linkage.<sup>9</sup>

#### *Modeling hMSC HC and PS Effects on the Single-Cell Cardiomyocyte Action Potential and Calcium Transient*

hMSC-cardiomyocyte HC interactions were simulated with our established model,<sup>6</sup> representing an empirically observed mixture of hMSC electrophysiological phenotypes.<sup>10</sup> Effects of hMSC PS were independently simulated using experimentally calibrated dose-response curves to adjust the maximum L-type calcium channel permeability ( $G_{LCa}$ ) and SERCA maximum uptake activity ( $V_{maxup}$ ) in the cardiomyocyte models according to the prescribed strength of hMSC treatment, as described next.

Unless noted otherwise, hMSC PS steady-state effects are modeled. Detailed methods for modeling transient effects of hMSC PS can also be found below.

#### Experimental Calibration of the Steady-State hMSC PS Model

We experimentally calibrated the sigmoidal dose response effects of hMSC PS on  $G_{LCa}$  and  $V_{maxup}$  using published experimental data and a modified version of methods previously described.<sup>11,12</sup>  $G_{LCa}$  and  $V_{maxup}$  were chosen because they have the strongest influence on action potential and calcium handling metrics, as presented in Figure S1 (i.e.,  $G_{to}$ , the transient outward conductance, was assumed to be constant). Briefly, we constructed a population of 2,500 models of single-cell myocyte electrophysiology by randomly assigning specific parameter values within physiologically and empirically relevant bounds (Supplementary Table 2) to characterize the following sigmoidal dose-response curves:

$$G'_{LCa} = G_{LCa} \left(1 + \frac{\Delta G_{LCa}}{1 + 10^{\frac{k_{LCa}(EC_{50,LCa} - x)}}}\right)$$

$$V'_{maxup} = V_{maxup} \left(1 + \frac{\Delta V_{maxup}}{1 + 10^{\frac{k_V(EC_{50,V} - x)}}}\right)$$

where  $G'_{LCa}$  and  $V'_{maxup}$  represent the fold changes of  $G_{LCa}$  and  $V_{maxup}$  based on prescribed hMSC PS dosages, respectively;  $\Delta G_{LCa}$  and  $\Delta V_{maxup}$  are the maximum saturated effects of hMSC PS on  $G_{LCa}$  and  $V_{maxup}$ , respectively;  $k_{LCa}$  and  $k_V$  are the

characteristic Hill coefficients for each respective curve;  $EC_{50,LCa}$  and  $EC_{50,V}$  are the characteristic half maximum effective concentrations for each respective curve; and  $x$  is the effective hMSC PS dosage, defined as  $\text{Log}_{10}$  of the percentage of hMSCs per myocyte. Each parameter set in the experimental calibration had 6 parameters:  $\Delta G_{LCa}$ ,  $\Delta V_{\text{maxup}}$ ,  $EC_{50,LCa}$ ,  $EC_{50,V}$ ,  $k_{LCa}$ , and  $k_V$ .

Our model-calibration algorithm determined whether a given set of model parameters should be added to an “accepted” population based on comparison of output simulated with empirical metrics. This process was constrained by the availability of experimental data at different hMSC dosages. Therefore, we used four dose-dependent output action potential and calcium transient metrics to calibrate the model, specifically: 1) rat myocyte APD<sub>90</sub> at 7% hMSC PS supplementation (APD<sub>90,7%</sub>);<sup>13</sup> 2) rat myocyte APD<sub>90</sub> at 28% hMSC PS supplementation (APD<sub>90,28%</sub>);<sup>13</sup> 3) mouse myocyte  $[Ca^{2+}]_{\text{peak}}$  at saturated hMSC PS ( $[Ca^{2+}]_{\text{peak},\infty}$ );<sup>14</sup> and 4) mouse myocyte  $\tau_{Ca}$  at saturated hMSC PS ( $\tau_{Ca,\infty}$ ).<sup>14</sup> Modified from Prinz et al., bounds on allowed output variability were set to one standard deviation around mean values.<sup>15</sup> Finally, the set of accepted model parameters that best represented, in a least squares sense, the average of all accepted output metrics was defined as the “least squares” or “best fit” model (Supplementary Table 3) and was used for in-depth simulations.

#### *Modeling hMSC PS Transient Effects*

To model transient effects of hMSC PS, we modified steady-state sigmoidal dose-response curves with best-fit equations to transient experimental data (Figure S3:

$$G'_{LCa}(t,x) = G_{LCa} \left(1 + \frac{\Delta G_{LCa}}{1 + 10^{\frac{k_{LCa}(EC_{50,LCa}-x)}{k_V}}} \right) (1 - e^{-t/\tau})$$

$$V'_{maxup}(t,x) = V_{maxup} \left(1 + \frac{\Delta V_{Maxup}}{1 + 10^{\frac{k_V(EC_{50,V}-x)}{k_{LCa}}}} \right) (1 - e^{-t/\tau})$$

where  $G'_{LCa}(t,x)$  and  $V'_{maxup}(t,x)$  represent the time- and hMSC dose-dependent fold changes of  $G_{LCa}$  and  $V_{maxup}$  based on prescribed hMSC PS dosages, respectively;  $t$  is time; and  $\tau$  is a time constant.

#### *hECT Tissue Construction*

hECTs were created from differentiated human embryonic stem cells (H7 cell line, NIH Registration #0061) and type-I collagen using methods previously described.<sup>16,17</sup>

#### *hECT Functional Test Metrics*

hECT twitch force and dynamics were assessed; hECT developed force (DF) was measured as the difference between maximum systolic and minimum diastolic force, while twitch dynamics were assessed by maximum rates of contraction ( $+dF/dt$ ) and relaxation ( $-dF/dt$ ). Beat rate variability, a proposed index of arrhythmogenicity,<sup>18,19</sup> was measured from a sequence of contractions in spontaneously beating hECTs using previously established methods.<sup>18</sup>

#### *Testing Contributions of HC and PS on hECT Contractile Function*

For unsupplemented control tissues (-hMSC), the cell-matrix solution was directly used for tissue construction in a custom 6-tissue bioreactor. For supplemented tissues (+hMSC), an additional 10% hMSCs were added to the tissue mix prior to hECT

formation. The two tissue types were cultured either separately or in a shared media/paracrine bath. Prior to using the hMSCs, their tri-lineage potential was confirmed (Figure S6). The function of both tissue types in each condition was then assessed using established methods.<sup>16,20</sup> Twitch force measurements were obtained on culture day 7 with hECTs beating during electrical field stimulation at 1 Hz pacing frequency.

**Modeling hMSC HC and PS Effects on Single-Cell Cardiomyocyte Excitation-Contraction**

To compare numerical results to empirical hECT contractile function data, our experimentally calibrated models of hMSC HC and PS effects were applied to Paci and coworker's single-cell model of human induced pluripotent stem cell-derived ventricular-like cardiomyocytes (hiPSC-CM)<sup>3</sup>—representing the primary cellular constituent of hECTs—linked to an established excitation-contraction coupling model.<sup>21</sup> Initial sarcomere length was modified to 1.9  $\mu\text{m}$  to be within the range of published experimental data on such cell types.<sup>22,23</sup> For each experimental condition, we performed in silico trials using all accepted sets of experimentally calibrated parameters. Twitch developed force (DF),  $+dF/dt$ , and  $-dF/dt$  were calculated for each simulation.

For contractile function sensitivity analysis, we applied the least squares model parameters to the single-cell Paci et al. hiPSC-CM<sup>3</sup>, ten Tusscher et al. human endocardial cardiomyocyte<sup>4</sup>, and Weiss et al. human ischemic<sup>5</sup> models with the same established excitation-contraction coupling model, with initial sarcomere lengths of 1.9, 2.1, and 2.1  $\mu\text{m}$ , respectively. We then performed a parameter sensitivity analysis (method described above) with output contractility metrics including DF,  $+dF/dt$ , and  $-dF/dt$ .

#### Calibrating HC Gap Junction Conductance to Experimental Conditions

Valiunas et al. reported a mean HC gap junction conductance between hMSCs and canine ventricular cardiomyocytes on glass coverslips of 1.5 nS, reaching as high as 11 nS with other cell types.<sup>24</sup> This experimental setup closely represented the conditions of published studies<sup>13,14</sup> we used to compare to our action potential and calcium handling model simulations. Therefore, a gap junction conductance of 1.5 nS was used to model hMSC HC effects on single-cell cardiomyocyte action potential and calcium handling.

The three-dimensional environment of hECTs formed with human pluripotent stem cell derived-cardiomyocytes differs from monolayer conditions, which may alter effective gap junction conductance between hMSCs and other cell types. Therefore, we measured the excitation-threshold voltage for pacing capture in hECTs with and without hMSC HC interventions, and calibrated the hMSC HC gap junction conductance in the excitation-contraction simulations to match the experimental mean threshold values (Figure S7). The resulting 9.1 nS HC gap junction conductance was used for excitation-contraction simulations when comparing to hECT contractile function results.

#### In Silico Diffuse Fibrosis Cardiac Tissue Configuration

A modified version of a monolayer spatial model of two-dimensional cardiac tissue with diffuse fibrosis was used.<sup>25,26</sup> Specifically, a 5 cm x 5 cm anisotropic cardiac tissue sheet was simulated, with structural remodeling accounted for by adding intercellular uncoupling at randomly inserted fibroblast locations. Moderate and high fibrosis were defined as fibroblasts comprising 21% and 40% of the total cell population, respectively (corresponding to fibrotic areas within experimental ranges<sup>27</sup>). Using these assumptions, the spatial model can be described as:

$$\frac{\partial V}{\partial t} = -\frac{I_{tot,k} + I_{stim}}{C_{m,k}} + D_{k,x} \frac{\partial^2 V}{\partial x^2} + D_{k,y} \frac{\partial^2 V}{\partial y^2}$$

where  $V$ ,  $I_{tot}$ ,  $I_{stim}$ ,  $C_m$ ,  $D$ , and  $k$  are the voltage, total ionic current, stimulus current, cell membrane capacitance, diffusion coefficient, and cell type (e.g., cardiomyocyte or fibroblast) at a given node, respectively.

Cardiomyocyte electrical activity was simulated with the ten Tusscher model of adult human endocardial myocytes,<sup>4</sup> while the electrical activity of fibroblasts was simulated using the MacCannell et al. active formulation.<sup>28</sup> Euclidian geometry was selected, with  $\Delta x = \Delta y = 0.01$  cm, and  $\Delta t = 0.01$  ms. Neumann-type boundary conditions were implemented to solve the partial differential equations. As performed elsewhere,<sup>6,26</sup> electrical anisotropy was modeled as  $D_{k,x} = 4D_{k,y}$ . All relevant model parameters can be found elsewhere.<sup>4,26,28</sup> All tissue simulations were executed in Python.

#### Modeling hMSC PS and HC Effects on Diffuse Fibrosis Cardiac Tissue

hMSCs were added at 0% (control), 20%, 40%, and 60% of the total cell population in the diffuse fibrosis adult human cardiac tissue simulations described above. To model hMSC HC effects, we assumed the delivered hMSCs engrafted at either low (1%), moderate (4.5%), or high (16%) levels, respectively approximating the minimum, median, and high values of stem cell engraftment reported in various studies.<sup>29-36</sup> Engraftment was defined as hMSCs that randomly inserted into the monolayer tissue with their own characteristic electrical activity and intercellular coupling, as described elsewhere.<sup>6</sup>

To model hMSC PS tissue-level effects, we developed a relationship (Online Figure II) between hMSC delivery levels (% of total left ventricular cell population) and anti-fibrotic effects ( $\alpha$ ) based on published data.<sup>31,33,37-42</sup> From this relationship, we replace  $\alpha$  percent of randomly distributed fibroblast nodes with cardiomyocyte nodes. Based on hMSC delivery levels, hMSC PS also affected L-type calcium channel and

SERCA activity at cardiomyocyte nodes using the “best fit” model (methods previously described). All relevant model parameters can be found in Figure 1, Figure S2, Supplementary Table 3, and elsewhere.<sup>6</sup>

### Vulnerable Window Analysis

The well-established cross-field stimulation protocol was applied to the 2-D tissue simulations.<sup>6,26,43</sup> Briefly, after achieving steady state, two S1 stimuli were applied at the left end of the tissue at a 1000 ms basic cycle length. An S2 stimulation was applied 100–500 ms after the second S1 stimulus—at 1 ms increments—in the bottom left corner of the tissue (1.25 cm wide × 2.5 cm high). For each tissue model, the VW was defined as the range of S1–S2 intervals that led to at least one spiral wave rotation. Mean and standard deviation of VW of three random tissue sheet configurations ( $n = 3$ ) were reported for each condition.

### Protein Microarray

To identify soluble factors secreted by hMSCs cultured within the supplemented hECTs, each set of hECTs was switched to serum free defined medium (SFDM) composed of RPMI 1640 (Life Technologies) medium with B27 supplement (Life Technologies), 1% penicillin- streptomycin (Corning) and 0.2% amphotericin B (Sigma-Aldrich) after pacing on day 7. A full change of SFDM was performed 24 hours later. After 48 hours, the entirety of the media was collected and stored at -20°C to await further analysis. The tissues were returned to NBS medium and function re-assessed on day 10 to confirm tissue viability. Media from four conditions from one experiment was collected: cell- and serum-free defined media control, -hMSC hECT controls, +hMSC hECTs, and the paracrine bath shared by -hMSC and +hMSC hECTs (see Figure 3).

Collected medium was thawed; protein concentration was then determined with a bicinchoninic acid (BCA) assay and sent to RayBiotech for analysis. Each of the four samples was loaded on the human L1000 glass slide antibody microarray (RayBiotech) at equal total protein concentration, each testing for 1000 known proteins in duplicate plus internal controls.

#### Computational Analysis of Protein Microarray

As recommended for RayBio®, positive control normalization without background data was used for the human L1000 glass slide. Factors with non-negative values across each condition were retained. For hierarchical clustering visualization, the MATLAB clustergram function was used. For the Bland-Altman plot, the MATLAB mairplot function was used to compare average -hMSC hECT control and paracrine bath protein microarray data. The 39 soluble factors up-regulated at least 2-fold were uploaded to Ingenuity Pathway Analysis (IPA®, Qiagen). The biological functions of the set of 39 factors were analyzed and reduced to only those with known relevance to cardiomyocytes. An interaction network between the remaining proteins and PI3K/Akt signaling was subsequently formed. Activation of PI3K/Akt signaling was tested via the Molecule Activity Predictor on the remaining proteins.

#### hMSC Conditioned Media and Exosomes Isolation

Conditioned media was collected from 10 cm dishes of 50% confluent hMSCs (passage less than 5) cultured in SFDM for five days. Exosomes were isolated from hMSC conditioned media via differential centrifugation using previously established methods<sup>44</sup> and characterized via dynamic light scattering using a NanoBrook ZetaPALS (Brookhaven, Holtsville, NY).

### Exosomes Taken Up by Human Stem-Cell Derived Cardiomyocytes and Fibroblasts

Exosomes from hMSC conditioned media were calcein-stained using methods previously described.<sup>45</sup> Calcein-stained hMSC exosomes were subsequently supplemented to Hoescht stained, fluorescence activated cell sorted, human stem cell-derived SIRPa+ cardiomyocytes and CD90+ fibroblasts for 48 hours in monolayer culture.

### Functional Assessment of hECTs Treated with hMSC Conditioned Media

Following 48 hours of tissue compaction, hECTs were cultured in SFDM until day 5. Following baseline contractile function testing at 0.5-Hz pacing on day 5, SFDM was replaced with the following treatments: 1) SFDM (Control); 2) fresh hMSC conditioned media (see above; hMSC CdM); 3) SFDM supplemented with exosomes isolated from fresh hMSC conditioned media (hMSC exo); or 4) hMSC exosomes-depleted conditioned media obtained from the supernatant of ultracentrifugation (hMSC exo-depl). hECTs were cultured an additional 5 days, and then DF was measured again.

### qRT-PCR

Total RNA was extracted from flash-frozen hECTs using the Quick-RNA MiniPrep kit (Zymo Research, Irvine, CA) after lysis using FastPrep Lysis Beads and Matrix Tubes (MP Products, Santa Ana, CA) and quantified using a NanoDrop 2000 (ThermoFisher, Rockville, MD). Reverse transcription was performed using the iScript cDNA synthesis kit (Biorad Laboratories, Hercules, CA) and quantitative PCR (10 ng cDNA/reaction) was performed using a two-step system with SYBR Advantage qPCR Premix (Clontech Laboratories, Mountain View, CA) on the ABI Prism 7500 Fast Real-Time PCR system (Applied Biosystems, Foster City, CA) according to manufacturer recommendations.

All primers used were against human and are shown as 5' to 3':

<b>Gene</b>	<b>Direction</b>	<b>Sequence (5'-3')</b>
β2M	Forward	GTATGCCTGCCGTGTGAAC
β2M	Reverse	CAAGCAAGCAGAATTGGAA
TNNT2	Forward	AAGAGGCAGACTGAGCGGGAAA
TNNT2	Reverse	AGATGCTCTGCCACAGCTCCTT
αMYHC	Forward	GGAAGACAAGGTCAACAGCCTG
αMYHC	Reverse	TCCAGTTCCGCTTGCTCGCT
βMYHC	Forward	GGAGTTCACACGCCCTCAAAGAG
βMYHC	Reverse	TCCTCAGCATCTGCCAGGTTGT
SERCA2a	Forward	CTGTCCATGTCACTCCACTTCC
SERCA2a	Reverse	AGCGGTTACTCCAGTATTGCAG
CASP3	Forward	TTAATAAAGGTATCCATGGAGAACACT
CASP3	Reverse	TTAGTGATAAAAATAGAGTTCTTTGTGAG
CASP9	Forward	TTCCCAGGTTTGTTCTG
CASP9	Reverse	CCTTCACCGAAACAGCATT
BCL2	Forward	CTGCACCTGACGCCCTTCACC
BCL2	Reverse	CACATGACCCCCACCGAACTCAAAGA
BAX	Forward	GGACGAACTGGACAGTAACATGG
BAX	Reverse	GCAAAGTAGAAAAGGGCGACAAC
LTCC	Forward	TGACTATTTGCCATTGTGTGG
LTCC	Reverse	GC GGAGGTAGGCATTGGG

Fold changes in gene expression were determined using the comparative Ct method ( $\Delta\Delta Ct$ ) with normalization to the housekeeping gene  $\beta 2M$ . This experiment was repeated in triplicate.

Statistical Testing and Analysis

Unless otherwise specified, results are presented as mean +/- standard deviation (SD) of n independent experiments. Statistical analyses were performed using MATLAB (The MathWorks, Natick MA). One-way analysis of variance (ANOVA), followed by Scheffe's post-hoc test, was used for multiple pairwise comparisons of unequal group sizes. One-way ANOVA, followed by Tukey's post-hoc test, was used for multiple pairwise comparisons of equal group sizes. Paired t-tests were used when comparing hECT contractile function pre- and post-treatment. Differences with a p-value less than 0.05 were considered statistically significant.

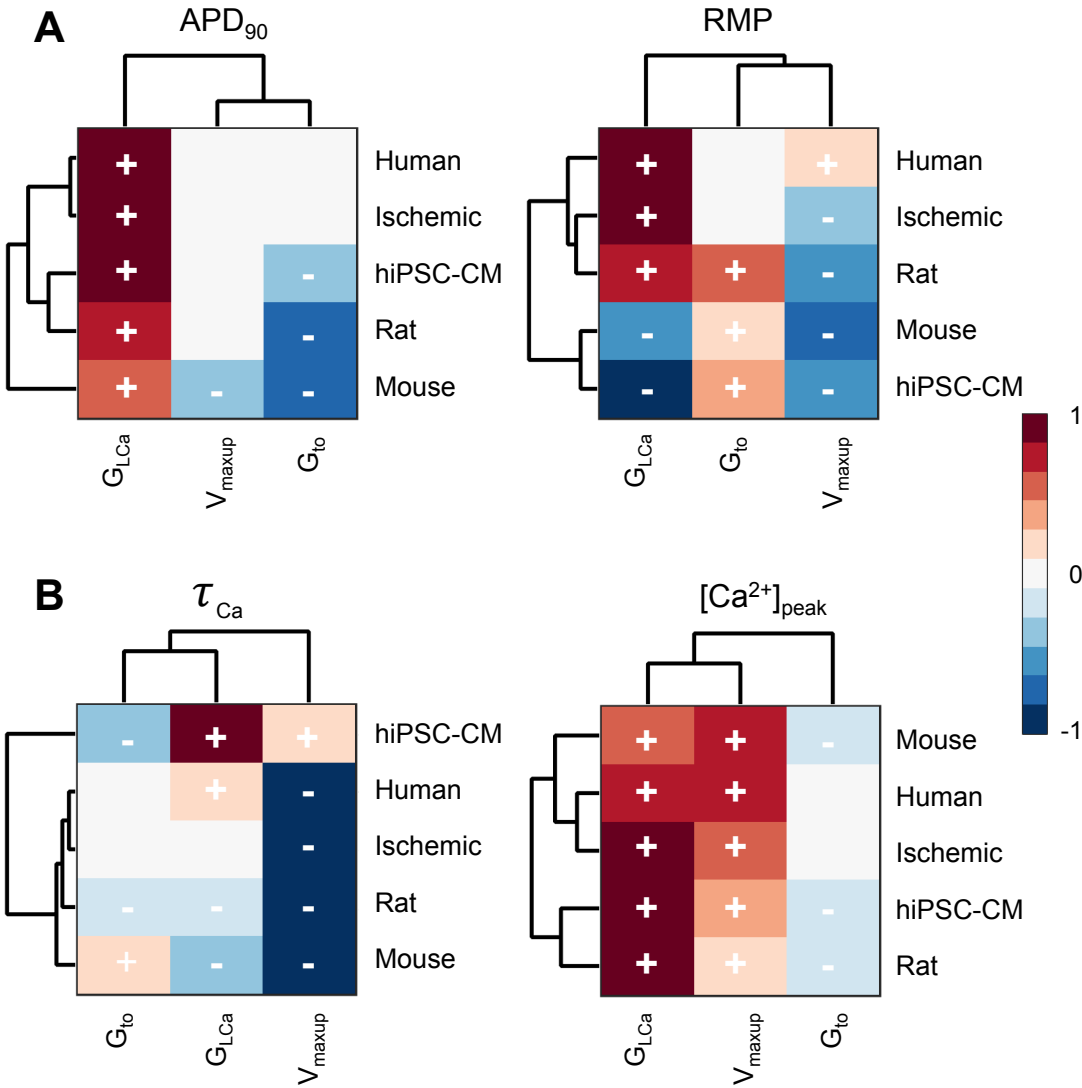


**Figure S1: Multi-Species Parameter Sensitivity Analysis of hMSC PS-Modulators of Cardiomyocyte Action Potential and Calcium Handling.** A multi-species parameter sensitivity analysis of L-type calcium current maximum permeability ( $G_{LCa}$ ), maximum SERCA uptake ( $V_{maxup}$ ), and transient outward current maximum conductance ( $G_{to}$ ) based on metrics of A) action potential and B) calcium handling for mouse ventricular myocyte (Mouse), rat cardiomyocyte (Rat), human induced pluripotent stem cell-derived cardiomyocytes (hiPSC-CM), adult human cardiomyocytes (Human), and adult ischemic human cardiomyocytes (Ischemic). This method: 1) accounts for the sensitivity of output metrics to model parameters; 2) provides insight into the variability among species and conditions commonly used in studies of hMSC effects; and 3) ranks output metric sensitivity to input parameters in an unbiased manner. Color scale as shown, with + and – designating positive and negative correlations, respectively. Non-standard abbreviations: APD<sub>90</sub> denotes action potential duration to 90% repolarization; RMP denotes resting membrane potential;  $\tau_{Ca}$  denotes calcium transient duration at 50% decay; [Ca<sup>2+</sup>]<sub>peak</sub> denotes diastolic-subtracted calcium transient amplitude.

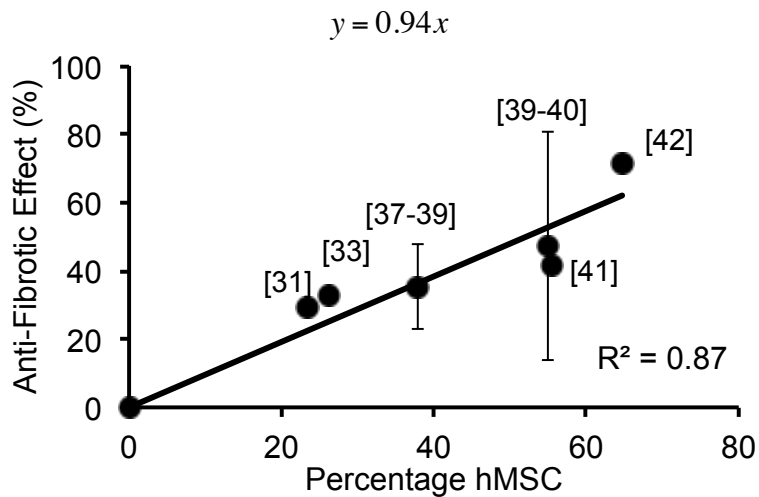


**Figure S2: Data Fitting hMSC PS Anti-Fibrotic Effects.** A linear regression with zero-intercept was used to describe the relationship between hMSC injection (as % cells of left ventricular cardiomyocytes) and the anti-fibrotic effect (% decrease in fibrosis). hMSC injection levels were normalized to the approximate number of cells in the left ventricle for a given species.<sup>46,47</sup> References for each data point are inset,<sup>31,33,37-42</sup> n = 1-3 per data point. Best-fit linear equation and  $R^2$  values are shown.

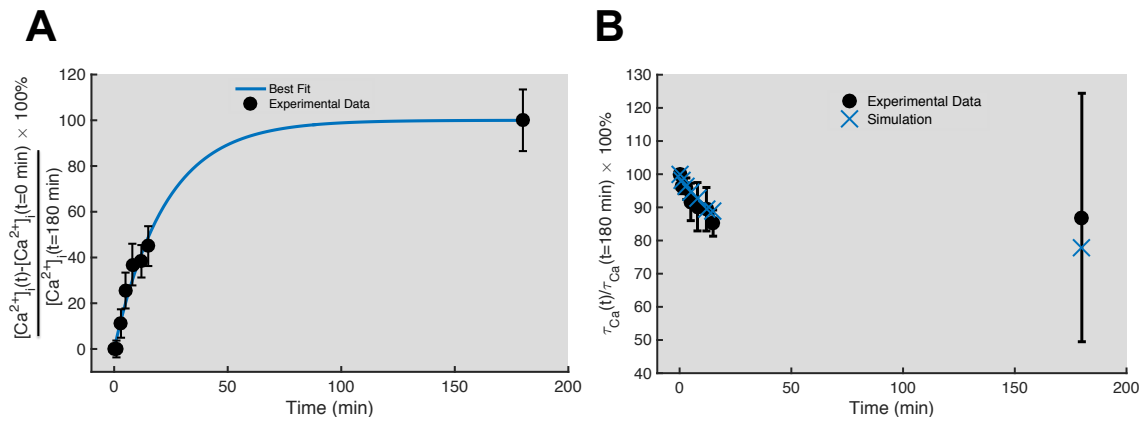


**Figure S3: Modeling Transient Effects of hMSC PS.** The computational model can be adapted to simulate transient effects of hMSC PS. A) Fitting the asymptotic function  $1 - e^{-t/\tau}$  to experimental data from Desantiago et al.<sup>14</sup> on the percent change of peak  $[\text{Ca}^{2+}]_i$  relative to control ( $t=0 \text{ min}$ ) and steady-state (assumed to be at  $t=180 \text{ min}$ ) in mouse ventricular cardiomyocytes treated with hMSC-conditioned media, yielding the best-fit time constant,  $\tau = 22.4 \text{ min}$ . B) Validation of this equation by simulating effects on  $\tau_{\text{Ca}}$  and comparing to experimental data from Desantiago et al.<sup>14</sup> In both plots, the mouse cardiomyocyte model was used with the least squares hMSC PS model at a saturated hMSC dose to match the reported experimental conditions.<sup>14</sup>

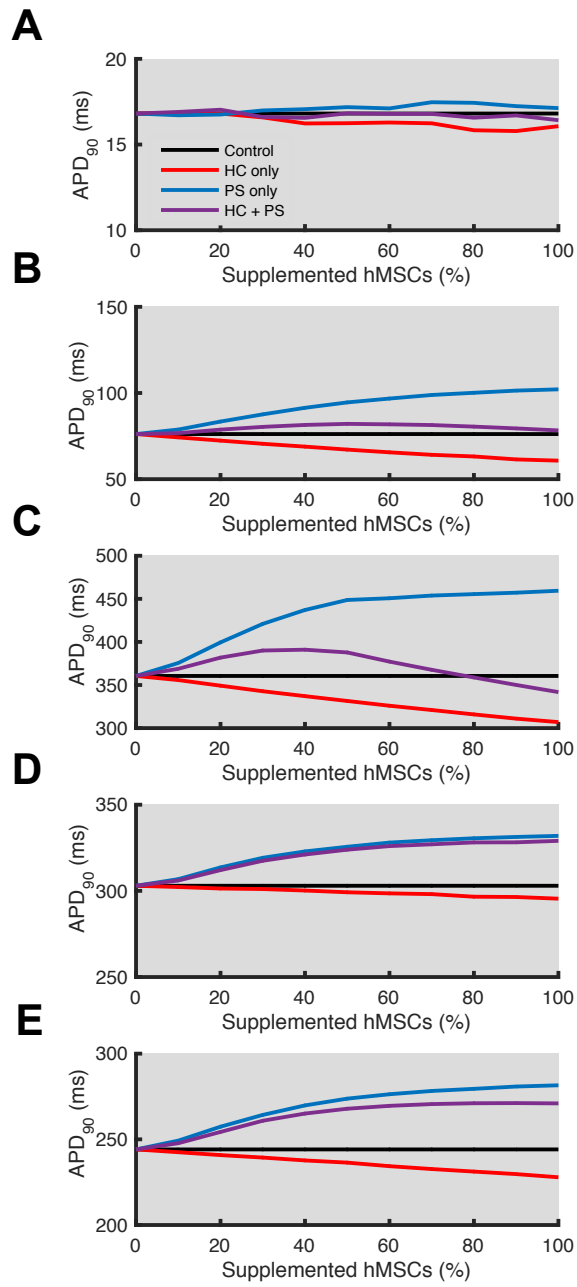


**Figure S4: Effects of hMSC HC and PS on Multi-Species Cardiomyocyte Action Potential Metrics.** hMSC HC and PS effects on APD<sub>90</sub> were simulated for: A) mouse, B) rat, C) human induced pluripotent stem cell-derived, D) adult human, and E) ischemic human cardiomyocytes at different hMSC dosages from 0% to 100% (i.e. 1:1 hMSC:cardiomyocyte ratio).

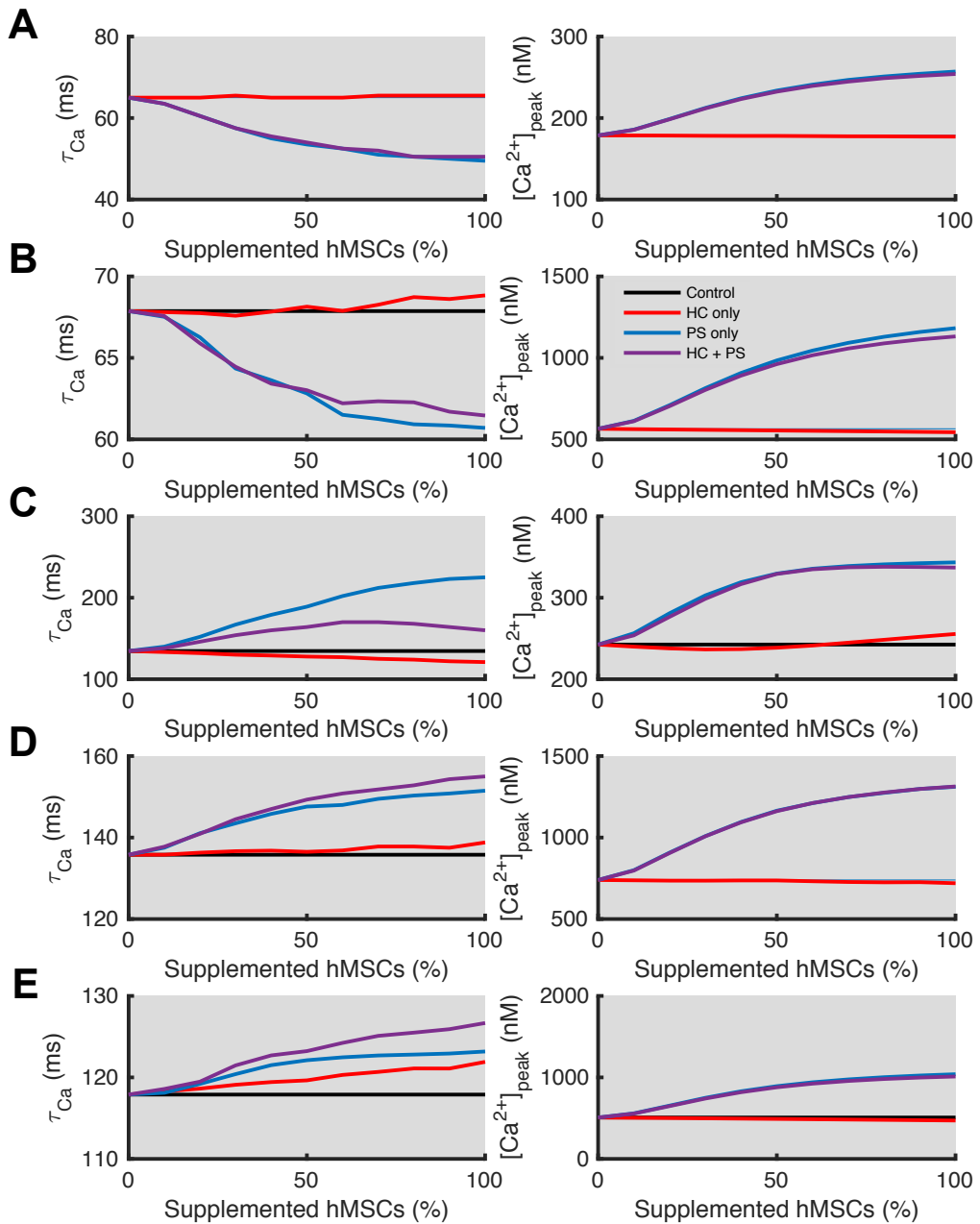


**Figure S5: Effects of hMSC HC and PS on Multi-Species Cardiomyocyte Calcium Handling Metrics.** hMSC HC and PS effects on calcium transient duration at 50% decay ( $\tau_{Ca}$ ; left inset), and diastolic-subtracted calcium transient amplitude ( $[Ca^{2+}]_{peak}$ ; right inset) were simulated for: A) mouse, B) rat, C) human induced pluripotent stem cell-derived, D) adult human, and E) ischemic human cardiomyocytes at different dosages.

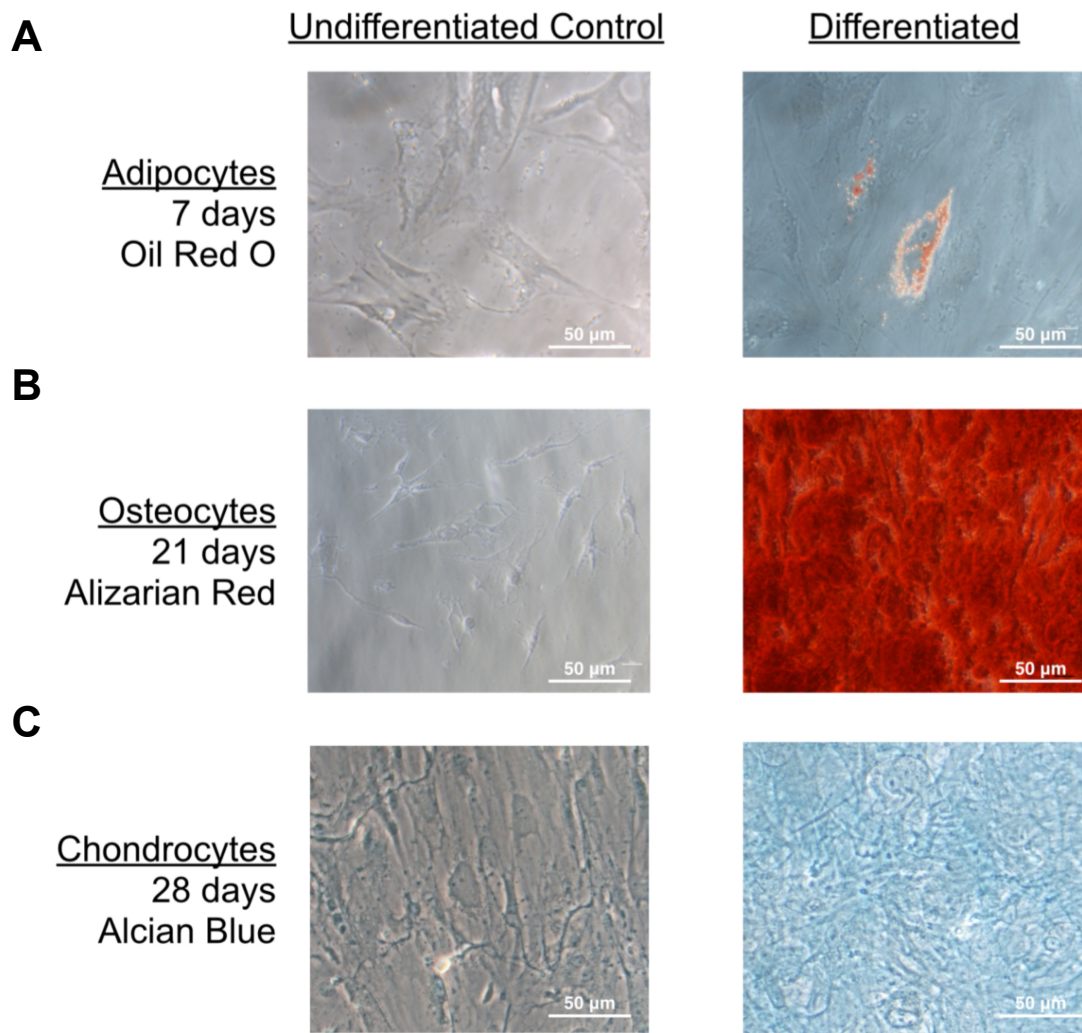


**Figure S6: Tri-Lineage Potential of hMSCs.** hMSCs display: A) adipogenic, B) osteogenic, and C) chondrogenic potential prior to adding them to hECTs.

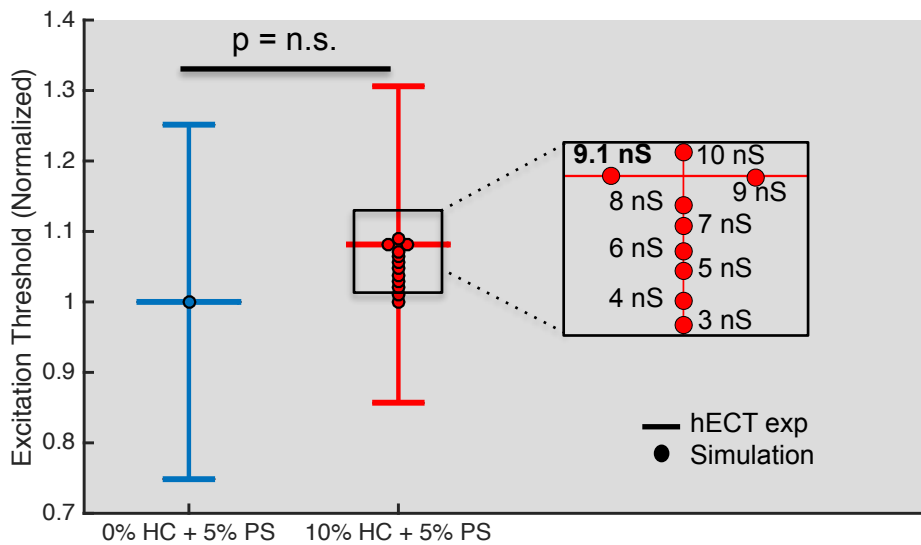


**Figure S7: Calibrating hMSC HC Gap Junction Conductance in 3-D Culture.** hMSC HC gap junction conductance was calibrated to hMSC 10% HC and 5% PS-treated hECTs ( $n = 11$ ) mean excitation threshold relative to hMSC 0% HC and 5% PS-treated hECTs ( $n = 10$ ). Experimental excitation threshold is defined as the minimum voltage pulse amplitude necessary to capture hECTs at 1 Hz pacing. Simulation excitation threshold was defined as the minimum voltage pulse necessary to excite the human induced pluripotent-stem cell derived cardiomyocyte model at 1 Hz, effectively matching experimental conditions. HC gap junction conductance was varied from 0 nS to 10 nS at 0.1 nS intervals (1 nS intervals shown). The best fit was achieved at 9.1 nS (bold). Data are normalized to control, mean +/- standard error of the mean.

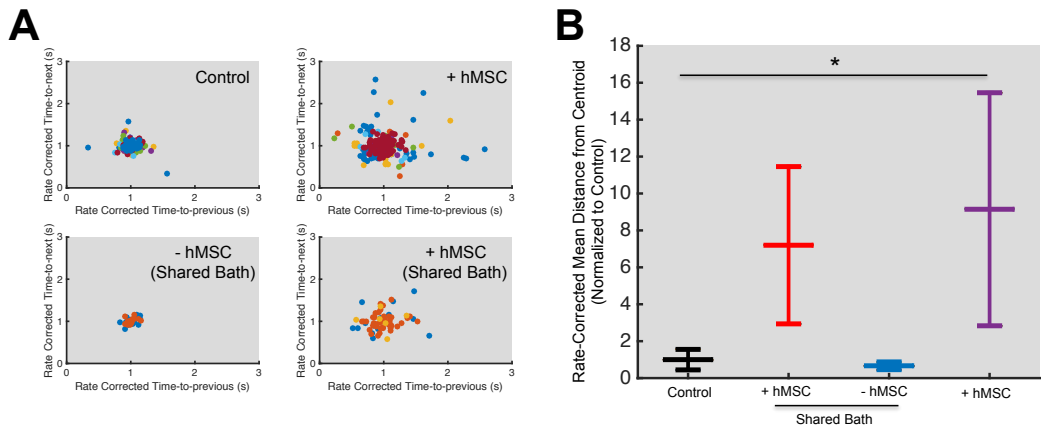


**Figure S8: hECT Spontaneous Beat Rate Variability Measurements Under hMSC HC and PS Interventions.** Using previously established methods, the spontaneous rate-corrected beat rate variability was measured for -hMSC, +hMSC, and alternating +hMSC and -hMSC hECTs in a shared media bath. A) Plot of collective rate corrected time-to-next and time-to-previous peaks for each group (hECT group shown in top right of plot), where different colors designate different hECT samples. B) Rate-corrected mean distance from centroid for -hMSC (black, n = 8), +hMSC (purple, n = 7), and alternating +hMSC (red, n = 3) and -hMSC (blue, n = 2) in a shared media bath. All data is normalized to control. \* p<0.05, mean +/- standard error of mean shown.

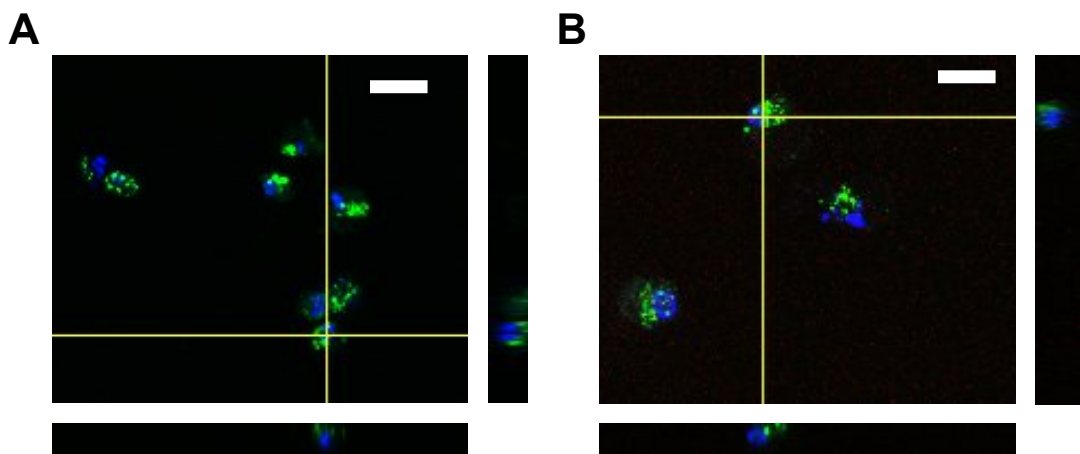


**Figure S9: hMSC Exosomes Taken Up by Cardiomyocytes and Fibroblasts.**  
Calcein-stained hMSC exosomes (green) are taken up by Hoechst stained (blue) human embryonic stem cell-derived SIRP $\alpha$ + cardiomyocytes (A) and CD90+ fibroblasts (B) within 48 hours of treatment. Scale bar = 20  $\mu$ m. Maximum intensity projections from confocal microscopy z-stacks shown with orthogonal projections at given locations (yellow lines).

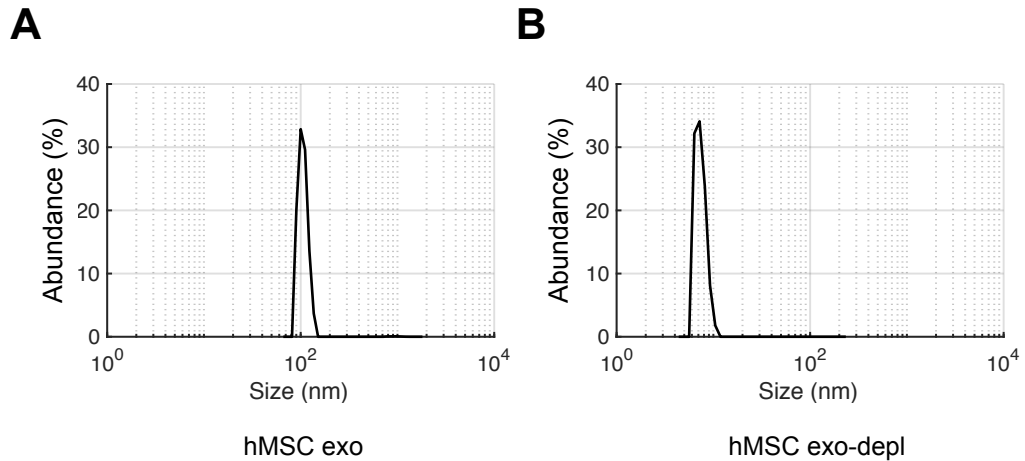


**Figure S10: Dynamic Light Scattering Analysis of Exosomes-Depleted and Exosomes-Enriched Fractions of the hMSC Secretome.** Confirmation via dynamic light scattering that the hMSC conditioned media was successfully separated in to A) a vesicular exosome-like fraction taken from the ultracentrifugation pellet with a mean diameter of 105.5 nm and B) a non-vesicular soluble fraction taken from the supernatant after ultracentrifugation.

**Supplementary Table 1: Coefficients of Determination for Multi-Species Parameter**

**Sensitivity Analysis on Action Potential and Calcium Handling Metrics.**

Coefficient of Determination				
Species	APD <sub>90</sub>	RMP	$\tau_{Ca}$	[Ca <sup>2+</sup> ] <sub>peak</sub>
Mouse	0.83	0.98	0.99	0.99
Rat	0.99	0.81	0.92	0.99
hiPSC	0.99	0.73	0.94	0.99
Healthy Human	0.99	0.94	0.99	0.99
Ischemic Human	0.99	0.99	0.98	0.99

**Supplementary Table 2: Bounds (Lower, Upper) and Justification for Experimentally-Based Calibration Model**

Parameter	Bounds	Justification
$\Delta G_{LCa}$	(0.27,0.62)	Within one standard error of experimental data. <sup>14</sup>
$\Delta V_{max\,up}$	(0,1)	0: Based on experimental data, <sup>14</sup> SERCA activity increases.  1: As performed elsewhere, the conductance is assumed to increase by a maximum of 100%. <sup>11,12</sup>
$EC_{50,LCa}$	$(\text{Log}_{10}(28), \text{Log}_{10}(200))$	$\text{Log}_{10}(28)$ : Experimental data <sup>13</sup> demonstrates a growth phase when supplementing 7% and 28% hMSC PS. Therefore, the half maximum effective concentration is assumed to be greater than $\text{Log}_{10}(28)$ .  $\text{Log}_{10}(200)$ : We assume the half maximum effective concentration is achieved prior to a 2:1 hMSC:myocyte ratio.
$EC_{50,v}$	$(0, \text{Log}_{10}(200))$	0: Due to limited experimental data, our lower bound is the minimum feasible value.  $\text{Log}_{10}(200)$ : As above, we assume the half maximum effective concentration is achieved prior to a 2:1 hMSC:myocyte ratio.

$k_{LCa}$	(0.6,5)	<p>0.6: The APD<sub>90</sub> slope between 7% and 28% hMSC PS was 0.45<sup>13</sup>, corresponding to a <math>G_{LCa}</math> slope of 0.6 (sensitivity coefficient of 0.75).</p> <p>Therefore, we assume <math>k_{LCa}</math> must be greater than 0.6.</p> <p>5: Given our lower bound on the half maximum effective concentraton, a k value of 5 will lead to no change in <math>G_{LCa}</math> at 7% hMSC dosage. This would lead to no effect on APD<sub>90</sub> at this level, conflicting with experimental data.<sup>13</sup></p>
$k_v$	(0,5)	<p>0: Due to limited experimental data, our lower bound is the minimum feasible value.</p> <p>5: Assumed to be the same upper limit as <math>k_{LCa}</math>.</p>

**Supplementary Table 3: Parameters for Least Squares “Best” Accepted Model**

Parameter	Value
$\Delta G_{LCa}$	0.61
$\Delta V_{\max up}$	0.017
$EC_{50,LCa}$	$\log_{10}(38.4)$
$EC_{50,V}$	$\log_{10}(45.9)$
$k_{LCa}$	1.77
$k_V$	3.51

**Supplementary Table 4: Coefficients of Determination for Contractile Function**

**Sensitivity Analysis**

Coefficient of Determination			
Species	Force	+dF/dt	-dF/dt
hiPSC	0.99	0.99	0.99
Mature hCM	0.99	0.99	0.99
Ischemic Mature hCM	0.98	0.98	0.98

**Supplementary Table 5: Immunogenic and Angiogenic Pathways Significantly Modulated by Up-Regulated Factors in Paracrine Bath**

Category	Function	p-value
Immune	Immune Cell Trafficking	1.96E-9 to 2.35E-6
	Hematological System Development and Function	7.85E-7 to 9.38E-2
	Inflammatory Response	6.89E-13 to 6.61E-2
	Cellular Movement	1.45E-15 to 3.98E-2
	Inflammatory Disease	2.86E-13 to 6.61E-2
	Lymphoid Tissue Structure and Development	1.19E-12 to 2.39E-6
	Immunological Disease	1.97E-10 to 4.29E-2
	Cell-mediated Immune Response	1.47E-8 to 1.83E-7
Angiogenesis	Angiogenesis	3.94E-13
	Vasculogenesis	8.82E-11
	Neovascularization	5.54E-07
	Branching	4.71E-07
	Tubulation	1.72E-06

**Supplementary Table 6: Up-Regulated Factors Linked to Cardiac Cell-Specific Pathways from Proteomic Analysis of hECT Conditioned Media**

<b>Factor</b>	<b>Fold Change</b>
FADD	5.3
Survivin	2.8
IGF-1	2.6
FoxO1	2.5
IL-1 R9	2.3
IGF-II	2.2
Caspase-8	2.2
KLF4	2.1

## **Supporting References:**

1. Bondarenko VE, Szigeti GP, Bett GC, Kim SJ, Rasmusson RL. Computer model of action potential of mouse ventricular myocytes. *Am J Physiol Heart Circ Physiol.* 2004;287:H1378-1403
2. Devenyi RA, Sobie EA. There and back again: Iterating between population-based modeling and experiments reveals surprising regulation of calcium transients in rat cardiac myocytes. *J Mol Cell Cardiol.* 2016;96:38-48
3. Paci M, Hyttinen J, Aalto-Setala K, Severi S. Computational models of ventricular- and atrial-like human induced pluripotent stem cell derived cardiomyocytes. *Ann Biomed Eng.* 2013;41:2334-2348
4. ten Tusscher KH, Panfilov AV. Alternans and spiral breakup in a human ventricular tissue model. *Am J Physiol Heart Circ Physiol.* 2006;291:H1088-1100
5. Weiss DL, Ifland M, Sachse FB, Seemann G, Dossel O. Modeling of cardiac ischemia in human myocytes and tissue including spatiotemporal electrophysiological variations. *Biomed Tech (Berl).* 2009;54:107-125
6. Mayourian J, Savizky RM, Sobie EA, Costa KD. Modeling electrophysiological coupling and fusion between human mesenchymal stem cells and cardiomyocytes. *PLoS Comput Biol.* 2016;12:e1005014
7. Cummins MA, Dalal PJ, Bugana M, Severi S, Sobie EA. Comprehensive analyses of ventricular myocyte models identify targets exhibiting favorable rate dependence. *PLoS Comput Biol.* 2014;10:e1003543
8. Sarkar AX, Sobie EA. Regression analysis for constraining free parameters in electrophysiological models of cardiac cells. *PLoS Comput Biol.* 2010;6:e1000914

9. Eisen MB, Spellman PT, Brown PO, Botstein D. Cluster analysis and display of genome-wide expression patterns. *Proc Natl Acad Sci U S A*. 1998;95:14863-14868
10. Li GR, Sun H, Deng X, Lau CP. Characterization of ionic currents in human mesenchymal stem cells from bone marrow. *Stem Cells*. 2005;23:371-382
11. Britton OJ, Bueno-Orovio A, Van Ammel K, Lu HR, Towart R, Gallacher DJ, Rodriguez B. Experimentally calibrated population of models predicts and explains intersubject variability in cardiac cellular electrophysiology. *Proc Natl Acad Sci U S A*. 2013;110:E2098-2105
12. Zhou X, Bueno-Orovio A, Orini M, Hanson B, Hayward M, Taggart P, Lambiase PD, Burrage K, Rodriguez B. In vivo and in silico investigation into mechanisms of frequency dependence of repolarization alternans in human ventricular cardiomyocytes. *Circ Res*. 2016;118:266-278
13. Askar SF, Ramkisoensing AA, Atsma DE, Schalij MJ, de Vries AA, Pijnappels DA. Engraftment patterns of human adult mesenchymal stem cells expose electrotonic and paracrine proarrhythmic mechanisms in myocardial cell cultures. *Circ Arrhythm Electrophysiol*. 2013;6:380-391
14. DeSantiago J, Bare DJ, Semenov I, Minshall RD, Geenen DL, Wolska BM, Banach K. Excitation-contraction coupling in ventricular myocytes is enhanced by paracrine signaling from mesenchymal stem cells. *J Mol Cell Cardiol*. 2012;52:1249-1256
15. Prinz AA, Bucher D, Marder E. Similar network activity from disparate circuit parameters. *Nat Neurosci*. 2004;7:1345-1352
16. Turnbull IC, Karakikes I, Serrao GW, Backeris P, Lee JJ, Xie C, Senyei G, Gordon RE, Li RA, Akar FG, Hajjar RJ, Hulot JS, Costa KD. Advancing functional

- engineered cardiac tissues toward a preclinical model of human myocardium.  
*FASEB J.* 2014;28:644-654
17. Cashman TJ, Josowitz R, Gelb BD, Li RA, Dubois NC, Costa KD. Construction of defined human engineered cardiac tissues to study mechanisms of cardiac cell therapy. *J Vis Exp.* 2016:e53447
  18. Cashman TJ, Josowitz R, Johnson BV, Gelb BD, Costa KD. Human engineered cardiac tissues created using induced pluripotent stem cells reveal functional characteristics of braf-mediated hypertrophic cardiomyopathy. *PLoS One.* 2016;11:e0146697
  19. Schaaf S, Shibamiya A, Mewe M, Eder A, Stohr A, Hirt MN, Rau T, Zimmermann WH, Conradi L, Eschenhagen T, Hansen A. Human engineered heart tissue as a versatile tool in basic research and preclinical toxicology. *PLoS One.* 2011;6:e26397
  20. Serrao GW, Turnbull IC, Ancukiewicz D, Kim DE, Kao E, Cashman TJ, Hadri L, Hajjar RJ, Costa KD. Myocyte-depleted engineered cardiac tissues support therapeutic potential of mesenchymal stem cells. *Tissue Eng Part A.* 2012;18:1322-1333
  21. Rice JJ, Winslow RL, Hunter WC. Comparison of putative cooperative mechanisms in cardiac muscle: Length dependence and dynamic responses. *Am J Physiol.* 1999;276:H1734-1754
  22. Pioner JM, Racca AW, Klaiman JM, et al. Isolation and mechanical measurements of myofibrils from human induced pluripotent stem cell-derived cardiomyocytes. *Stem Cell Reports.* 2016;6:885-896
  23. Ribeiro AJ, Ang YS, Fu JD, Rivas RN, Mohamed TM, Higgs GC, Srivastava D, Pruitt BL. Contractility of single cardiomyocytes differentiated from pluripotent

- stem cells depends on physiological shape and substrate stiffness. *Proc Natl Acad Sci U S A.* 2015;112:12705-12710
24. Valiunas V, Doronin S, Valiuniene L, Potapova I, Zuckerman J, Walcott B, Robinson RB, Rosen MR, Brink PR, Cohen IS. Human mesenchymal stem cells make cardiac connexins and form functional gap junctions. *J Physiol.* 2004;555:617-626
  25. Kazbanov IV, ten Tusscher KH, Panfilov AV. Effects of heterogeneous diffuse fibrosis on arrhythmia dynamics and mechanism. *Sci Rep.* 2016;6:20835
  26. Gomez JF, Cardona K, Martinez L, Saiz J, Trenor B. Electrophysiological and structural remodeling in heart failure modulate arrhythmogenesis. 2d simulation study. *PLoS One.* 2014;9:e103273
  27. Kawara T, Derksen R, de Groot JR, Coronel R, Tasseron S, Linnenbank AC, Hauer RN, Kirkels H, Janse MJ, de Bakker JM. Activation delay after premature stimulation in chronically diseased human myocardium relates to the architecture of interstitial fibrosis. *Circulation.* 2001;104:3069-3075
  28. MacCannell KA, Bazzazi H, Chilton L, Shibukawa Y, Clark RB, Giles WR. A mathematical model of electrotonic interactions between ventricular myocytes and fibroblasts. *Biophys J.* 2007;92:4121-4132
  29. Leiker M, Suzuki G, Iyer VS, Carty JM, Jr., Lee T. Assessment of a nuclear affinity labeling method for tracking implanted mesenchymal stem cells. *Cell Transplant.* 2008;17:911-922
  30. Le Visage C, Gournay O, Benguirat N, Hamidi S, Chaumsumier L, Mougenot N, Flanders JA, Isnard R, Michel JB, Hatem S, Letourneur D, Norol F. Mesenchymal stem cell delivery into rat infarcted myocardium using a porous polysaccharide-based scaffold: A quantitative comparison with endocardial injection. *Tissue Eng Part A.* 2012;18:35-44

31. Tang YL, Tang Y, Zhang YC, Qian K, Shen L, Phillips MI. Improved graft mesenchymal stem cell survival in ischemic heart with a hypoxia-regulated heme oxygenase-1 vector. *J Am Coll Cardiol.* 2005;46:1339-1350
32. Kurtz A. Mesenchymal stem cell delivery routes and fate. *Int J Stem Cells.* 2008;1:1-7
33. Iso Y, Spees JL, Serrano C, Bakondi B, Pochampally R, Song YH, Sobel BE, Delafontaine P, Prockop DJ. Multipotent human stromal cells improve cardiac function after myocardial infarction in mice without long-term engraftment. *Biochem Biophys Res Commun.* 2007;354:700-706
34. Hale SL, Dai W, Dow JS, Kloner RA. Mesenchymal stem cell administration at coronary artery reperfusion in the rat by two delivery routes: A quantitative assessment. *Life Sci.* 2008;83:511-515
35. Freyman T, Polin G, Osman H, Crary J, Lu M, Cheng L, Palasis M, Wilensky RL. A quantitative, randomized study evaluating three methods of mesenchymal stem cell delivery following myocardial infarction. *Eur Heart J.* 2006;27:1114-1122
36. van der Spoel TI, Vrijen KR, Koudstaal S, Sluijter JP, Nijssen JF, de Jong HW, Hoefer IE, Cramer MJ, Doevedans PA, van Belle E, Chamuleau SA. Transendocardial cell injection is not superior to intracoronary infusion in a porcine model of ischaemic cardiomyopathy: A study on delivery efficiency. *J Cell Mol Med.* 2012;16:2768-2776
37. Wang D, Zhang F, Shen W, Chen M, Yang B, Zhang Y, Cao K. Mesenchymal stem cell injection ameliorates the inducibility of ventricular arrhythmias after myocardial infarction in rats. *Int J Cardiol.* 2011;152:314-320

38. Hwang HJ, Chang W, Song BW, et al. Antiarrhythmic potential of mesenchymal stem cell is modulated by hypoxic environment. *J Am Coll Cardiol.* 2012;60:1698-1706
39. Citro L, Naidu S, Hassan F, Kuppusamy ML, Kuppusamy P, Angelos MG, Khan M. Comparison of human induced pluripotent stem-cell derived cardiomyocytes with human mesenchymal stem cells following acute myocardial infarction. *PLoS One.* 2014;9:e116281
40. Richardson JD, Bertaso AG, Psaltis PJ, Frost L, Carbone A, Paton S, Nelson AJ, Wong DT, Worthley MI, Gronthos S, Zannettino AC, Worthley SG. Impact of timing and dose of mesenchymal stromal cell therapy in a preclinical model of acute myocardial infarction. *J Card Fail.* 2013;19:342-353
41. Liu JF, Wang BW, Hung HF, Chang H, Shyu KG. Human mesenchymal stem cells improve myocardial performance in a splenectomized rat model of chronic myocardial infarction. *J Formos Med Assoc.* 2008;107:165-174
42. Mathieu E, Lamirault G, Toquet C, Lhommet P, Rederstorff E, Source S, Biteau K, Hulin P, Forest V, Weiss P, Guicheux J, Lemarchand P. Intramyocardial delivery of mesenchymal stem cell-seeded hydrogel preserves cardiac function and attenuates ventricular remodeling after myocardial infarction. *PLoS One.* 2012;7:e51991
43. Greisas A, Zlochiver S. Modulation of spiral-wave dynamics and spontaneous activity in a fibroblast/myocyte heterocellular tissue--a computational study. *IEEE Trans Biomed Eng.* 2012;59:1398-1407
44. Thery C, Amigorena S, Raposo G, Clayton A. Isolation and characterization of exosomes from cell culture supernatants and biological fluids. *Curr Protoc Cell Biol.* 2006;Chapter 3:Unit 3 22

45. Gray WD, French KM, Ghosh-Choudhary S, Maxwell JT, Brown ME, Platt MO, Searles CD, Davis ME. Identification of therapeutic covariant microRNA clusters in hypoxia-treated cardiac progenitor cell exosomes using systems biology. *Circ Res*. 2015;116:255-263
46. Schipke J, Banmann E, Nikam S, Voswinckel R, Kohlstedt K, Loot AE, Fleming I, Muhlfeld C. The number of cardiac myocytes in the hypertrophic and hypotrophic left ventricle of the obese and calorie-restricted mouse heart. *J Anat*. 2014;225:539-547
47. Eisele JC, Schaefer IM, Randel Nyengaard J, Post H, Liebetanz D, Bruel A, Muhlfeld C. Effect of voluntary exercise on number and volume of cardiomyocytes and their mitochondria in the mouse left ventricle. *Basic Res Cardiol*. 2008;103:12-21

**Chapter 7: Exosomal microRNA-21-5p Mediates Mesenchymal Stem Cell Paracrine Effects on Human Cardiac Tissue Contractility**

*Note: The following chapter is a modified draft of an original first-author research article published in Circulation Research:*

Mayourian J, Ceholski DK, Gorski PA, Mathiyalagan P, Murphy JF, Salazar SI, Stillitano F, Hare JM, Sahoo S, Hajjar RJ, Costa KD. Exosomal microRNA-21-5p Mediates Mesenchymal Stem Cell Paracrine Effects on Human Cardiac Tissue Contractility. *Circulation Research*. 2018; in press.

JM conceived the idea, collected and analyzed the computational and tissue engineering functional data, and wrote the manuscript. The current *Circulation Research* CTA states, "authors may use parts of the work (eg, tables, figures) in subsequent works without requesting permission from the AHA."

## 7.1 Abstract

**Rationale:** The promising clinical benefits of delivering human mesenchymal stem cells (hMSCs) for treating heart disease warrant a better understanding of underlying mechanisms of action. hMSC exosomes increase myocardial contractility; however, the exosomal cargo responsible for these effects remains unresolved.

**Objective:** This study aims to identify lead cardioactive hMSC exosomal microRNAs to provide a mechanistic basis for optimizing future stem cell-based cardiotherapies.

**Methods and Results:** Integrating systems biology and human engineered cardiac tissue (hECT) technologies, partial least squares regression analysis of exosomal microRNA profiling data predicted microRNA-21-5p (miR-21-5p) levels positively correlate with contractile force and calcium handling gene expression responses in hECTs treated with conditioned media from multiple cell types. Furthermore, miR-21-5p levels were significantly elevated in hECTs treated with the exosome-enriched fraction of the hMSC secretome (hMSC-exo) versus untreated controls. This motivated experimentally testing the human-specific role of miR-21-5p in hMSC-exo-mediated increases of cardiac tissue contractility. Treating hECTs with miR-21-5p alone was sufficient to recapitulate effects observed with hMSC-exo on hECT developed force and expression of associated calcium handling genes (e.g., SERCA2a and L-type calcium channel). Conversely, knockdown of miR-21-5p in hMSCs significantly diminished exosomal pro-contractile and associated calcium handling gene expression effects on hECTs. Western blots supported miR-21-5p effects on calcium handling gene expression at the protein level, corresponding to significantly increased calcium transient amplitude and decreased decay time constant in comparison to miR-scramble control. Mechanistically, co-treating with miR-21-5p and LY294002, a PI3K inhibitor, suppressed these effects. Finally, mathematical simulations

predicted the translational capacity for miR-21-5p treatment to restore calcium handling in mature ischemic adult human cardiomyocytes.

**Conclusion:** miR-21-5p plays a key role in hMSC-exo-mediated effects on cardiac contractility and calcium handling, likely via PI3K signaling. These findings may open new avenues of research to harness the role of miR-21-5p in optimizing future stem cell-based cardiotherapies.

## **7.2 Novelty and Significance**

### ***What is Known?***

- Human mesenchymal stem cells (hMSCs) are an emerging and promising cardiotherapeutic approach.
- hMSC paracrine factors can modulate cardiac excitation-contraction coupling and thereby contractility.
- Exosomes are primarily responsible for hMSC paracrine-mediated increases in human engineered cardiac tissue (hECT) contractility and associated calcium handling gene expression; however, the exosomal cargo responsible for these effects remains unresolved.

### ***What New Information Does This Article Contribute?***

- Bioinformatics data predicting microRNA-21-5p (miR-21-5p) as a lead cardioactive exosomal miR in therapeutic hMSC-based paracrine signaling.
- Experimental hECT data demonstrating exosomal miR-21-5p mediates hMSC paracrine effects on hECT contractility.
- Mechanistic support of miR-21-5p increasing cardiac calcium handling and thereby contractility via the PI3K signaling cascade.

The molecular modulators of myocardial contractility in hMSC-based cardiotherapies remain unresolved, hindering efforts to maximize therapeutic efficacy. In this study, we utilized an integrated systems biology and tissue engineering approach to identify key hMSC cardioactive exosomal microRNAs (miRs). Bioinformatics and experimental data support miR-21-5p as a lead cardioactive hMSC exosomal miR. Indeed, delivery of miR-21-5p recapitulates effects of hMSC exosome treatment on hECT contractile function, while knocking down miR-21-5p in hMSCs diminishes exosomal enhancement of contractility. The effects of miR-21-5p on calcium handling and contractility are supported at both the mRNA and protein levels. Mechanistically,

miR-21-5p increases calcium handling and thereby contractility likely via the PI3K signaling cascade. Finally, we modified a computational model of excitation-contraction coupling to predict the translational capacity for miR-21-5p treatment to restore calcium handling in adult human ischemic cardiomyocytes. These findings support harnessing the role of exosomal miRs, such as miR-21-5p, in optimizing future stem cell-based cardiotherapies.

### 7.3 Introduction

Human bone marrow-derived mesenchymal stem cells (hMSCs) are an emerging and promising approach to treat ischemic and non-ischemic cardiomyopathies.<sup>1,2</sup> To date, phase II clinical trials of hMSC delivery have supported the conduct of phase III trials.<sup>3-5</sup> Despite this advancement, there remains a need to enhance and refine stem cell-based treatment strategies for myocardial diseases through rational design. It is therefore of great interest to better understand underlying hMSC mechanisms of action to optimize future stem cell-based cardiotherapies.

Acting predominantly through paracrine signaling mechanisms, hMSCs have well recognized immunomodulatory, pro-angiogenic, and anti-fibrotic effects on diseased myocardium.<sup>1</sup> Additionally, hMSC paracrine factors can modulate cardiac excitation-contraction coupling and contractility.<sup>6-8</sup> We recently demonstrated the exosomal fraction of the hMSC secretome—taken up by both SIRP $\checkmark^+$ /CD90 $^-$  human pluripotent stem cell-derived cardiomyocytes (hPSC-CMs) and SIRP $\checkmark^-$ /CD90 $^+$  hPSC-fibroblasts comprising our human engineered cardiac tissues (hECTs)<sup>6</sup>—to be largely responsible for hMSC paracrine-mediated increases in hECT contractility and associated calcium handling gene expression.<sup>6</sup> While exosomal microRNAs (miRs) are widely thought to mediate intercellular communications and gene regulation,<sup>9-11</sup> the specific exosomal miRs responsible for hMSC-mediated cardioactivity remain largely unresolved.

Advancements in systems biology have facilitated associating complex networks of biological inputs and functional outputs via partial least squares regression (PLSR).<sup>9,11</sup> This method has shown promise for predicting cardioactive anti-fibrotic and pro-angiogenic exosomal miR cargo released by cardiac progenitor cells, using classic tube formation and fibrosis assays as functional outputs.<sup>9,11</sup> However, in the context of human cardiac contractile function, other assays are necessary; to this end, our custom multi-hECT platform has proven valuable as a contractility assay to test paracrine potency.<sup>6,7</sup>

In this study, we hypothesized that integrating systems biology and tissue engineering approaches would help identify lead cardioactive hMSC exosomal miRs responsible for increasing human cardiac tissue contractility. We first predicted microRNA-21-5p (miR-21-5p) as a lead cardioactive hMSC exosomal miR via PLSR. Next, we experimentally tested the human-specific role of miR-21-5p in hMSC exosomal effects on hECT contractile function, as well as cardiomyocyte calcium handling. Finally, we investigate the underlying mechanism of miR-21-5p-mediated effects on cardiomyocyte calcium handling and contractility, and predicted how these findings may translate to ischemic human adult cardiomyocytes. Altogether, we demonstrate a key role of miR-21-5p in hMSC exosomal treatments to increase hECT contractility likely via PI3K signaling, suggesting a specific molecular mediator to exploit for optimizing future stem cell-based cardiotherapies.

## 7.4 Methods

An expanded methods section is available in the Supplement. All data, methods, and study materials are available upon request by contacting Joshua Mayourian ([joshua.mayourian@icahn.mssm.edu](mailto:joshua.mayourian@icahn.mssm.edu)) or the corresponding author.

### 7.4.1 Partial Least Squares Regression

PLSR was performed with the nonlinear iterative partial least squares algorithm, as described elsewhere.<sup>9,11</sup> Similar to our previous work,<sup>6</sup> predicted direct activation (Figure 1) was performed via the Ingenuity Pathway Analysis (IPA®, Qiagen) Molecule Activity Predictor.

### 7.4.2 hECT Contractility Assay

hECTs were created from hPSC-CMs and type-I collagen using methods previously described.<sup>6</sup> Baseline functional analysis was performed on culture day 5, followed by a single treatment with either: 1) serum-free defined media (SFDM); 2) fresh hMSC conditioned media

(hMSC-CdM); 3) exosome-depleted hMSC conditioned media (hMSC-exo-depl); 4) hMSC exosome-enriched SFDM (hMSC-exo); 5) SFDM supplemented with 2 nM of naked human microRNA mimic negative control (miR-scr-con; Thermo Fisher Scientific); 6) SFDM supplemented with 2 nM of naked human microRNA-21-5p mimic (miR-21-5p; Thermo Fisher Scientific); 7) exosomes from naked human microRNA inhibitor negative control (Thermo Fisher Scientific) treated hMSCs (hMSC-exo:miR-scr-con); or 8) exosomes from miR-21-5p inhibitor (Thermo Fisher Scientific) treated hMSCs (hMSC-exo:miR-21-5p-KD). Following five days of post-treatment functional analysis (culture day 10), hECTs were flash-frozen for real time quantitative polymerase chain reaction (qRT-PCR). All primers used can be found in the Supplement.

#### *7.4.3 Western Blots of Lysate from hPSC-CM Monolayers*

hPSC-CM monolayers in 6-well tissue culture plates were used for western blots as previously described.<sup>12</sup> hPSC-CM monolayers were treated for 48 hours with either 10 nM miR-scr-con or 10 nM miR-21-5p. See Table S1 for specific characteristics of antibodies used for western blots.

#### *7.4.4 Calcium Transient Measurements*

Calcium transients were performed on hPSC-CMs using the IonOptix Calcium Imaging System (Westwood, MA) as previously described.<sup>12</sup> hPSC-CMs were treated for 48 hours with either: 1) 10 nM miR-scr-con without LY294002 (miR-scr-con - LY); 2) 10 nM miR-21-5p without LY294002 (miR-21-5p - LY); 3) 10 nM miR-scr-con with 10 µM LY294002 (miR-scr-con + LY); or 4) 10 nM miR-21-5p with 10 µM LY294002 (miR-21-5p + LY).

#### *7.4.5 Single-Cell Cardiomyocyte Electrophysiology Models*

Multiple single-cell cardiomyocyte electrophysiological models were utilized in this study, including the: Paci et al. human induced pluripotent stem cell-derived ventricular-like cardiomyocyte model;<sup>13</sup> ten Tusscher et al. human healthy cardiomyocyte model;<sup>14</sup> and Weiss et al. human ischemic cardiomyocyte model.<sup>15</sup> All single-cell models were numerically integrated with MATLAB's (The MathWorks, Natick MA) stiff ordinary differential equation solver (ode15s) until steady state was achieved.

#### *7.4.6 Experimental Calibration of miR-21-5p Effects on Single-Cell Cardiomyocyte Electrophysiology*

Effects of miR-21-5p were simulated using experimentally calibrated<sup>6,16,17</sup> adjustments to the baseline L-type calcium channel (LTCC) maximum permeability ( $G_{LCa}$ ) and sarcoendoplasmic reticulum calcium-ATPase (SERCA2a) maximum uptake activity ( $V_{maxup}$ ) parameters in the single-cell cardiomyocyte models described above.

We experimentally calibrated the effects of hMSC miR-21-5p on  $G_{LCa}$  and  $V_{maxup}$  using original calcium transient experimental data found herein and a modified version of methods previously described.<sup>6,16,17</sup>  $G_{LCa}$  and  $V_{maxup}$  were chosen because LTCC and SERCA2a mRNA levels are modulated by miR-21-5p, as demonstrated herein. Briefly, we constructed a population of 1,000 models of the single-cell Paci et al. human induced pluripotent stem cell-derived ventricular-like cardiomyocyte electrophysiology model<sup>13</sup> by randomly assigning empirically relevant parameter values to characterize changes in maximal fluxes due to miR-21-5p:

$$G'_{LCa} = G_{LCa} \times \Delta G_{LCa}$$

$$V'_{maxup} = V_{maxup} \times \Delta V_{maxup}$$

where  $G'_{LCa}$  and  $V'_{maxup}$  represent the updated values of maximum LTCC permeability and SERCA2a maximum uptake activity due to miR-21-5p effects, respectively, and  $\Delta G_{LCa}$  and

$\Delta V_{\text{maxup}}$  represent fold changes in baseline LTCC maximum permeability and SERCA2a maximum uptake activity parameters due to miR-21-5p effects, respectively. Motivated by empirical data herein,  $\Delta V_{\text{maxup}}$  was randomly assigned between 1 and 4, whereas  $\Delta G_{\text{LCa}}$  was randomly assigned between 1 and 2.

Our model-calibration algorithm determined whether a given set of model parameters should be added to an “accepted” population based on comparison of simulated outputs to the following metrics from experimental data within this study: 1) calcium transient amplitude ( $[\text{Ca}^{2+}]_i$  Amplitude); and 2) decay time constant ( $\tau_{\text{Ca}}$ ). Modified from Prinz et al., bounds on allowed output variability were set to 1 standard deviation around mean values.<sup>18</sup> Select accepted parameter sets were input into the Weiss et al.<sup>15</sup> ischemic human cardiomyocyte model.

#### 7.4.7 Statistical Analyses

Descriptive statistics are presented as mean $\pm$ S.E.M., with comparative statistical methods described in the corresponding figure legend. p-values less than 0.05 were considered statistically significant.

### 7.5 Results

#### 7.5.1 Lead candidate cardioactive hMSC exosomal miRs predicted via PLSR

To predict key cardioactive hMSC exosomal miR cargo, PLSR was used to form relationships between the relative abundance of specific exosomal miRs from a set of parent cells releasing exosomes and resultant hECT contractile force responses as well as relevant calcium handling and apoptotic gene expression. More specifically, we sought to predict miRs that may increase SERCA2a and LTCC expression, decrease the BAX/BCL2 expression ratio, and increase contractile force in our hECT system similar to hMSC-exo treatment in our previous work.<sup>6</sup>

In this analysis, the parent cells included hMSCs, human adult cardiac fibroblasts (hACFs), and human foreskin fibroblasts (hFFs) with previously established<sup>6,7</sup> parent cell dependent paracrine effects on hECT contractility. More specifically, conditioned media from hMSCs<sup>6</sup> and hACFs,<sup>7</sup> but not hFFs,<sup>7</sup> significantly increased hECT contractile function, although mediated through distinct mechanisms.<sup>9,10</sup> While hMSC exosomes are the main contributors to increasing contractility via mechanisms described above, hACF soluble factors (e.g., transforming growth factor- $\beta$ ) are largely responsible for increasing contractility via hypertrophy, as well as sodium and potassium channel remodeling.<sup>7,19,20</sup>

Hierarchical clustering of published exosomal miR profiling data representative of these parent cells (obtained from NIH/NCBI GEO-series GSE71241, GSE76175, and Pope et al.<sup>21</sup> for hMSC, rACF and hFF, respectively; rACF was used due to lack of available hACF data) demonstrates grouping primarily by cell type (Figure 1A). Notably, several of the top 20 cardiac-related hMSC exosomal miRs were differentially expressed in the other fibroblast cell types (Figure 1A), motivating the systematic PLSR method to predict key cardioactive miRs.

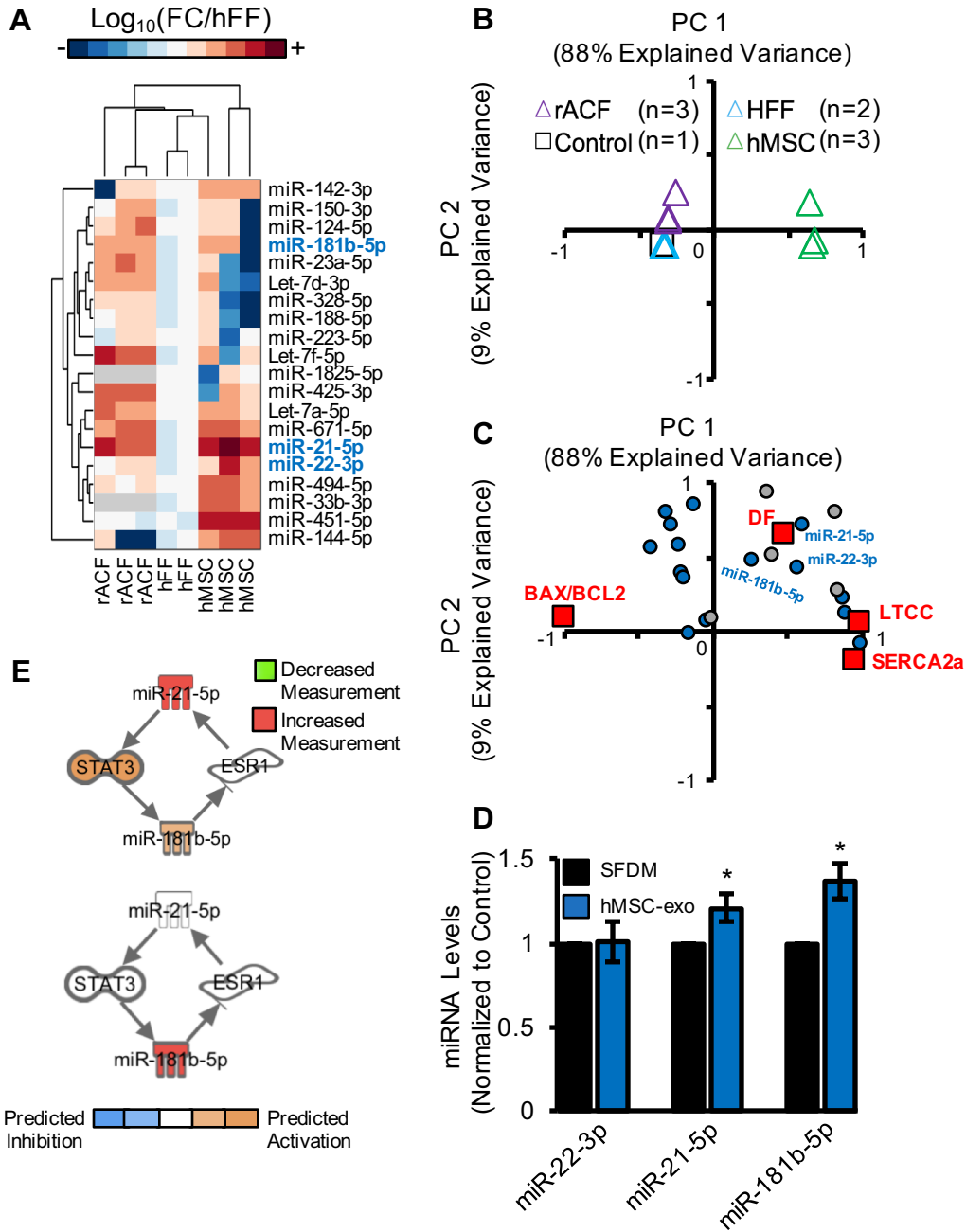


**Figure 1: Predicting Lead Cardioactive hMSC Exosomal miRs via PLSR. (A)** Heatmap and hierarchical clustering of expression of top 20 cardiac-related hMSC exosomal miRs compared to their expression in human foreskin fibroblasts (hFFs) and rat adult cardiac fibroblasts (rACFs). Expression levels represented as fold change (FC) relative to the average for hFF. Select miRs experimentally investigated are bolded and in blue. Grey boxes indicate data not available. **(B)** Partial least squares regression (PLSR) score plot suggests cell-type dependent

separation mainly across principal component (PC) 1 (x-axis), not 2 (y-axis). **(C)** Correlation loading plot from PLSR suggests several PI3K/Akt-related (blue) and -unrelated (grey) miRs from panel A co-vary with hECT developed force (DF), L-type calcium channel (LTCC) gene expression, and sarcoendoplasmic reticulum calcium-ATPase (SERCA2a) gene expression. **(D)** Expression of miR-22-3p, miR-21-5p, and miR-181b-5p in hECTs five days after hMSC-exo treatment relative to SFDM-treated controls. \* $p<0.05$ , p-values from unpaired t-tests ( $n=4$ ). **(E)** Ingenuity Pathway Analysis (IPA®, Qiagen) predictions suggest miR-21-5p positively regulates miR-181b-5p (top), but not vice versa (bottom). Nonstandard abbreviations: B-cell lymphoma 2 (BCL2); BCL2-associated X protein (BAX).

PLSR was performed on the expression of the top 20 cardiac-related hMSC exosomal miRs across the above parent cells (as well as SFDM control), matched to hECT developed force (DF) as well as calcium handling (i.e., SERCA2a and LTCC) and apoptotic (i.e., BAX/BCL2) gene expression responses. In agreement with the hierarchical clustering (Figure 1A), the PLSR score plot (Figure 1B) shows parent cell type-dependent clustering: fibroblast parent cells (i.e., rACFs and hFFs) were grouped near the origin along the negative x-axis with SFDM control, whereas hMSC parent cells uniquely clustered toward the positive x-axis (Figure 1B).

In the correlation loading plot, expression of both calcium handling genes—SERCA2a and LTCC—clustered on the positive x-axis (Figure 1C), whereas the expression of the apoptotic BAX/BCL2 ratio was on the negative x-axis. DF was uniquely along the positive y-axis, while also being in the positive x direction. This is consistent with the parent cell distribution in the score plot, as: 1) the hMSC exosomal groups were uniquely to the right of the x-axis (effectively corresponding to our previous empirical findings<sup>6</sup>); 2) SFDM and hFF exosomal groups were near the origin (both previously found to have null effects on contractility and associated gene expression<sup>7</sup>); and 3) the rACF exosomal group was also near the origin, as

our model inputs are specific to exosomal miRs (i.e., neglect soluble factors) and rACF effects on contractility are largely soluble factor (e.g., transforming growth factor- $\beta$ ) dependent.<sup>19,20</sup>

Altogether, given our focus on cardioactive hMSC-exo miRs, we sought miRs that: 1) cluster to the right of the positive x-axis, thus positively correlating with SERCA2a and LTCC gene expression and negatively correlating with BAX/BCL2 gene expression ratio; 2) cluster with DF; and 3) are known to modulate myocyte PI3K/Akt signaling, a pathway previously identified to be involved in hMSC paracrine-mediated increases in cardiac contractility.<sup>6</sup> The correlation loading plot shows several miRs that meet these criteria in the upper right hand quadrant (Figure 1C); these include several miRs that modulate myocyte PI3K/Akt signaling (Figure 1C, blue dots; grey dots denote miRs not known to modulate myocyte PI3K/Akt signaling) including miR-21-5p,<sup>22</sup> miR-22-3p,<sup>23</sup> and miR-181b-5p.<sup>24</sup>

Experimentally, we found that treatment of hECTs with hMSC-exo led to significantly increased miR-21-5p expression relative to SFDM control, whereas miR-22-3p expression remained unchanged (Figure 1D). In addition, treating hECTs with hMSC-CdM (containing exosomes and soluble factors) had significantly greater miR-21-5p expression relative to hMSC-exo-depl (Figure S1). Interestingly, while miR-181b-5p abundance was relatively low in hMSC exosomes (Figure 1A) and is only slightly positive of the x-axis in the correlation loading plot, hECTs treated with hMSC-exo also led to significantly increased miR-181b-5p expression relative to control. IPA® predictions suggest miR-21-5p positively regulates miR-181b-5p (Figure 1E, top), but not vice versa (Figure 1E, bottom). Indeed, experimentally treating hECTs with miR-21-5p significantly increased expression of miR-181b-5p, but not miR-22-3p, versus miR-scr-con treated hECT controls (Figure 2A).

Altogether, this motivated directly testing the human-specific role of miR-21-5p—the only top 5 most abundant hMSC exosomal miR across at least three independent studies<sup>7,25-27</sup>—in increasing hECT contractile function. To investigate this in our hECT bioreactor system, we

examined the cardioactive effects of miR-21-5p alone, as well as the effects of exosomes released from miR-21-5p knockdown hMSCs.

#### *7.5.2 miR-21-5p effects on hECT contractile function*

Successful delivery of miR-21-5p (Figure 2A) significantly increased 0.5 Hz-paced hECT DF five days post-treatment relative to pre-treatment baseline (Figure 2B), comparable to effects of hMSC-exo treatment.<sup>6</sup> To examine the time-dependence of treatment effects, daily monitoring of spontaneously beating hECTs showed that miR-21-5p treatment led to a significant increase in spontaneous DF on days 3-5 post-treatment relative to day 0 pre-treatment (Figure 2C); these findings were likely not confounded by the force-frequency relationship, as there was no significant difference in beat rate between miR treatment groups despite a significant effect of time (Figure 2D).

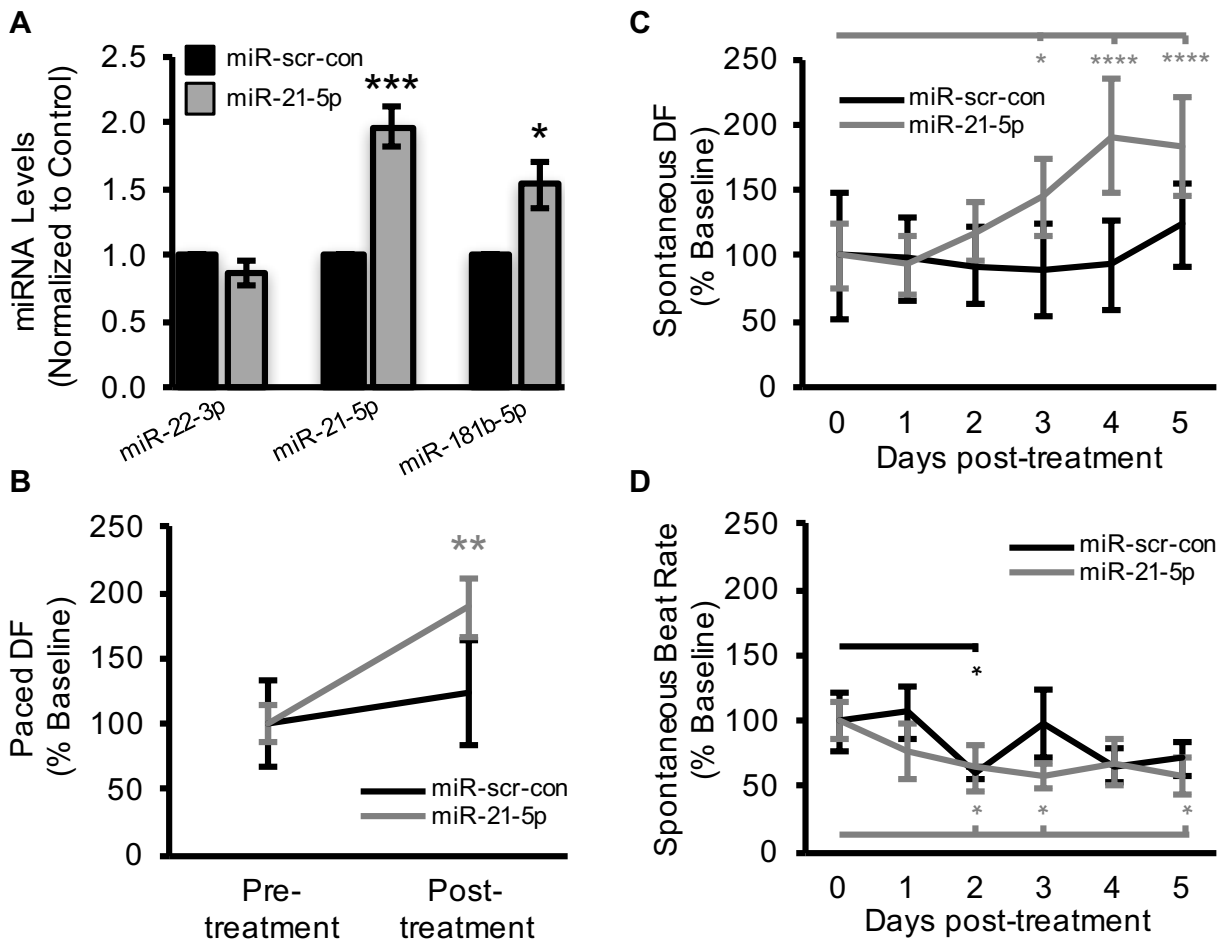


**Figure 2: miR-21-5p Effects on hECT Contractility.** (A) Expression of miR-22-3p, miR-21-5p, and miR-181b-5p in hECTs five days after miR-21-5p treatment relative to miR-scr-con. p-values from unpaired t-tests ( $n=3-5$ ). (B) Five days after miR-21-5p treatment, hECT developed force (DF) was significantly increased during 0.5 Hz pacing, whereas miR-scr-con negative controls had no significant effect. p-values from repeated measures ANOVA followed by Bonferroni's multiple comparisons test ( $n=5$ ). Daily measurements of (C) DF and (D) beat rate in unpaced hECTs during spontaneous beating. p-values from repeated measures ANOVA followed by Dunnett's multiple comparisons test ( $n=4-5$ ). In all panels, \* $p<0.05$ , \*\* $p<0.01$ , \*\*\* $p<0.001$ , \*\*\*\* $p<0.0001$ .

### *7.5.3 Knockdown of miR-21-5p in hMSCs diminishes exosomal effects on hECT contractile function*

With just a modest (less than 40%; see Discussion and Detailed Methods in Data Supplement for explanation) yet statistically significant decrease in miR-21-5p, but not miR-181b-5p, expression in hMSC parent cells (Figure S2), delivery of hMSC-exo:miR-21-5p-KD significantly decreased miR-21-5p and miR-181-5p expression in hECTs in comparison to the hMSC-exo:miR-scr-con experimental group (Figure 3A). This again suggests miR-21-5p delivery is mediating changes in miR-181b expression in hECTs during hMSC-exo treatment. More importantly, hMSC-exo:miR-21-5p-KD significantly diminished the pro-contractile effects that were observed in the hMSC-exo:miR-scr-con experimental group during pacing post-treatment (Figure 3B). In support of our previous findings,<sup>6</sup> treating hECTs with hMSC-exo:miR-scr-con significantly increased DF during 0.5 Hz pacing five days post-treatment relative to pre-treatment baseline (Figure 3B).

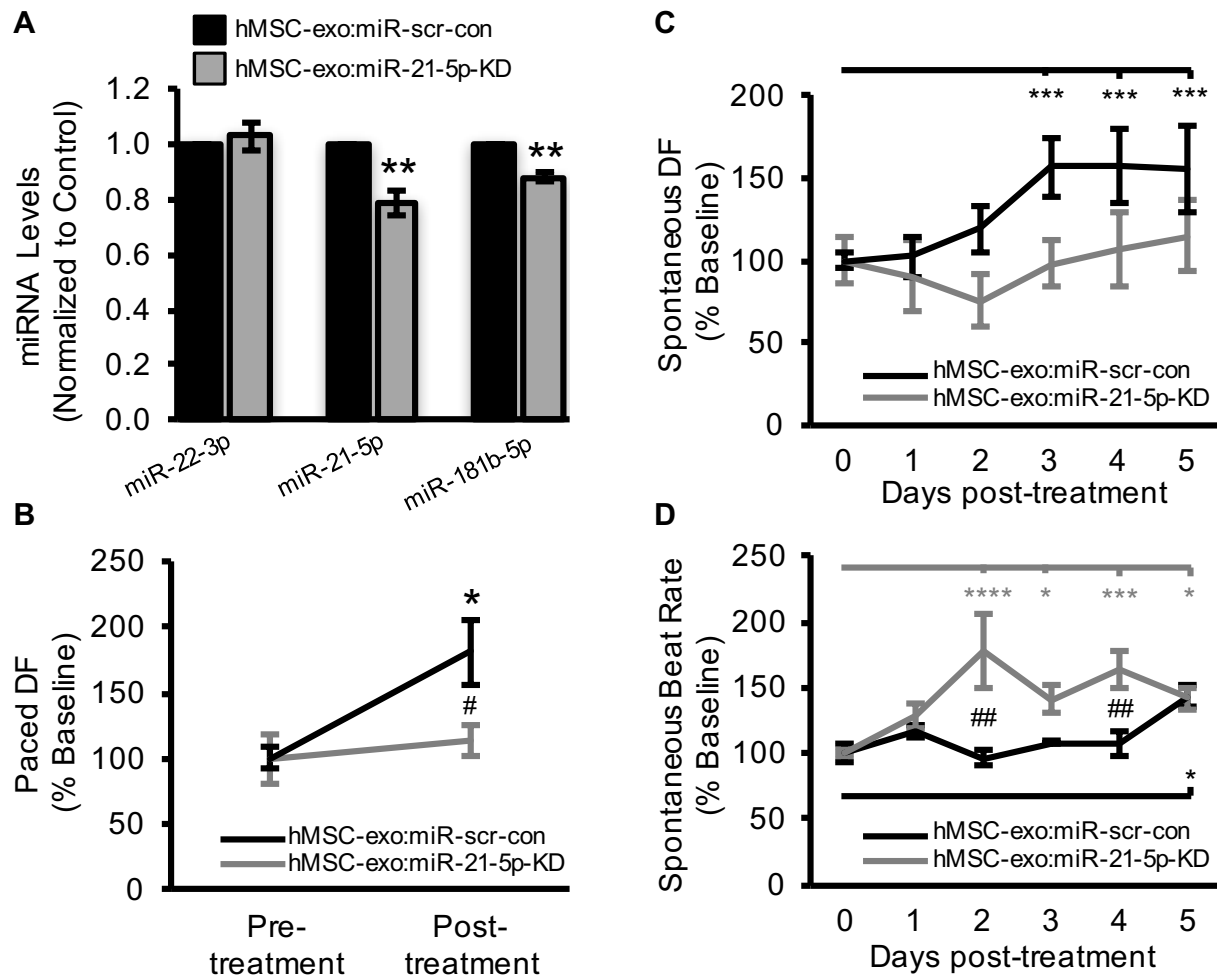


**Figure 3: Knockdown of miR-21-5p in hMSCs Diminishes Pro-Contractile Effects of Exosomes on hECT Contractility.** (A) Expression of miR-22-3p, miR-21-5p, and miR-181b-5p in hECTs five days after hMSC-exo:miR-21-5p-KD treatment relative to hMSC-exo:miR-scr-con. p-values from unpaired t-tests (n=3). (B) Five days after hMSC-exo:miR-scr-con treatment significantly increased hECT developed force (DF) during 0.5 Hz pacing in comparison to hMSC-exo:miR-21-5p-KD, which had no significant effect. p-values from repeated measures ANOVA followed by Bonferroni's multiple comparisons test (n=4). Daily measurements of (C) DF and (D) beat rate in unpaced hECTs during spontaneous beating. p-values from repeated measures ANOVA followed by Dunnett's multiple comparisons test (n=4). In all panels, \*p<0.05, \*\*p<0.01, \*\*\*p<0.001, #p<0.05, ##p<0.01.

\*\*p<0.01, \*\*\*p<0.001, \*\*\*\*p<0.0001. # denotes statistical significance between groups at a given time point, <sup>#</sup>p<0.05, <sup>##</sup>p<0.01.

To examine the time dependence of these treatment effects, daily monitoring of spontaneously beating hECTs showed that hMSC-exo:miR-scr-con treatment, but not hMSC-exo:miR-21-5p-KD, led to significant increases in spontaneous DF on days 3-5 post-treatment relative to day 0 pre-treatment (Figure 3C). While the spontaneous beat rate of the hMSC-exo:miR-21-5p-KD-treated hECTs was significantly higher than hMSC-exo:miR-scr-con on days 2 and 4 (Figure 3D), spontaneous beat rates reached a maximum of approximately 0.5 Hz in both groups and there was no statistical difference on days 3 and 5, making it unlikely these findings were largely confounded by the force-frequency relationship that is relatively flat for hECTs in this low frequency range.<sup>28</sup>

#### *7.5.4 miR-21-5p Increases Calcium Handling Gene Expression*

The hECT functional measurements in Figures 2 and 3 were corroborated by molecular characterization using prospective qRT-PCR of cardiac-specific, calcium handling, and apoptotic genes. Revealing a gene expression profile remarkably similar to our prior observations with hMSC-exo treatment<sup>6</sup> (Figure S3), miR-21-5p supplementation significantly increased hECT mRNA levels of LTCC and SERCA2a (Figure 4A) and decreased the  $\alpha/\beta$  myosin heavy chain ratio (Figure 4A). In addition, analogous to our prior observations with hMSC-exo treatment<sup>6</sup> (Figure S3), miR-21-5p modestly yet significantly decreased the BAX/BCL2 ratio (Figure 4B), a marker of possible anti-apoptotic effects.<sup>29</sup>

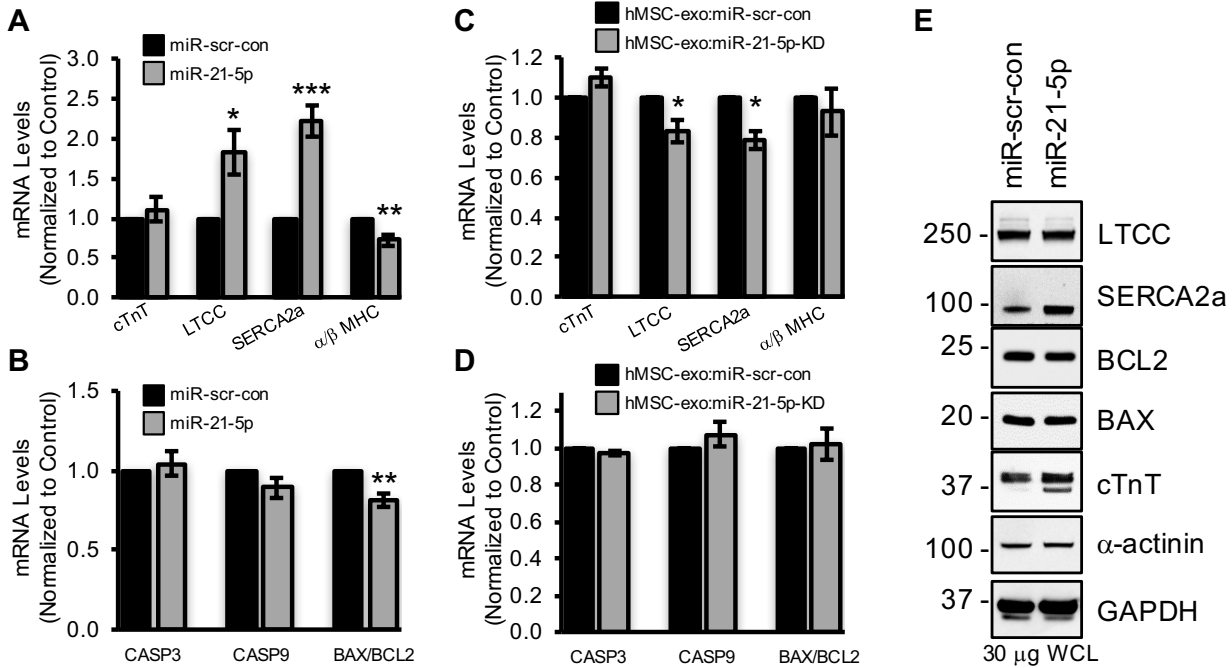


**Figure 4: Molecular Characterization of miR-21-5p Effects on hECTs and hPSC-CM Monolayers.**

**Monolayers.** hECTs treated with miR-scr-con vs. miR-21-5p (**A-B**) and hMSC-exo:miR-scr-con vs hMSC-exo:miR-21-5p-KD (**C-D**) were snap-frozen for qRT-PCR on day five post-treatment, where expression of (**A, C**) cardiac-specific, calcium-handling, and (**B, D**) apoptotic genes were studied. p-values from one-way ANOVA with post hoc Tukey test (n=3-5). (**E**) Western blot of hPSC-CM monolayers treated for 48 hours with miR-21-5p or miR-scr-con. Nonstandard abbreviations: cardiac troponin-T (cTnT); L-type calcium channel (LTCC); sarcoendoplasmic reticulum calcium-ATPase (SERCA2a); caspase-3 (Casp3); caspase-9 (Casp9); B-cell lymphoma 2 (BCL2); BCL2-associated X protein (BAX); myosin heavy chain (MHC); glyceraldehyde 3-phosphate dehydrogenase (GAPDH). In all panels, \*p<0.05, \*\*p<0.01, \*\*\*p<0.001.

When depleting hMSCs of miR-21-5p (Figure S2), delivery of hMSC-exo:miR-21-5p-KD significantly decreased mRNA levels of LTCC and SERCA2a in hECTs in comparison to hMSC-exo:miR-scr-con treatment (Figure 4C). However, there were no significant effects on the  $\alpha/\beta$

myosin heavy chain ratio (Figure 4C) nor the BAX/BCL2 ratio (Figure 4D). Altogether, both hECT experiments in Figures 4A and 4C support miR-21-5p altering expression of calcium handling genes; however, the effects on apoptotic gene expression are relatively unclear (Figures 4B and 4D).

To better understand these findings at the protein level, western blots were performed on hPSC-CM monolayers treated with miR-scr-con or miR-21-5p (Figure 4E). While there was no discernible effect on non-specific LTCC protein levels, miR-21-5p increased cardiomyocyte-specific SERCA2a protein levels independent of non-specific (i.e., GAPDH and  $\alpha$ -actinin) or myocyte-specific (i.e., cTnT) loading controls, leading to an approximately 2- to 3-fold increase in comparison to miR-scr-con treatment (Figure 4E). In comparison, miR-21-5p had no discernable effect on BAX/BCL2 protein level (Figure 4E). Altogether, these findings motivate further investigation into the mechanism by which miR-21-5p increases calcium handling and thereby contractility.

#### *7.5.5 miR-21-5p Increases hPSC-CM Calcium Transients Likely via the PI3K Signaling Cascade*

To mechanistically corroborate our hECT findings, we examined the effects of miR-21-5p on hPSC-CM calcium transients with or without the PI3K inhibitor LY294002 (LY); for sample calcium transients of each experimental group, see Figure 5A. In the absence of LY, treatment with miR-21-5p significantly increased calcium transient amplitude (Figure 5B) in comparison to miR-scr-con; in the presence of LY, these effects were abolished (Figure 5C). In addition, in the absence of LY, treating hPSC-CMs with miR-21-5p decreased the calcium transient decay time constant (Figure 5D) relative to miR-scr-con; in the presence of LY, these effects were modestly attenuated (Figure 5E).

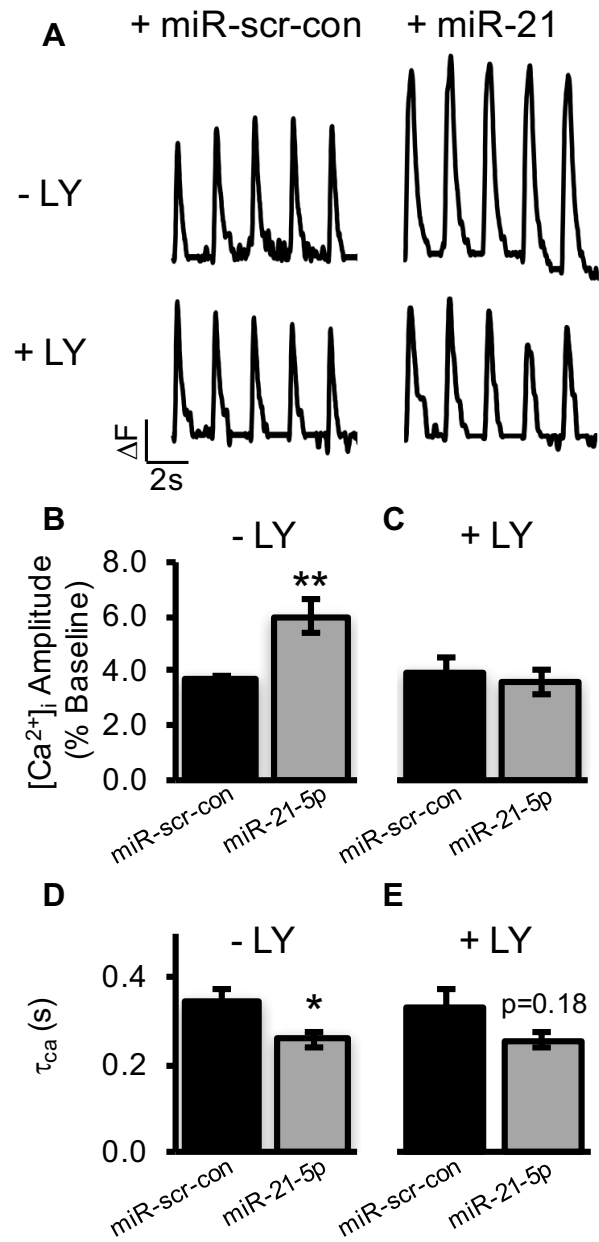


**Figure 5: miR-21-5p Increases hPSC-CM Calcium Transients Likely via the PI3K Signaling Cascade.** (A) Sample calcium transients from hPSC-CMs treated with miR-21-5 or miR-scr-con with or without LY294002 (LY), a PI3K inhibitor. (B-C) Calcium transient amplitude of hPSC-CMs treated with miR-21-5p or miR-scr-con (B) without or (C) with LY. (D-E) Calcium transient decay time constant ( $\tau_{ca}$ ) of hPSC-CMs treated with miR-21-5p or miR-scr-con (D) without or (E)

with LY. For each panel, unpaired student t-tests were performed between respective miR-scr-con and miR-21-5p experimental groups (n=5-6 per condition). \*p<0.05, \*\*p<0.01.

#### *7.5.6 Predicting the Effects of miR-21-5p in Ischemic Adult Human Cardiomyocytes*

To corroborate our experimental findings on miR-21-5p effects on LTCC and SERCA2a expression and to predict how miR-21-5p effects on immature hPSC-CM calcium transients may translate to mature ischemic adult human cardiomyocytes, we adopted established computational methods<sup>6,16,17</sup> by closely matching simulation outputs to corresponding experimental recordings (Figure 6). To do so, we generated a large initial population of 1,000 model variants with empirically relevant (based on western blot data in Figure 4E) randomly chosen parameter sets to increase maximum LTCC and SERCA2a flux constants in a human induced pluripotent stem cell-derived cardiomyocyte electrophysiology model<sup>13</sup> by 1- to 2-fold and 1- to 4-fold changes, respectively. The initial population was then filtered to retain (Figure 6A, white dots) only select models that were consistent (i.e., within  $\pm 1$  standard deviation) with two calcium transient metrics from Figure 5: amplitude and decay time constant ( $[Ca^{2+}]_i$  Amplitude and  $\tau_{Ca}$ , respectively).

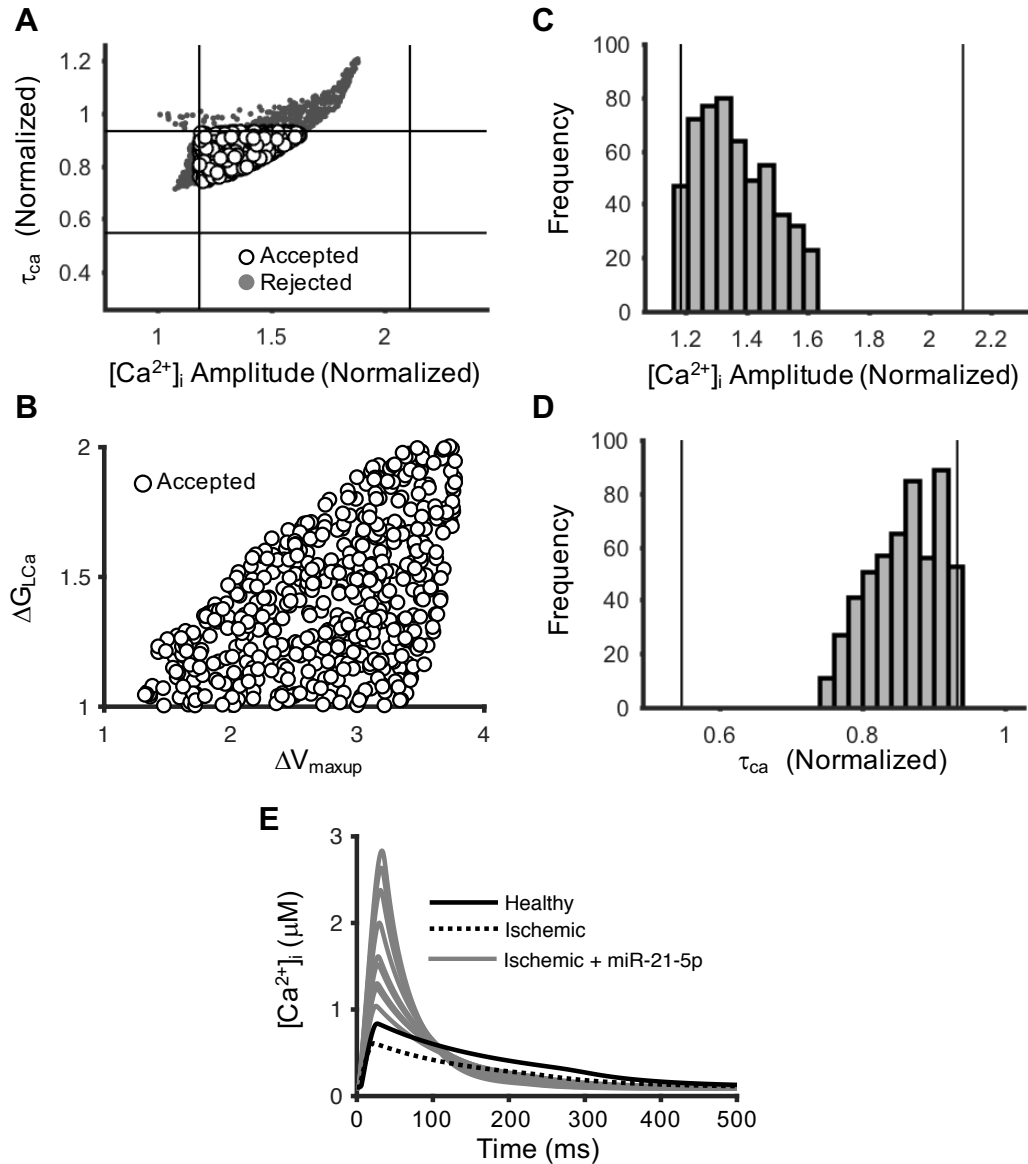


**Figure 6: Experimentally Calibrating miR-21-5p Effects on Human Cardiomyocyte Calcium Transients.** miR-21-5p effects on immature human cardiomyocyte L-type calcium channel (LTCC) and sarcoendoplasmic reticulum calcium-ATPase (SERCA2a) activity were experimentally calibrated. **(A)** Scatter plots of the initial population (grey dots) filtered (white dots) to be within 1 standard deviation (boxed region) of calcium transient decay time constant ( $\tau_{\text{ca}}$ ), and calcium transient amplitude ( $[\text{Ca}^{2+}]_i$  amplitude) metrics from Figure 5. **(B)** Accepted sets of calibrated model parameters. **(C-D)** Histograms illustrating distributions of the output

simulation metrics—**(C)**  $[Ca^{2+}]_i$  Amplitude and **(D)**  $\tau_{Ca}$ —resulting from the accepted population of calibrated models. **(E)** Ten select accepted model parameters were subsequently input into ischemic adult human cardiomyocyte models to predict miR-21-5p effects on calcium transients (grey) in comparison to healthy (black line) and ischemic (dotted black line) adult human cardiomyocytes. Nonstandard abbreviations:  $\Delta G_{LCa}$  and  $\Delta V_{maxup}$  denote fold changes in LTCC and SERCA2a maximal flux constants, respectively, due to miR-21-5p effects.

This calibration process reduced the initial population of 1,000 model variants to 535 accepted model parameter sets (Figure 6B). The histograms in Figures 6C and 6D illustrate the distribution of output simulation metrics  $[Ca^{2+}]_i$  Amplitude and  $\tau_{Ca}$ , respectively, resulting from the range of accepted model parameters. Figure 6B further shows the distribution of the 535 accepted  $\Delta G_{LCa}$  and  $\Delta V_{maxup}$  parameter sets used to experimentally calibrate effects of miR-21-5p on calcium handling. In agreement with our western blot findings (Figure 4E), 10 of 535 accepted models have no discernable (i.e., less than 1 percent) changes in LTCC activity, suggesting increased SERCA2a activity alone was sufficient to recapitulate the effects on calcium transients from Figure 5. On the other hand, all of the accepted models had discernable changes in SERCA2a activity. Interestingly, the same 10 accepted models with no discernable changes in LTCC (i.e., along the x-axis) ranged from approximately 1.5- to 3-fold changes in SERCA2a, which also agrees with our western blot findings in Figure 4E. These 10 select models that are in agreement with our empirical findings were therefore chosen as the finalized set of accepted models of miR-21-5p effects on calcium handling.

Next, using the 10 finalized accepted models described above, we predicted miR-21-5p effects on adult human ischemic cardiomyocytes. As expected, in the absence of miR-21-5p, adult human ischemic cardiomyocytes were simulated to have diminished calcium handling in comparison to adult human healthy cardiomyocytes (Figure 6E). However, in the presence of

miR-21-5p, adult human ischemic cardiomyocytes were predicted to restore or even exceed healthy cell calcium transients.

## 7.6 Discussion

The molecular mediators of myocardial contractility in hMSC-based cardiotherapies remain largely unresolved, hindering efforts to maximize therapeutic efficacy. In this study, we utilized an integrated systems biology and tissue engineering approach to identify key cardioactive exosomal miRs. First, we provide bioinformatics and experimental data supporting miR-21-5p as a lead cardioactive exosomal miR in therapeutic hMSC-based paracrine signaling (Figure 1). Next, using our hECT system, we provide the first (to our knowledge) human-specific experimental data revealing: 1) miR-21-5p effects are remarkably similar to hMSC-exo effects on hECT contractile function (Figure 2); and 2) knockdown of miR-21-5p in hMSCs diminishes exosomal pro-contractile effects (Figure 3). The effects of miR-21-5p on calcium handling and contractility are supported at both the mRNA and protein levels (Figure 4). Finally, we mechanistically support miR-21-5p increases calcium handling and thereby contractility via the PI3K signaling cascade (Figure 5), and use a computational model to predict how these findings may translate to adult human cardiomyocytes (Figure 6). Based on these findings, we provide a schematic of our working hypothesis as to how hMSC-exo increases cardiac contractile function (Figure 7).

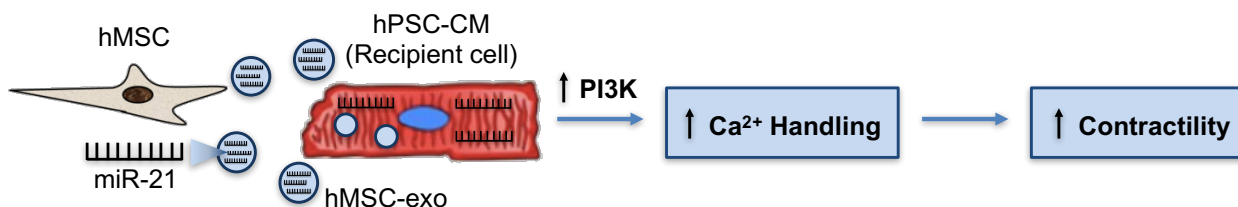


**Figure 7: Working Hypothesis for hMSC Paracrine-Mediated Increases in Cardiac Contractility.** hMSCs (parent cells) release exosomes (hMSC-exo) that are taken up by

recipient human pluripotent stem cell-derived cardiomyocytes (hPSC-CMs). hMSC-exo delivery of miR-21-5p increases hPSC-CM calcium handling gene expression, calcium handling, and thus contractility via the PI3K signaling cascade.

#### *7.6.1 PLSR for Predicting Lead Cardioactive Exosomal miRs*

Bioinformatics has proven successful for investigating pro-angiogenic, anti-fibrotic, and immunomodulatory paracrine mechanisms of stem cell therapies.<sup>30</sup> However, in the context of stem cell paracrine effects on cardiac contractility and calcium handling, *in silico* analysis is a relatively nascent approach.<sup>11</sup> Building on previous stem cell applications of PLSR,<sup>9,11</sup> we demonstrate the utility of using hECT functional and gene expression responses in the PLSR cue-signal-response paradigm in order to identify key hMSC exosomal miRs responsible for increasing human cardiac contractility.

In addition to the 98.3% predictability achieved with this trained PLSR model, the clustering of parent cell groups in the score plot further provided confidence in the predictive power of this methodology. Like our previous work, hMSC parent cell groups positively correlated with DF as well as LTCC and SERCA2a expression, whereas it negatively correlated with the BAX/BCL2 expression ratio.<sup>6</sup> As expected, hFF and SFDM parent cell groups had weak correlations with these responses. Finally, rACF groups were also near the origin, consistent with the established theory that these parent cells affect contractility largely via soluble factor (e.g., transforming growth factor- $\beta$ ) mechanisms.<sup>19,20</sup>

Clustering with miR-21-5p, both miR-22-3p and miR-181b-5p were among the lead PLSR-predicted miRs that correlated with hECT twitch force in the upper right-hand quadrant (i.e., positive x-axis and positive y-axis). Interestingly, these three clustering miRs affect common pathways (i.e., cardiomyocyte PI3K/Akt signaling<sup>22-24</sup>), and are each established oncomiRs.<sup>31-33</sup> To further support this, these three oncomiRs negatively correlate with the apoptotic BAX/BCL2 expression ratio (Figure 1C). The similarity between these miRs supports

the validity of this method, while also providing insight into the previously hypothesized role of cardiac-specific oncogenes for cardiotherapeutics.<sup>34</sup>

#### *7.6.2 Role of miR-21-5p in hMSC Exosome-Mediated Increases in Cardiac Contractility*

It is first important to note that miR-21 guide (i.e., miR-21-5p) and passenger (i.e., miR-21-3p) strands each have distinct cardioactive effects,<sup>10,35,36</sup> which may obscure findings when overexpressing or deleting pre-miR-21. For the purpose of our study, due to: 1) the high abundance of miR-21-5p (not miR-21-3p) in hMSC exosomes (Figure 1A); 2) the predicted correlation of miR-21-5p with DF and calcium handling gene expression (Figure 1C); 3) the experimental validation of increased miR-21-5p expression in hMSC-exo treated hECTs (Figure 1D); and 4) our focus on identifying key exosomal cargo for hMSC therapeutics, we focused the current study on the miR-21 guide strand miR-21-5p.

The effects of miR-21 on calcium handling have been previously examined in a non-human cardiomyocyte setting. For example, miR-21 has been previously shown to bind to phospholamban strongly<sup>37</sup> or activate endothelial nitric oxide synthase,<sup>38</sup> both of which increase SERCA2a activity.<sup>8,37</sup> Herein, we demonstrate through miR-21-5p delivery and knockdown experiments that miR-21-5p increases human-specific cardiac contraction and modulates LTCC and SERCA2a calcium handling gene expression. These findings are further supported at the protein level via western blots. Next, we mechanistically support these effects via the PI3K signaling cascade. These findings support our previous findings that hMSC-exo increases hECT contractility,<sup>6</sup> while also providing novel insight into specific cargo contributing to these effects with a likely mechanism of action.

#### *7.6.3 Robustness of hMSC Exosome and miR-21-5p Effects Across Human Stem Cell Lines*

In this work, we confirm that hMSC-exo pro-contractile effects occur across two hPSC lines. In our previous work, hMSC-exo increased contractility in hECTs comprised of human

embryonic stem cell-derived cardiomyocytes.<sup>6</sup> In this work, the hMSC-exo:miR-scr-con increases contractility in hECTs comprised of human cardiomyocytes derived from induced pluripotent stems reprogrammed from a healthy volunteer's dermal fibroblasts (Figure 3).

Furthermore, we confirm that miR-21-5p effects occur across the same two hPSC lines. For example, in Figure 2, we show that hECTs comprised of human embryonic stem cell-derived cardiomyocytes treated with miR-21-5p increase contractility, while in Figure 3, we show that knockdown of miR-21-5p in hMSCs abolished pro-contractile effects of exosomes on hECTs comprised of human induced pluripotent stem cell-derived cardiomyocytes. In addition, in Figure 4, we confirm miR-21-5p effects at the mRNA and protein level using both human embryonic and induced pluripotent stem cell-derived cardiomyocytes. Finally, in Figure 5, we yet again confirm miR-21-5p effects on calcium transients in human induced pluripotent stem cell-derived cardiomyocytes. Altogether, this demonstrates the robustness of hMSC-exo and miR-21-5p effects on derived human cardiomyocytes across hPSC lines.

#### *7.6.4 Kinetics of hMSC-exo and miR-21-5p Effects on hECT Contractility*

In comparison to nearly instantaneous β-adrenergic signaling mechanisms,<sup>39</sup> paracrine mechanisms are expected to be slower and longer-lasting. In our recent work, hMSC-exo effects were evident at least five days post-treatment; however, until this current study, we had not yet ascertained the time dependence of treatment effects. In this work, we better understand hMSC exosome (Figure 3), as well as miR-21-5p (Figure 2), time-dependent treatment effects on hECTs. Both hMSC exosomes and miR-21-5p begin to increase hECT contractility approximately 72 hours post-treatment (Figures 2-3). These effects persist for at least five days post-treatment. Unfortunately, the multi-day kinetics of miR-21-5p and hMSC exosomes would likely make it unfeasible to study these responses in short-term ex vivo contractility assays, such as the Langendorff isolated heart model, for which maximum viability is 24 hours.<sup>40</sup> Therefore, to extend our findings from hECTs to another relevant system, we developed a

mathematical model to predict how the results on hPSC-CMs might translate to mature ischemic human cardiomyocytes (Figure 6).

#### *7.6.5 Human-Specific Effects of miR-21-5p on Cardiac Tissue Remodeling*

It is important to note that the activity of miR-21 is not limited to myocytes, as it has been shown to also alter cardiac tissue-level remodeling; this is clearly an important consideration for optimizing cardiotherapeutics. Interestingly, the cardiac remodeling effects of miR-21 have been inconclusive among murine studies. For example, one group found that miR-21 contributes to adverse cardiac remodeling by targeting specific non-myocyte cardiac cell populations,<sup>35,36</sup> whereas another group reported a null contribution of miR-21 to stress-induced cardiac remodeling.<sup>41</sup> In yet another study, miR-21 overexpression was cardioprotective in the setting of ischemia.<sup>10</sup>

In our hECTs comprised of approximately 4:1 human stem cell-derived myocytes to fibroblasts (Figure S4), treatment with miR-21-5p leads to increased expression of the transforming growth factor- $\beta$  signaling pathway, pro-angiogenic vascular endothelial growth factor- $\alpha$  and angiopoietin-1, and hypertrophic atrial natriuretic factor and brain natriuretic peptide (Figure S5). While not addressing the conflicting data previously described, these findings nevertheless: 1) are consistent with gene expression effects of hMSC exosomes on hECTs (Figure S5); 2) are consistent with various findings established on hMSCs<sup>42-45</sup>; 3) complement previous in vitro and in vivo work specifically on miR-21-5p<sup>46,47</sup> and its role in hMSC exosome-mediated effects on cardiac tissue remodeling<sup>46</sup>; and 4) underscore the need to further investigate how miR-21-5p—alone or in the context of hMSC exosomes—affects remodeling in human-specific cardiac tissue.

#### *7.6.6 Limitations and Future Directions*

Several limitations of the study should be noted. First, we acknowledge that while this is (to our knowledge) the first study of miR-21-5p effects on engineered human cardiac tissue, the simplified hECT model system does not fully represent native human myocardium. Nevertheless, the controlled biocomplexity enables isolation of hMSC-mediated effects on myocyte contractility that may be obscured by other processes *in vivo*, and provides insight into cardiac tissue remodeling and twitch force not possible in traditional 2-D monolayer assays.

Second, we recognize that hPSC-CMs have immature calcium handling, not representative of adult myocytes. To address this, we developed a mathematical model that predicted how miR-21-5p effects on calcium handling may translate to mature human cardiomyocytes. Given that miR-21-5p can increase SERCA2a protein levels and thereby calcium handling and contraction, our findings may even be able to build on recent efforts to improve hPSC-CM maturation<sup>48</sup> by utilizing miR-21-5p or other synthetic miRs as a conditioning media supplement.

Third, we note the incomplete knockdown of miR-21-5p in hMSCs (Figure S2). This was likely a consequence of culturing hMSCs in SFDM for five days after the initial two days of miR-21-5p inhibitor treatment; we utilized this experimental design to be consistent with our previous successful methodology to treat hECTs with hMSC exosomes.<sup>6</sup> Nevertheless, even with roughly a 40% knockdown achieved, we still observed diminished effects on hECT contractility and associated calcium handling gene expression (Figures 3 and 4, respectively), showing the potent cardioactive effects of miR-21-5p in hMSC exosomes. Further knockdown may have provided further insight into the role of miR-21-5p on BAX/BCL2 and  $\alpha/\beta$  myosin heavy chain gene expression.

Fourth, we acknowledge that hECTs were treated for a maximum of five days prior to molecular characterization in order to be consistent with our previous work.<sup>6</sup> While the time-dependent data on the effects of hMSC-exo and miR-21-5p helped justify focusing on the 5-day time point for these studies, it will be necessary to perform extended time course and dose-

response experiments in follow-up studies examining the translational potential of these findings.

Finally, multiple paracrine factors may also impact hMSC-mediated effects on human myocardial contractility. For example, the incomplete miR-21-5p knockdown efficiency may have contributed to null effects on the BAX/BCL2 and  $\alpha/\beta$  myosin heavy chain gene expression ratios; alternatively, this may reflect overlapping or compensatory roles of other hMSC exosomal miRs or proteins. Nonetheless, the remarkable similarity between miR-21-5p and intact hMSC-exo effects on hECTs, the diminished cardioactivity of exosomes when knocking down miR-21-5p in hMSCs, and the known abundance and role of miR-21-5p in hMSCs<sup>7</sup> and other cardiotherapeutic stem cell exosomes (e.g., cardiac progenitor cells)<sup>49</sup> emphasizes the need to study miR-21-5p in the context of stem cell-based or even synthetic miR-based<sup>50</sup> cardiotherapies.

## 7.7 Conclusions

In summary, this study integrates systems biology analysis and hECT technology to predict and experimentally validate exosomal miRs responsible for hMSC paracrine-mediated increases in myocardial contractility and expression of associated calcium handling genes. miR-21-5p is identified as a lead cardioactive hMSC exosomal miR; treatment with miR-21-5p nearly reproduced the effects of hMSC-exo on hECT contractile function and underlying molecular characteristics, while knockdown of miR-21-5p in hMSCs diminished exosomal pro-contractile effects on hECTs. The miR-21-5p modulation of calcium handling gene expression (e.g., SERCA2a) was supported at the protein level. Mechanistically, miR-21-5p increases calcium handling and thereby contractility likely through the PI3K signaling cascade. Altogether, these findings help elucidate the human-specific cardioactive role of miR-21-5p, which could be used to maximize the efficacy of future stem cell-based therapies for heart failure.

## 7.8 References

1. Karantalis V, Hare JM. Use of mesenchymal stem cells for therapy of cardiac disease. *Circ Res.* 2015;116:1413-1430
2. Hare JM, DiFede DL, Rieger AC, et al. Randomized comparison of allogeneic versus autologous mesenchymal stem cells for nonischemic dilated cardiomyopathy: Poseidon-dcm trial. *J Am Coll Cardiol.* 2017;69:526-537
3. Heldman AW, DiFede DL, Fishman JE, et al. Transendocardial mesenchymal stem cells and mononuclear bone marrow cells for ischemic cardiomyopathy: The tac-hft randomized trial. *JAMA.* 2014;311:62-73
4. Meyer GP, Wollert KC, Lotz J, Pirr J, Rager U, Lippolt P, Hahn A, Fichtner S, Schaefer A, Arseniev L, Ganser A, Drexler H. Intracoronary bone marrow cell transfer after myocardial infarction: 5-year follow-up from the randomized-controlled boost trial. *Eur Heart J.* 2009;30:2978-2984
5. Fisher SA, Doree C, Mathur A, Martin-Rendon E. Meta-analysis of cell therapy trials for patients with heart failure. *Circ Res.* 2015;116:1361-1377
6. Mayourian J, Cashman TJ, Ceholski DK, Johnson BV, Sachs D, Kaji DA, Sahoo S, Hare JM, Hajjar RJ, Sobie EA, Costa KD. Experimental and computational insight into human mesenchymal stem cell paracrine signaling and heterocellular coupling effects on cardiac contractility and arrhythmogenicity. *Circ Res.* 2017;121:411-423
7. Mayourian J, Ceholski DK, Gonzalez DM, Cashman TJ, Sahoo S, Hajjar RJ, Costa KD. Physiologic, pathologic, and therapeutic paracrine modulation of cardiac excitation-contraction coupling. *Circ Res.* 2018;122:167-183
8. DeSantiago J, Bare DJ, Semenov I, Minshall RD, Geenen DL, Wolska BM, Banach K. Excitation-contraction coupling in ventricular myocytes is enhanced by paracrine signaling from mesenchymal stem cells. *J Mol Cell Cardiol.* 2012;52:1249-1256

9. Gray WD, French KM, Ghosh-Choudhary S, Maxwell JT, Brown ME, Platt MO, Searles CD, Davis ME. Identification of therapeutic covariant microRNA clusters in hypoxia-treated cardiac progenitor cell exosomes using systems biology. *Circ Res*. 2015;116:255-263
10. Bang C, Batkai S, Dangwal S, et al. Cardiac fibroblast-derived microRNA passenger strand-enriched exosomes mediate cardiomyocyte hypertrophy. *J Clin Invest*. 2014;124:2136-2146
11. Agarwal U, George A, Bhutani S, Ghosh-Choudhary S, Maxwell JT, Brown ME, Mehta Y, Platt MO, Liang Y, Sahoo S, Davis ME. Experimental, systems, and computational approaches to understanding the microRNA-mediated reparative potential of cardiac progenitor cell-derived exosomes from pediatric patients. *Circ Res*. 2017;120:701-712
12. Ceholski DK, Turnbull IC, Pothula V, Lecce L, Jarrah AA, Kho C, Lee A, Hadri L, Costa KD, Hajjar RJ, Tarzami ST. Cxcr4 and cxcr7 play distinct roles in cardiac lineage specification and pharmacologic beta-adrenergic response. *Stem Cell Res*. 2017;23:77-86
13. Paci M, Hyttinen J, Aalto-Setala K, Severi S. Computational models of ventricular- and atrial-like human induced pluripotent stem cell derived cardiomyocytes. *Ann Biomed Eng*. 2013;41:2334-2348
14. ten Tusscher KH, Panfilov AV. Alternans and spiral breakup in a human ventricular tissue model. *Am J Physiol Heart Circ Physiol*. 2006;291:H1088-1100
15. Weiss DL, Ifland M, Sachse FB, Seemann G, Dossel O. Modeling of cardiac ischemia in human myocytes and tissue including spatiotemporal electrophysiological variations. *Biomed Tech (Berl)*. 2009;54:107-125
16. Britton OJ, Bueno-Orovio A, Van Ammel K, Lu HR, Towart R, Gallacher DJ, Rodriguez B. Experimentally calibrated population of models predicts and explains intersubject variability in cardiac cellular electrophysiology. *Proc Natl Acad Sci U S A*. 2013;110:E2098-2105

17. Zhou X, Bueno-Orovio A, Orini M, Hanson B, Hayward M, Taggart P, Lambiase PD, Burrage K, Rodriguez B. In vivo and in silico investigation into mechanisms of frequency dependence of repolarization alternans in human ventricular cardiomyocytes. *Circ Res.* 2016;118:266-278
18. Prinz AA, Bucher D, Marder E. Similar network activity from disparate circuit parameters. *Nat Neurosci.* 2004;7:1345-1352
19. Cartledge JE, Kane C, Dias P, Tesfom M, Clarke L, McKee B, Al Ayoubi S, Chester A, Yacoub MH, Camelliti P, Terracciano CM. Functional crosstalk between cardiac fibroblasts and adult cardiomyocytes by soluble mediators. *Cardiovasc Res.* 2015;105:260-270
20. Liau B, Jackman CP, Li Y, Bursac N. Developmental stage-dependent effects of cardiac fibroblasts on function of stem cell-derived engineered cardiac tissues. *Sci Rep.* 2017;7:42290
21. Pope SM, Lasser C. Toxoplasma gondii infection of fibroblasts causes the production of exosome-like vesicles containing a unique array of mrna and mirna transcripts compared to serum starvation. *J Extracell Vesicles.* 2013;2
22. Sayed D, He M, Hong C, Gao S, Rane S, Yang Z, Abdellatif M. Microrna-21 is a downstream effector of akt that mediates its antiapoptotic effects via suppression of fas ligand. *J Biol Chem.* 2010;285:20281-20290
23. Xu XD, Song XW, Li Q, Wang GK, Jing Q, Qin YW. Attenuation of microrna-22 derepressed pten to effectively protect rat cardiomyocytes from hypertrophy. *J Cell Physiol.* 2012;227:1391-1398
24. Li TJ, Chen YL, Gua CJ, Xue SJ, Ma SM, Li XD. Microrna 181b promotes vascular smooth muscle cells proliferation through activation of pi3k and mapk pathways. *Int J Clin Exp Pathol.* 2015;8:10375-10384

25. Baglio SR, Rooijers K, Koppers-Lalic D, Verweij FJ, Perez Lanzon M, Zini N, Naaijkens B, Perut F, Niessen HW, Baldini N, Pegtel DM. Human bone marrow- and adipose-mesenchymal stem cells secrete exosomes enriched in distinctive mirna and tRNA species. *Stem Cell Res Ther.* 2015;6:127
26. Phinney DG, Di Giuseppe M, Njah J, et al. Mesenchymal stem cells use extracellular vesicles to outsource mitophagy and shuttle microRNAs. *Nat Commun.* 2015;6:8472
27. Nakamura Y, Miyaki S, Ishitobi H, Matsuyama S, Nakasa T, Kamei N, Akimoto T, Higashi Y, Ochi M. Mesenchymal-stem-cell-derived exosomes accelerate skeletal muscle regeneration. *FEBS Lett.* 2015;589:1257-1265
28. Turnbull IC, Karakikes I, Serrao GW, Backeris P, Lee JJ, Xie C, Senyei G, Gordon RE, Li RA, Akar FG, Hajjar RJ, Hulot JS, Costa KD. Advancing functional engineered cardiac tissues toward a preclinical model of human myocardium. *FASEB J.* 2014;28:644-654
29. Del Poeta G, Venditti A, Del Principe MI, Maurillo L, Buccisano F, Tamburini A, Cox MC, Franchi A, Bruno A, Mazzone C, Panetta P, Suppo G, Masi M, Amadori S. Amount of spontaneous apoptosis detected by bax/bcl-2 ratio predicts outcome in acute myeloid leukemia (aml). *Blood.* 2003;101:2125-2131
30. Ranganath SH, Levy O, Inamdar MS, Karp JM. Harnessing the mesenchymal stem cell secretome for the treatment of cardiovascular disease. *Cell Stem Cell.* 2012;10:244-258
31. Liu Y, Uzair Ur R, Guo Y, et al. Mir-181b functions as an oncomir in colorectal cancer by targeting pdcd4. *Protein Cell.* 2016;7:722-734
32. Yan LX, Wu QN, Zhang Y, Li YY, Liao DZ, Hou JH, Fu J, Zeng MS, Yun JP, Wu QL, Zeng YX, Shao JY. Knockdown of mir-21 in human breast cancer cell lines inhibits proliferation, in vitro migration and in vivo tumor growth. *Breast Cancer Res.* 2011;13:R2
33. Budd WT, Seashols-Williams SJ, Clark GC, Weaver D, Calvert V, Petricoin E, Dragomir EA, O'Hanlon K, Zehner ZE. Dual action of mir-125b as a tumor suppressor and oncomir-22 promotes prostate cancer tumorigenesis. *PLoS One.* 2015;10:e0142373

34. Cottage CT, Bailey B, Fischer KM, Avitabile D, Collins B, Tuck S, Quijada P, Gude N, Alvarez R, Muraski J, Sussman MA. Cardiac progenitor cell cycling stimulated by pim-1 kinase. *Circ Res*. 2010;106:891-901
35. Thum T, Gross C, Fiedler J, et al. MicroRNA-21 contributes to myocardial disease by stimulating map kinase signalling in fibroblasts. *Nature*. 2008;456:980-984
36. Ramanujam D, Sassi Y, Laggerbauer B, Engelhardt S. Viral vector-based targeting of mir-21 in cardiac nonmyocyte cells reduces pathologic remodeling of the heart. *Mol Ther*. 2016;24:1939-1948
37. Soller KJ, Yang J, Veglia G, Bowser MT. Reversal of phospholamban inhibition of the sarco(endo)plasmic reticulum ca<sup>2+</sup>-atpase (serca) using short, protein-interacting rnas and oligonucleotide analogs. *J Biol Chem*. 2016;291:21510-21518
38. Qiao S, Olson JM, Paterson M, Yan Y, Zaja I, Liu Y, Riess ML, Kersten JR, Liang M, Warltier DC, Bosnjak ZJ, Ge ZD. MicroRNA-21 mediates isoflurane-induced cardioprotection against ischemia-reperfusion injury via akt/nitric oxide synthase/mitochondrial permeability transition pore pathway. *Anesthesiology*. 2015;123:786-798
39. Eschenhagen T. Beta-adrenergic signaling in heart failure-adapt or die. *Nat Med*. 2008;14:485-487
40. Wiechert S, El-Armouche A, Rau T, Zimmermann WH, Eschenhagen T. 24-h langendorff-perfused neonatal rat heart used to study the impact of adenoviral gene transfer. *Am J Physiol Heart Circ Physiol*. 2003;285:H907-914
41. Patrick DM, Montgomery RL, Qi X, Obad S, Kauppinen S, Hill JA, van Rooij E, Olson EN. Stress-dependent cardiac remodeling occurs in the absence of microRNA-21 in mice. *J Clin Invest*. 2010;120:3912-3916

42. Lai RC, Arslan F, Lee MM, Sze NS, Choo A, Chen TS, Salto-Tellez M, Timmers L, Lee CN, El Oakley RM, Pasterkamp G, de Kleijn DP, Lim SK. Exosome secreted by msc reduces myocardial ischemia/reperfusion injury. *Stem Cell Res.* 2010;4:214-222
43. Kyurkchiev D, Bochev I, Ivanova-Todorova E, Moudjeva M, Oreshkova T, Belemezova K, Kyurkchiev S. Secretion of immunoregulatory cytokines by mesenchymal stem cells. *World J Stem Cells.* 2014;6:552-570
44. Todorova D, Simoncini S, Lacroix R, Sabatier F, Dignat-George F. Extracellular vesicles in angiogenesis. *Circ Res.* 2017;120:1658-1673
45. Xu RX, Chen X, Chen JH, Han Y, Han BM. Mesenchymal stem cells promote cardiomyocyte hypertrophy in vitro through hypoxia-induced paracrine mechanisms. *Clin Exp Pharmacol Physiol.* 2009;36:176-180
46. Wang K, Jiang Z, Webster KA, et al. Enhanced cardioprotection by human endometrium mesenchymal stem cells driven by exosomal microrna-21. *Stem Cells Transl Med.* 2017;6:209-222
47. Liu LZ, Li C, Chen Q, Jing Y, Carpenter R, Jiang Y, Kung HF, Lai L, Jiang BH. Mir-21 induced angiogenesis through akt and erk activation and hif-1alpha expression. *PLoS One.* 2011;6:e19139
48. Parikh SS, Blackwell DJ, Gomez-Hurtado N, Frisk M, Wang L, Kim K, Dahl CP, Fiane A, Tonnessen T, Kryshťal DO, Louch WE, Knollmann BC. Thyroid and glucocorticoid hormones promote functional t-tubule development in human-induced pluripotent stem cell-derived cardiomyocytes. *Circ Res.* 2017;121:1323-1330
49. Xiao J, Pan Y, Li XH, Yang XY, Feng YL, Tan HH, Jiang L, Feng J, Yu XY. Cardiac progenitor cell-derived exosomes prevent cardiomyocytes apoptosis through exosomal mir-21 by targeting pdcd4. *Cell Death Dis.* 2016;7:e2277

50. Lesizza P, Prosdocimo G, Martinelli V, Sinagra G, Zacchigna S, Giacca M. Single-dose intracardiac injection of pro-regenerative micrornas improves cardiac function after myocardial infarction. *Circ Res*. 2017;120:1298-1304

## Chapter 7 Supplementary Material

### Detailed Methods

#### Collection of Exosomal microRNA Data

We utilized previously published exosomal microRNA data in this study. Specifically, the data for exosomal miR content released by serum-free cultured human mesenchymal stem cells (hMSCs), rat adult cardiac fibroblasts (rACFs; due to the lack of available data using human ACFs), and human foreskin fibroblasts (hFFs) were obtained from the NIH/NCBI gene expression omnibus (GEO) online database series GSE71241, series GSE76175, and from a study by Pope et al.,<sup>1</sup> respectively. Given the variability in experimental preparations and miR profiling techniques from study to study, we normalized all miR content within a given sample of a study to the corresponding maximally expressed miR.

#### Hierarchical Clustering Analysis

Briefly, hierarchical clustering was performed on the exosomal miR expression vector elements with a Euclidean distance metric and average linkage,<sup>2</sup> normalized to corresponding mean hFF exosomal miR expression.

#### Partial Least Squares Regression

Partial least squares regression (PLSR) was performed with the nonlinear iterative partial least squares algorithm, as described elsewhere,<sup>3</sup> using Unscrambler® X (CAMO Software). PLSR was performed on the expression of the top 20 cardiac-related hMSC exosomal miRs across hMSC, rACF, and hFF parent-cells (as well as SFDM control, assumed to have negligible miR abundance in comparison to the hMSC, rACF, and hFF groups), matched to hECT responses of developed force (DF) as well as gene expression of sarcoendoplasmic reticulum calcium-ATPase (SERCA2a), L-type calcium channel (LTCC), and BAX/BCL2 ratio. Explained variance for input miR expression data is shown in the figures.

Predictability of the trained model corresponds to the predicted vs. reference coefficient of determination.

#### *hPSCs Used in this Study*

Both human embryonic stem cell-derived cardiomyocytes (hESC-CMs; H7 cell line, NIH Registration #0061) and human induced pluripotent stem-cell derived cardiomyocytes (hiPSC-CMs) were used in this study. The hiPSC line (SKiPS-31.3) was derived by the reprogramming of human dermal fibroblast obtained from a skin biopsy of a 45-year-old volunteer with informed consent (Staten Island University Hospital, Staten Island, NY), as described elsewhere.<sup>4-6</sup>

In Figures 1, 2, and 4A-B, hESC-CMs were used. In Figures 3, 4C-E, and 5, hiPSC-CMs were used. Established small molecule differentiation protocols were used to derive cardiomyocytes from both cell lines between passages 40 and 70.<sup>7,8</sup>

#### *hECT Tissue Construction*

hECTs were created from unsorted (approximately 4:1 SIRP $\alpha^+$ /CD90 $^-$  myocytes to CD90 $^+$ /SIRP $\alpha^-$  fibroblasts, using cell sorting methods previously described<sup>5</sup>; see Figure S5 for representative data) differentiated human embryonic stem cells (H7 cell line, NIH Registration #0061) or human induced pluripotent stem cells (SKiPS-31.3) and type-I collagen using methods previously described by our group.<sup>7,9</sup> Briefly, on day 20-30 post-differentiation, monolayer cultures of human stem cell derived cardiomyocytes were dissociated using 0.025% trypsin. After centrifugation (300g for 5min), hPSC-CMs were re-suspended in RPMI 1640+B27 culture media (Thermo Fisher Scientific, Rockville, MD), and then centrifuged again (300g for 5min). The supernatant media was removed and the cell pellet was combined with ice cold collagen type I (Life Technologies, Carlsbad, CA) and Matrigel (Corning, Corning, NY) at a ratio of 1:8:1 (v/v/v) as previously described.<sup>7,9</sup> The combined cell-matrix suspension was pipetted

into a custom made multi-tissue bioreactor<sup>7</sup> with six pairs of integrated flexible end posts and removable wells that each hold 40 µL of the cell-matrix suspension; they were placed in the incubator (37°C and 5% CO<sub>2</sub>) for 2 hours to allow the collagen to polymerize. Afterwards, the hECTs were bathed with high glucose DMEM supplemented with 10% newborn bovine serum (Atlanta Biologicals, Lawrenceville, GA), 1% penicillin/streptomycin (GIBCO, Carlsbad, CA), and 0.2% amphotericin B (Sigma-Aldrich, St. Louis, MO) culture media for approximately 48 hours. After approximately 48 hours, the wells were removed; hECT multi-tissue bioreactors were then transferred into culture dishes containing RPMI 1640+B27 serum-free defined media (SFDM) until pre-treatment pacing on day 5 of culture.

#### *hECT Functional Test Metrics*

Evaluation of hECT contractile function was performed using real-time noninvasive optical tracking of the integrated flexible end posts in the multi-tissue bioreactor. The measured post deflection was used to calculate developed force (DF) by applying a beam-bending equation from elasticity theory as previously described.<sup>10,11</sup> hECTs within the bioreactor were transferred to a laminar airflow hood while submerged in culture media at room temperature. The post deflection was captured in real-time with a high-speed camera (approximately 50 frames/s) and a custom LabVIEW program (National Instruments, Austin, TX). The contractility of hECTs was evaluated without and with electrical stimulation for spontaneous beat rate and developed force measurements, respectively. hECT DF was measured as the difference between maximum systolic and minimum diastolic force.

#### *hMSC Conditioned Media and Exosome Isolation*

For Figure 1, conditioned media was collected from 10 cm dishes of 50% confluent clinical grade<sup>12,13</sup> bone marrow-derived hMSCs (passage number less than 5) after they were cultured in SFDM for five days. The exosome-enriched (hMSC-exo) and exosome-depleted

(hMSC-exo-depl) fractions of hMSC conditioned media (hMSC-CdM) were collected from differential centrifugation using previously established methods<sup>14</sup> and characterized via dynamic light scattering using a NanoBrook ZetaPALS as previously demonstrated (Brookhaven, Holtsville, NY).<sup>10</sup>

For Figure 3, commercial bone marrow-derived hMSCs (Lonza, passage number less than 5) at approximately 90% confluence were treated with 3 nM of naked hsa-miR-21 inhibitor (miR-21-KD; Thermo Fisher Scientific mirVana® miRNA inhibitor, Assay ID MH10206) or 3 nM naked mirVana miRNA Inhibitor, Negative Control #1 (miR-scr-con; Catalog # 4464077) for 48 hours. After 48 hours, the plates were washed with 1x PBS twice and switched to SFDM. Conditioned media was collected from 10 cm dishes of respective groups after they were cultured in SFDM for five days. The exosome-enriched fractions of conditioned media from hMSCs treated with either miR-21-KD or miR-scr-con (hMSC-exo:miR-21-KD or hMSC-exo:miR-scr-con, respectively) were collected from differential centrifugation using previously established methods<sup>14</sup> and characterized via dynamic light scattering using a NanoBrook ZetaPALS as previously demonstrated (Brookhaven, Holtsville, NY).<sup>10</sup>

#### Functional Assessment of Treated hECTs

Following 48 hours of tissue compaction, hECTs were cultured in SFDM until culture day 5. Following baseline contractile function testing at 0.5-Hz pacing on culture day 5, SFDM was replaced with one of the following treatments: 1) SFDM (Control); 2) fresh hMSC conditioned media (hMSC-CdM); 3) exosome-depleted fraction of hMSC conditioned media (hMSC-exo-depl); 4) exosome-enriched fraction of fresh hMSC conditioned media (hMSC-exo); 5) SFDM with 2 nM of naked mirVana miRNA Mimic, Negative Control #1 (Thermo Fisher Scientific mirVana® miRNA mimic, Catalog # 4464058; abbreviated as miR-scr-con); 6) SFDM with 2 nM of naked hsa-miR-21-5p (Thermo Fisher Scientific mirVana® miRNA mimic, Catalog # 4464066; abbreviated as miR-21-5p); 7) hMSC-exo:miR-scr-con; or 8) hMSC-exo:miR-21-KD.

hECTs were cultured an additional 5 days post-treatment, during which daily non-invasive measurements of spontaneous DF and beat rate were made. On the fifth day post-treatment, DF was measured again at 0.5-Hz pacing. After testing, the hECTs were flash-frozen for molecular analysis by real time quantitative polymerase chain reaction (qRT-PCR).

#### Western Blot

See Table S1 for specific characteristics of antibodies used for western blot. hiPSC-CMs were resuspended in RIPA buffer (Boston Bioproducts) containing protease inhibitor cocktail (Roche) and PMSF (Sigma). The whole cell lysates were sonicated and then centrifuged at 17,000 x g for 15 min at 4°C. Protein concentration was measured using the 2D Quant Kit (GE Health Care Life sciences, USA). 30 µg of protein extracts were separated on 4-12% NuPAGE gel (Invitrogen) and transferred to nitrocellulose membrane (Bio-Rad). The membrane was blocked with 1% BSA and probed with primary antibodies against Cav1.2 calcium channel (LTCC; EMD Millipore), SERCA2a (21st Century Biochemicals), BCL2 (Cell Signaling), BAX (Abcam), cTnT (Abcam), α-actinin (Sigma), or GAPDH (Sigma). Subsequently, the membrane was incubated with corresponding secondary antibodies (Sigma) and visualized using a ChemiDoc Touch Imaging System (Bio-Rad).

#### Calcium Transients

hPSC-CMs were dissociated with 0.025% trypsin (PromoCell Detach 2 kit), plated on matrigel-coated German glass coverslips (Neuvitro, Vancouver, WA), and cultured in RPMI 1640+B27 for 48 hours. hPSC-CMs were loaded with a calcium-sensitive fluorescent dye for 15 minutes at 37°C (1 µg/ml Fura-2 AM, cell permeant; ThermoFisher, Rockville, MD) and the ratios of fluorescence intensities (excitation ratio of 340/380 nm) were recorded using the IonOptix system (Ionoptix, Milton, MA). The electrically-induced calcium transients were

triggered by pulses from a MyoPacer (IonOptix, Milton, MA) at 40V and 0.5 Hz and measurements were obtained at room temperature. Calcium traces were analyzed using IonWizard software (IonOptix) to calculate the baseline, amplitude (peak height), and tau (time of relaxation).

#### qRT-PCR

Total RNA (including miRs) was extracted from flash-frozen hECTs using the Quick-RNA MiniPrep kit (Zymo Research, Irvine, CA) after lysis using FastPrep Lysis Beads and Matrix Tubes (MP Products, Santa Ana, CA) and quantified using a NanoDrop 2000 (Thermo Fisher Scientific). Reverse transcription was performed using the iScript cDNA synthesis kit (Biorad Laboratories, Hercules, CA) for gene expression and qScript microRNA cDNA Synthesis Kit (Quanta Biosciences, Beverly, MA) for miR quantification (this includes a polyA tailing reaction and first-strand cDNA synthesis reaction). Quantitative PCR (10 ng cDNA/reaction) was performed using a two-step system with SYBR Advantage qPCR Premix (Clontech Laboratories, Mountain View, CA) on the ABI Prism 7500 Fast Real-Time PCR system (Applied Biosystems, Foster City, CA) according to manufacturer recommendations.

All primers used were anti-human and are shown as the 5' to 3' sequence:

<b>Gene</b>	<b>Direction</b>	<b>Sequence (5'→3')</b>
β2M	Forward	GTATGCCTGCCGTGTGAAC
β2M	Reverse	CAAGCAAGCAGAATTGGAA
cTnT	Forward	AAGAGGCAGACTGAGCGGGAAA
cTnT	Reverse	AGATGCTCTGCCACAGCTCCTT
ANF	Forward	ACAATGCCGTGTCCAACGCAGA
ANF	Reverse	CTTCATTGGCTCACTGAGCAC

BNP	Forward	AAGGGTCTGGCTGCTTG
BNP	Reverse	CAGCCAGGACTTCCTCTTAATG
αMYHC	Forward	GGAAGACAAGGTCAACAGCCTG
αMYHC	Reverse	TCCAGTTCCGCTTGCTCGCT
βMYHC	Forward	GGAGTTCACACGCCTCAAAGAG
βMYHC	Reverse	TCCTCAGCATCTGCCAGGTTGT
SERCA2a	Forward	CTGTCCATGTCACTCCACTTCC
SERCA2a	Reverse	AGCGGTTACTCCAGTATTGCAG
CASP3	Forward	TTAATAAAGGTATCCATGGAGAACACT
CASP3	Reverse	TTAGTGATAAAAATAGAGTTCTTTGTGAG
CASP9	Forward	TTCCCAGGTTTGTTCCCTG
CASP9	Reverse	CCTTTCACCGAAACAGCATT
BCL2	Forward	CTGCACCTGACGCCCTTCACC
BCL2	Reverse	CACATGACCCCACCGAACTCAAAGA
BAX	Forward	GGACGAACTGGACAGTAACATGG
BAX	Reverse	GCAAAGTAGAAAAGGGCGACAAC
LTCC	Forward	TGACTATTTGCCAATTGTGTGG
LTCC	Reverse	CGGGAGGTAGGCATTGGG
VEGF-α	Forward	TTGCCTTGCTGCTCTACCTCCA
VEGF-α	Reverse	GATGGCAGTAGCTGCGCTGATA
ANGPT1	Forward	CAACAGTGTCCCTCAGAAGCAGC
ANGPT1	Reverse	CCAGCTTGATATACATCTGCACAG
TGF-β1	Forward	TACCTGAACCCGTGTTGCTCTC
TGF-β1	Reverse	GTTGCTGAGGTATGCCAGGAA
TGF-β2	Forward	AAGAAGCGTGCTTGGATGCGG

TGF- $\beta$ 2	Reverse	ATGCTCCAGCACAGAAGTTGGC
TGF- $\beta$ 1R	Forward	GACAAACGTCAGGTTCTGGCTCA
TGF- $\beta$ 1R	Reverse	CCGCCACTTCCTCTCCAACT
TGF- $\beta$ 2R	Forward	GTCTGTGGATGACCTGGCTAAC
TGF- $\beta$ 2R	Reverse	GACATCGGTCTGCTTGAAGGAC
hsa-miR-21-5p <sup>a</sup>	Forward	GCTAGCTTATCAGACTGATGTTGAAA
hsa-miR-22-3p <sup>a</sup>	Forward	CGAAGCTGCCAGTTGAAGAAC
hsa-miR-181b-5p <sup>a</sup>	Forward	CGACGACGAACATTCAATTGC

<sup>a</sup> Universal reverse primer is included in qScript microRNA cDNA kit.

Fold changes in gene expression were determined using the comparative Ct method ( $\Delta\Delta Ct$ ) with normalization to the housekeeping gene beta-2-microglobulin ( $\beta 2M$ ). Fold changes in miR levels were calculated in the same way, but normalized to the small nucleolar RNA SNORD44 (primers are included in the qScript microRNA cDNA synthesis kit). This experiment was repeated in triplicate.

**Online Table I:** Specific characteristics of antibodies used

Antibody	Catalog Number	Source	Host	Immunoglobulin Fragment	Dilution	Validation
Anti-Cav1.2 calcium channel (LTCC)	MAB13170	Millipore	Mouse Monoclonal	Recombinant protein corresponding to rabbit Cav1.2 calcium channel at the cytoplasmic domain proximal to the C-terminus.	1:1000 (WB)	Mouse brain tissue lysate
Anti-SERCA2a	Custom made	21st Century Biochemicals	Rabbit Polyclonal	Carboxy terminus of human SERCA2a.	1:3000 (WB)	Human, rat, and mouse cardiac tissue lysates
Anti-Bax	ab32503	Abcam	Rabbit Monoclonal	Synthetic N-terminal peptide within Human Bax (amino acids 1-100).	1:1000 (WB)	HeLa cell lysate
Anti-Bcl-2	4223	Cell Signaling	Rabbit Monoclonal	Synthetic peptide corresponding to residues	1:1000 (WB)	Extracts from various cell lines

				surrounding Gly47 of human Bcl-2.		
Anti- $\alpha$ -actinin	A7732	Sigma	Mouse Monoclonal	Purified rabbit skeletal $\alpha$ -actinin.	1:10000 (WB)	Rat skeletal muscle lysate
Anti-GAPDH	G8795	Sigma	Mouse Monoclonal	Rabbit GAPDH.	1:10000 (WB)	A431 total cell lysate
Anti-cTnT	ac45932	Abcam	Rabbit Polyclonal	Synthetic peptide conjugated to KLH derived from within residues 50 - 150 of human cardiac Troponin T.	1:10000 (WB)	Human fetal heart tissue lysate

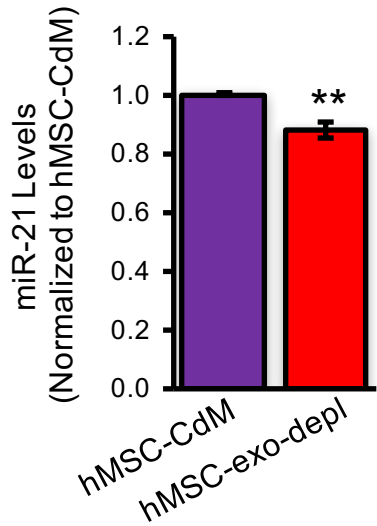


**Figure S1:** Expression of miR-21-5p in hHECTs five days after hMSC-CdM treatment in comparison to hMSC-exo-depl treatment. \*\* $p<0.01$ , p-values from unpaired t tests ( $n=4$ ).

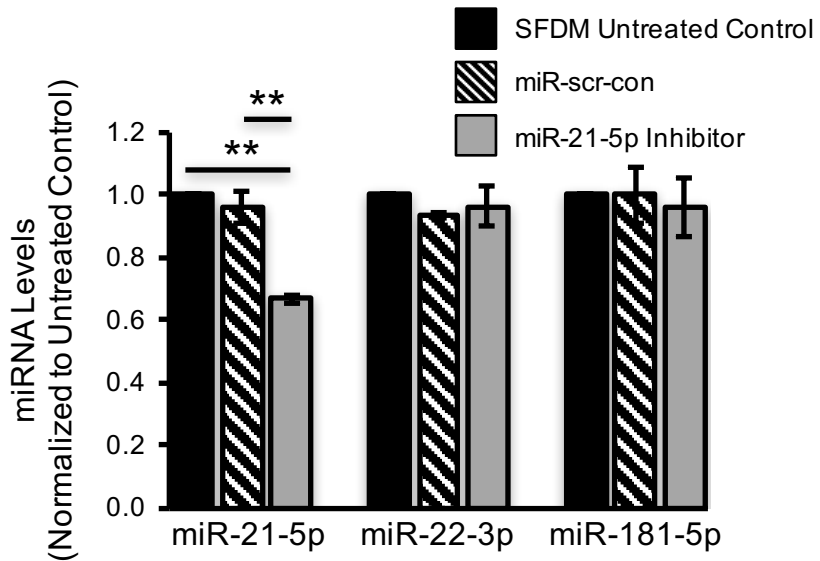


**Figure S2:** After two days of treatment with SFDM (SFDM Untreated Control; solid black), miR-scr-con (miR-scr-con; black and white pattern), or miR-21 inhibitor (miR-21-5p Inhibitor; gray) and subsequent culture in SFDM for five days, hMSCs were snap-frozen for qRT-PCR on culture day 7, where expression of miR-21-5p, miR-22-3p, and miR-181b-5p were studied.

\*\*p<0.01; p values from 1-way ANOVA with post hoc Tukey test. (n=3).

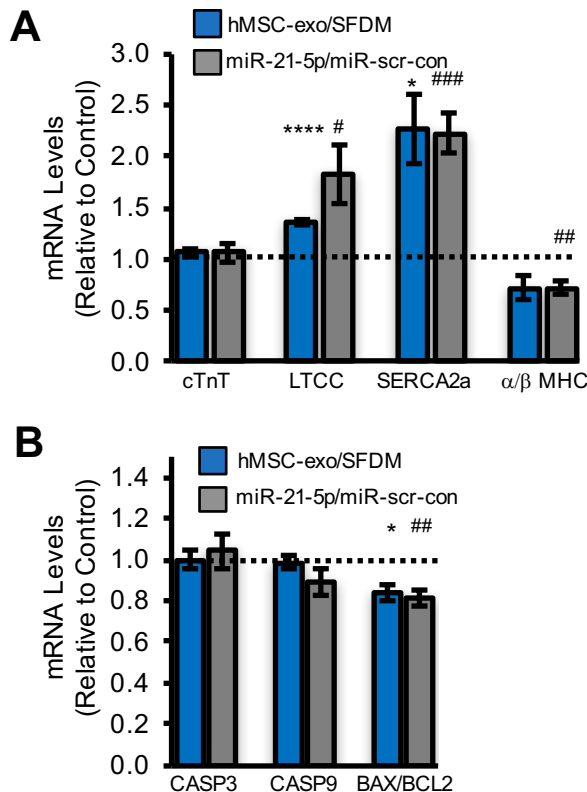


**Figure S3:** hECTs treated with SFDM control, hMSC-exo, miR-con, and miR-21-5p were snap-frozen for qRT-PCR on culture day 10 (five days post-treatment), where expression of (**A**) cardiac-specific and calcium-handling genes, as well as (**B**) apoptotic genes was studied. hMSC-exo (blue) and miR-21-5p (gray) treated groups were normalized to their respective controls (SFDM and miR-scr-con, respectively). \* $p<0.05$ , \*\* $p<0.01$ , \*\*\* $p<0.001$ ; \*\*\*\* $p<0.0001$ ; p-values from unpaired t test between hMSC-exo and SFDM ( $n=3$ ). Gene expression data for SFDM and hMSC-exo groups adapted from Mayourian et al.<sup>10</sup> In all panels, # $p<0.05$ , ## $p<0.01$ , ### $p<0.001$ ; p-values from unpaired t test miR-scr-con vs. miR-21-5p ( $n=5$ ). Nonstandard abbreviations: cardiac troponin-T (cTnT); L-type calcium channel (LTCC); sarcoendoplasmic reticulum calcium-ATPase (SERCA2a); myosin heavy chain (MHC); caspase-3 (Casp3); caspase-9 (Casp9); B-cell lymphoma 2 (BCL2); BCL2-associated X protein (BAX).

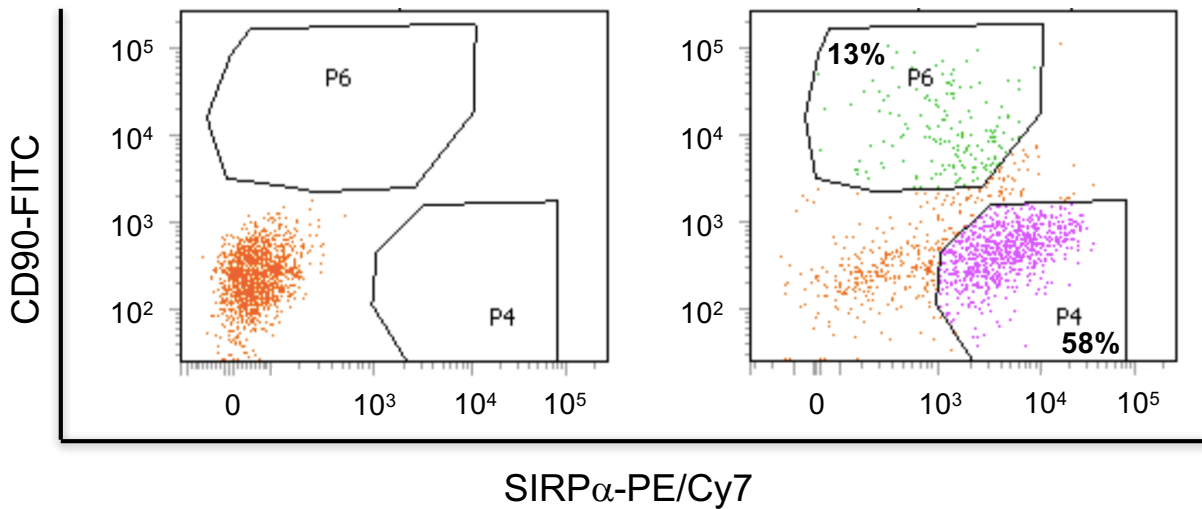


**Figure S4:** Representative flow cytometry results from cardiomyocyte differentiations of human embryonic stem cells suggest approximately 4:1 SIRP $\alpha$ <sup>+</sup>/CD90<sup>-</sup> myocytes (P4) to CD90<sup>+</sup>/SIRP $\alpha$ <sup>+</sup> fibroblasts (P6).

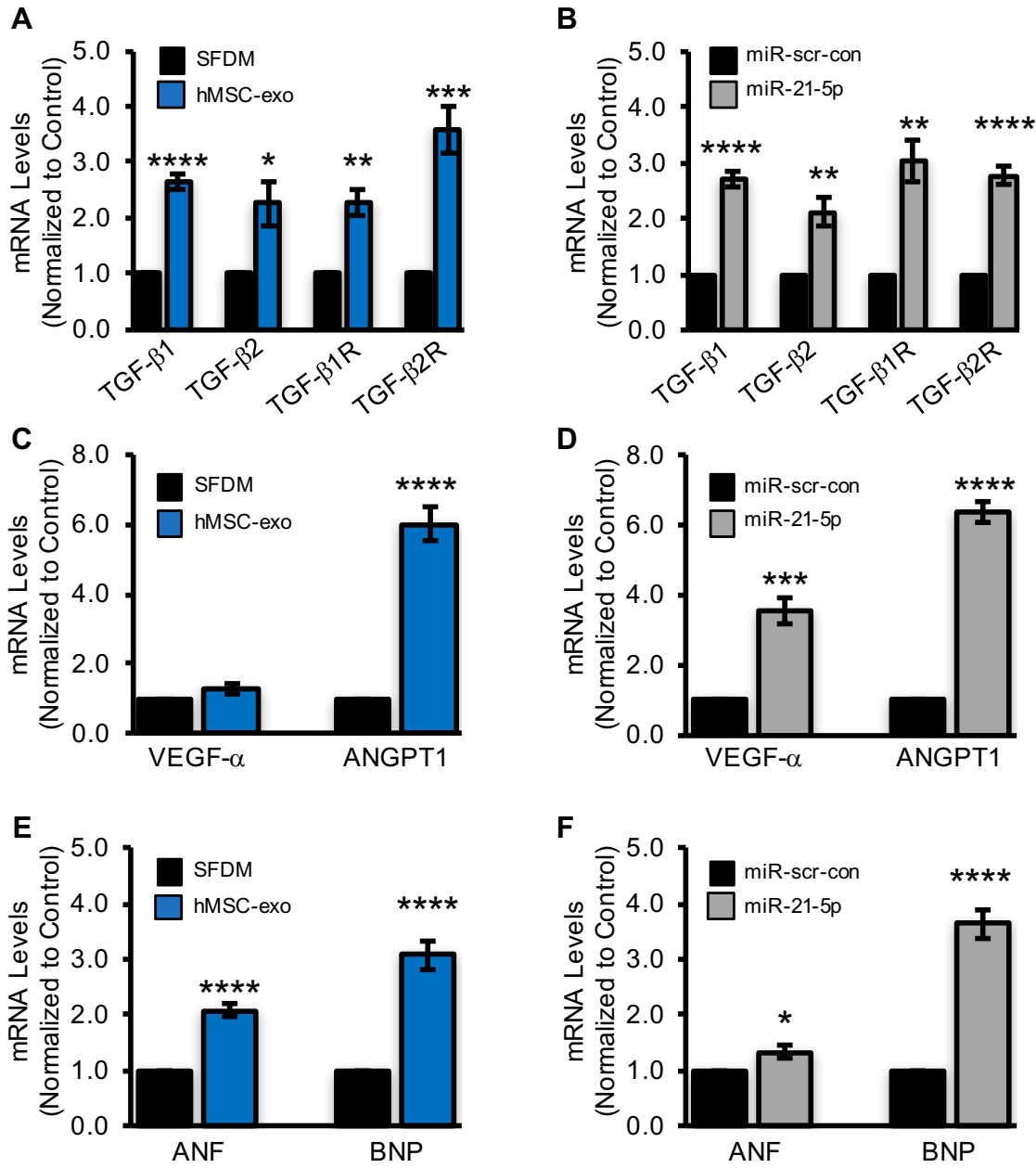


**Figure S5:** hECTs treated with SFDM vs. hMSC-exo (**A, C, E**) and miR-scr-con vs. miR-21-5p (**B, D, F**) were snap-frozen for qRT-PCR five days post-treatment, where expression of (**A-B**) transforming growth factor- $\beta$  signaling, (**C-D**) pro-angiogenic, and (**E-F**) hypertrophic markers were examined. p-values from unpaired t tests (n=4). Nonstandard abbreviations: transforming growth factor- $\beta$ 1 (TGF- $\beta$ 1); transforming growth factor- $\beta$ 2 (TGF- $\beta$ 2); TGF- $\beta$ 1 receptor (TGF- $\beta$ 1R); TGF- $\beta$ 2 receptor (TGF- $\beta$ 2R); vascular endothelial growth factor- $\alpha$  (VEGF- $\alpha$ ); angiopoietin-1 (ANGPT1); atrial natriuretic factor (ANF); brain natriuretic peptide (BNP). In all panels, \*p<0.05, \*\*p<0.01, \*\*\*p<0.001, \*\*\*\*p<0.0001.

**Supplementary References:**

1. Pope SM, Lasser C. Toxoplasma gondii infection of fibroblasts causes the production of exosome-like vesicles containing a unique array of mRNA and miRNA transcripts compared to serum starvation. *J Extracell Vesicles*. 2013;2.
2. Eisen MB, Spellman PT, Brown PO, Botstein D. Cluster analysis and display of genome-wide expression patterns. *Proc Natl Acad Sci U S A*. 1998;95:14863-14868.
3. Gray WD, French KM, Ghosh-Choudhary S, Maxwell JT, Brown ME, Platt MO, Searles CD, Davis ME. Identification of therapeutic covariant microRNA clusters in hypoxia-treated cardiac progenitor cell exosomes using systems biology. *Circ Res*. 2015;116:255-263.
4. Galende E, Karakikes I, Edelmann L, Desnick RJ, Kerenyi T, Khoueiry G, Lafferty J, McGinn JT, Brodman M, Fuster V, Hajjar RJ, Polgar K. Amniotic fluid cells are more efficiently reprogrammed to pluripotency than adult cells. *Cell Reprogram*. 2010;12:117-125.
5. Karakikes I, Senyei GD, Hansen J, Kong CW, Azeloglu EU, Stillitano F, Lieu DK, Wang J, Ren L, Hulot JS, Iyengar R, Li RA, Hajjar RJ. Small molecule-mediated directed differentiation of human embryonic stem cells toward ventricular cardiomyocytes. *Stem Cells Transl Med*. 2014;3:18-31.
6. Ceholski DK, Turnbull IC, Pothula V, Lecce L, Jarrah AA, Kho C, Lee A, Hadri L, Costa KD, Hajjar RJ, Tarzami ST. Cxcr4 and cxcr7 play distinct roles in cardiac lineage specification and pharmacologic beta-adrenergic response. *Stem Cell Res*. 2017;23:77-86.
7. Cashman TJ, Josowitz R, Gelb BD, Li RA, Dubois NC, Costa KD. Construction of defined human engineered cardiac tissues to study mechanisms of cardiac cell therapy. *J Vis Exp*. 2016:e53447.

8. Bhattacharya S, Burridge PW, Kropp EM, Chuppa SL, Kwok WM, Wu JC, Boheler KR, Gundry RL. High efficiency differentiation of human pluripotent stem cells to cardiomyocytes and characterization by flow cytometry. *J Vis Exp.* 2014;52010
9. Turnbull IC, Karakikes I, Serrao GW, Backeris P, Lee JJ, Xie C, Senyei G, Gordon RE, Li RA, Akar FG, Hajjar RJ, Hulot JS, Costa KD. Advancing functional engineered cardiac tissues toward a preclinical model of human myocardium. *FASEB J.* 2014;28:644-654
10. Mayourian J, Cashman TJ, Ceholski DK, Johnson BV, Sachs D, Kaji DA, Sahoo S, Hare JM, Hajjar RJ, Sobie EA, Costa KD. Experimental and computational insight into human mesenchymal stem cell paracrine signaling and heterocellular coupling effects on cardiac contractility and arrhythmogenicity. *Circ Res.* 2017;121:411-423
11. Serrao GW, Turnbull IC, Ancukiewicz D, Kim DE, Kao E, Cashman TJ, Hadri L, Hajjar RJ, Costa KD. Myocyte-depleted engineered cardiac tissues support therapeutic potential of mesenchymal stem cells. *Tissue Eng Part A.* 2012;18:1322-1333
12. Heldman AW, DiFede DL, Fishman JE, et al. Transendocardial mesenchymal stem cells and mononuclear bone marrow cells for ischemic cardiomyopathy: The tac-hft randomized trial. *JAMA.* 2014;311:62-73
13. Hare JM, Fishman JE, Gerstenblith G, et al. Comparison of allogeneic vs autologous bone marrow-derived mesenchymal stem cells delivered by transendocardial injection in patients with ischemic cardiomyopathy: The poseidon randomized trial. *JAMA.* 2012;308:2369-2379
14. Thery C, Amigorena S, Raposo G, Clayton A. Isolation and characterization of exosomes from cell culture supernatants and biological fluids. *Curr Protoc Cell Biol.* 2006;Chapter 3:Unit 3 22

## **Chapter 8: Summary and Future Directions**

In summary, my thesis applies tissue engineering and computational approaches to advance the field of stem cell-based cardioterapies with five independent projects that cohesively address the following three linked questions: 1) what are the relative contributions of the two predominant components of the hMSC-cardiomyocyte interactome—namely paracrine signaling (PS) and heterocellular coupling (HC)—in modulating cardiac contractility and arrhythmogenicity? 2) is the soluble or insoluble exosomal fraction of the hMSC paracrine secretome primarily responsible for these dominant paracrine-mediated effects on contractility? and 3) which microRNA cargo is responsible for the hMSC exosome-enriched fraction largely modulating contractility, and through what mechanism?

First, Projects I and II of the dissertation established the utility and methodology, respectively, of human engineered cardiac tissues (hECTs) and systems biology approaches to investigate paracrine signaling (PS) and heterocellular coupling (HC) effects on excitation-contraction coupling (Chapters 2-4). Next, using an *in silico* approach, Project III provides novel electrophysiological models of hMSCs, predicts possible arrhythmogenic effects of hMSCs when directly coupled to healthy hCMs, and proposes that isolating a subset of hMSCs absent of hEAG1 activity may offer increased safety as a cell delivery cardioterapy at low levels of hMSC-hCM coupling (Chapter 5). Project IV builds on the HC model from Project III and integrates experimental and computational approaches to help unravel relative contributions of hMSC PS and HC effects on human cardiac contractility and arrhythmogenicity, resolve disparate reports of potential pro-arrhythmic risks of hMSCs *in vitro* versus anti-arrhythmic benefits of hMSCs *in vivo*, and provide novel insight into the role of exosomes in hMSC paracrine-mediated effects on contractility (Chapter 6). Finally, Project V identifies miR-21-5p as a lead candidate exosomal cargo responsible for hMSC paracrine-mediated increases in human engineered cardiac tissue contractility via the PI3K/Akt signaling cascade (Chapter 7).

Altogether, this dissertation provides novel experimental and computational insight into hMSC effects on human cardiac tissue contractility and arrhythmogenicity. These findings support the safety of hMSC-based therapies in diseased myocardium *in silico*, and may open up new avenues of research to harness the role of hMSC exosomes and their cargo (e.g., miR-21-5p) in optimizing future stem cell-based cardiotherapies. To this end, the findings of each project motivate future work, as discussed in detail below.

## **8.1 Project I Future Directions**

As noted in Chapter 2, one recognized limitation of hECTs is the relatively immature cardiac phenotype that more closely mimics newborn human heart muscle rather than healthy adult myocardium; this reflects an ongoing scientific challenge with stem cell-derived cardiomyocytes and other cell types. Thus, one area of future work involves promoting phenotypic maturation of human stem cell-derived cardiomyocytes and hECTs, possibly involving treatment with miR-21-5p in combination with other recent additives such as triiodothyronine thyroid hormone and dexamethasone.<sup>1</sup> In addition, it would be of interest to test the paracrine effects of human adult cardiac fibroblasts and human dermal fibroblasts on hECT models of disease, such as the cryo-injury or doxorubicin cardiomyopathy-induced models developed in Project II.

## **8.2 Project II Future Directions**

Chapters 3 and 4 provide the current state of tissue engineering and mathematical modeling, respectively, to study cardiac disease and therapeutics. Further, they provide insight into the current state of both fields, motivating several areas of future work: 1) studying the dose-dependent effects of the doxorubicin-induced cardiomyopathy model; 2) molecular characterization of injured hECT models; 3) extending Chapter 4 to provide a primer to non-mathematicians to cardiac excitation-contraction coupling modeling studies; and 4) developing

novel *in silico* approaches to enhance next-generation regulatory standards for drug cardiotoxicity screening by building off the Lancaster and Sobie model.<sup>2</sup>

While beyond the scope of this focused thesis, we address item 4 in Supplementary Chapter 9 (Project VI).

### **8.3 Project III Future Directions**

Upon completion of this project, immediate areas for future work (based on limitations discussed in Chapter 5) included: 1) improving the computational models based on advancements in empirical data on hMSC electrophysiology; 2) considering the effects of microfibrosis or random microscale obstacles in combination with hMSC anti-fibrotic paracrine effects; 3) examining the electrical and electromechanical effects of hMSC models coupled with ischemic hCM models; 4) modeling the interplay between electrophysiological effects and paracrine signaling in the hMSC-hCM interactome; 5) empirically confirming our simulations, demonstrating that Type C hMSCs minimize the impact on action potential duration and reduce the vulnerable window at low levels of hMSC insertion, offering a potential strategy for improving the safety of cardiac cell therapies; and 6) applying similar techniques to model HC effects of other cardiotherapeutic stem cells of interest, such as human cardiac progenitor cells, on cardiomyocyte electrophysiology.

After publishing this work, I addressed items 2-4 in Project IV. Developing a model of cardiac progenitor cell electrophysiology is currently in progress to address item 6.

### **8.4 Project IV Future Directions**

Upon completion of this project, crucial areas of future work (based on limitations discussed in detail in Chapter 6) included: 1) testing how hMSC paracrine effects on contractile function of healthy hECTs translates to hECT models of heart disease; and 2) further studying the role of hMSC exosomes and their molecular cargo that may be responsible for increased

contractility in vitro and in vivo. Since publication of this work, I addressed item 2 in Project V by further studying the role of hMSC exosomes and their cargo in vitro using hECT. Crucial future work remains to test hMSC exosomal cardioactivity in healthy and diseased in vivo models. To test translation of hMSC paracrine effects on diseased hECTs, I have developed a doxorubicin cardiomyopathy-induced model, as presented in Project II; future work involves testing exosome potency on this model. Finally, this project provides a framework to test the paracrine potency of other stem cells—such as cardiac progenitor stem cells—on our hECT platform.

## **8.5 Project V Future Directions**

Upon completion of this project, crucial areas of future work (based on limitations discussed in detail in Chapter 7) include: 1) building on recent efforts to improve hPSC-CM maturation<sup>1</sup> by utilizing miR-21-5p or other synthetic miRs as a conditioning media supplement; 2) performing extended time course and dose-response experiments in follow-up studies examining the translational potential of these findings; 3) testing miR-21-5p cardioactivity in diseased hECT models; and 4) harnessing the potency of miR-21-5p in the context of stem cell-based or even synthetic miR-based<sup>3</sup> cardiotherapies.

## **8.6 References**

1. Parikh SS, Blackwell DJ, Gomez-Hurtado N, Frisk M, Wang L, Kim K, Dahl CP, Fiane A, Tonnessen T, Kryshlal DO, Louch WE, Knollmann BC. Thyroid and glucocorticoid hormones promote functional t-tubule development in human-induced pluripotent stem cell-derived cardiomyocytes. *Circ Res.* 2017;121:1323-1330
2. Lancaster MC, Sobie EA. Improved prediction of drug-induced torsades de pointes through simulations of dynamics and machine learning algorithms. *Clin Pharmacol Ther.* 2016;100:371-379
3. Lesizza P, Prosdocimo G, Martinelli V, Sinagra G, Zacchigna S, Giacca M. Single-dose intracardiac injection of pro-regenerative micrornas improves cardiac function after myocardial infarction. *Circ Res.* 2017;120:1298-1304

**Supplementary Chapter 9: Improved Prediction of Drug Torsadogenicity by Machine  
Learning with Tissue-level Electrophysiology Simulations**

*Note: The following chapter is in preparation for submission as an original first-author research article.*

JM conceived the idea, collected and analyzed the data, and wrote the manuscript.

## **9.1 Abstract**

Background: Drug-induced Torsades de Pointes (TdP) is a potentially lethal cardiotoxic risk that has been the leading cause for withdrawal and relabeling of a diversity of therapeutic compounds. Clearly, it is of interest for pharmaceutical companies to inexpensively yet effectively screen the torsadogenic risk of drugs under development for the clinic.

Objective: To investigate the predictive value of a machine-learning framework that incorporates in silico simulations of clinically relevant cardiac tissue-level electrophysiology for automated discrimination of TdP from non-TdP drugs.

Methods: We examined the performance of linear support vector machine classifiers receiving single-cell and tissue-level action potential and calcium transient metric inputs under normokalemic and hypokalemic conditions on a panel of up to 116 published drug responses.

Results: Four simulation-based classifiers (normokalemic single-cell, hypokalemic single-cell, normokalemic tissue-level, and hypokalemic tissue-level) individually outperformed conventional hERG inhibition-based assay classification that had a 38.8% misclassification rate. Interestingly, the normokalemic tissue-level classifier led to the lowest misclassification rate of 13.8%, with feature selection analysis implicating action potential duration heterogeneity as a key metric accessible in tissue-level, but not single-cell, simulations. However, under hypokalemia, tissue-level mean action potential duration and upstroke velocity superseded action potential duration heterogeneity as top predictive features, thus providing no added benefit in drug classification versus normokalemia. Finally, using a simulated library of 100 hypothetical drugs, we identified the inward rectifier and slow delayed rectifier K<sup>+</sup> channels as unconventional modulators of TdP risk.

Conclusions: Our findings demonstrate the superiority of tissue-level assays for TdP risk, suggest monitoring of two atypical ion channels to improve sensitivity of TdP risk assessment, and present novel in silico approaches to enhance next-generation regulatory standards for drug cardiotoxicity screening.

## 9.2 Introduction

Torsades de Pointes (TdP) is a rare but lethal form of polymorphic ventricular tachycardia, where a prolonged QT interval precedes cyclic shifting of the QRS axis.<sup>1</sup> In addition to congenital long QT syndrome, anti-arrhythmic and non-cardiac drugs altering repolarization have been implicated in causing TdP.<sup>2</sup>

Drug-induced TdP is a leading cause of drug relabeling or withdrawal from the market, only second to drug-induced hepatotoxicity;<sup>3,4</sup> this has led to the establishment of regulatory cardiotoxicity testing<sup>5-7</sup>—including in vitro measurements on hERG current inhibition, animal model QT assays, and clinical examination of QT interval in healthy volunteers—that is both expensive and of limited specificity.<sup>8,9</sup> Given early drug development attrition rates of 80-90% and only 10% commercial success,<sup>10,11</sup> it is of great interest for pharmaceutical companies to inexpensively and predictively screen whether a drug under development is torsadogenic.

Recent work has demonstrated the promise of integrating systematic simulations with machine learning to predict pharmacological toxicity.<sup>12</sup> In this study, we focus on applying this quantitative systems pharmacology approach in the context of clinically relevant, hypokalemic conditions<sup>13</sup> and higher fidelity, tissue-level prognostic factors such as spatial dispersion of repolarization.<sup>14-17</sup> More specifically, we investigate the predictive value of a machine-learning framework that incorporates normokalemic or clinically relevant hypokalemic cardiac tissue-level electrophysiology simulation data for automated discrimination of TdP from non-TdP drugs.

To do so, we first compare classification performance of algorithms that incorporate normokalemic and hypokalemic single-cell simulation data versus corresponding higher-order tissue-level *in silico* measurements. Next, we provide physiological insight into TdP by identifying key features in the normokalemic tissue-level classifier that lead to its superior classification relative to the other classifiers. Finally, we predict the torsadogenic risk of several atypical drug targets, including cardiomyocyte channels, pumps, and exchangers.

## 9.2 Methods

### 9.2.1 Models and simulations

Single-cell classifier model development is described in detail elsewhere.<sup>12</sup> For the tissue-level classifier, each drug was simulated in three human ventricular myocyte transmural 1-D tissue-level models, made up of half endocardial cells and half epicardial cells, as performed elsewhere.<sup>18</sup> To avoid any potential bias and to be consistent with the single-cell classifier study design, we conducted simulations in three independent models: 1) O'Hara, Virág, Varró, and Rudy;<sup>19</sup> (2) ten Tusscher and Panfilov;<sup>20</sup> and (3) Grandi, Pasqualini, and Bers.<sup>21</sup> Drug effects were simulated with a simple pore block model described elsewhere.<sup>12</sup> Simulated 1-D tissue strands were electrically stimulated at rates of 0.5 Hz, 1 Hz, and 2 Hz to steady state. For each drug under each of the 9 conditions (three pacing rates for three one-dimensional tissue strand models), we calculated the mean and standard deviation of 13 metrics that are analogous to the single-cell metrics from the population of action potentials and calcium transients within the tissue strand, totaling 26 measurements per drug. All models were tested under normokalemia (extracellular potassium concentration of 5.4 mM) and hypokalemia (extracellular potassium concentration of 2.5 mM).

Action potential metrics include: 1) upstroke velocity; 2) peak membrane voltage; 3) action potential duration (APD) at 50% repolarization ( $APD_{50}$ ); 4) APD at -60 mV; 5)  $APD_{90}$ ; 6) action potential triangulation; and 7) resting membrane potential. Calcium transient metrics include: 8) diastolic intracellular calcium; 9) background-subtracted calcium transient amplitude; 10) peak intracellular calcium; 11) calcium transient duration at 50% return to baseline; 12) calcium transient duration at 90% return to baseline; and 13) calcium transient triangulation (see Figure 1 for schematic representation of each metric).

Simulations examined each drug at its effective free therapeutic plasma concentration (EFTPC); each tissue model was simulated with its baseline, published parameters with a space step of 0.01 cm, time step of 0.0025 ms, and diffusion constant of 0.00154 cm<sup>2</sup>/ms.

### *9.2.2 Databases*

Drug inhibition of three currents (i.e., rapid delayed rectifier K<sup>+</sup> current, L-type Ca<sup>2+</sup> current, and fast Na<sup>+</sup> current) was incorporated into our simulations using reported half-maximal inhibitory concentrations (IC<sub>50</sub>) for the first 86 drugs published in the Kramer et al. and Mirams et al. studies.<sup>22,23</sup>

Drug inhibition of seven currents (i.e., the aforementioned three currents, in addition to the late Na<sup>+</sup> current, transient outward current, slow delayed rectifier K<sup>+</sup> current, and the inward-rectifier potassium current) was incorporated into our simulations using reported IC<sub>50</sub> for the final 30 drugs published in the Crumb et al. study.<sup>24</sup> Altogether, 116 arrhythmogenic and non-arrhythmogenic drugs were examined in this study.

We defined the binary torsadogenicity of the drugs in our training set using the CredibleMeds database (<https://www.crediblemeds.org>) and the study from Champeroux et al., as described elsewhere.<sup>12</sup> Supplemental Table 1 shows IC<sub>50</sub> values and torsadogenicity definitions for all drugs used in this study.

### *9.2.3 Evaluating Classification Performance*

The output simulation datasets were used to train a support vector machine classifier with a linear kernel. Classifier performance was evaluated through various methods, including: 1) calculating the area under a receiver operating characteristic curve (auROC); 2) leave-one-out cross-validation (LOOCV); and 3) holdout cross-validation.

### *9.2.4 Feature selection*

Within each single-cell and tissue-level model, we performed a feature selection to identify the two metrics that best represent the generalizable classifier of all metrics. To do so, we built a support vector machine classifier on each feature individually, and selected the

feature with the best area under the receiver operating characteristic curve (auROC),<sup>26</sup> which was defined as “Feature 1”. Next, for each model, we built a support vector machine classifier on the respective “Feature 1” and the remaining metrics. “Feature 2” was defined as the metric complementary to “Feature 1” that led to the highest auROC. In general, adding a third feature provided no performance benefit.

#### *9.2.5 Hypothetical drug simulations*

One hundred hypothetical drugs were generated to interact with the  $\text{Na}^+/\text{Ca}^{2+}$  exchanger, sarcoplasmic reticulum  $\text{Ca}^{2+}$  ATPase, background calcium current, background sodium current, inward rectifier  $\text{K}^+$  current, ryanodine receptor, transient outward current, slow delayed rectifier potassium channel, and the  $\text{Na}^+/\text{K}^+$  pump for each of the 1-D transmural tissue strands at 0.5 Hz, 1 Hz, and 2 Hz. To do so, we randomly perturbed maximum flux parameters for each of these nine components from 50% to 200%.

#### *9.2.6 Software*

All single-cell models were implemented in MATLAB (The MathWorks, Natick, MA) and numerically integrated using a stiff ordinary differential equation solver (ode15s). The MATLAB function pca was used to calculate principal components. The support vector machine classifier was generated using the MATLAB function fitcsvm with a linear kernel. All tissue-level models were implemented in Python and numerically integrated using Euler’s method.

#### *9.2.7 Statistical analysis*

To compare head-to-head classification performance between the single-cell and tissue-level classifiers during holdout cross-validation, a repeated measures ANOVA was used with the Tukey post-hoc test. To calculate parameter significance to hypothetical drug risk, the Wilcoxon rank sum test was used for each model at each pacing frequency.

### 9.3 Results

#### 9.3.1 Cardiac electrophysiological responses to clinical drugs

As inputs to our machine learning classifier, we simulated the electrophysiological effects of 116 clinically relevant drugs at EFTPC in three independent human ventricular myocyte models at 0.5, 1, and 2 Hz pacing under normokalemia (Figure 1A) and hypokalemia (Figure 1B). In both conditions, it appeared that TdP drugs prolonged APD (Figure 1A-B, top) and increased the peak calcium transient (Figure 1A-B, bottom), while non-TdP drugs generally shortened APD (Figure 1A-B, top) and decreased the peak calcium transient relative to baseline (Figure 1A-B, bottom). These effects were exacerbated under hypokalemia.

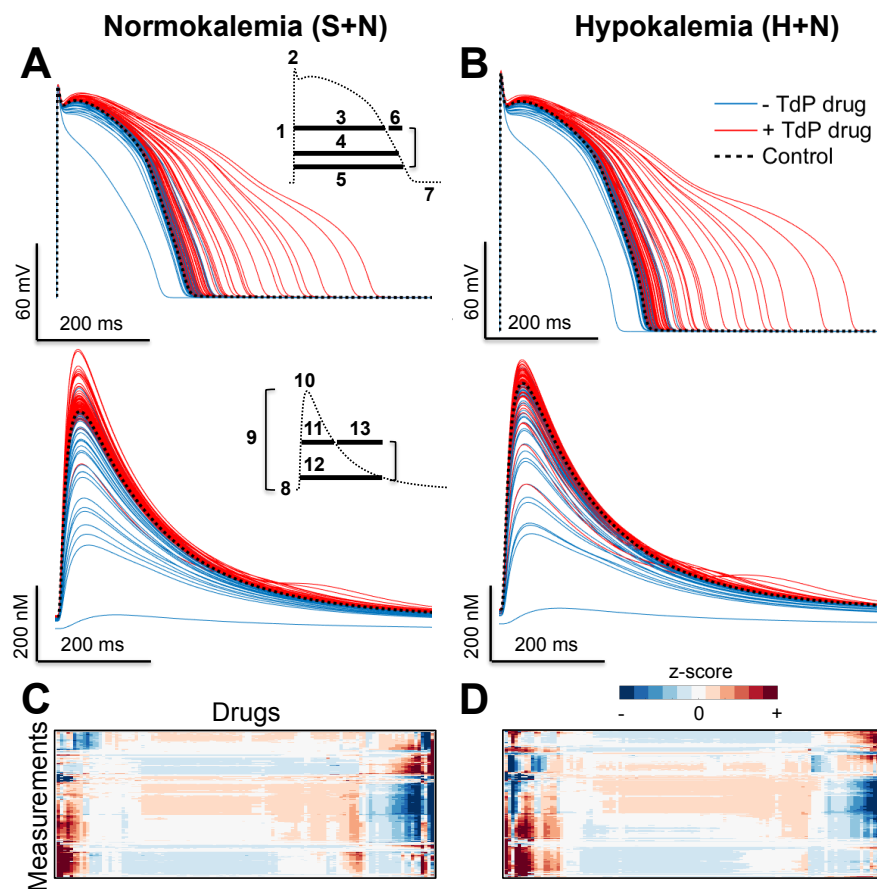


**Figure 1. Drug response in human ventricular single-cell models.** Action potential (top) and calcium transient (bottom) traces for the O'Hara, Virág, Varró, and Rudy <sup>19</sup> epicardial model under A) normokalemia and B) hypokalemia at 1 Hz pacing under exposure to each of 116

drugs. Torsadogenic (+TdP) and non-torsadogenic (-TdP) drugs are in red and blue, respectively (control in black). Seven action potential and six calcium transient metrics are inset.

Heatmap of hierarchical clustered z-scores (color bar inset) for each metric under C)

normokalemic and D) hypokalemic conditions.

These trends were also evident under normokalemia and hypokalemia in three transmural human ventricular models at 0.5, 1, and 2 Hz pacing. Importantly, action potential (Figure 2A-B, top) and calcium handling (Figure 2A-B, bottom) waveforms vary from the endocardial to the epicardial end of the tissue, yielding a distribution of action potential and calcium transient metrics throughout the tissue.

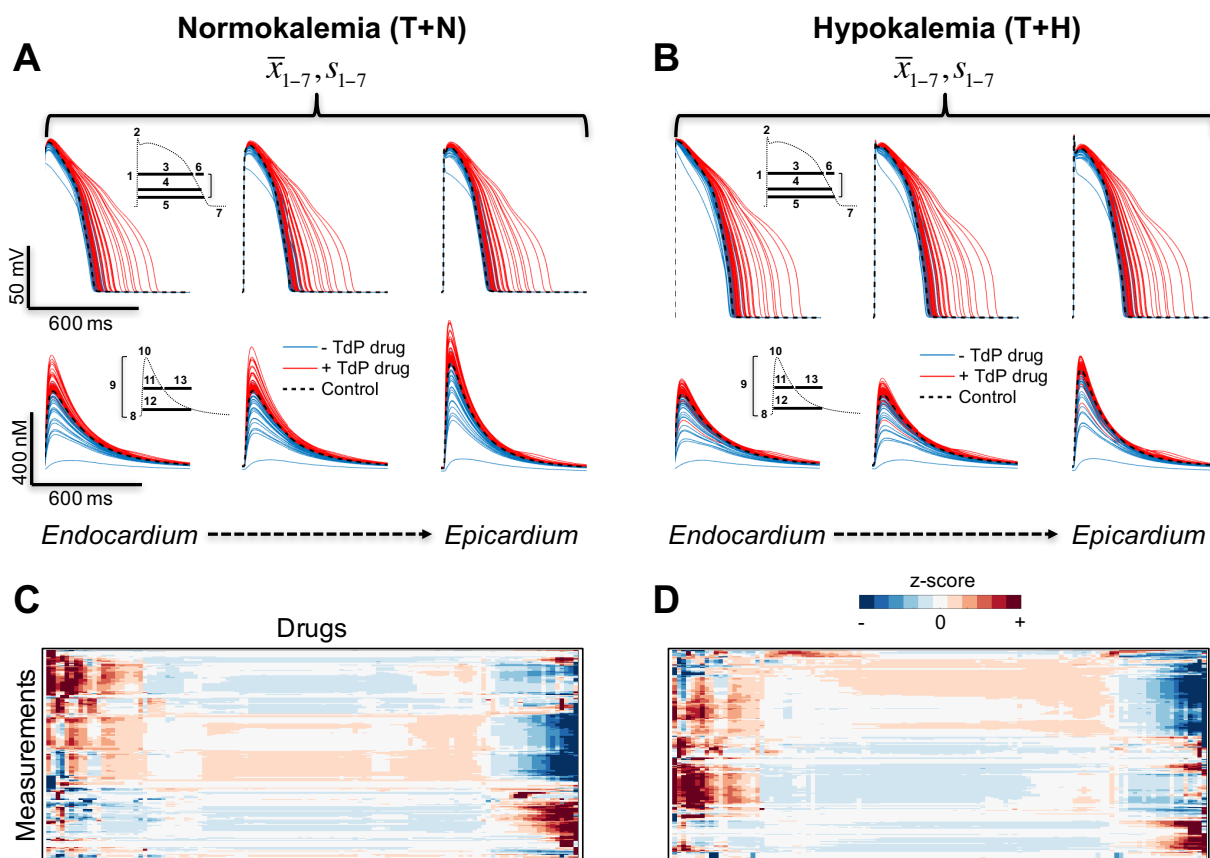


**Figure 2. Drug response in human ventricular tissue-level models.** Action potential (top) and calcium transient (bottom) traces for the endocardial end (left), middle (center), and epicardial end (right) of the O'Hara, Virág, Varró, and Rudy<sup>19</sup> 1-D transmural model under A) normokalemia and B) hypokalemia at 1 Hz pacing under exposure to each of 116 drugs. Torsadogenic (+TdP) and non-torsadogenic (-TdP) drugs are in red and blue, respectively (control in black). Mean ( $\bar{x}$ ) and standard deviation (s) of seven action potential and six calcium transient metrics are inset. Heatmap of hierarchical clustered z-scores (color bar inset) for each metric under C) normokalemia and D) hypokalemia.

Nevertheless, such crude qualitative descriptions may not comprehensively capture all relevant torsadogenic and non-torsadogenic effects of this drug set, warranting an unbiased, systematic method to further dissect the utility of these datasets to predict TdP and non-TdP drugs. Therefore, we formed high-dimensional matrices (116 by 312) of pseudo-data from a total of 13 action potential and calcium transient metrics (Figure 1, inset) for normokalemic (Figure 1C) and hypokalemic (Figure 1D) single-cell conditions. Similarly, we formed high-dimensional matrices (116 by 234) of pseudo-data from the mean and standard deviation of these 13 metrics for corresponding transmural tissue conditions (Figure 2C-D).

Principal component analysis suggests the high-dimensional matrices of pseudo-data have distinct characteristics that depend on fidelity (i.e., single-cell versus tissue-level) and potassium levels (Figure 3A). For example, tissue-level classifiers had an overall lower explained variance across the first five principal components, while hypokalemic conditions led to lower explained variance in the first principal component relative to the corresponding normokalemic dataset (Figure 3A). To test the predictive power and utility of simulating drug effects on each condition, we incorporated the high-dimensional matrices of pseudo-data into a linear support vector machine.

### *9.3.2 Comparison of Classifier Performances*

Classifiers incorporating simulation data outperformed a classifier based on conventional hERG block data. These trends were independent of which drug datasets were included in the analysis (Figure 3B-C). For example, using all 116 drugs, auROC improved from approximately 0.8 for the conventional classifier to over 0.95 for all classifiers incorporating simulation data (Figure 3B), while the misclassification rate reduced from 38.8% to 13.8-24.1% (Figure 3C). To this end, the extent of LOOCV misclassification rate improvement was dependent on input simulation datasets; using the single-cell normokalemic dataset (S+N), the misclassification rate dropped to 24.1%, while the single-cell hypokalemic dataset (S+H) further reduced the misclassification rate to 18.1% (Figure 3C). Interestingly, hypokalemic conditions did not improve classification performance in tissue-level simulations. Using the tissue-level normokalemic dataset (T+N), the misclassification rate was 13.8%; under hypokalemia (T+H), this increased to 16.4% (Figure 3C). Hierarchical clustering shows both unique and common drugs correctly classified for each dataset (Figure 3D).

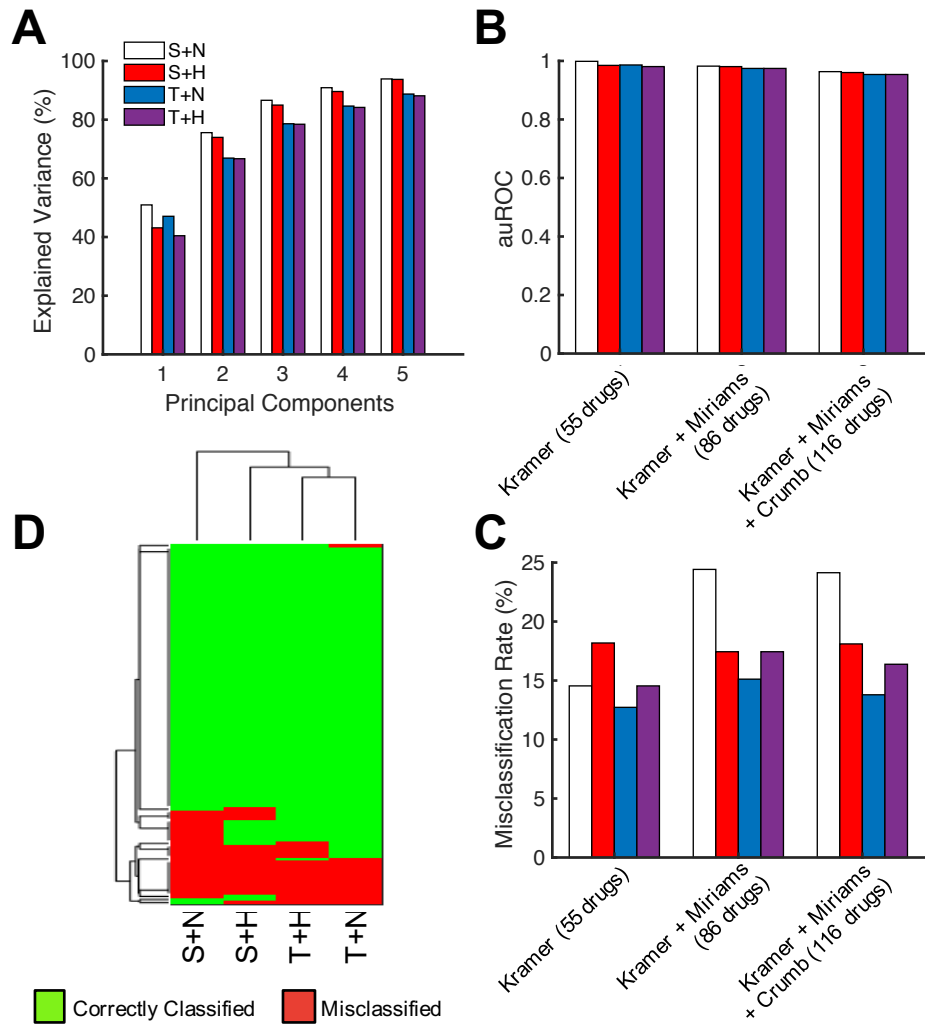


**Figure 3. Comparison of classifier performances.** A) Variance explained by the first five principal components. B) Area under the curve for receiver operating characteristic analysis (auROC) for S+N, S+H, T+N, and T+H datasets. C) Misclassification rates for S+N, S+H, T+N, and T+H datasets under LOOCV. D) Hierarchical clustering of drugs correctly classified (green) and misclassified (red) by each dataset.

To comprehensively compare classifier performances, we quantified misclassification rates head-to-head using identical training and testing datasets for both algorithms under holdout cross-validation. More specifically, we performed 100 cross-validation tests with 50%

(Figure 4A), 33% (Figure 4B), 25% (Figure 4C), and 10% (Figure 4D) holdout for the 116 drug panel. Consistent with our findings during LOOCV, we find that the T+N classifier outperformed S+N, S+H, and T+H classifiers (Figures 4B-4D); these effects were more noticeable at smaller holdout levels. Altogether, these findings suggest the T+N classifier outperforms all other classifiers tested, warranting further analyses to identify major electrophysiological features captured in the T+N classifier to differentiate between TdP and non-TdP drugs.

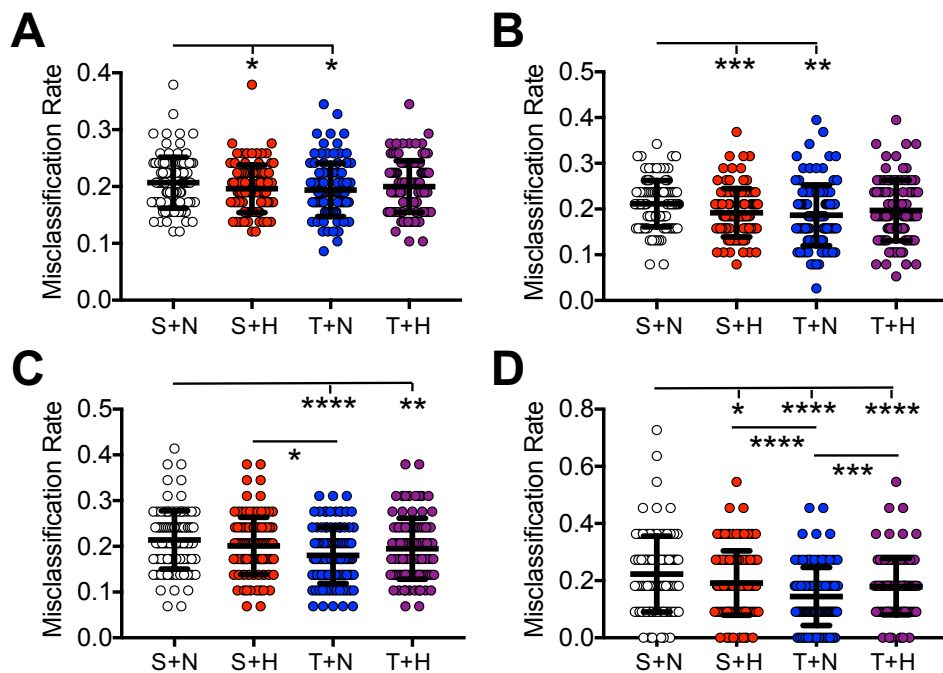


**Figure 4. Comparison of single-cell and tissue-level classifier performances.** A) Misclassification rates via A) 50%, B) 33%, C) 25%, and D) 10% holdout cross-validation for the S+N, S+H, T+N, and T+H classifiers using the Kramer et al.<sup>22</sup>, Mirams et al.<sup>23</sup>, and Crumb et al.<sup>24</sup> datasets. \* $p<0.05$ , \*\* $p<0.01$ , \*\*\* $p<0.001$ , \*\*\*\* $p<0.0001$  using repeated measures ANOVA.

### 9.3.3 Key Features of Normokalemic Tissue-Level Metrics

While principal components analysis helped uncover variations between our drug simulation pseudo-data high-dimensional matrices (Figure 3A), it provides limited physiological

insight into the predictive power of electrophysiological metrics. To identify key metrics that facilitate accurate drug classification, we performed feature selection on all metrics for S+N, S+H, T+N, and T+H datasets.

Complementing previous work,<sup>12</sup> action potential duration and diastolic calcium were top features of the S+N dataset (Figure 5A). For the S+H dataset (Figure 5A), there was a higher prevalence of action potential duration metrics as top features, as well as upstroke velocity, a characteristic known to be affected by hypokalemia.<sup>27</sup> In T+N, APD<sub>90</sub> heterogeneity and mean APD triangulation were most commonly selected as Features 1 and 2, respectively (Figure 5A). However, under hypokalemia (T+H), APD<sub>90</sub> heterogeneity was no longer the top feature, whereas mean upstroke velocity was top Feature 2. Altogether, this suggests APD<sub>90</sub> heterogeneity is a key metric for accurate classification of torsadogenic drugs.

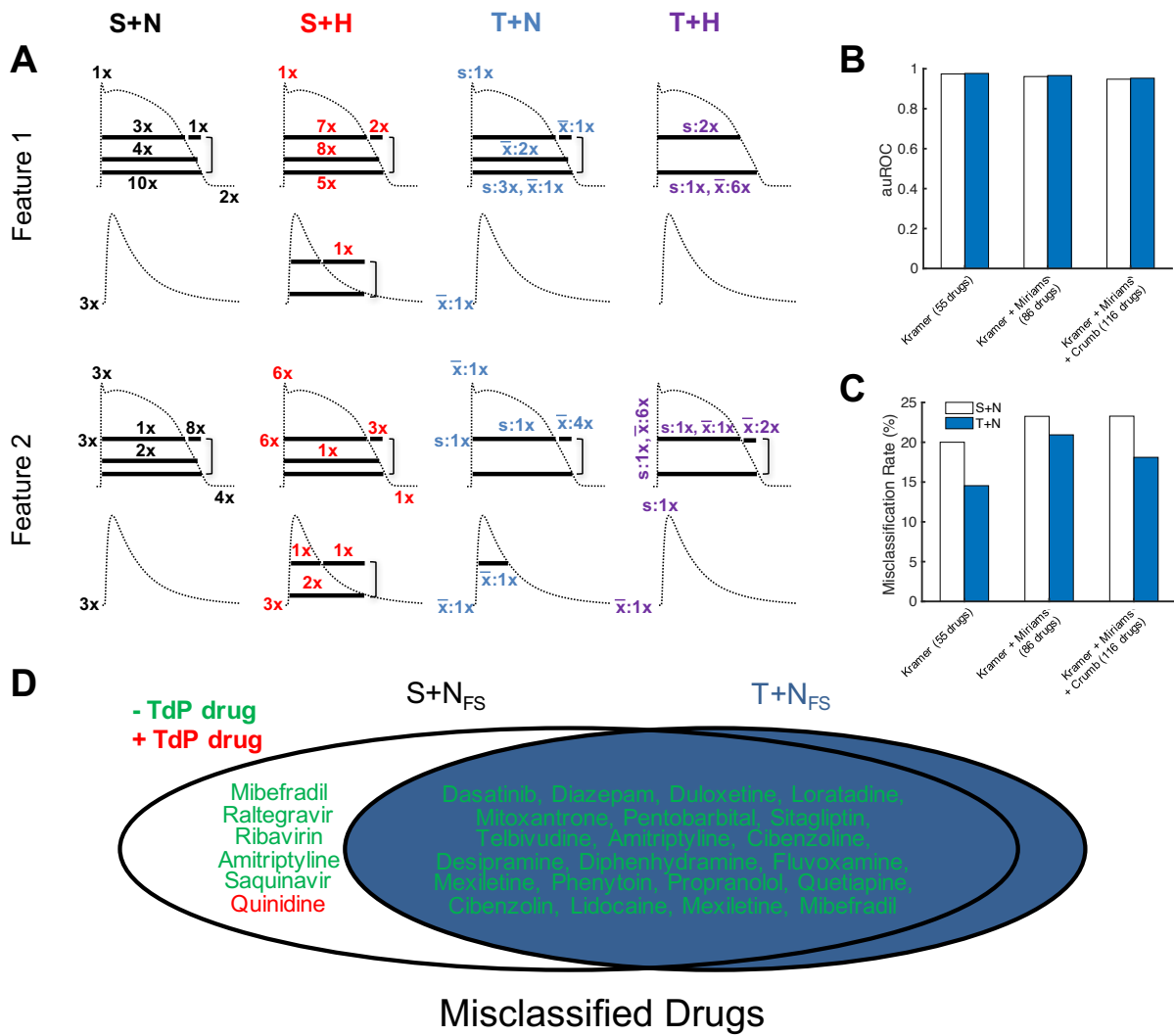


**Figure 5. Top features of classifiers.** A) Feature selection from S+N, S+H, T+N, and T+H classifiers led to several action potential and calcium transient metrics selected “x” number of times for single-cell, as well as tissue-level mean ( $\bar{x}$ ) and standard deviation (s) action potential and calcium transient metrics. B) auROC for top two features from normokalemic OVVR single-cell epicardial (S+N<sub>FS</sub>) and tissue-level models (T+N<sub>FS</sub>) at 1 Hz. C) Misclassification rates for S+N<sub>FS</sub> and T+N<sub>FS</sub> datasets under LOOCV. D) Venn diagram of misclassified drugs by S+N<sub>FS</sub> (left) and T+N<sub>FS</sub> (right) during LOOCV.

Interestingly, feature selection on the normokalemic OVVR single-cell epicardial ( $S+N_{FS}$ ) and tissue-level model ( $T+N_{FS}$ ) classifiers at 1 Hz both output diastolic calcium and APD at 50% repolarization as the top two features (Figure 5A). However,  $T+N_{FS}$  led to  $APD_{50}$  heterogeneity, rather than mean  $APD_{50}$ , as observed in  $S+N_{FS}$ . Thus, a direct comparison between  $T+N_{FS}$  and  $S+N_{FS}$  can provide physiological insight into the utility of single-cell versus tissue-level heterogeneity APD metrics in predicting torsadogenicity.

Similar to the trends using the overall datasets (Figure 3B-C),  $S+N_{FS}$  and  $T+N_{FS}$  led to similar auROCs (Figure 5B), whereas  $T+N_{FS}$  led to lower LOOCV misclassification rates (Figure 5C) independent of which drug datasets were included in the analysis. As shown in Figure 5D, six drugs were uniquely misclassified by  $S+N_{FS}$  (mibepradil, raltegravir, ribavirin, amitriptyline, saquinavir, quinidine), whereas no drugs were uniquely misclassified by  $T+N_{FS}$ . Importantly, one of the six misclassified drugs, quinidine, was a false negative in the  $S+N_{FS}$  classifier, a true positive in the  $T+N_{FS}$  classifier.

All misclassified drugs in the  $T+N_{FS}$  classifier during LOOCV were false positives, demonstrating the utility of APD heterogeneity and diastolic calcium as metrics for safely classifying torsadogenic drugs. Nevertheless, given that twenty-one false positives emerged from LOOCV for the tissue-level classifier, it is clearly still necessary to further improve accuracy of the classifier; classification improvement may be possible by obtaining a larger array of inhibition measurements on additional pumps, transporters, and channels that are not typically considered for inducing torsadogenicity.

#### 9.3.4 Simulations with hypothetical drug to identify unconventional modulators of TdP risk

To theoretically develop insight into potential atypical modulators of TdP risk, we generated 100 hypothetical drugs that alter the maximum ion flux parameters of the  $\text{Na}^+/\text{Ca}^{2+}$  exchanger, sarcoplasmic reticulum  $\text{Ca}^{2+}$  ATPase, background calcium current, background sodium current,  $I_{K1}$ , ryanodine receptor,  $I_{to}$ ,  $I_{Ks}$ , and the  $\text{Na}^+/\text{K}^+$  pump (each of which is distinct

from those targeted by the Kramer et al.<sup>22</sup> and Mirams et al.<sup>23</sup> drug sets). By simulating the electrophysiological effects of these hypothetical drugs on the OVVR,<sup>19</sup> tTP,<sup>20</sup> and GPB<sup>21</sup> normokalemic transmural tissues at 0.5, 1, and 2 Hz, we could apply the SVM classifier from the respective selected features (Figure 5A) to: 1) predict which hypothetical drugs would theoretically be torsadogenic; and 2) identify unconventional modulators of TdP risk via a Wilcoxon rank sum test between TdP and non-TdP drugs.

Figure 6A shows the wheel of fortune plots for each model at 0.5 Hz, 1 Hz, and 2 Hz pacing frequencies, where the top four statistically significant targets (parameter names inset, with the outermost parameter being the most statistically significant) have variable levels of correlation with distance from the decision boundary (labeled in Figure 6A as DfDB). In each wheel of fortune plot (Figure 6A), each radial slice represents one hypothetical drug's modulation of the top four statistically significant parameters and the resultant distance from the decision boundary. Targeted parameter's correlations with the distance from the decision boundary were dependent on the type of transmural model and pacing frequency (Figure 6A); therefore, to comprehensively identify the most significant targets across all models and pacing frequencies, we performed a Wilcoxon rank sum test and subsequent hierarchical clustering on all hypothetical drug sets (Figure 6B).

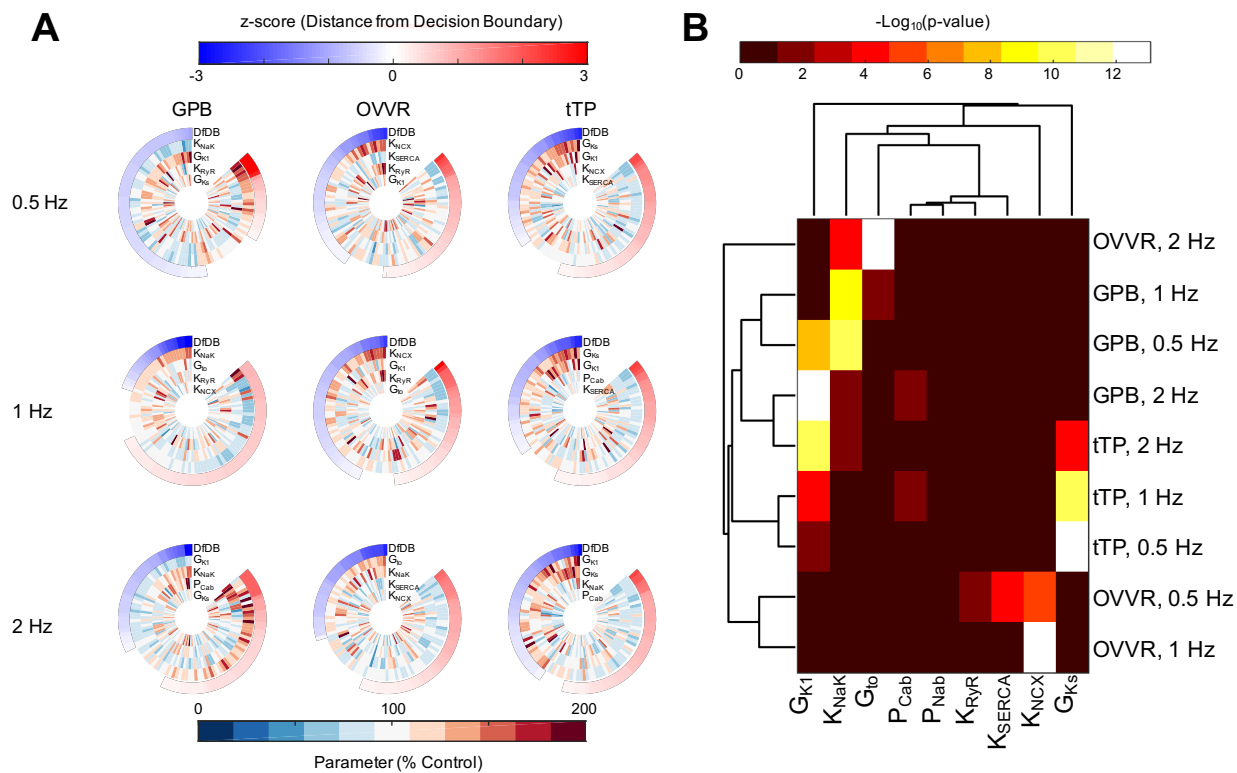


**Figure 6. Identification of potential TdP modulators using hypothetical drug set.**

Identifying the most important drug targets in a hypothetical drug set. A) Wheel of fortune plots for the OVVR,<sup>19</sup> tTP,<sup>20</sup> and GPB<sup>21</sup> models at 0.5 Hz, 1 Hz, and 2 Hz pacing frequencies. Each radial slice represents one drug's modulation of parameters (dark red-white-dark blue scalebar; top four statistically significant parameters shown) and the resultant distance from the decision boundary (light red-white-light blue scalebar). Slices are sorted counter-clockwise from most non-TdP distance (negative) to most TdP distance (positive) from the decision boundary. Targets were ordered based on statistical significance (outermost being the most statistically significant). Parameters were modulated for: Na<sup>+</sup>/Ca<sup>2+</sup> exchanger (K<sub>NCX</sub>), sarcoplasmic reticulum Ca<sup>2+</sup> ATPase (K<sub>SERCA</sub>), background calcium current (P<sub>cab</sub>), background sodium current (P<sub>nab</sub>), I<sub>K1</sub> (G<sub>K1</sub>), ryanodine receptor (K<sub>RyR</sub>), I<sub>to</sub> (G<sub>to</sub>), I<sub>Ks</sub> (G<sub>Ks</sub>), and the Na<sup>+</sup>/K<sup>+</sup> pump (K<sub>NaK</sub>). B) Hierarchical clustering of statistical significance for each parameter using the Wilcoxon rank sum test for the OVVR,<sup>19</sup> tTP,<sup>20</sup> and GPB<sup>21</sup> models at 0.5 Hz, 1 Hz, and 2 Hz pacing frequencies.

As shown in Figure 6B, the same models at different pacing frequencies generally clustered together, while drug targets clustered based on statistical significance. All targets, except for the background sodium current, were found to be statistically significant in at least one model (for a tabular form of target statistical analyses, see Online Table II). Based on the hierarchical clustering, it appeared that  $I_{K1}$  and  $I_{Ks}$  have the largest unconventional influence on TdP risk, and that off-target drug interactions with these ion transport pathways may further contribute to torsadogenic risk.

#### 9.4 Discussion

Developing an in silico method for distinguishing between torsadogenic and non-torsadogenic drugs has important implications for pharmaceutical companies. If such a classifier can sufficiently distinguish between drug toxicity (i.e., on par with experimental assays), it may reduce rejection of truly safe drugs and shift attrition of dangerous drugs early in the development process, thus avoiding the enormous investment of QT studies in humans and animals that provide marginal increase in predictive power. Alternatively, if such a classifier is insufficient (i.e., not as predictive as classical in vitro experimental assays), this work nevertheless provides insight into the continued need for such experimental assays, and potential avenues to improve classification. In this study, we investigate the predictive value of a machine-learning framework that incorporates in silico simulations of clinically relevant cardiac tissue-level electrophysiology for automated discrimination of TdP from non-TdP drugs.

Overall, this study provides: 1) a head-to-head comparison of classification performance of algorithms that incorporate normokalemic and hypokalemic single-cell simulation data versus corresponding higher-order tissue-level in silico measurements; 2) physiological insight into TdP by identifying key features, including APD heterogeneity, in the normokalemic tissue-level classifier that lead to its superior classification; and 3) predictions of unconventional targets of

drugs that may increase TdP risk. These findings support the use of tissue-level metrics to complement classifying torsadogenic risk, and demonstrate the promise of systematic quantitative physiology simulations in predicting electrophysiological TdP-toxicity.

#### *9.4.1 Physiological and empirical insight developed from the tissue-level classifier*

One of the many advantages of performing both single-cell and higher fidelity tissue-level simulations is that we can predict cellular and tissue-level electrophysiological drug responses, both of which are directly relevant to the experimental setting. Further, testing the role of normokalemic versus hypokalemic conditions on drug responses are directly relevant to the clinical setting. Altogether, our simulations can: 1) assist the design of in vitro cellular studies as well as ex vivo tissue-level studies by identifying which metrics derived from the action potential and calcium transient under normokalemia or hypokalemia are useful in predicting TdP risk (Figure 5); and 2) prioritize which conventional and unconventional channels to examine (Figure 6).

No assumptions on particular physiological responses to emphasize were made in classifier development. Instead, to maximize classification performance, we first used the entire drug simulation pseudo-data high-dimensional matrices as inputs to the classifier. However, this provides limited physiological insight; to address this, we exhaustively performed feature selection on all models (Figure 5). Interestingly, we found that for T+N, APD<sub>90</sub> heterogeneity and mean APD triangulation were most commonly selected as Features 1 and 2, respectively (Figure 5A). However, under hypokalemia (T+H), APD<sub>90</sub> heterogeneity was no longer the top feature, while mean upstroke velocity was top Feature 2. Altogether, this suggests APD<sub>90</sub> heterogeneity is a key metric for accurate classification of torsadogenic drugs.

Another important result was that a variety of targets—many of which have been previously hypothesized—were found to be unconventional targets of TdP. For example, as suggested by our simulations, the  $\text{Na}^+/\text{Ca}^{2+}$  exchanger has been proposed to play a role in torsadogenicity.<sup>28</sup> Furthermore, recipients of digoxin, which targets the  $\text{Na}^+/\text{K}^+$  pump, are at a higher risk of TdP even though it shortens the QT interval.<sup>29,30</sup> Finally,  $I_{\text{K}_1}$ ,  $I_{\text{K}_5}$ , and  $I_{\text{to}}$  were all statistically significant parameters when testing hypothetical drugs, and have already been proposed and investigated as drug targets.<sup>24</sup>

#### *9.4.2 Limitations and future work*

While T+N leads to an improved TdP classification performance, several limitations of this study should be noted. First, while our classifier developed herein includes a variety of pertinent tissue-level metrics, several remain omitted (due to computational expense), such as: 1) the vulnerable window, an established pro-arrhythmic marker;<sup>31,32</sup> 2) temporal dispersion of repolarization (previously described); 3) reverse-rate dependence;<sup>33</sup> and 4) APD/conduction velocity restitution slope. Other metrics suggested previously, such as the electromechanical window,<sup>34</sup> have also not yet been incorporated into the classifier. Second, a simple one-dimensional cable geometry with 50% endocardial cells and 50% epicardial was selected in this study for consistency, as Grandi et al. do not provide a midmyocardial cell formulation. However, more complex geometries that also include midmyocardial cells are relevant to TdP induction; for example, Akar et al. demonstrated that midmyocardial cells play a central role in the development of TdP arrhythmias in long-QT syndrome.<sup>17</sup> Third, this work does not account for pharmacokinetic risk factors<sup>35</sup> and structural heart diseases<sup>36-38</sup> known to enhance TdP risk. Such factors can be introduced into our model by assuming non-uniform drug penetrance throughout the tissue or introducing fibrosis, respectively.

Therefore, despite the high accuracy of the current T+N classifier in distinguishing between TdP and non-TdP drugs, future work should incorporate these limitations described in future versions of a tissue-level classifier in hopes to improve classification performance and develop further physiological insight into TdP.

## **9.5 Conclusions**

In summary, this study: 1) demonstrates linear support vector machine classifiers receiving tissue-level metric inputs under normokalemic conditions leads to superior performance; 2) provides physiological insight into the role of APD heterogeneity in superior classification; and 3) predicts of unconventional targets of drugs that may increase TdP risk. Our findings underscore the value of tissue-level assays for TdP risk, and present novel *in silico* approaches to enhance next-generation regulatory standards for drug cardiotoxicity screening.

## **9.6 Clinical Perspectives**

**9.6.1 Competency in Medical Knowledge:** Torsades de Pointes (TdP) is a rare but lethal form of polymorphic ventricular tachycardia, where a prolonged QT interval precedes cyclic shifting of the QRS axis. Drug-induced TdP is a leading cause of drug relabeling or withdrawal from the market, only second to drug-induced hepatotoxicity. In silico approaches may enhance next-generation regulatory standards for drug cardiotoxicity screening.

**9.6.2 Translational Outlook:** Simulating drug effects on higher fidelity representations of the human heart may lead to inexpensive and accurate drug cardiotoxicology screenings.

**References:**

1. Sauer AJ, Newton-Cheh C. Clinical and genetic determinants of torsade de pointes risk. *Circulation*. 2012;125:1684-1694
2. Yap YG, Camm AJ. Drug induced qt prolongation and torsades de pointes. *Heart*. 2003;89:1363-1372
3. Shah RR. Drug-induced qt interval prolongation: Does ethnicity of the thorough qt study population matter? *Br J Clin Pharmacol*. 2013;75:347-358
4. Shah RR. Can pharmacogenetics help rescue drugs withdrawn from the market? *Pharmacogenomics*. 2006;7:889-908
5. Fermini B, Hancox JC, Abi-Gerges N, et al. A new perspective in the field of cardiac safety testing through the comprehensive in vitro proarrhythmia assay paradigm. *J Biomol Screen*. 2016;21:1-11
6. Cavero I, Crumb W. Ich s7b draft guideline on the non-clinical strategy for testing delayed cardiac repolarisation risk of drugs: A critical analysis. *Expert Opin Drug Saf*. 2005;4:509-530
7. Shah RR. Drugs, qtc interval prolongation and final ich e14 guideline : An important milestone with challenges ahead. *Drug Saf*. 2005;28:1009-1028
8. Redfern WS, Carlsson L, Davis AS, Lynch WG, MacKenzie I, Palethorpe S, Siegl PK, Strang I, Sullivan AT, Wallis R, Camm AJ, Hammond TG. Relationships between preclinical cardiac electrophysiology, clinical qt interval prolongation and torsade de pointes for a broad range of drugs: Evidence for a provisional safety margin in drug development. *Cardiovasc Res*. 2003;58:32-45
9. Gintant G. An evaluation of herg current assay performance: Translating preclinical safety studies to clinical qt prolongation. *Pharmacol Ther*. 2011;129:109-119
10. Fermini B, Fossa AA. The impact of drug-induced qt interval prolongation on drug discovery and development. *Nat Rev Drug Discov*. 2003;2:439-447

11. Shah RR. Drug-induced prolongation of the qt interval: Regulatory dilemmas and implications for approval and labelling of a new chemical entity. *Fundam Clin Pharmacol.* 2002;16:147-156
12. Lancaster MC, Sobie EA. Improved prediction of drug-induced torsades de pointes through simulations of dynamics and machine learning algorithms. *Clin Pharmacol Ther.* 2016;100:371-379
13. Chvilicek JP, Hurlbert BJ, Hill GE. Diuretic-induced hypokalaemia inducing torsades de pointes. *Can J Anaesth.* 1995;42:1137-1139
14. Antzelevitch C. Role of transmural dispersion of repolarization in the genesis of drug-induced torsades de pointes. *Heart Rhythm.* 2005;2:S9-15
15. Antzelevitch C. Role of spatial dispersion of repolarization in inherited and acquired sudden cardiac death syndromes. *Am J Physiol Heart Circ Physiol.* 2007;293:H2024-2038
16. Antzelevitch C. Ionic, molecular, and cellular bases of qt-interval prolongation and torsade de pointes. *Europace.* 2007;9 Suppl 4:iv4-15
17. Akar FG, Yan GX, Antzelevitch C, Rosenbaum DS. Unique topographical distribution of m cells underlies reentrant mechanism of torsade de pointes in the long-qt syndrome. *Circulation.* 2002;105:1247-1253
18. Gomez JF, Cardona K, Martinez L, Saiz J, Trenor B. Electrophysiological and structural remodeling in heart failure modulate arrhythmogenesis. 2d simulation study. *PLoS One.* 2014;9:e103273
19. O'Hara T, Virag L, Varro A, Rudy Y. Simulation of the undiseased human cardiac ventricular action potential: Model formulation and experimental validation. *PLoS Comput Biol.* 2011;7:e1002061
20. ten Tusscher KH, Panfilov AV. Alternans and spiral breakup in a human ventricular tissue model. *Am J Physiol Heart Circ Physiol.* 2006;291:H1088-1100

21. Grandi E, Pasqualini FS, Bers DM. A novel computational model of the human ventricular action potential and ca transient. *J Mol Cell Cardiol*. 2010;48:112-121
22. Kramer J, Obejero-Paz CA, Myatt G, Kuryshev YA, Bruening-Wright A, Verducci JS, Brown AM. Mice models: Superior to the herg model in predicting torsade de pointes. *Sci Rep*. 2013;3:2100
23. Mirams GR, Cui Y, Sher A, Fink M, Cooper J, Heath BM, McMahon NC, Gavaghan DJ, Noble D. Simulation of multiple ion channel block provides improved early prediction of compounds' clinical torsadogenic risk. *Cardiovasc Res*. 2011;91:53-61
24. Crumb WJ, Jr., Vicente J, Johannesen L, Strauss DG. An evaluation of 30 clinical drugs against the comprehensive in vitro proarrhythmia assay (cipa) proposed ion channel panel. *J Pharmacol Toxicol Methods*. 2016;81:251-262
25. Champeroux P, Viaud K, El Amrani AI, Fowler JS, Martel E, Le Guennec JY, Richard S. Prediction of the risk of torsade de pointes using the model of isolated canine purkinje fibres. *Br J Pharmacol*. 2005;144:376-385
26. Baldi P, Brunak S, Chauvin Y, Andersen CA, Nielsen H. Assessing the accuracy of prediction algorithms for classification: An overview. *Bioinformatics*. 2000;16:412-424
27. Gettes L, Surawicz B. Effects of low and high concentrations of potassium on the simultaneously recorded purkinje and ventricular action potentials of the perfused pig moderator band. *Circ Res*. 1968;23:717-729
28. Milberg P, Pott C, Fink M, Frommeyer G, Matsuda T, Baba A, Osada N, Breithardt G, Noble D, Eckardt L. Inhibition of the na<sup>+</sup>/ca<sup>2+</sup> exchanger suppresses torsades de pointes in an intact heart model of long qt syndrome-2 and long qt syndrome-3. *Heart Rhythm*. 2008;5:1444-1452
29. Roden DM. Drug-induced prolongation of the qt interval. *N Engl J Med*. 2004;350:1013-1022

30. Ritter JM. Drug-induced long qt syndrome and drug development. *Br J Clin Pharmacol.* 2008;66:341-344
31. Mayourian J, Savizky RM, Sobie EA, Costa KD. Modeling electrophysiological coupling and fusion between human mesenchymal stem cells and cardiomyocytes. *PLoS Comput Biol.* 2016;12:e1005014
32. Mayourian J, Cashman TJ, Ceholski DK, Johnson BV, Sachs D, Kaji DA, Sahoo S, Hare JM, Hajjar RJ, Sobie EA, Costa KD. Experimental and computational insight into human mesenchymal stem cell paracrine signaling and heterocellular coupling effects on cardiac contractility and arrhythmogenicity. *Circ Res.* 2017;121:411-423
33. Cummins MA, Dalal PJ, Bugana M, Severi S, Sobie EA. Comprehensive analyses of ventricular myocyte models identify targets exhibiting favorable rate dependence. *PLoS Comput Biol.* 2014;10:e1003543
34. van der Linde HJ, Van Deuren B, Somers Y, Loenders B, Towart R, Gallacher DJ. The electro-mechanical window: A risk marker for torsade de pointes in a canine model of drug induced arrhythmias. *Br J Pharmacol.* 2010;161:1444-1454
35. Frommeyer G, Eckardt L. Drug-induced proarrhythmia: Risk factors and electrophysiological mechanisms. *Nat Rev Cardiol.* 2016;13:36-47
36. Pedersen HS, Elming H, Seibaek M, Burchardt H, Brendorp B, Torp-Pedersen C, Kober L, Group DS. Risk factors and predictors of torsade de pointes ventricular tachycardia in patients with left ventricular systolic dysfunction receiving dofetilide. *Am J Cardiol.* 2007;100:876-880
37. Torp-Pedersen C, Moller M, Bloch-Thomsen PE, Kober L, Sandoe E, Egstrup K, Agner E, Carlsen J, Videbaek J, Marchant B, Camm AJ. Dofetilide in patients with congestive heart failure and left ventricular dysfunction. Danish investigations of arrhythmia and mortality on dofetilide study group. *N Engl J Med.* 1999;341:857-865

38. Chugh SS, Reinier K, Singh T, Uy-Evanado A, Socoteanu C, Peters D, Mariani R, Gunson K, Jui J. Determinants of prolonged qt interval and their contribution to sudden death risk in coronary artery disease: The oregon sudden unexpected death study. *Circulation*. 2009;119:663-670

## Chapter 9 Supplementary Materials

### **Online Table I: Half-maximal Inhibitory Concentrations and Torsades de Pointes**

**Risk Definitions for All 116 Drugs Used in Study.** Drug inhibition of currents and respective torsadogenicity risk definitions. First 55 drugs were published in the Kramer et al. study.<sup>1</sup> Next 31 drugs were published in the Mirams et al. study.<sup>2</sup> Final 30 drugs were published in the Crumb et al. study.<sup>3</sup> We defined the torsadogenicity of the drugs in our training set using the CredibleMeds database (<https://www.crediblemeds.org>) and the study from Champeroux et al.<sup>4</sup> Non-standard abbreviations: Torsades de Pointes (TdP); Fast Sodium Channel, Early (Na Early); L-type Calcium Channel(CaL); Rapid Delayed Rectifier K<sup>+</sup> Chanel (hERG); Inward Rectifier K<sup>+</sup> Channel (K1); Fast Sodium Channel, Late (Na Late); Transient Outward Channel (TO); Slow Delayed Rectifier K<sup>+</sup> Chanel (KS); Maximal Effective Free Therapeutic Plasma Concentration (EFTPC<sub>max</sub>); Half-maximal inhibitory concentration (IC<sub>50</sub>); Data not available (NaN).

Drug Name	TdP Risk	Na Early IC <sub>50</sub> (nM)	CaL IC <sub>50</sub> (nM)	hERG IC <sub>50</sub> (nM)	K1 IC <sub>50</sub> (nM)	Na Late IC <sub>50</sub> (nM)	TO IC <sub>50</sub> (nM)	KS IC <sub>50</sub> (nM)	EFTPC <sub>max</sub> (nM)
Amiodarone	1	15900	1900	860	NaN	NaN	NaN	NaN	0.8
Astemizole	1	3000	1100	4	NaN	NaN	NaN	NaN	0.3
Bepridil	1	2300	1000	160	NaN	NaN	NaN	NaN	35
Ceftriaxone	0	555900	153800	445700	NaN	NaN	NaN	NaN	23170
Chlorpromazine	1	3000	3400	1500	NaN	NaN	NaN	NaN	38
Cilostazol	1	93700	91200	13800	NaN	NaN	NaN	NaN	128
Cisapride	1	337000	11800	20	NaN	NaN	NaN	NaN	3
Clozapine	1	15100	3600	2300	NaN	NaN	NaN	NaN	71
Dasatinib	0	76300	81100	24500	NaN	NaN	NaN	NaN	41

Diazepam	0	306400	30500	53200	NaN	NaN	NaN	NaN	29
Diltiazem	0	22400	760	13200	NaN	NaN	NaN	NaN	122
Disopyramide	1	168400	1036700	14400	NaN	NaN	NaN	NaN	742
Dofetilide	1	162100	26700	30	NaN	NaN	NaN	NaN	2
Donepezil	1	38500	34300	700	NaN	NaN	NaN	NaN	3
Droperidol	1	22700	7600	60	NaN	NaN	NaN	NaN	16
Duloxetine	0	5100	2800	3800	NaN	NaN	NaN	NaN	16
Flecainide	1	6200	27100	1500	NaN	NaN	NaN	NaN	753
Halofantrine	1	331200	1900	380	NaN	NaN	NaN	NaN	172
Haloperidol	1	4300	1300	40	NaN	NaN	NaN	NaN	4
Ibutilide	1	42500	62500	18	NaN	NaN	NaN	NaN	140
Lamivudine	0	1571400	54200	2054000	NaN	NaN	NaN	NaN	19540
Linezolid	0	2644500	105400	1147200	NaN	NaN	NaN	NaN	59110
Loratadine	0	28900	11400	6100	NaN	NaN	NaN	NaN	0.4
Methadone	1	31800	37400	3500	NaN	NaN	NaN	NaN	507
Metronidazole	0	2073200	177900	1340200	NaN	NaN	NaN	NaN	187000
Mibepradil	0	5600	510	1700	NaN	NaN	NaN	NaN	12
Mitoxantrone	0	93500	22500	539400	NaN	NaN	NaN	NaN	225
Moxifloxacin	1	1112000	173000	86200	NaN	NaN	NaN	NaN	10960
Nifedipine	0	88500	12	44000	NaN	NaN	NaN	NaN	8
Nilotinib	1	13300	17500	1000	NaN	NaN	NaN	NaN	172
Nitrendipine	0	21600	25	24600	NaN	NaN	NaN	NaN	3
Paliperidone	1	109000	193900	780	NaN	NaN	NaN	NaN	69
Paroxetine	1	9800	3900	1900	NaN	NaN	NaN	NaN	14
Pentobarbital	0	2686000	299000	1433900	NaN	NaN	NaN	NaN	5171
Phenytoin	0	72400	21900	147000	NaN	NaN	NaN	NaN	4360
Pimozide	1	1100	240	40	NaN	NaN	NaN	NaN	0.5
Piperacillin	0	2433800	1226000	3405100	NaN	NaN	NaN	NaN	1378000
Procainamide	1	746600	389500	272400	NaN	NaN	NaN	NaN	54180
Quinidine	1	14600	6400	720	NaN	NaN	NaN	NaN	3237

Raltegravir	0	824200	246700	782800	NaN	NaN	NaN	NaN	7000
Ribavirin	0	2997500	622500	967000	NaN	NaN	NaN	NaN	27880
Risperidone	1	43400	34200	260	NaN	NaN	NaN	NaN	2
Saquinavir	0	12100	1900	16900	NaN	NaN	NaN	NaN	130
Sertindole	1	6900	6300	33	NaN	NaN	NaN	NaN	2
Sitagliptin	0	1220800	147100	174700	NaN	NaN	NaN	NaN	442
Solifenacin	1	1500	4300	280	NaN	NaN	NaN	NaN	3
Sotalol	1	7013900	193300	111400	NaN	NaN	NaN	NaN	14690
Sparfloxacin	1	2555000	88800	22100	NaN	NaN	NaN	NaN	1766
Sunitinib	1	16500	33400	1200	NaN	NaN	NaN	NaN	13
Telbivudine	0	1095200	713900	422700	NaN	NaN	NaN	NaN	19720
Terfenadine	1	2000	930	50	NaN	NaN	NaN	NaN	9
Terodiline	1	7400	4800	650	NaN	NaN	NaN	NaN	145
Thioridazine	1	1400	3500	500	NaN	NaN	NaN	NaN	980
Verapamil	0	32500	200	250	NaN	NaN	NaN	NaN	88
Voriconazole	1	1550500	414200	490900	NaN	NaN	NaN	NaN	7563
Ajmaline	1	8200	71000	1040	NaN	NaN	NaN	NaN	1500
Amiodarone	1	4800	270	30	NaN	NaN	NaN	NaN	0.5
Amitriptyline	0	20000	11600	3280	NaN	NaN	NaN	NaN	41
Bepridil	1	3700	211	33	NaN	NaN	NaN	NaN	33
Chlorpromazine	1	4300	NaN	1470	NaN	NaN	NaN	NaN	38
Cibenzoline	0	7800	30000	22600	NaN	NaN	NaN	NaN	976
Cisapride	1	14700	NaN	6.5	NaN	NaN	NaN	NaN	4.9
Desipramine	0	1520	1709	1390	NaN	NaN	NaN	NaN	108
Diltiazem	0	9000	450	17300	NaN	NaN	NaN	NaN	122
Diphenhydramine	0	41000	228000	5200	NaN	NaN	NaN	NaN	34
Dofetilide	1	300000	60000	5	NaN	NaN	NaN	NaN	2
Fluvoxamine	0	39400	4900	3100	NaN	NaN	NaN	NaN	377
Haloperidol	1	7000	1700	27	NaN	NaN	NaN	NaN	3.6
Imipramine	1	3600	8300	3400	NaN	NaN	NaN	NaN	106

Mexiletine	0	43000	100000	50000	NaN	NaN	NaN	NaN	4129
Mibepradil	0	980	156	1800	NaN	NaN	NaN	NaN	12
Nifedipine	0	37000	60	275000	NaN	NaN	NaN	NaN	7.7
Nitrendipine	0	36000	0.35	10000	NaN	NaN	NaN	NaN	3.02
Phenytoin	0	49000	103000	100000	NaN	NaN	NaN	NaN	4500
Pimozone	1	54	162	20	NaN	NaN	NaN	NaN	1
Prenylamine	1	2520	1240	65	NaN	NaN	NaN	NaN	17
Propafenone	1	1190	1800	440	NaN	NaN	NaN	NaN	241
Propranolol	0	2100	18000	2828	NaN	NaN	NaN	NaN	26
Quetiapine	0	16900	10400	5800	NaN	NaN	NaN	NaN	33
Quinidine	1	16600	15600	300	NaN	NaN	NaN	NaN	924
Risperidone	1	102000	73000	150	NaN	NaN	NaN	NaN	1.81
Sertindole	1	2300	8900	14	NaN	NaN	NaN	NaN	1.59
Tedisamil	1	20000	NaN	2500	NaN	NaN	NaN	NaN	85
Terfenadine	1	971	375	8.9	NaN	NaN	NaN	NaN	9
Thioridazine	1	1830	1300	33	NaN	NaN	NaN	NaN	208
Verapamil	0	41500	100	143	NaN	NaN	NaN	NaN	81
Amiodarone	1	4577	1281	941	NaN	4577	3758	NaN	0.7
Amitriptyline	0	5760	1291	3660	NaN	5760	2543	2737	36.4
Azithromycin	1	NaN	NaN	70796	NaN	NaN	88764	470131	1937
Bepridil	1	2929	2808	149	NaN	2929	NaN	NaN	31.5
Chloroquine	1	NaN	NaN	6889	10595	NaN	NaN	NaN	249.5
Chlorpromazine	1	4536	8192	1118	9270	4536	NaN	NaN	34.5
Cibenzolin	0	21752	NaN	2097	NaN	21752	NaN	NaN	673
Cisapride	1	NaN	NaN	12	NaN	NaN	NaN	NaN	2.6
Diltiazem	0	NaN	112	6569	NaN	NaN	NaN	NaN	127.5
Dofetilide	1	NaN	NaN	1	NaN	NaN	NaN	NaN	2.1
Flecainide	1	6677	25599	692	NaN	6677	9266	NaN	752.9
Lidocaine	0	NaN	NaN	NaN	NaN	NaN	NaN	NaN	2560.4
Lopinavir	1	NaN	15601	5170	NaN	NaN	NaN	NaN	703.7

Mexiletine	0	NaN	NaN	NaN	NaN	NaN	NaN	NaN	2503.2
Mibepradil	0	5866	652	307	NaN	5866	NaN	NaN	10.6
Moxifloxacin	1	NaN	NaN	93041	NaN	NaN	NaN	50321	3562.5
Nilotinib	1	NaN	NaN	91	NaN	NaN	NaN	NaN	60.4
Ondansetron	1	NaN	22551	1492	NaN	NaN	NaN	NaN	358.5
Propafenone	1	3886	1550	481	NaN	3886	NaN	NaN	131
Quinideine	1	NaN	NaN	343	NaN	NaN	3487	4899	842.9
Quinine	1	24151	27178	5170	NaN	24151	79254	37453	3956.7
Ranolazine	1	NaN	NaN	6490	NaN	NaN	NaN	NaN	1948.2
Ritonavir	1	NaN	8228	5157	NaN	NaN	NaN	NaN	436.9
Rufinamide	0	NaN	264448	NaN	NaN	NaN	NaN	NaN	83126.9
Saquinavir	0	15568	3161	3477	NaN	15568	NaN	NaN	417.2
Sertindole	1	NaN	NaN	11	NaN	NaN	NaN	NaN	1.6
Sotalol	1	NaN	NaN	86369	NaN	NaN	NaN	NaN	14686.4
Terfenadine	1	NaN	700	19	NaN	NaN	NaN	NaN	9
Toremifene	1	NaN	NaN	NaN	NaN	NaN	NaN	NaN	26.3
Verapamil	0	NaN	202	499	NaN	NaN	NaN	NaN	45

**Online Table II: Target Statistical Analysis for Features Selected.** 100 hypothetical drugs were developed that alter the maximum ion flux parameters nine different channels/pumps/exchangers for each of three models at 0.5 Hz, 1 Hz, and 2 Hz pacing frequencies. p-values calculated based on a Wilcoxon rank sum test. Non-standard abbreviations: Na<sup>+</sup>/Ca<sup>2+</sup> exchanger (K<sub>NCX</sub>), sarcoplasmic reticulum Ca<sup>2+</sup> ATPase (K<sub>SERCA</sub>), background calcium current (P<sub>Cab</sub>), background sodium current (P<sub>Nab</sub>), inward rectifier K<sup>+</sup> current (G<sub>K1</sub>), ryanodine receptor (K<sub>RyR</sub>), transient outward current (G<sub>to</sub>), slow delayed rectifier K<sup>+</sup> current (G<sub>Ks</sub>), and the Na<sup>+</sup>/K<sup>+</sup> pump (K<sub>Nak</sub>), OVVR (O'Hara, Virág, Varró, and Rudy)<sup>5</sup>, tTP (ten Tusscher and Panfilov)<sup>6</sup>, GPB (Grandi, Pasqualini, and Bers)<sup>7</sup>.

Model	Pacing Frequency (Hz)	p-value
<b>GPB</b>	0.5	K <sub>NCX</sub> : 0.674041977471054 K <sub>Nak</sub> : 0.000000000205233 P <sub>Cab</sub> : 0.227563173440738 K <sub>SERCA</sub> : 0.377460277152025 P <sub>Nab</sub> : 0.576495411058863 G <sub>K1</sub> : 0.000000040518132 G <sub>Ks</sub> : 0.207013050292954 K <sub>RyR</sub> : 0.183263577262273 G <sub>to</sub> : 0.798628590836248
<b>OVVR</b>	0.5	K <sub>NCX</sub> : 0.000001628123625 K <sub>Nak</sub> : 0.930830507925886 P <sub>Cab</sub> : 0.271060476680985

		$K_{SERCA}: 0.000229790750870$ $P_{Nab}: 0.892289330801650$ $G_{K1}: 0.181314179474227$ $G_{Ks}: 0.343202909215237$ $K_{RyR}: 0.015521220408865$ $G_{to}: 0.529721100795771$
<b>tTP</b>	0.5	$K_{NCX}: 0.103680408358771$ $K_{NaK}: 0.972497583969101$ $P_{Cab}: 0.439959092937976$ $K_{SERCA}: 0.117533634148559$ $P_{Nab}: 0.634239146384027$ $G_{K1}: 0.019414630310622$ $G_{Ks}: 0.0000000000000078$ $K_{RyR}: 0.863138813112596$ $G_{to}: 0.654017566808777$
<b>GPB</b>	1	$K_{NCX}: 0.254382017007445$ $K_{NaK}: 0.000000000529340$ $P_{Cab}: 0.991501047525420$ $K_{SERCA}: 0.234250879398880$ $P_{Nab}: 0.677826936380097$ $G_{K1}: 0.963183583726357$ $G_{Ks}: 0.263367948838279$ $K_{RyR}: 0.202416735363476$ $G_{to}: 0.039117501790067$
<b>OVVR</b>	1	$K_{NCX}: 0.000000000000094$

		$K_{NaK}$ : 0.807475865906504 $P_{Cab}$ : 0.839987647721254 $K_{SERCA}$ : 0.326249222520009 $P_{Nab}$ : 0.503885099508908 $G_{K1}$ : 0.089352557309880 $G_{Ks}$ : 0.671051209677503 $K_{RyR}$ : 0.181294891670863 $G_{to}$ : 0.225720812569721
<b>tTP</b>	1	$K_{NCX}$ : 0.464129621655011 $K_{NaK}$ : 1.000000000000000 $P_{Cab}$ : 0.029594716070837 $K_{SERCA}$ : 0.224174619869185 $P_{Nab}$ : 0.614150947796915 $G_{K1}$ : 0.000113108633425 $G_{Ks}$ : 0.000000000033566 $K_{RyR}$ : 0.376695359072601 $G_{to}$ : 0.803650524291250
<b>GPB</b>	2	$K_{NCX}$ : 0.366347672402917 $K_{NaK}$ : 0.012919512672122 $P_{Cab}$ : 0.048508608081901 $K_{SERCA}$ : 0.410029169115338 $P_{Nab}$ : 0.354957628597884 $G_{K1}$ : 0.000000000000098 $G_{Ks}$ : 0.125508218879065 $K_{RyR}$ : 0.913678161080672

		$G_{to}: 0.233103135601288$
<b>OVVR</b>	2	$K_{NCX}: 0.152873794852429$ $K_{NaK}: 0.000155226698850$ $P_{Cab}: 0.450222030503043$ $K_{SERCA}: 0.071339359917748$ $P_{Nab}: 0.752599990813519$ $G_{K1}: 0.623323383747838$ $G_{Ks}: 0.752599990813519$ $K_{RyR}: 0.504721979166207$ $G_{to}: 0.000000000000754$
<b>tTP</b>	2	$K_{NCX}: 0.314079413146938$ $K_{NaK}: 0.045542639082389$ $P_{Cab}: 0.093829629452796$ $K_{SERCA}: 0.085996610819622$ $P_{Nab}: 0.327521547557602$ $G_{K1}: 0.00000000095069$ $G_{Ks}: 0.000029345008887$ $K_{RyR}: 0.261048049598572$ $G_{to}: 0.370052046628317$

### **Supporting References:**

1. Kramer J, Obejero-Paz CA, Myatt G, Kuryshev YA, Bruening-Wright A, Verducci JS, Brown AM. Mice models: Superior to the herg model in predicting torsade de pointes. *Sci Rep.* 2013;3:2100
2. Mirams GR, Cui Y, Sher A, Fink M, Cooper J, Heath BM, McMahon NC, Gavaghan DJ, Noble D. Simulation of multiple ion channel block provides improved early prediction of compounds' clinical torsadogenic risk. *Cardiovasc Res.* 2011;91:53-61
3. Crumb WJ, Jr., Vicente J, Johannesen L, Strauss DG. An evaluation of 30 clinical drugs against the comprehensive in vitro proarrhythmia assay (cipa) proposed ion channel panel. *J Pharmacol Toxicol Methods.* 2016;81:251-262
4. Champeroux P, Viaud K, El Amrani AI, Fowler JS, Martel E, Le Guennec JY, Richard S. Prediction of the risk of torsade de pointes using the model of isolated canine purkinje fibres. *Br J Pharmacol.* 2005;144:376-385
5. O'Hara T, Virag L, Varro A, Rudy Y. Simulation of the undiseased human cardiac ventricular action potential: Model formulation and experimental validation. *PLoS Comput Biol.* 2011;7:e1002061
6. ten Tusscher KH, Panfilov AV. Alternans and spiral breakup in a human ventricular tissue model. *Am J Physiol Heart Circ Physiol.* 2006;291:H1088-1100
7. Grandi E, Pasqualini FS, Bers DM. A novel computational model of the human ventricular action potential and ca transient. *J Mol Cell Cardiol.* 2010;48:112-121